LARGE p_T PROCESSES IN $p\overline{p}$ COLLISIONS AT 2 TeV

(Measurement of the $t\bar{t}$ Production Cross Section in $p\bar{p}$ collisions at $\sqrt{s} = 1.96$ TeV in the Dielectron Final States at the DØ Experiment)

THESIS SUBMITTED TO THE UNIVERSITY OF DELHI
FOR THE DEGREE OF

DOCTOR OF PHILOSOPHY

ASHISH KUMAR

SUPERVISORS: PROF. R. K. SHIVPURI
PROF. D. P. GOYAL

DEPARTMENT OF PHYSICS & ASTROPHYSICS
UNIVERSITY OF DELHI
DELHI 110 007
INDIA

2005

Declaration

This thesis presents a measurement of the top-antitop quark production cross section in proton-antiproton collisions at the centre-of-mass energy ($\sqrt{s}$) of 1.96 TeV in di electron decay mode using 384 pb $^{-1}$ of data collected with the Run II upgraded DØ detector at Fermilab. Most of the work presented in this thesis has been published or is in the process of publication.

This work has been done under the supervision of Prof. R. K. Shivpuri and Prof. D. P. Goyal. This work has been done by the candidate himself and to the best of his knowledge, no part of this work has earlier been submitted for any degree or diploma of this or any other university.

Ashish

(ASHISH KUMAR)

Candidate

R.K. Shivpuri

(Prof. R. K. SHIVPURI)

Supervisor

D P Goyal

(Prof. D. P. GOYAL)

Supervisor

M. P. Srivastava

Prof. M. P. Srivastava 24/8/05

Head

Department of Physics & Astrophysics

University of Delhi

Delhi 110 007

“Theory guides.
Experiment decides”.

–An old saying.

Dedicated To

My Grand Father, Parents & Shivpuri Sir

ACKNOWLEDGEMENTS

This dissertation marks the culmination of my long and arduous journey as a Ph.D. student and it is a great pleasure to express my gratitude to those people who have supported and helped me arriving finally and happily at this point. This page is devoted to them although it is almost impossible to mention every person by name and it is more than a word of thanks that I owe to them. I hope to be able to reciprocate someday by giving; perhaps to another set of people, what I have received from these.

First and foremost, I wish to express my heartfelt thanks to my thesis supervisor and mentor Prof. R.K. Shivpuri for introducing me to the arena of experimental particle physics and for his relentless care, undying support and excellent guidance during the last five precious years of my career. It is a privilege and pleasure to work with him and I was lucky enough to make my way to his lab. I must say that his care, dedication and planning for his students is remarkable. Despite being incredibly busy, the doors of his office was always open to me and he always took time to listen to whatever I needed to discuss and allowed me a lot of freedom in my research. His vast knowledge, deep insights, ability to approach problems from different perspectives and tremendous experience were laid out in front of me to learn from, and I did my best to not let such unique opportunity pass by. His enthusiasm and encouragement have made my years of work enjoyable and rewarding. I thank him for teaching the basics of particle physics in a unique and elegant manner. I started working with him on the QCD phenomenology and because of his able guidance all the results of the study were published in the PRD, which gave me confidence. Then he gave me the opportunity to work in the stimulating environment at the DØ experiment at Fermilab on the exciting topic "the top quark". He taught me more than just physics. I remember his emphasis for being flexible, adaptable and with strengthened roots. He has also been a guardian for me and always of tremendous help when I needed his useful advice and support. I have been so fortunate to have Prof. Shivpuri as my guide. I am also thankful to him for skimming this thesis thoroughly and patiently and carefully correcting the same.

I was also fortunate to have Prof. Brajesh Choudhary as my local guardian during my stay at Fermilab who provided invaluable help all along from the beginning. His long experience of working at Fermilab was of tremendous help. He has been guiding and generously supporting my efforts starting from finding the interesting analysis topic, making me understand the intricacies of the analysis, to the completion of analysis. He embedded me in the company of Harry Weerts and Bob Kehoe who helped

me a lot in making me learn the ropes and winds of cross-section analysis quickly. He has been very friendly, open and caring to me all along and I am very thankful for inspiring conversations and sagacious advice. His systematic approach, aggressive well-coordinated effort, marvelous insight in physics, incredible communication skill and brilliant way of cutting any topic to simple but not too simple was a source of inspiration for me. I owe a debt of gratitude for steady proof reading the drafts of this thesis and improving it in many aspects with his comments. I learnt a lot from his regular stimulating discussions on physics and beyond (here it does not refer to physics beyond the SM).

I express my sincere thanks to Prof. D. P. Goyal for his constant support, patience and trust in my work. I am obliged to the Head of Department of Physics, Prof. M. P. Srivastava for providing the necessary facilities in the department. I am also thankful to Prof. Feroze Ahmed for his regular encouragement. Special thanks to Werner Vogelsang (BNL) for the tremendous co-operation with theoretical calculations and important feedback during our adventure with direct photon study.

A special thank to Gene Fisk, at Fermilab, for his consistent support, care, encouragement during my stay here and for providing the opportunity to present my analysis results in the American Physical Society Meeting 2005 at Tempa, Florida. A special thanks to Harry Weerts for his encouragement and for providing the opportunity to attend the Hadron Collider Physics Symposium 2004 at Michigan State University.

Many thanks to the members of our center (CDRST) at Delhi consisting of Ashutosh Bhardwaj, Namrata, Kirti Ranjan, Sudeep Chatterjee, Ajay Shrivastava, Manoj Jha, Nayeem, Sushil Chauhan, Pooja Gupta, Ashutosh Srivastava and Shilpee Arora. This work would not have been accomplished without the open and friendly working atmosphere in the lab. The presence of knowledgeable colleagues who were always ready to help and support with their experience was an asset for me and it provided inspiration and boost. Working together has been a pleasure. I appreciate very much the constant help and useful advice from Ashutosh, Namrata and Kirti who were an invaluable resource. Manoj has been a valued friend for so many years. I thank him for the wonderful friendship and for the key help with his software skills. I would like to thank Shilpee for taking the pain of going through the fabric of my thesis to pin-point the co-ordinates of the corrections. I am thankful to Bipul Bhuyan for motivating me to join this field and for encouraging me throughout.

I was very lucky to have my senior Kirti alongside both at Delhi and at Fermilab. His experience, expertise and meticulousness has been of utmost help to me through-

out, particularly during the initial days when we were starting up with the analysis at DØ . I worked in close association with him in the top group and really enjoyed his company and learnt a lot from the day to day discussions regarding the analysis. Special thanks for his efforts in proofreading my thesis and hurling useful suggestions.

Running a mega-experiment such as DØ is a huge team effort. This study would not have been possible without the excellent work of all the people, scientists, as well as technical and the administrative staff, at the Tevatron Accelerator Complex and the DØ experiment. I want to thank the whole DØ collaboration and the Accelerator crew for the excellent progress over the last years in running the experiment and producing the data that I had the privilege to analyze.

I would like to thank several individuals for helping me in a multitude of ways while I was at DØ . Working with Bob was really a wonderful and enriching experience. I gained a lot from his tremendous knowledge of physics, experience with the DØ detector and expertise with top quark physics. I worked in close association with Joe Kozminski and his help made the tricky tasks of operating in the Top Group and learning the ropes at DØ easy. Joe was of tremendous help whenever I got stuck and he always spent time to make me understand the analysis techniques by coming to my platform. His experience with the top cross-section analysis and electron ID contributed greatly to the completion of my work on both the fronts. I owe a lot to him for the regular enlightening discussions I had which sharpened my understanding.

Further thanks go to the members of top group and its inspiring leadership (Aurelio Juste, Arnalf Quadt, Chris Tully, Christophe Clement, Lisa Shabalina and Flera Rizatdinova) for a stimulating work environment and lively meetings, and for the tremendous team work. Special thanks to Christophe who kept pushing forward the analysis through critical suggestions and crucial direction. I would like to thank Gordon Watts for discussions related to Luminosity and Len Christophek & Miroslav Kopal for feedback regarding trigger. I thank Jon Hays and Jan Stark for the fruitful discussions on electron ID. I am also thankful to Vishnu for discussions and suggestions whenever I needed them.

I really enjoyed working for the calorimeter operations and learnt a lot about the hardware issues through discussions with Dean Schamberger, Pierre Petroff, Robert Zitoun, and Leslie Groer. I thank Dean & Pierre for his time and patience, and for showing me how to fix hardware problems and pull cables. I would like to thank other members of the calorimeter group: Mike Arov, Junjie Jhu, Silke Duensing, Norm Buchanan, Matt Welstein, Ingo Torchiani, Adam Yurkewich and Jean Roch Vlimant.

I thank my Delhi colleagues at DØ , Kirti and Nayeem for the continuous cooperation and pleasant work atmosphere both at the place of stay and in the office, and also for making sure that life was never boring.

My stay at Fermilab has been made enjoyable by many of my friends and I would like to express my gratitude to them especially Burair, Sarosh, Venkat, Wade, Alex, Nikolac, Pieter, Prolay, Jyothsna, Subhendu, and Piyali. I would like to express my thanks to Shekhar & Tanuja for their care and regular dinners which reminded me of my home in India. Thanks to Vishnu & Madhu, Mrinmoy and Bornali, Shailesh & Vandana, Harpreet & Geeti, Prem & Prajkata, Mani Tripathi and Nirmalya for all the nice times I had with them which represented life away from physics.

Travelling back in time to the days of M.Sc., I would like to thank my teachers for their direction and motivation.. I would also like to thank my friends for their support and care: Adarsh, Puja, Sonika, Smitha, Sumit, Ashish Tyagi, Vishal, and Anurag. Going further back, I am grateful to my 'Alma Mater' Sainik School Tilaiya which gave me the firm foundation and pierced basic etiquette especially self discipline and punctuality into my veins.

I wish to express my deep gratitude to Mr. P.C. Gupta for his continuous motivation, encouragement and support. He is a terrific human being and a great inspiring force. I also thank Mr. G.D. Sharma, Mr. Rajendra Mishra, Mohammed Yunus, Dinesh Chandra and Satya Narayan for the continuous assistance.

I thank my best friends Deepak, Manish, Rajesh, Raman, Nitish, Gajadhar, Kushal, Waquar, Sujit, Sumit for sticking it out with me for marvelous moments. Special Thanks to Manoj Sir for his consistent love, support and encouragement over the years.

I would like to thank Department of Science and Technology (DST) and Council and Scientific and Industrial Research (CSIR), Govt. of India for the financial support.

Thanks, Maa and Papa, for a lifetime of unconditional love and endless understanding. I am grateful to my grandfather whose utmost care shaped my career. I am thankful to my brothers, sisters, uncles, aunts, cousins and nieces for their countless support , patience and encouragement they gave me which helped me accomplish what I wanted.

ASHISH KUMAR

LIST OF PUBLICATIONS

1. "*Measurement of the $t\bar{t}$ Production Cross Section in $p\bar{p}$ Collisions at $\sqrt{s}$=1.96 TeV in dilepton final states*", DØ Collaboration (V. M. Abazov et. al.), **Phy. Lett. B, 626, 55 (2005)**.

2. "*Study of Parton k_T Smearing Effects in Direct Photon Production at the Fermilab Tevatron*", Ashish Kumar et. al., **Phys. Rev. D, 68, 014017 (2003)**.

3. "*Study of direct photon production at the CERN LHC*", Ashish Kumar et. al., **Phys. Rev. D, 67, 014016 (2003)**.

Conference & DØ Notes

1. "*Measurement of the $t\bar{t}$ Production Cross Section at $\sqrt{s}$=1.96 TeV in Dilepton Final States using 370 pb^{-1} of DØ Data*" (**Preliminary DØ Results for Summer 2005 Conferences**), DØ Note 4850. To be submitted to PRD.

2. "*Measurement of the ttbar Production Cross section at $\sqrt{s}$ = 1.96 TeV in ee and $\mu\mu$ final states using 370 pb^{-1} of Pass 2 data*", S. Anderson et al., DØ Note 4827 (2005).

3. "*Electron Likelihood Study*", Ashish Kumar et. al., DØ Note 4769 (2005).

4. "*Measurement of the ttbar Production Cross section at $\sqrt{s}$ = 1.96 TeV in Dilepton final states*", S. Anderson et al., DØ Note 4683, 2004.

5. "*Measurement of the ttbar Production Cross section at center of mass energy 1.96 TeV in Dilepton final states*", S. Anderson et al., DØ Note 4623 (2004).

6. "*Calorimeter Event Quality Using Level 1 Confirmation*", K. Ranjan et. al. DØ Note 4554 (2004).

7. "*Oversmearing of Missing Transverse Energy in $Z \rightarrow ee + X$ Monte Carlo Events*", Ashish Kumar et. al., DØ Note 4551 (2004).

8. "*Missing Transverse Energy Studies in $Z \rightarrow ee + X$ and $Z \rightarrow \mu\mu + X$ Events*", Ashish Kumar et. al., DØ Note 4480 (2004).

9. "*Measurement of the ttbar Xsec in the dilepton channels at sqrt(s) = 1.96 TeV (topological)*", S. Anderson ... Ashish Kumar et al., DØ Note 4420 (2004).

Contents

1 Introduction & Phenomenological Motivation **1**

1.1 A Brief History of Particle Physics 2

1.2 The Standard Model 6

1.2.1 Fundamental Particles and Interactions 6

1.2.2 Electroweak Interactions 9

1.2.3 The Strong Interaction and QCD 9

1.2.4 Higgs Mechanism and Electroweak symmetry breaking 11

1.2.5 Limitations of the Standard Model 12

1.3 The Top Quark : The "King" of Fermions 14

1.3.1 Evidence for the existence of the top quark 14

1.3.2 The Road to the top quark discovery 17

1.3.3 What is so special about the Top Quark? 21

1.3.4 Role of the Top Quark Mass in the Standard Model 22

1.3.5 Top Quark Production 25

1.3.6 Top Quark Decay 30

1.3.7 Measurement of Top Pair Production Cross-section 33

1.3.8 Dilepton final states of $t\bar{t}$ 34

1.3.9 Top Quark Measurements at the Tevatron 36

1.3.10 An outline of the dissertation 38

2 The DØ Detector at Tevatron **40**

2.1 The Fermilab Accelerator Complex 41

2.1.1 Run II Upgrades 44

2.2 $p\bar{p}$ Collisions 45

2.3 Luminosity and Cross-Sections 46

2.4 Particle Detection at Collider Detectors 48

2.5 Overview of the DØ Detector in Run II 49

2.6 The DØ Detector Components 50

2.6.1 Coordinate System and Kinematic Quantities 51
2.6.2 Inner Tracking System 54
2.6.3 Preshower Detectors 56
2.6.4 Calorimeter System 58
2.6.5 DØ Calorimeters 59
2.6.6 Electromagnetic Calorimeter 60
2.6.7 Hadronic Calorimeters 61
2.6.8 Calorimeter Electronics 64
2.6.9 Calorimeter Performance 66
2.6.10 Muon System 67
2.7 Trigger and Data Acquisition(DAQ) Systems 68

3 Data and Monte Carlo Samples 71
3.1 Signal Triggers 71
3.1.1 Trigger efficiencies 74
3.2 Data Set 76
3.2.1 Data Quality Selection 77
3.3 Monte Carlo 80
3.3.1 Monte Carlo Samples 81

4 Event Reconstruction and Object Identification 84
4.1 Electrons 85
4.1.1 Electromagnetic Cluster Reconstruction 85
4.1.2 Electromagnetic Cluster Identification 88
4.1.3 Electron Likelihood 91
4.2 Electron Likelihood Studies 94
4.2.1 Sample Selection 94
4.2.2 Discriminating variables 95
4.2.3 Correlations 98
4.2.4 Kinematic dependences of variables 100
4.2.5 3-parameter Likelihood 100
4.2.6 Electron Efficiencies and Scale Factors 102
4.2.7 Electron Energy Resolution and Smearing 104
4.2.8 Electron Charge 106
4.2.9 Kinematic distributions of electrons 106
4.3 Jets 106
4.3.1 Jet Reconstruction 107

4.3.2 Jet Identification 109
4.3.3 Jet Energy Scale 110
4.3.4 Jet Energy Resolution 112
4.3.5 Jet/EM Separation 113
4.3.6 Jet Scale Factor 114
4.3.7 Kinematic Distributions of Jets 114
4.4 Missing Transverse Energy 115
4.4.1 Corrections to $\not\!\!E_T$ 117
4.4.2 Motivation for $\not\!\!E_T$ study 118
4.4.3 Study of $\not\!\!E_T$ behavior in data and Monte Carlo 118
4.4.4 $\not\!\!E_T$ Oversmearing 120
4.5 Vertex and Track 123
4.6 Primary Vertex Selection 124
4.6.1 Primary Vertex Cut Efficiencies, and Scale Factors 125

5 Measurement of $t\bar{t}$ Production Cross Section 126
5.1 Event Signature and Backgrounds 126
5.1.1 Physics Backgrounds 127
5.1.2 Instrumental Backgrounds 128
5.2 Event Selection and Optimization 129
5.2.1 Signal Selection Criteria 131
5.3 $t\bar{t}$ Event Selection Efficiencies 134
5.4 Estimation of Physics Backgrounds 136
5.4.1 $Z/\gamma^* \to \tau^+\tau^-$ 136
5.4.2 Diboson production (WW, WZ) 137
5.5 Instrumental Backgrounds : Fake $\not\!\!E_T$ 138
5.5.1 Method 139
5.5.2 $\not\!\!E_T$ and $\not\!\!E_T$ Fake Rates 140
5.6 Instrumental Backgrounds : Fake Electron 145
5.6.1 Electron Fake Rates 146
5.6.2 Background Yield 148
5.7 Expectations and Observations 150
5.7.1 Kinematic distributions 152
5.8 Systematic Uncertainties 159
5.9 Cross Section 163
5.9.1 Combined Dilepton Results 164

6 Summary **168**

A The parton model description of the top pair production **171**

B The $\sqrt{s}$ dependence of the $\sigma_{t\bar{t}}$ **173**

C Candidate Events **174**

List of Figures

1.1 A example of fermion triangle diagram which could cause an anomaly. 15
1.2 The Feynman diagrams describing the b quark decay in the Standard Model (a) and in the case when the b-quark is an isospin singlet (b,c). 16
1.3 B_d^0-$\overline{B_d^0}$ mixing diagrams. 16
1.4 Quark Masses and their uncertainties. 22
1.5 Virtual top quark loops contributing to the W and Z boson masses. . 23
1.6 Virtual Higgs boson loops contributing to the W and Z boson masses. 23
1.7 Lines of constant Higgs mass on a plot of the W boson mass (m_W) and the top quark mass (m_t) from ref.[69]. Contour curves of 65% confidence level in the (m_t,m_W) plane, for the indirect (LEP1, SLD data) and direct (LEP2, $p\overline{p}$ data) determination of the Higgs boson mass in a global fit to the electroweak precision data. 24
1.8 Single top quark production via the weak interaction. The main contributions at the Tevatron arise from the s-channel process (left) and the t-channel (right). 26
1.9 Lowest order Feynman diagrams for the production of $t\overline{t}$ pairs at the Tevatron : quark-antiquark annihilation and gluon-gluon fusion. . . . 26
1.10 The quark, anti-quark, and gluon densities on the proton as a function of the longitudinal momentum fractions x at $Q^2 = m_t^2$ from CTEQ5D [73]. 28
1.11 The top quark mass dependence of the $t\overline{t}$ cross-section at NNLO using CTEQ6M parton densities [80]. 29
1.12 Standard model decay of $t\overline{t}$ pairs into dilepton channel. 30
1.13 Pie chart of the event decay channels at Born level. 32
1.14 The highlights of Top quark mass measurements from Run 1. 37

2.1 Schematic of the Fermilab accelerator chain. Adapted from [105]. . . 42
2.2 Tevatron bunch scheme for Run I (top) and Run II (bottom). 45
2.3 Side view of the DØ detector [111]. 51

2.4 Diagram of p_T in the DØ coordinate system. 52
2.5 DØ tracking system [111]. 54
2.6 DØ Run II Silicon Microstrip Tracker detector. 55
2.7 Overall view of the DØ calorimeter system [111]. 60
2.8 A quarter of the calorimeter in the $r-z$ plane of the detector showing the tower geometry. 62
2.9 Unit Cell in the Calorimeter. 63
2.10 Calorimeter electronics readout chain [111]. 64
2.11 Calorimeter channel configuration in terms of depth and η. 65
2.12 Electronics signal shape from the calorimeter cell, after the preamplifier and after the shaper. 66
2.13 DØ trigger scheme with typical trigger rates (left). L1 and L2 trigger data pathway (right). 69

3.1 CEM(1,11) trigger turn-on curve. 75

4.1 Signal and background discrimination of 7 parameter likelihood in the central (left) and endcap (right) calorimeter regions. 94
4.2 Signal-to-background discriminations of f_{EM}, H-Matrix χ^2_{Cal7}, DCA, and E_T/p_T in the CC (left) and EC (right) 96
4.3 Signal-to-background discriminations of $Prob(\chi^2_{spatial})$, f_{iso}, number of tracks (N_{trks}) in 0.05 cone and total track p_T ($\sum p_T^{trk}$) in 0.4 cone in the CC (left) and EC (right) 97
4.4 Correlations between (a) f_{EM} and H-Matrixχ^2_{Cal7}, (b)f_{EM} and f_{iso}, and (c) χ^2_{Cal7} and f_{iso} for the signal sample in the central calorimeter region. 100
4.5 Signal-to-background discrimination of the 3-parameter likelihood in the CC (top-left) and EC (top-right). Background efficiency vs. signal efficiency after preselection for various 3-parameter likelihood cuts in the CC (bottom-left) and EC (bottom-right). 101
4.6 Background efficiency vs. signal efficiency for various likelihood cuts for the 4-parameter likelihood with E_T/p_T in the CC (top-left) and EC (top-right). Identical distributions for the 4-parameter likelihood with f_{iso} are shown in bottom-left and bottom-right plots. 102
4.7 Invariant dielectron mass spectrum in ee events with zero or more jets. The right plot is zoomed in the region of Z mass. 105

4.8 p_T, η and ϕ distributions of leading electron in $Z \to ee$ events. Distributions of dielecton system : $|\overrightarrow{p_T^{e1}} + \overrightarrow{p_T^{e2}}|$, $\Delta\phi(e^1, e^2)$ and $\Delta R(e^1, e^2)$. . 107
4.9 Distributions of good jet multiplicity and the five jet quality variables (EMF, CHF, HotF, n90 and L1Conf) in $Z \to ee$ events. 111
4.10 Distributions of p_T and η of leading (left) and next-leading (right) jets above p_T >20 GeV in $Z \to ee+ \geq 2$ jet events in data and Monte Carlo. 115
4.11 $\not\!\!E_T$ distributions in data and Monte Carlo for the inclusive Z sample (top-left), Z+ 0 jet events (top-right), Z+ 1 jet events (bottom-left) and Z+ ≥2 jets events (bottom-left). Effect of $\not\!\!E_T$ oversmearing is also demonstrated (discussed later). 119
4.12 $\not\!\!E_T$ fake rates in data and Monte Carlo for the inclusive Z sample (top-left), Z+ 0 jet events (top-right), Z+ 1 jet events (bottom-left) and Z+ ≥2 jet events (bottom-right). Effect of $\not\!\!E_T$ oversmearing is also demonstrated (discussed later). 120
4.13 $\not\!\!E_{xy}$ resolutions and the corresponding smearing factors vs unclustered Scalar E_T for inclusive inclusive Z sample (top-left), Z+ 0 jet events (top-right), Z+ 1 jet events (bottom-left) and Z+ ≥2 jet events (bottom-right). 122

5.1 Leading electron p_T (left) and $\not\!\!E_T$ (right) distributions in $Z/\gamma^*(\to \tau^+\tau^- \to e^+e^-\nu\overline{\nu})+ \geq 2$ jets events. 127
5.2 Leading electron p_T (left) and $\not\!\!E_T$ (right) distributions in $W^+W^-(\to e^+e^-\nu\overline{\nu})+ \geq 2$ jets events. 128
5.3 Distribution of sphericity in $e^+e^- + \geq 2$ jets events for $t\bar{t}$, WW, $Z \to \tau\tau$ and $Z \to ee$ Monte Carlo samples. 130
5.4 $\not\!\!E_T$ vs. invariant mass of the two electrons in the event. The distributions are shown after requiring two tight electrons and 2 jet cuts for: data (top left), top (top right), WW (middle left), WZ (middle right), $Z \to \tau\tau$ (bottom left), and $Z \to ee + 2$ jets Alpgen Monte Carlo. Also shown is the applied cut on $\not\!\!E_T$ vs electron invariant mass. 133
5.5 $\not\!\!E_T$ distributions for single photon, tight dielectron, and $Z \to ee$ Alpgen Monte Carlo samples with all cuts applied. The 1 jet case is on the left and ≥ 2 jet case on the right. 142
5.6 $\not\!\!E_T$ fake rates for single photon, tight dielectron, $Z \to ee$ Alpgen Monte Carlo samples with all cuts applied. The 1 jet case is on the left and ≥ 2 jet case on the right. 143
5.7 Electron fake rate, f_e, as a function of η_{det} for different jet multiplicities. 146

5.8 Electron fake rate f_e as a function of p_T for different jet multiplicities. The plot on the left shows CC electrons while the one on the right shows EC electrons. 147
5.9 Distributions of the p_T and η of the leading electron for the background, $t\bar{t}$ and data in $e^+e^- + \geq 2$ jets events (see line 3 of Table 5.11). . . . 153
5.10 Distributions of the p_T and η of the leading jet for the background, $t\bar{t}$ and data in $e^+e^- + \geq 2$ jets events (see line 3 of Table 5.11). 153
5.11 Distributions of the jet multiplicity on linear (left) and log (right) scales for the background, $t\bar{t}$ and in $e^+e^- + \geq 2$ jets events (see line 3 of Table 5.11). 154
5.12 Distributions of the H_T^{jet} (left) and sphericity (right) for the background, $t\bar{t}$ and in $e^+e^- + \geq 2$ jets events (see line 3 of Table 5.11). . 154
5.13 Distributions of the $\not{E}_T$ on linear (left) and log (right) scales for the background, $t\bar{t}$ and data in $e^+e^- + \geq 2$ jets events. (see line 3 of Table 5.11). 154
5.14 Distributions of the dielectron invariant mass (left) and $\Delta\phi(j^1, \not{E}_T)$ (right) for the background, $t\bar{t}$ and data in $e^+e^- + \geq 2$ jets events. (see line 3 of Table 5.11). 155
5.15 Distributions of the p_T and η of leading electron for the background, $t\bar{t}$ and data after requiring two jets and removing the Z window (Table 5.11). 155
5.16 Distributions of the p_T and η of leading jet for the background, $t\bar{t}$ and data after requiring two jets and removing the Z window (Table 5.11). 155
5.17 Distributions of the number of jet on linear (left) and log (right) scales in the event for the background, $t\bar{t}$ and data after requiring two jets and removing the Z window (Table 5.11) 156
5.18 Distributions of the $\not{E}_T$ on linear (left) and log (right) scales for the background, $t\bar{t}$ and data after Z mass cut (Table 5.11). 156
5.19 Distributions of the H_T^{jet} (left) and sphericity (right) for the background, $t\bar{t}$ and data after Z mass cut (Table 5.11). 156
5.20 Distributions of the p_T of leading (left) and next-leading (right) electron for the background, $t\bar{t}$ and data after all cuts. 157
5.21 Distributions of the η of leading (left) and next-leading (right) electron for the background, $t\bar{t}$ and data after all cuts. 157
5.22 Distributions of the number of jet (left) and dielectron invariant mass (right) in the event for the background, $t\bar{t}$ and data after all cuts.. . 157

5.23 Distributions of the p_T of leading (left) and next-leading (right) jet for the background, $t\bar{t}$ and data after all cuts. 158
5.24 Distributions of the η of leading (left) and next-leading (right) jet for the background, $t\bar{t}$ and data after all cuts. 158
5.25 Distributions of the H_T^{jet} (left) and H_T^e (right) for the background, $t\bar{t}$ and data aafter all cuts. 158
5.26 Distributions of the $\not\!\!E_T$ (left) and sphericity (right) for the background, $t\bar{t}$ and data after all cuts. 159
5.27 Expectation and Observation in different jet multiplicities before the sphericity cut (left) and and after all cuts (right). 159
5.28 Observed and predicted distributions for lepton p_T and η for the various backgrounds and the signal. 166
5.29 Observed and predicted distributions for the various backgrounds and the signal. From top to bottom, leading-lepton p_T, jet p_T, $\not\!\!E_T$, aplanarity, scalar sum of jet p_T (H_T) and scalar sum of jet p_T and leading lepton p_T (H_T). 167

6.1 The preliminary DØ results for the different cross-section analyses [175]. The bands represent the theoretical predictions for the $t\bar{t}$ cross-section, for m_t =175 GeV. Listed are the measured cross-sections from the different analyses, with their statistical and systematic uncertainties quoted separately. Also shown is the integrated luminosity on which each measurement is based. The result from the dilepton analysis discussed in the dissertation is also quoted as "dilepton topological (370 pb^{-1})". 170

A.1 The parton-model description of $t\bar{t}$ production. 171

B.1 QCD predictions for hard scattering cross sections at the Tevatron and the LHC. 173

C.1 Run 166779 Event 121971122: RZ view (upper right), XY view (upper left), Lego view (lower). Electrons, jets and $\not\!\!E_T$ are shown by red, blue and yellow respectively. 176
C.2 Run 170016 Event 16809090: RZ view (upper right), XY view (upper left), Lego view (lower). 177
C.3 Run 178177 Event 13511001: RZ view (upper right), XY view (upper left), Lego view (lower). 178

C.4 Run 178737 Event 50812363: RZ view (upper right), XY view (upper left), Lego view (lower). 179
C.5 Run 192663 Event 4006566: RZ view (upper right), XY view (upper left), Lego view (lower). 180

List of Tables

1.1 Three generations of elementary particles. 8
1.2 Fundamental forces and gauge bosons. 8
1.3 Summary of lower limits on the top-quark mass from searches at $p\overline{p}$ colliders. 20
1.4 Cross-sections at next-to-leading-order (NLO) in QCD for single top production at the Tevatron and LHC [71]. The associated uncertainties are ∼5%. 25
1.5 Theoretical predictions of the relative contributions from the quark-antiquark annihilation and gluon-gluon fusion processes to the leading order $t\bar{t}$ cross-section at the Tevatron and LHC. 29
1.6 Theoretical predictions for $t\bar{t}$ cross-section for m_t =175 GeV for Tevatron Run I, Run II and LHC. In the first technique, the full next to leading log (NLL) resummation is computed for the inclusive cross-section. 30
1.7 Leading order and best known branching fractions [70] of the real W^+ boson decay. Identical for the charge conjugates of the modes above (W^-). 31
1.8 Branching fractions [70] of the real τ^- lepton decay. 33
1.9 $t\bar{t}$ decay channels, Born level and best known branching fractions [70]. Leptonic decay of W include both the decay modes : $W \rightarrow \ell\nu$ and $W \rightarrow \tau\nu \rightarrow \ell + \nu\nu\nu$. The branching fractions considered for the DØanalyses are denoted by ee, $\mu\mu$ and $e\mu$, e+jets and μ+jets, and all-jets. 33
1.10 The Tevatron Run I results on top pair production cross-section, the theoretical prediction being 4.5-6.2 pb. 36
1.11 The Tevatron Run II results on top pair production cross-section. . . 38

2.1 Tevatron operating parameters in Run Ib and Run Run IIa. Run Ib is the period of running from 1992 to 1996 and Run IIa is the period of running which started in 2002 and is still in progress. 45
2.2 Layer depths in the calorimeter. 61

3.1 Summary of the dielectron triggers broken down by trigger list version. 73
3.2 Breakdown of integrated luminosities by trigger list version at the different satges. 77
3.3 Monte Carlo samples used in the present analysis, together with generators, parton diustribution function, number of events and cross section for the various processes. The cross sections indicated for the inclusive Pythia $Z \to ee$ and $Z \to \mu\mu$ samples are for the central mass bins and derived from the DØ measured cross sections. The cross section for the Pythia $Z \to \tau\tau$ sample is also derived from the cross section measured in data. 83

4.1 Correlation coefficiencts between the discriminating variables for the signal sample in the central (top) and endcap (bottom) calorimeter. 99
4.2 Single medium electron efficiencies in $Z \to ee$ data and Pythia Monte Carlo integrated on the whole data and Monte Carlo samples. The errors on the efficiencies are statistical only. These efficiencies are valid for the 15 GeV p_T cut used in the dielectron analysis. 103
4.3 Scale factors and oversmearing parameters for MC electrons [151]. . 105
4.4 Energy resolution parameters for high-p_T electrons [151]. 105
4.5 Efficiencies and scale factors for oppositely charged electron pairs when both are in CC, one of them in CC, and both in EC. 106
4.6 Jet energy resolution constants for jets in data and Monte Carlo. . . 113
4.7 Oversmearing parameters for each jet multiplicity bin obtained from the fit parameters in Figure 4.13 123
4.8 Primary vertex cut efficiencies (in %) in Zee data and MC and a scale factor as a function of jet multiplicity. All errors are statistical. . . . 125

4.9 Primary vertex scale factors used in the dilepton channels. Statistical errors are taken as the uncorrelated sum of the statistical errors from the dielectron and dimuon samples. Where statistically significant, the differences in efficiencies between $Z \to ee$ and $Z \to \mu\mu$ are taken as systematics. This is the case for the primary vertex efficiency in events with one or more jet bin efficiency and for the distance between the $d0reco$ and the $d0root$ primary vertices. 125

5.1 Event selections in the $t\bar{t} \to ee$ analysis. "Tight" refers to tight electron identification criteria in section 4.1.2. 132

5.2 Efficiencies of object identification and kinematic selection on $t\bar{t} \to ee$ Monte Carlo.. The efficiency is computed with respect to $t\bar{t} \to ee$ events where both electrons are allowed to come from either $W \to e$ or $W \to \tau \to e$. The scale factors for which systematic and statistical errors are correlated among channels are given without errors, and their uncertainties are instead included in the section 5.8. 134

5.3 Summary of the correction factors relating Monte Carlo and data efficiencies. Errors are statistical only. 135

5.4 Predicted diboson backgrounds at each cut level. Errors are statistical only. 138

5.5 $\not\!\!E_T$ fake rates measured in the tight sample, in the single photon sample and in Alpgen Z+1 jet and Z+2jet Monte Carlo. 144

5.6 $\not\!\!E_T$ fake ratios, numbers of tight events below the $\not\!\!E_T$ cut, and total expected $\not\!\!E_T$ fakes for the last two cut levels. 144

5.7 Signal and physics backgrounds contribution to N_{Tight} for the last two cut levels. 144

5.8 Electron fake rate f_e for different jet multiplicities. 147

5.9 Numbers of events in data with one tight and one loose electron, N_{lt}, passing the progression of cuts listed. 148

5.10 Numbers of events in data with two loose electrons, N_{ll}, passing the progression of cuts listed. 149

5.11 Expected signal and different backgrounds at each level of selection. Errors are statistical and systematic added in quadrature. 150

5.12 Observation in data and total expectation from signal and backgrounds at the different levels of selection. Errors are statistical and systematic added in quadrature 151

5.13 Summary of expectations and observations alon with statistical and systematic errors for $t\bar{t}$ in the $\rightarrow ee$ channel. 151
5.14 Signal Efficiency, Signal to background Ratio and Figure of Merit at different levels after the 2 jet requirement and also comparison with the previous Analysis using 243 pb^{-1} data. 152
5.15 Summary of the relative systematic uncertainties for signal and backgound in % 163
5.16 Number of observed events, estimated background , $t\bar{t}$ selection efficiency, decay branching ratio for $t\bar{t} \rightarrow e^+e^- + X$, and integrated luminosity for the dielectron channel. 164
5.17 Expected background and observed and expected signal yields. The expected signal yield assumes a 7 pb production cross section. The errors shown are the quadratic sum of the statistical and the systematic errors. 165
5.18 Number of observed events, estimated background, $t\bar{t}$ selection efficiency, decay branching ratio for $t\bar{t} \rightarrow ll' + X$ including the $W \rightarrow \tau\nu \rightarrow (e, \mu)\nu\nu$ contribution, and integrated luminosity for each channel. 165
5.19 Summary of systematic uncertainties on $\sigma_{t\bar{t}}$. 166

C.1 Kinematics for event 121971122 in run 166779. 174
C.2 Kinematics for event 16809090 in run 170016. 174
C.3 Kinematics for event 13511001 in run 178177. 175
C.4 Kinematics for event 50812363 in run 178737. 175
C.5 Kinematics for event 4006566 in run 192663. 175

Chapter 1

Introduction & Phenomenological Motivation

"If the universe is the answer, what was the question?" –Leon Lederman.

Particle physics, as a unique discipline, endeavors to address the fundamental questions of the universe we live in. It strives to describe the physical world as fundamentally as possible by identifying the most basic building blocks of nature and understanding the basic forces that operate amongst them. As a philosopher looks at the world and wonders what it all means, a particle physicist will wonder what it's all made of and what makes this work. Historically, what is meant by a fundamental particle has changed as physicist's knowledge has improved and experiments have probed deeper and deeper unveiling different levels of substructure. During the 20th century, physicists made great strides in this field. The current culmination of this centuries long human effort can be best described in what is called the "Standard Model" of particle physics. This chapter starts with a brief overview of the particle physics and the Standard Model, and then it reviews the role of the top quark in the context of the Standard Model and presents the motivation of the measurement of top quark cross-section and properties. In addition previous experimental measurements

of the top quark cross section and mass are reviewed.

1.1 A Brief History of Particle Physics

The quest of mankind to understand the fundamental building blocks of nature has a long, rich history. The ancient Indians believed the universe to be made of five basic elements: space, earth, air, fire, and water. Similar views also prevailed in other civilizations as well. About 600 B.C., an Indian philosopher named Kanada formulated some ideas about the indivisible particles. These were further pursued by the Greek philosophers Leucippos and Democritus in 500 B.C. who proposed that everything on earth was composed of small indivisible entities, - "the atomos", the Greek word for indivisible. This concept reduces the great diversity of macroscopic phenomena to a small number of fundamental structures and their interactions. This understanding has evolved from its roots in natural philosophy and metaphysics into an area of natural science in which experiments attempt to confirm or disapprove theories that describe the nature of the elementary constituents.

The Democritus' idea remained philosophical until 1802 when Dalton propounded the atomic theory which considered chemical elements to be made up of atoms. Mendeleev organized the elements into a periodic table in 1869 which predicted the existence of additional elements. It helped cement the Dalton's view. The theory of atoms represents a first important step towards the understanding of nature. By 1900 there were over 80 known elements which led to postulate that the atoms are made of smaller, 'sub-atomic' constituents.

Modern particle physics began, one might say, in 1897, when J.J. Thompson discovered the electron, which confirmed the idea of atomic substructure [1]. Throughout the next several decades chemists and physicists worked to understand the structure of the atom. The classical physics of Newton and Maxwell did not describe the emerging world inside the atom. The work of Max Planck, Niels Bohr, Werner Heisenberg,

Erwin Schrődinger and others heralded the birth of quantum mechanics, a new set of physical laws to describe the behaviour of particles at the microscopic scale [2]. In 1911, Rutherford demonstrated that atoms consist of a compact positively charged nucleus and a cloud of negative charge from electrons [3]. Later, with the discovery of protons (1919) and neutrons (1932) [4], it became clear that the nucleus is composed of neutrons and protons. Thus by the early 1930's, physicists had succeeded in developing an understanding that ordinary matter consists of three particles : protons, neutrons and electrons.

However, the theory raised new problems. One such problem was the compactness of nucleus. Confining several positive charges into such a small region (1fm=10^{-15} m) results in a strong repulsive electrostatic force. If any nuclei are to be stable then the protons must be bound together by a force powerful, enough to overcome this repulsion. This force was called the 'strong' force.

In 1927, Paul Dirac combined the theory of relativity and quantum mechanics into a single theory called 'quantum field theory' (QFT)[5] . In doing so, he also predicted the existence of 'antimatter' particles, each of which has the same mass but opposite charge as its corresponding matter particle. The discovery of the anti-electron (positron) in 1933 was a triumph of Dirac's theory and it soon became apparent that the structure of nature was much more complicated.

The observation of radioactive decay of atomic nuclei in 1930 added another piece to the puzzle. Enrico Fermi associated these decays with neutron decay which produces a proton, an electron and an anti-neutrino, a new species of particles [6]. This process can be explained by neither electromagnetic nor strong interactions, and so requires a new type of process called 'weak' interactions.

The advent of modern particle physics as a distinct field of study began in 1940s with the work of Feynman, Schwinger, and Tomonaga, who developed quantum electrodynamics (QED) [7], which explained electromagnetic phenomena at a basic level

in terms of the exchange of photons (the particles of light). The QED predictions were tested with striking precision and success. Thus by the mid-1930s the overall picture was emerging that the description of particle physics needed a quantum field theory incorporating electromagnetic, strong and weak interactions.

Yukawa in 1934 postulated that strong interaction is transmitted via the exchange of a particle called 'pion' between the proton and the neutron [8]. Anderson and Neddermeyer searched for this particle in cosmic rays, but found itself a different particle called the muon (μ). The muon is a particle with the same quantum number as the electron, but with a larger mass. Eventually the pion was discovered by Cecil Powell in cosmic ray experiments at Bristol in 1947.

Throughout the 1940s and 1950s, a bewildering variety of particles were found in scattering experiments. This was referred to as 'particle zoo'. The emergence of powerful particle accelerators and detectors showed us the only plausible and attractive path to learn about the heart of the matter at the smallest scale. In an attempt to organize these particles they were classified into leptons (light weight), mesons (medium weight) and baryons (heavy weight). The electron, muon, and the neutrino belonged to the species of leptons. Murray Gell-Mann organized the hadrons (mesons and baryons) further in 1961 with his Eightfold way, reminiscent of the periodic table of elements. The increasing no of hadrons suggested substructure, analogous to the atomic substructure suggested by the periodic table of atoms.

In 1960-64, Gell-Mann and Zweig proposed the 'quark model' according to which the hadrons were made out of three fundamental constituents called 'quarks', which were of three types denoted by up, down, and strange (u,d,s) [9]. Mesons are composed of a quark-antiquark pair and baryons are comprised of three quarks. By enumerating all possible combinations this model accounted for all the hadrons then observed, and also predicted the existence of a new particle, the Ω^-. A major success of the static quark model was the observation of Ω^- in 1964. In the late 1960s scattering

of electrons off protons at the End Station A experiments at SLAC demonstrated the existence of substructure in the proton, in a manner very similar to the way the scattering experiments of Rutherford proved the existence of substructure in the atom.

In 1974, a fourth quark called 'charm' was discovered (at SLAC and BNL) and the quark model emerged as a fundamental theory of particle physics. This was because of the fact that the structure and characteristics of all known hadrons could be explained in terms of the 'quarks'. Another 'quark', the 'bottom' quark was discovered in 1977 and the last quark 'top' was discovered in 1995. Also in 1970s, a new theoretical framework was being developed to explain the interactions between quarks called Quantum Chromodynamics (QCD). Throughout the 1970s, physicists worked to put together the theories into a self-consistent whole. Glashow, Salam and Weinberg unified the electromagnetic and weak interactions into the electroweak theory [10] [11] [12], which, together with Quantum Chromodynamics, forms the Standard Model (SM) of particle physics. However, the fourth fundamental force of nature, gravity, which is perhaps the most important for all the macroscopic phenomena, is not included in the theoretical framework of the SM.

In fact, high energy physics is widely used as a synonym for particle physics, which gets its name because high energies are needed to create fundamental particles and to probe the sub-structures of particles and forces between them at distances of the order of 10^{-15}m [13],[14] . The usual method to achieve these high energies is to accelerate particles, such as protons and electrons, and collide them. By measuring characteristics of the particles produced in the debris of the collision we gain an insight into the fundamental particles and their interactions.

According to our present status of knowledge, leptons and quarks are elementary i.e, they are point-like and do not appear to have a substructure. Our present understanding of the elementary particles and their interactions is encapsulated in the

Standard Model of particle physics [15] . The Standard Model is in fact a comprehensive theory which has been extremely successful and describes nature remarkably well.

1.2 The Standard Model

The Standard Model (SM) [16] [17] [18] is the theoretical basis of modern particle physics which cohesively binds the amalgamation of all of the last century's data of elementary particles and their interactions. Formulated in the 1960s and 1970s, it has withstood close to four decades of experimental tests and provides a very good description of all currently observed phenomena (at distance scales of $\approx 10^{-15}$m). Predictions associated with the model have been confirmed by many experiments to a spectacular degree of precision. An excellent review of the SM cornerstones as well as the experiments that have confirmed it can be found in [19].

1.2.1 Fundamental Particles and Interactions

According to the SM, there are two classes of fundamental particles that shape our universe: the spin $\frac{1}{2}$ fermions, which are the matter particles and spin 1 gauge bosons, which are the force carriers between fermions.

The fermions are further classified into leptons (l) and quarks (q). There are six flavors of leptons : the electron (e), the muon (μ), the tau (τ), and their corresponding neutrinos (ν_e, ν_μ, ν_τ). The charged leptons interact via the electromagnetic and weak forces, while the neutrinos which carry no charge interact only via the weak force. In the SM, the neutrinos were presumed to be massless, but experimentally their masses have been constrained to be quite small [20] .

There are also six flavors of quarks : up (u), down (d), charm (c) , strange (s), top (t) and bottom (b). Unlike the leptons, they possess fractional electric charges

- either $+\frac{2}{3}$e or $-\frac{1}{3}$e, where e is the charge of the electron. In addition, quarks also possess an internal degree of freedom called color (color was proposed to eliminate Pauli exclusion principle violations within hadrons), which can take three possible states : red, blue and green. In strong interactions, color plays a role similar to the role of electric charge in electromagnetic interactions. Quarks interact via the strong force as well as the electromagnetic and weak forces. The strong interaction binds the quarks into a spectrum of particles called hadrons, such as nucleons : proton (uud) and neutron (udd).

Table 1.1 lists the fundamental fermions and a few of their most important properties [21] . The leptons and quarks are grouped in three families or generations. Those in the first generation including the electron, up and down quarks constitute all of the ordinary matter that we are familiar with. Two other families are the replications with higher masses. These particles can be produced in cosmic rays and in high-energy particle collisions. Thus we have 24 fundamental fermions: 6 leptons & 18 quarks.

Each particle in Table 1.1 has a corresponding antiparticle which has the same mass and spin, but opposite values for some other properties, such as electric charge. For example, the positron (e^+) and anti-neutrino ($\overline{\nu_e}$) are the anti-particles of the electron (e) and electron neutrino (ν_e), respectively. This brings the total number of fundamental fermions to 24x2=48. Combinations of these fundamental particles make up the visible matter in the universe. For instance, the six quarks combine in particle-antiparticle pairs (mesons), or in particle or antiparticle triplets (baryons), to form all of the known hadrons.

The fermions interact with each other via the three forces contained in the Standard Model: strong, electromagnetic and weak forces. The fourth physical force, gravity, is not addressed by the Standard Model. In reality, the gravitational force is much weaker to have any effect on the dynamics of particles studied here. The gauge

Gen	Leptons (spin=$\frac{1}{2}$)			Quarks (spin=$\frac{1}{2}$)		
	Flavors	Charge	Mass (MeV)	Flavors	Charge	Mass (MeV)
1	e	-1	0.511	u	$+2/3$	$1.5-4.5$
	ν_e	0	$< 3\times10^{-6}$	d	$-1/3$	$5-8.5$
2	μ	-1	105.7	c	$+2/3$	$(1.0-1.4)\times10^3$
	ν_μ	0	< 0.19	s	$-1/3$	$80-155$
3	τ	-1	1777	t	$+2/3$	$(178.0\pm4.3)\times10^3$
	ν_τ	0	< 18.2	b	$-1/3$	$(4.0-4.5)\times10^3$

Table 1.1: Three generations of elementary particles.

bosons are the mediators of the forces between different particles. The Standard Model treats each interaction as a field and interprets the excitations of the field as particles. An interaction between two particles is viewed as a process in which these two particles exchange a virtual gauge boson (some quantized state of the interacting field) . The term 'gauge' boson arises from the fact that the standard model is a gauge theory, in which the interactions are described by an invariance under 'gauge' transformations. The quanta of the EM force is the photon. The weak force has three quanta, $W^\pm$ and Z^0. The quanta of the strong force are the eight gluons. Thus, there are 12 force carrying particles in the SM. The main properties of the forces and their force-carriers are summarized in the Table 1.2 [21]. The gauge bosons couple to the fermions with a strength appropriate with the force. The strengths of the couplings are not constant, but in fact change with the energy scale.

Force	Gauge Boson	Charge	Spin	Mass (GeV/c^2)	Range	Rel. Strength
Strong	Gluon (g)	0	1	0	$10^{-15}m$	1
EM	Photon(γ)	0	1	0	∞	1/137
Weak	$W^\pm$	±1	1	80.423 ± 0.039	$10^{-18}m$	10^{-5}
	Z^0	0	1	91.188 ± 0.002		
Gravity	Graviton (G)	0	2	0	∞	10^{-38}

Table 1.2: Fundamental forces and gauge bosons.

1.2.2 Electroweak Interactions

The electromagnetic interactions are described by the theory of quantum electrodynamics (QED). In this theory, all particles which carry electric charge may interact with each other via the exchange of photons. Since the photon is massless, the interaction is long range and falls off like $\frac{1}{r^2}$. The strength of the EM force, which can be parameterized by a coupling constant, increases as the interaction energy increases (alternatively, as the interaction distance decreases).

The weak interaction has a very short range and exists between any of the leptons and quarks. It is responsible for the radioactive β-decay of nuclei. This interaction is mediated by three massive gauge bosons, $W^{\pm}$ or Z^0 (mass$\sim$100 GeV), and hence it has a short range. It is called 'weak' because, at low energies (of the order of muon or electron rest mass energy), its strength is approximately four orders of magnitude smaller than the strength of the electromagnetic force. It should be noted however, that, the strengths of these forces depend both on the coupling strengths of the gauge bosons to the fermions, and on the masses of the gauge bosons. At low energies, the high mass of the weak bosons reduces the effective strengths of the weak force, but at high energies where on-shell weak bosons can be exchanged, the weak boson is actually stronger than the electromagnetic force. In the SM, EM and weak interactions have been unified in the Glashow-Salam-Weinberg (GSW) model, and is known as 'Electroweak' force.

1.2.3 The Strong Interaction and QCD

The strong interaction is described by Quantum Chromodynamics (QCD). As the name suggests, the 'color' charge is responsible for this interaction. Particles with non zero color charge can interact with each other via the exchange of gluons. It is a short-range force which is responsible for binding the quarks into hadrons. QCD differs from QED in three important ways. First, instead of just one kind of charge

in QED, there are three kinds of color charge in QCD. Second, photons in QED are uncharged and so they cannot couple to each other; whereas gluons also carry color charge (one unit each of color and anticolor) and so they do directly interact with each other through strong force. This self-interaction between gluons brings the third and the major difference between the QED and QCD. In QED, an electric charge polarizes the vacuum due to the virtual electron-positron pairs which surround it. The charge density is higher near the charge and results in an effective coupling constant given by

$$\alpha_E = \frac{\alpha(\mu)}{1 - \frac{\alpha(\mu)}{3\pi} ln(\frac{Q^2}{\mu^2})} \tag{1.1}$$

where Q is related to the energy of the probe and μ is lower cutoff energy.

In QCD, a quark is surrounded by not only virtual quark-antiquark pairs, but by virtual gluon pairs as well. The virtual gluon pairs decrease the effective strong coupling constant near the quarks, whereas quark-antiquark pairs increase the effective coupling. The gluon pairs' effect dominates and α_s is decreased near the quarks. The strong coupling constant has the form:

$$\alpha_s(Q^2) = \frac{12\pi}{(33 - 2n_f) ln(\frac{Q^2}{\wedge^2})} \tag{1.2}$$

where n_f is the number of quark flavors, $\wedge$ is QCD scaling parameter, and Q is momentum transfer during the interaction. At lower energies (large distances), the strong coupling constant grows rapidly and becomes large which explains why quarks always confine themselves in the color neutral combinations of mesons or baryons. This phenomenon of confinement of quarks in a hadron is called color-confinement. At large interaction energies typical of modern high-energy experiments (E >10 GeV i.e. short distances), α_s approaches zero and so quarks (essentially bound up in hadrons) behave as if they were free particles. This is known as "asymptotic freedom". This is the reason that perturbative methods can be used for high momentum transfer QCD

calculations. However, at lower energies, the coupling strength becomes large enough that perturbative theory breaks down.

Even in high-energy collisions, the quarks do not remain free for very long. Within a time scale typical of strong interactions ($\sim 10^{-24}$ s), quark anti-quark pairs are pulled out of the vacuum which bind with the quarks from the hard scattering to form composite particles. This process is referred to as fragmentation or hadronization. Hence, in high energy collisions of hadrons, although it is the quarks and gluons which are fundamental participants in the interaction, only the composite hadrons are available to the experimenters. Because of conservation of energy and momentum, the hadrons which are produced form a collimated jet of hadronic particles along the direction of the original quark.

Fragmentations are "soft" processes and hence non-perturbative techniques are applied. Consequently, when describing the hadronic collisions which inevitably involve these non-perturbative interactions, one must rely on measured and parameterized parton (quark or gluon) momentum distributions for the initial state hadrons and fragmentation functions which describe how the final state partons evolve into hadron jets. The technique of separating the "hard-scattering" from "soft" processes is called "factorization".

1.2.4 Higgs Mechanism and Electroweak symmetry breaking

Mathematically, the Standard Model is a quantum field theory based on the idea of local gauge invariance [16]. It is built with two separate gauge theories, quantum chromodynamics (QCD) and electroweak. The gauge symmetry group of the SM is $SU(3)_C \times SU(2)_L \times U(1)_Y$, where C refers to color, L refers to weak isospin, and Y is weak hypercharge. This gauge group includes the symmetry group of the strong interactions $SU(3)_C$, and the symmetry group of the electroweak interactions ($SU(2)_L \times U(1)_Y$). At low energy (<250 GeV) the $SU(2)$ symmetry is broken into

the $U(1)_{em}$ group which corresponds to the electromagnetic interactions.

The gauge symmetry of the interactions requires the gauge bosons (force carriers) to be massless as is the case for photons and the gluons. This is obviously a problem for the SM which contains the massive $W^{\pm}$ and the Z^0 bosons for the weak interaction. In the SM, this is most simply achieved through the Higgs mechanism [22], which introduces an additional field with an associated particle, the spin 0 Higgs boson. Unlike the other fields, the higgs field has a non-zero vacuum expectation value (around 250 GeV), and the massless gauge bosons of the weak interactions can acquire their mass through interaction with the Higgs field. This process explicitly breaks the symmetry of the interactions, and hence is called electroweak symmetry breaking. The Higgs mechanism can also be used to generate the masses of the fermions, simply by introducing couplings to the Higgs field. The strengths of these couplings then determine the masses of the fermions. However, despite decades of direct and indirect searches, the associated Higgs particle predicted by the Standard Model has yet to be discovered. As a sequel to the arduous quest, the Tevatron Run II is charged with the major task of searching for this elusive particle.

1.2.5 Limitations of the Standard Model

The Standard Model (SM) has been enormously successful in explaining a wide variety of physics from microscopic phenomena to the early universe. One striking example of this is the prediction of the W and Z bosons as well as their masses, which were later experimentally verified by the UA1 and UA2 experiments at CERN in 1980s [23] [24]. Another example of the success of the SM is the discovery of the top quark in 1995 and the observation of tau neutrino in 2000, at Fermilab, predicted by the SM. However, most physicists believe that it is far from the ultimate theory of fundamental particles and interaction that we are seeking.

First, it is incomplete. Gravitation, the most important force in the macroscopic

world, is not included in the Standard Model. The strong and electroweak interactions can not be unified under its framework. It is natural to suppose that in the ultimate fundamental theory, all four basic interactions are in fact different manifestations of one underlying force.

Second, it is not satisfactory. Many parameters in the SM, such as masses and weak mixing decay angles, are not predicted but must be determined by the experiment. There are many features that are not explained in the SM, such as why there are generations and only three generations. The introduction of Higgs mechanism also seems ad hoc, and the existence of Higgs has not yet been confirmed.

Thirdly, there are too many parameters in the SM. Whereas large number of parameters improve agreement with experiments (which we know is a fact!), yet this erodes the universality of the model.

Finally, there exists the so-called hierarchy problem, which arises from the huge differences in energy scales of the various interactions : the QCD scale is of the order of 1 GeV ($\sim M_{Meson}$); the electroweak scale is of 100 GeV ($\sim M_{W,Z}$); the scale of grand unification (GUT) is $\sim 10^{16}$; while the Plancks mass scale is $\sim 10^{19}$ GeV.

Because of these (and other) problems, physicists today believe that the SM is not the final solution to the question of how the universe works. The SM, as we know it today, is more likely just an approximation of the truth. To overcome the above difficulties, many new theories have been developed beyond the SM, such as Grand Unified Theories (GUT), Supersymmetric theories (SUSY), etc, but none has been firmly verified by experiments. To test our understanding of elementary particles and their interactions we must probe nature with increasing scrutiny, building progressively larger and more complicated experiments. The tools to analyze the data from these experiments have become increasingly complex with time and necessity. Both result in large collaborations of people to design, build, and execute the experiments.

1.3 The Top Quark : The "King" of Fermions

The top quark was discovered in 1995 by the DØ [25] and the CDF [26] collaborations in proton-antiproton annihilations at the Fermilab Tevatron Collider. The discovery marked the culmination of the intensive experimental efforts in the search for the heaviest fundamental fermion which lasted for around two decades. Observation of the top quark is the latest in a long series of triumphs for the Standard Model. The top quark completed the fermionic spectrum of the Standard Model. It stands out by its large mass, about 200 times larger than the mass of the proton and 35 times higher than the mass of the next-heaviest 'bottom' quark. Whether this property of the top quark is a mere accident or a manifestation of a deeper physical process is an unanswered question in particle physics. In this section we review the exciting theoretical and experimental developments leading to the discovery of the top quark. There exist several excellent reviews of the work that led to the discovery and the work done thereafter [27] [28] [29] [30] .

1.3.1 Evidence for the existence of the top quark

The journey towards the top quark began in 1973 when a three generation scheme was proposed by Kobayashi and Maskava in order to explain CP violation in $K^0\overline{K^0}$ system [31]. The tau lepton (τ) was the first particle of the third-generation to be discovered in 1975 at SLAC [32]. A short time later, in 1977, the Υ was discovered at Fermilab [33], which was interpreted as a $b\overline{b}$ bound state. The charge of the b quark was found to be $Q_b = -\frac{1}{3}$ by measuring the leptonic width of the Υ resonance at the DORIS e^+e^- storage ring [34]. Several strong reasons made physicists believe that the top quark must exist.

The renormalizability of the Standard Model requires the cancellation of triangle anomalies - a problem that arises from the interaction of three gauge bosons via

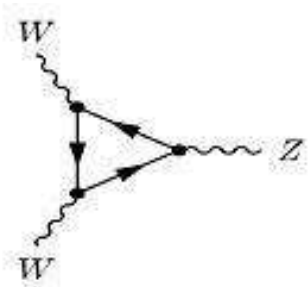

Figure 1.1: A example of fermion triangle diagram which could cause an anomaly.

a closed loop of fermions as shown in Figure 1.1. It turns out that the fermion contribution within each generation cancel if the electric charges of all left-handed fermions sum to zero [35]:

$$\sum Q_L = -1 + 3 \times [(\frac{2}{3}) + (-\frac{1}{3})] = 0 \tag{1.3}$$

The factor 3 is the number of color charges for each quark flavor. For this to work for the third generation, the top quark with $Q = +\frac{2}{3}$ must exist.

The most compelling experimental evidence came from the observation of the forward-backward asymmetry in $e^+e^- \rightarrow Z/\gamma \rightarrow b\overline{b}$ process that is sensitive to the weak isospin of the left-handed and right-handed b quarks. Measurements at e^+e^- colliders (LEP, SLC, PEP, PETRA, and TRISTAN) found the third component of the isospin for the left-handed (I_3^L) and right-handed (I_3^R) b quark to be close to -0.5 and 0, respectively [37]. This according to the Standard Model indicated the presence of a quark doublet, i.e., the b quark must have a weak isospin partner with $I_3^L = +\frac{1}{2}$.

An additional proof came from comparison of production rates for the $b \rightarrow cl^-\overline{\nu_l}$ and $b \rightarrow sl^-l^+$ processes. If the b quark were an isospin singlet, it could not decay into c-quark and a lepton pair through a standard weak process shown in Figure 1.2a. The only possibility would be that b-quark converts ("mixes") to a lighter quark which, being an isospin doublet, decays weekly (Figure 1.2b). But in that case there should exist another process (Figure 1.2c) which should lead to a $b \rightarrow sl^-l^+$ production at

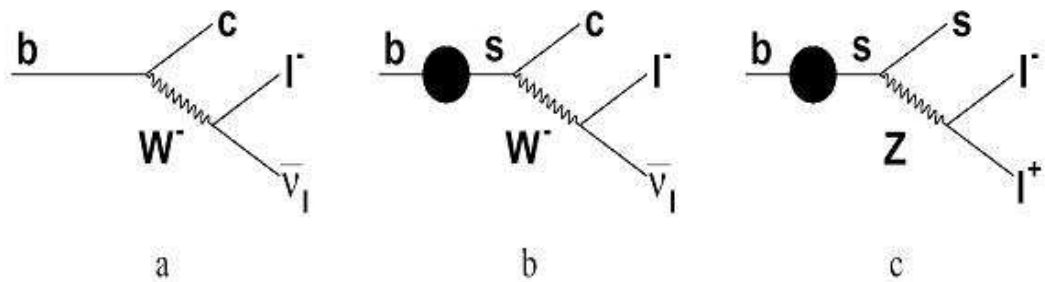

Figure 1.2: The Feynman diagrams describing the b quark decay in the Standard Model (a) and in the case when the b-quark is an isospin singlet (b,c).

a comparable rate [38]. However, such a process ("flavor changing neutral current") was found to be suppressed by several orders of magnitude [39], which indicated that b is a part of a doublet.

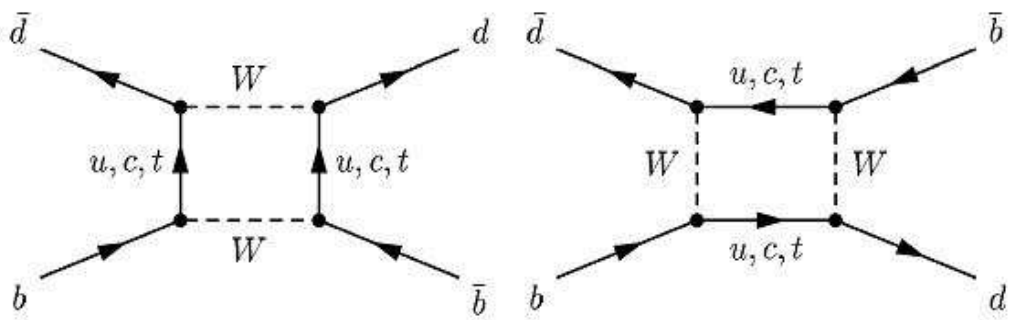

Figure 1.3: B_d^0-$\overline{B_d^0}$ mixing diagrams.

There was other indirect experimental evidence which indicated the existence of the top quark. The observed rate of B_d^0-$\overline{B_d^0}$ mixing (Figure 1.3) is proportional to $|V_{td}|^2$, the Cabibbi-Kobayashi-Maskawa (CKM) matrix element for the t and d quark coupling [40] [41]. This implied that a massive top quark is needed in the loops so that the b quark can decay indirectly via an intermediate state containing a virtual t quark to the d quark. This indicated that the b quark has a weak isospin partner, the top quark, with isospin $I_3 = +\frac{1}{2}$.

The precise measurements of Z width by experiments at the LEP and SLC ruled

out the existence of a fourth-generation neutrino with a mass $M_\nu \leq \frac{M_z}{2}$ [41]. Thus, unless the fourth-generation neutrino is very massive, no additional generations are allowed in the context of the Standard Model. The top quark is therefore the last fermion expected in the Standard Model.

1.3.2 The Road to the top quark discovery

The existence of a sixth quark has been expected since the discovery of the bottom quark itself and has become an absolute theoretical necessity within the Standard Model after the measurement of the $T_3 = -\frac{1}{2}$ weak isospin of the b quark [42]. Experimental searches for the top quark began immediately following the discovery of the companion b quark in the late 1970's. However, due to the top quark's unexpectedly large mass, it took nearly two decades to find a direct evidence for its existence. During this exciting period with extensive searches at e^+e^- and hadronic colliders, the experiments reached higher and higher energies; but in the absence of direct evidence, the lower limit on the top quark mass shifted to higher and higher values, until finally it was discovered at Fermilab in 1995. We present a brief historical survey of the top quark searches. A more complete review is given in reference [27].

A: Search for top quark at e^+e^- colliders

Using a naive extrapolation of the up- to down-type quark mass ratios in the first two generations, the top quark mass was speculated to be in the range of 10-20 GeV, and hence was expected to be just around the corner. This provided considerable impetus for the searches at e^+e^- colliders. In e^+e^- collisions, top quarks would be produced in $t\bar{t}$ pairs through e^+e^- annihilation into a γ or Z . Since at the leading order this is a purely electroweak process, the production cross-section can be accurately calculated. At center of mass energies ($\sqrt{s}$) well below the Z mass, where annihilation of the e^+e^- pair into a photon dominates, $t\bar{t}$ production would manifest itself as an increase by an amount $\delta R \approx 3Q_{top}^2 = 4/3$ in the ratio $R = \sigma(e^+e^- \rightarrow hadrons)/\sigma(e^+e^- \rightarrow \mu^+\mu^-)$,

well above the energy threshold for the production of a $t\bar{t}$ pair [27].

Between 1979 and 1984, measurements of R were performed at the PETRA (DESY) in the $\sqrt{s}$ range between 12 and 46.8 GeV [43]. The value of R was found to be consistent with Standard Model expectations without a top-quark contribution. Event topology studies gave no evidence for excesses of spherical, aplanar, or low-thrust events that could be attributed to $t\bar{t}$ production. Existence of the top quark with mass below 23.3 GeV was ruled out at the 95% Confidence level (CL).

Similar searches at the TRISTAN (KEK) collider during 1987-90 with $\sqrt{s}$ of 61.4 GeV resulted in lower limit on the top mass of 30.2 GeV [44]. During 1989-90, the SLC (SLAC) and LEP (CERN) e^+e^- colliders with $\sqrt{s} \sim M_z$ became operational. Studies of event topologies and measurements of the Z width were found to be inconsistent with a $Z \to t\bar{t}$ contribution and resulted in a lower limit on the top-quark mass as high as 45.8 GeV [45].

B: Search for top quark at $p\bar{p}$ colliders

With the emergence of $p\bar{p}$ colliders in 1980's, first at CERN and then at Fermilab, and with evidence from e^+e^- experiments pointing towards a very high mass for the top quark, focus in the search for top rapidly shifted to hadron colliders. The obvious advantage of hadron colliders for the top physics is the large center-of-mass energy, which enables the exploration of high mass regions. However, in contrast to e^+e^- collisions, hadronic collisions have large backgrounds which make it impossible to search directly for the top quark in a model-independent way. It is necessary to concentrate on particular signatures based on the Standard Model decay modes of the top quark.

In parallel to the searches in e^+e^- collisions, direct searches were performed during the 1980's by the UA1 and UA2 experiments at the CERN $Sp\bar{p}S$ collider, $\sqrt{s} =$ 630 GeV. At this energy, and at the available luminosities, the CERN experiments were sensitive to top mass values not exceeding 70 GeV, the top quark being mostly

produced via an intermediate on-shell W, decaying to $t\overline{b}$. A top quark with mass below the Wb threshold was then expected to undergo a 3-body decay to a $bf\overline{f'}$ final state, with $f\overline{f'}$ being a weak isospin doublet such as $\nu_l\overline{l}$ or $u\overline{d}$ [46] [27].

In 1984, the UA1 almost claimed the discovery of the top quark with a mass of 40 ± 10 GeV based on an integrated luminosity of 200 nb^{-1} [47] [48] [49]. These first reports were, however, not supported by a subsequent UA1 analysis with a higher-statistics data sample of 700 nb^{-1}, as well as a more complete evaluation of the backgrounds. This resulted in the limit M_{top} >44 GeV at the 95% CL [50]. More sensitive searches for the top quark were performed in the period 1988-1990 and the 95% CL mass limits went from 52 GeV (UA1, 1988), to 60 GeV (UA1, 1990 [51]), and to 69 GeV (UA2, 1990 [52]).

The first high-statistics run of the Tevatron collider also took place in 1988-89, with an integrated luminosity of 4 pb^{-1} recorded by the CDF collaboration. At the Tevatron $\sqrt{s}$ of 1.8 TeV , the top production in the relevant M_{top} range is dominated by the $p\overline{p} \rightarrow t\overline{t}$ process. However, no events consistent with $t\overline{t}$ were found in the different final states resulting in the first limits from the CDF in 1990: $M_{top} > 72$ GeV from searches in electron-muon + jets final states [53], $M_{top} > 77$ GeV from searches in electron plus jets final states [54], and $M_{top} > 85$ GeV from searches in dilepton final states [55].

The first direct limit on the top mass exceeding the threshold for the decay into real W and a b quark came in 1992 from the CDF: $M_{top} > 91$ at 95% CL [56]. With the top quark being so massive, hopes to observe the top quark at the CERN $Sp\overline{p}S$ were abandoned, because of the small top production cross-section at $\sqrt{s} = 630$ GeV. A lower limit of $M_{top} > 131$ GeV at the 95% CL was established by DØ in 1994 from the Run Ia (1992-93 collider run) data with an integrated luminosity of 13.5 pb^{-1} [57]. The lower limits on the top mass from the $p\overline{p}$ experiments at CERN and Fermilab are summarized in Table.

Experiment	Integrated Luminosity	Mode	Mass Limit (95%CL)	Year
UA1	0.7 pb^{-1}	e + jets, μ + jets	> 44 GeV	1988
UA1	5.4 pb^{-1}	μ + jets	> 52 GeV	1988
UA1	5.4 pb^{-1}	μ + jets, $\mu\mu$	> 60 GeV	1988
UA2	7.5 pb^{-1}	e + jets	> 69 GeV	1990
CDF	4.0 pb^{-1}	eμ	> 72 GeV	1990
CDF	4.0 pb^{-1}	e + jets	> 77 GeV	1990
CDF	4.0 pb^{-1}	dileptons (ee,eμ,$\mu\mu$)	> 85 GeV	1992
CDF	4.0 pb^{-1}	dileptons and l+jets+b tag	> 91 GeV	1992
DØ	13.5 pb^{-1}	dileptons and l+jets	> 131 GeV	1994

Table 1.3: Summary of lower limits on the top-quark mass from searches at $p\overline{p}$ colliders.

C: Direct Evidence and Discovery

In 1994, the CDF collaboration reported finding evidence for the top quark, with a cross-section of $13.9^{+6.1}_{-4.8}$ pb and a mass of $174 \pm 10^{+13}_{-12}$ GeV, based on analysis of Run Ia data set with an integrated luminosity of 19.3 pb^{-1} [58]. The excess in the number of top candidate events over the background prediction was 2.8 standard deviations (σ). However, because the excess of signal events was not large enough to rule out the background fluctuations, CDF stopped short of claiming discovery. With the optimized requirements for higher top masses, a statistically not very significant excess of events (1.9 σ) was also found in Run Ia DØ data [59].

With the addition of the data from the first half of Run IB, a statistically convincing excess of events emerged from the analyses of the data sets from both collaborations and in March 1995, both DØ and CDF announced the discovery of the top quark. DØ reported a cross-section of 6.4 ± 2.2 pb and a mass of $199^{+19}_{-21} \pm 22$ GeV on the basis of 50 pb^{-1} of data [60]. CDF measured a cross-section of $6.8^{+3.6}_{-2.4}$ pb and a mass of $176 \pm 8 \pm 10$ GeV on the basis of 67 pb^{-1} of data [61]. The two uncertainties quoted on the measurements are the statistical and systematic ones, respectively.

1.3.3 What is so special about the Top Quark?

In the Standard Model, the top quark is defined as the weak isospin partner of the bottom quark. As such, it is a spin-$\frac{1}{2}$ fermion of electric charge $+\frac{2}{3}$ and transforms as a color anti-triplet under the $SU(3)$ gauge group of strong interactions. Its quantum numbers have not yet been measured directly, although a large amount of direct and indirect evidence supports the SM assignments [62] [63] [64]. The top quark is very unique from other quarks which makes its study very interesting.

1. The most striking observed feature that sets the top quark apart from the other quarks is its very large mass. With its mass of about 175 GeV [65], it is as massive as a gold atom and approximately 35 times heavier that the next-heaviest quark, bottom (b), and is the heaviest elementary particle known (see Figure 1.4). That the mass is very close to the electro-weak scale suggests the tantalizing possibility that the top quark may play a special role in the breaking of electro-weak symmetry and therefore in the origin of fermion masses.

2. The Yukawa couplings relate the matter content of the SM to the Higgs field [66]. The top quark mass (m_t) is fundamentally related to the Higgs vacuum expectation value (ν) by $m_t = \frac{Y_t \nu}{\sqrt{2}}$, where Y_t is the Yukawa coupling. With ν =246 GeV and m_t =175 GeV, Y_t appears to be close to 1, a theoretically interesting value, leading to speculations that new physics may be accessible via the study of the top quark [29] [67].

3. An important consequence of a heavy top quark is that it has a very short lifetime of about 5×10^{-25}s, an order of less than the characteristic QCD hadronization time scale, $\tau_{had} \approx 2.8\times10^{-24}$s [29]. Therefore, it does not have time to bind with other quarks before it decays. Thus, the decay of top quarks offers a unique window on the properties of a bare quark such as spin correlations free from long-range effects of QCD (such as confinement). The spin correlation information carried by top quarks is expected to be preserved in their decay products and should be directly observable

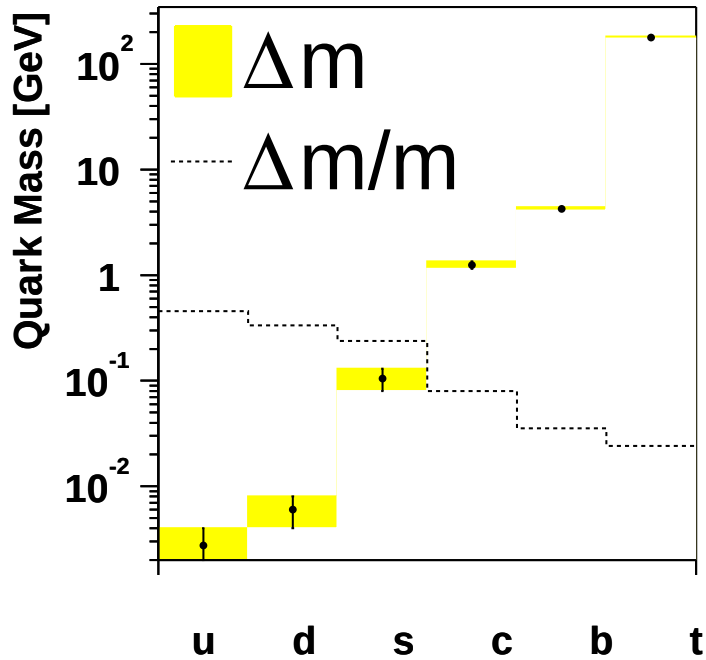

Figure 1.4: Quark Masses and their uncertainties.

in their angular correlations.

4. The sheer enormousness of the top's mass makes its decays fertile ground for new particle searches. Theorists speculate that if supersymmetric partners exist and are lighter than the top, they might show up in top events. For instance, a top may decay to its supersymmetric partner ('stop').

1.3.4 Role of the Top Quark Mass in the Standard Model

The top quark plays an important role in the precision electroweak analysis. At leading-order, all electroweak quantities depend on just three parameters : electromagnetic coupling constant (α), the Fermi Constant (G_F) and the Weinberg angle (θ_W). For instance, the W mass at tree level can be expressed by [67]:

$$M_w^2 = \frac{\frac{\pi\alpha}{\sqrt{2}G_F}}{sin^2\theta_W};\ where\ sin^2\theta_W \equiv 1 - \frac{m_W^2}{m_Z^2} \tag{1.4}$$

Considering also one-loop radiative (higher-order) corrections Δr, the expression is modified to [67]

$$m_w^2 = \frac{\frac{\pi\alpha}{\sqrt{2}G_F}}{sin^2\theta_W(1-\Delta r)} \tag{1.5}$$

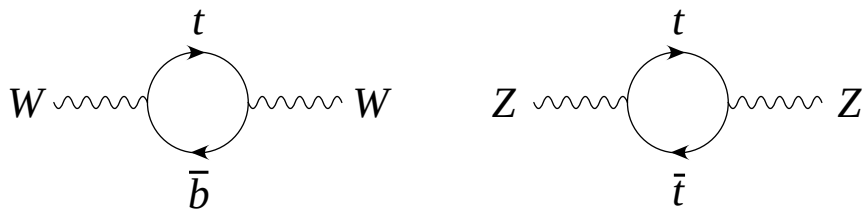

Figure 1.5: Virtual top quark loops contributing to the W and Z boson masses.

Figure 1.6: Virtual Higgs boson loops contributing to the W and Z boson masses.

Contributions to Δr originating from the top quark and Higgs boson by the one-loop diagrams shown in Figure 1.5 and Figure 1.6 (which contribute to the W and Z masses) are given by:

$$(\Delta r)_{top} \approx -\frac{3G_F m_t^2}{8\sqrt{2}\pi^2 \tan^2\theta_W} \tag{1.6}$$

$$(\Delta r)_{Higgs} \approx \frac{11G_F M_Z^2 \cos^2\theta_W}{24\sqrt{2}\pi^2} \ln\frac{m_H^2}{m_Z^2}. \tag{1.7}$$

The radiative correction depends quadratically on the top quark mass (m_t), but only logarithmically on the Higg boson mass (m_H). Therefore Δr is not nearly as sensitive to m_H as it is to m_t. This was used to successfully predict the top quark mass several years before it was discovered. With the additional contribution from the Higgs boson to Δr, precision measurements of m_t and m_W can be used to constrain the mass of the undiscovered Higgs boson.

A graphical representation of this relationship is shown in Figure 1.7 [68] [69].

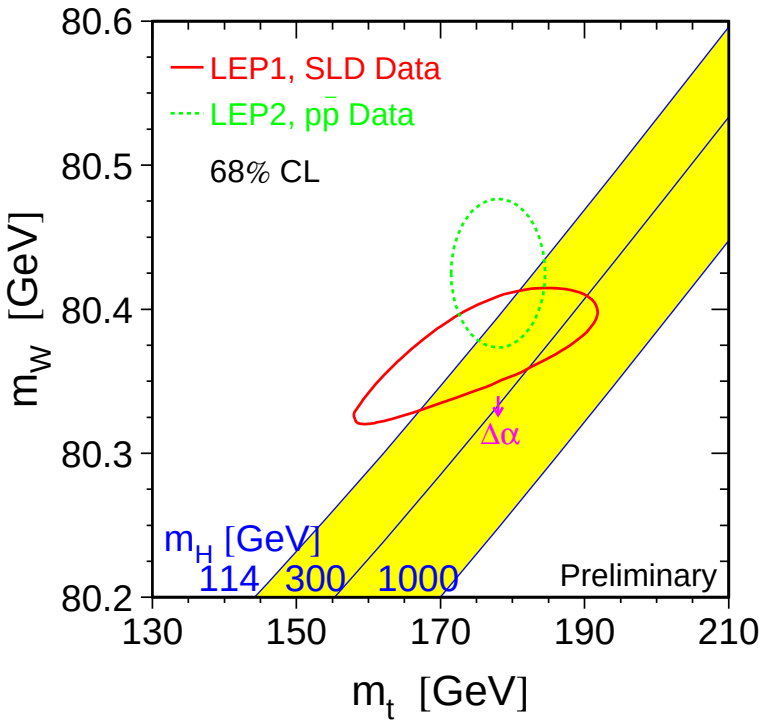

Figure 1.7: Lines of constant Higgs mass on a plot of the W boson mass (m_W) and the top quark mass (m_t) from ref.[69]. Contour curves of 65% confidence level in the (m_t,m_W) plane, for the indirect (LEP1, SLD data) and direct (LEP2, $p\overline{p}$ data) determination of the Higgs boson mass in a global fit to the electroweak precision data.

The diagonal bands are lines of constant Higgs mass ranging from the current lower bound on m_H (114 Gev) to the upper bound [70], around 1 TeV. The dashed ellipse is a 68% CL from direct measurements of m_t and m_W. The solid ellipse is a 68% CL from indirect constraints on precision electroweak data. It can be seen that the direct and indirect measurements are in good agreement and prefer a low value of the Higgs mass.

σ(pb)	s-channel	t-channel
Tevatron Run I ($\sqrt{s}$ = 1.8 TeV, $p\overline{p}$)	0.7 pb	1.4 pb
Tevatron Run II ($\sqrt{s}$ = 2.0 TeV,$p\overline{p}$)	0.9 pb	2.1 pb
LHC ($\sqrt{s}$ = 14.0 TeV, pp)	10.6 pb	250 pb

Table 1.4: Cross-sections at next-to-leading-order (NLO) in QCD for single top production at the Tevatron and LHC [71]. The associated uncertainties are ∼5%.

1.3.5 Top Quark Production

In proton-antiproton collisions at the Tevatron Collider, the top quarks can be produced by two mechanisms: single top production via electroweak interactions and top-antitop $t\overline{t}$ pair production via strong interactions.

Single Top Production

There are two dominant processes for single top production : $q'\overline{q} \rightarrow t\overline{b}$ (known as W^* or s-channel process) and $q'g \rightarrow tqb$ (also known as Wg fusion or t-channel process), whose leading-order diagrams are shown in Figure 1.8. Table 1.4 shows the cross-sections at next-to-leading-order (NLO) for the individual subprocesses for a top quark mass of 175 GeV [71]. Since the single top production cross-section is directly proportional to the CKM matrix element $|V_{tb}|^2$, it provides a unique opportunity to directly measure the matrix element value, and check the unitarity of the CKM matrix. Single top production is however very difficult to disentangle from the backgrounds, and has not yet been observed in experiments. The ongoing Run II analysis at DØ has found no evidence for a single top quark signal and has reported the 95% CL upper limits on its production cross-section to be 6.4 pb in the s-channel and 5.0 pb in the t-channel [72]. In this thesis, we only consider top quarks produced in pairs.

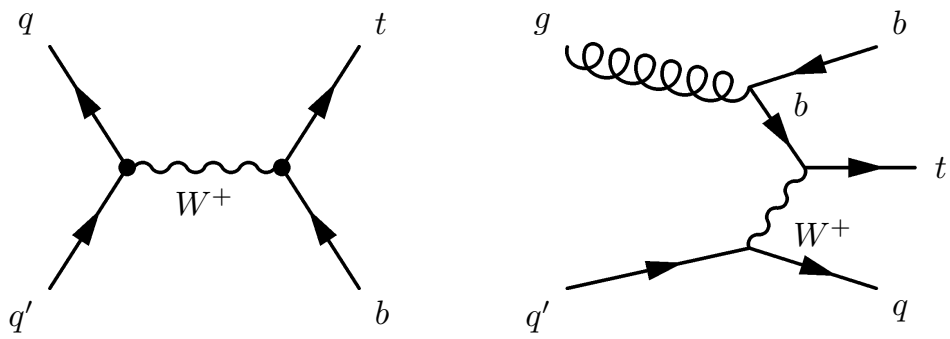

Figure 1.8: Single top quark production via the weak interaction. The main contributions at the Tevatron arise from the s-channel process (left) and the t-channel (right).

Top Pair Production

At the Tevatron center of mass energy, top quarks are dominantly produced as $t\bar{t}$ pairs. In the standard model, at the lowest-order QCD, $O(\alpha_s^2)$, $t\bar{t}$ pairs are produced via two subprocesses : quark-antiquark annihilation ($q\bar{q} \rightarrow t\bar{t}$) and gluon-gluon fusion ($gg \rightarrow t\bar{t}$) [29]. Figure 1.9 shows the corresponding leading-order (LO) Feynman diagrams.

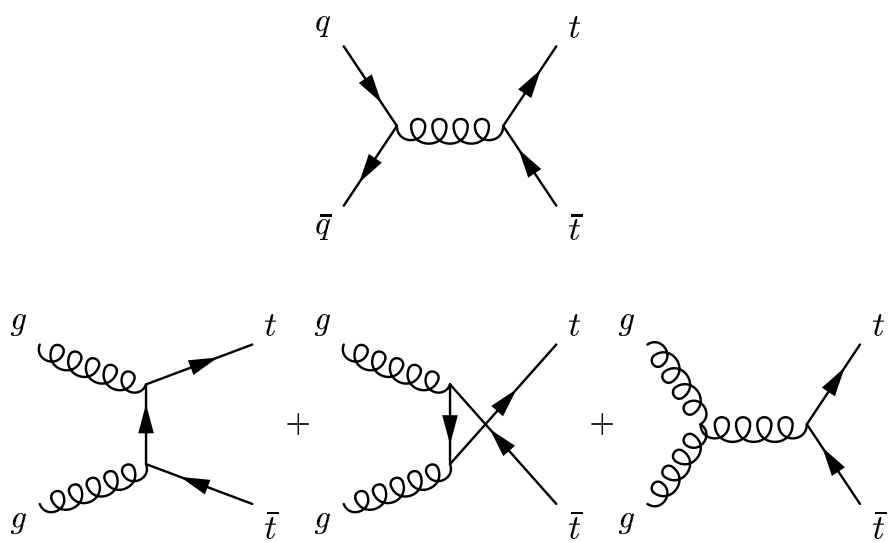

Figure 1.9: Lowest order Feynman diagrams for the production of $t\bar{t}$ pairs at the Tevatron : quark-antiquark annihilation and gluon-gluon fusion.

The $t\bar{t}$ pair production proceeds through a hard-scattering process involving initial-

state light quarks q and gluon g. The total $t\bar{t}$ pair production cross-section for $p\bar{p} \rightarrow t\bar{t} + X$ at the center of mass energy $\sqrt{s}$ can be expressed as a convolution of the parton distributions functions (PDF's) for the incoming hadrons and the cross-section of the partonic processes:

$$\sigma^{p\bar{p}\rightarrow t\bar{t}+X}(s, m_t) = \sum_{i,j=q,\bar{q},g} \int dx_i dx_j f_i(x_i, \mu^2)\overline{f_j}(x_j, \mu^2)\hat{\sigma}^{ij\rightarrow t\bar{t}}(\hat{s}, \mu^2, m_t) \tag{1.8}$$

where the summation indices i and j run over all $q\bar{q}$ and gg pairs. The partons i and j carry momentum fractions $x_{i,j}$ of the proton and antiproton. The parton momenta inside the proton and antiproton are described by the PDF's, $f_i(x_i, \mu^2)$ and $\overline{f_j}(x_j, \mu^2)$, respectively. The parton-level cross-section $\hat{\sigma}$ depends on the center-of-mass energy of the parton-parton interaction, $\sqrt{\hat{s}} = \sqrt{x_i x_j . s}$. The cross-section σ also depends on the renormalization and factorization scale. The former is introduced due to renormalization procedure and the latter comes from splitting (factorizing) of the perturbative ($\hat{\sigma}$) and non-perturbative parts (f_i,$\overline{f_j}$) of the cross-section. As both scales are arbitrary, the same scale, μ, is used for both. A common choice for μ is the energy needed at production threshold per parton ($\mu = m_t$).

At the Tevatron with a $p\bar{p}$ center of mass energy of 1.96 TeV, the $t\bar{t}$ is mainly produced just above the kinematically allowed threshold, $\sqrt{\hat{s}} \geq 2m_t$ (see Appendix-A). The partonic cross-sections of the two LO subprocesses ($q\bar{q} \rightarrow t\bar{t}$ and $gg \rightarrow t\bar{t}$) are of the form [35]:

$$\hat{\sigma}^{q\bar{q}\rightarrow t\bar{t}}(\hat{s}) \simeq \frac{4}{9}\frac{\pi\alpha_s^2}{\hat{s}}\beta \tag{1.9}$$

$$\hat{\sigma}^{gg\rightarrow t\bar{t}}(\hat{s}) \simeq \frac{7}{48}\frac{\pi\alpha_s^2}{\hat{s}}\beta \tag{1.10}$$

where $\beta = \sqrt{1-\rho}$ (with $\rho = 4m_t^2/\hat{s} \leq 1$) is the velocity of the top quarks in the $t\bar{t}$ center-of-mass frame. It can be seen that there is a relative enhancement of the

cross-section from $q\overline{q}$ process as compared to the cross-section from gg process by a factor of $\sim$3.

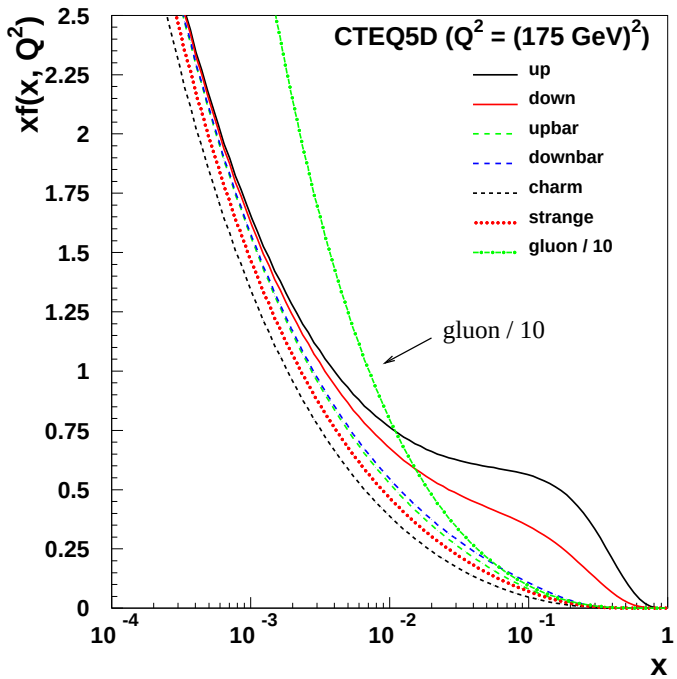

Figure 1.10: The quark, anti-quark, and gluon densities on the proton as a function of the longitudinal momentum fractions x at $Q^2 = m_t^2$ from CTEQ5D [73].

Near the threshold ($\sqrt{\hat{s}} = 2m_t$) and for the case when parton momenta are equal, it is seen that $x_i = x_j = 2m_t/\sqrt{s} \approx 0.18$ (see Appendix-A) for a top quark mass $m_t =$ 175 GeV and $\sqrt{s} = 1.96$ TeV. For these values of x, the q and $\overline{q}$ momentum densities are much larger than the gluon momentum density (see Figure 1.10) which leads to further enhancement of the $q\overline{q}$ partonic cross-section over the gg cross-section. As a result, at the Tevatron energies, the $q\overline{q} \rightarrow t\overline{t}$ dominates, contributing 85% of the cross-section and the $gg \rightarrow t\overline{t}$ contributing 15%. This is in contrast to the situation at the Large Hadron Collider (LHC), where gluon fusion provides the dominant contribution due to increased gluon density. Table 1.5 lists the relative contributions to the total $t\overline{t}$ cross-section for the two colliders. The higher the center-of-mass energy, the higher the contribution from gluon fusion process.

Hadron Collider	$q\bar{q} \to t\bar{t}$	$gg \to t\bar{t}$
Tevatron Run I ($\sqrt{s} = 1.8$ TeV, $p\bar{p}$)	90%	10%
Tevatron Run II ($\sqrt{s} = 2.0$ TeV,$p\bar{p}$)	85%	15%
LHC ($\sqrt{s} = 14.0$ TeV, pp)	10%	90%

Table 1.5: Theoretical predictions of the relative contributions from the quark-antiquark annihilation and gluon-gluon fusion processes to the leading order $t\bar{t}$ cross-section at the Tevatron and LHC.

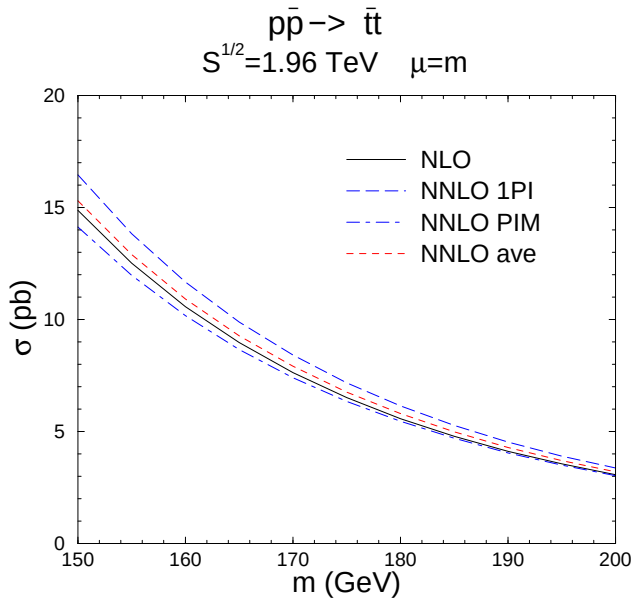

Figure 1.11: The top quark mass dependence of the $t\bar{t}$ cross-section at NNLO using CTEQ6M parton densities [80].

With the extension of the Feynman diagrams, e.g. involving gluon radiation in the initial and final state, the theoretical prediction of the $t\bar{t}$ cross-section ($\sigma_{t\bar{t}}$) has been calculated up to next-to-leading-order (NLO) [74] - [78] and even next-to-next-leading-order (NNLO, or order σ_s^4) precision [79] [80] . Figure 1.11 shows the NNLO predictions for the $\sigma_{t\bar{t}}$ as a function of the mass of the top quark [80]. The latest NLO and NNLO calculations for the $\sigma_{t\bar{t}}$ are listed in Table 1.6 for the Tevatron and LHC regime. All cross-sections are quoted for a top quark mass of 175 GeV, however, the world average is now 178 GeV. This change in the top quark mass corresponds to a drop of the ttbar cross-section by approx 10%. The uncertainties in the theoretical

Hadron Collider	σ (NLL resummation)	σ(NNLO)
Tevatron Run I ($\sqrt{s}$ = 1.8 TeV, $p\overline{p}$)	$5.19^{+0.52}_{-0.68}$ pb [78]	5.24 ± 0.31 pb [79]
Tevatron Run II ($\sqrt{s}$ = 1.96 TeV,$p\overline{p}$)	$6.70^{+0.71}_{-0.88}$ pb [78]	6.77 ± 0.42 pb [80]
LHC ($\sqrt{s}$ = 14.0 TeV, pp)	833^{+52}_{-39} pb [77]	$872.8^{+23}_{-27.6}$ pb [79]

Table 1.6: Theoretical predictions for $t\overline{t}$ cross-section for m_t =175 GeV for Tevatron Run I, Run II and LHC. In the first technique, the full next to leading log (NLL) resummation is computed for the inclusive cross-section.

calculations are dominated by the PDF and α_s uncertainties.

1.3.6 Top Quark Decay

The top quark decays via weak interaction. The SM predicts a branching fraction $BR(t \to Wb) > 0.998$, because $|V_{tb}| \simeq 1$. The decay modes $t \to sW$ and $t \to dW$ are highly suppressed by the CKM matrix vectors $|V_{ts}|$ and $|V_{td}|$. Experimental results on the ratio of branching fractions, $Br(t \to Wb)/Br(t \to Wq)$ [82] [83] [84], show consistency with the SM expectation. The total width of the top quark, Γ_t, is $\simeq 1.50$ GeV, (for $m_t = 178$ GeV)[29]. This Γ_t corresponds to the very short lifetime of the top quark of about 5×10^{-25} s. Thus the top quark decays before it hadronizes, almost 100% of the time to a bottom quark and a W boson.

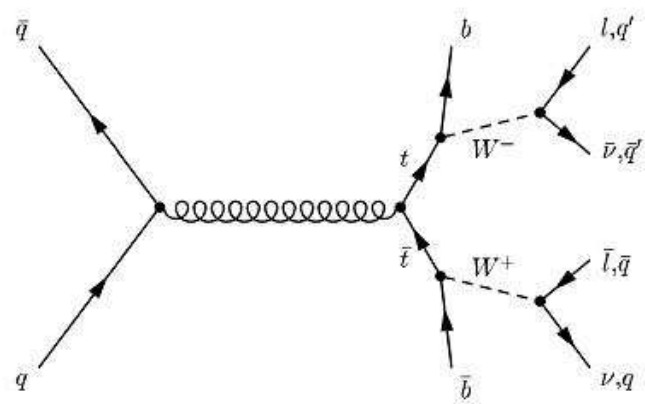

Figure 1.12: Standard model decay of $t\overline{t}$ pairs into dilepton channel.

The decay mode of the $t\overline{t}$ pair is determined by the fate of two W bosons, as

Decay mode	BR at Born level	BR[39]
$W^+ \to e^+\nu_e$	1/9	$(10.68 \pm 0.12)\%$
$W^+ \to \mu^+\nu_\mu$	1/9	$(10.68 \pm 0.12)\%$
$W^+ \to \tau^+\nu_\tau$	1/9	$(10.68 \pm 0.12)\%$
$W^+ \to u\overline{d},\ c\overline{s}$	$2 \cdot 3 \cdot 1/9 = 6/9$	$(67.96 \pm 0.35)\%$

Table 1.7: Leading order and best known branching fractions [70] of the real W^+ boson decay. Identical for the charge conjugates of the modes above (W^-).

shown in Fig. 1.12. Each W boson may decay leptonically into a lepton (l) and the corresponding neutrino (ν_l), or hadronically into a pair of quarks ($q\overline{q'}$) . While all three ($e\nu_e$, $\mu\nu_\mu$, $\tau\nu_\tau$) leptonic decays are kinematically allowed, the hadronic W decay modes are kinematically limited to first and second generation $q\overline{q'}$ pairs ($u\overline{d}, c\overline{s}$). Since every quark comes in three colors, there are six possible hadronic decay modes. Hence, the probability for a W boson to decay in each of the two available quark final states is approximately $\frac{1}{3}$, while for each leptonic channel it is $\frac{1}{9}$. A summary of the possible W decay modes is shown in Table 1.7. Due to the color confinement effect, we can not directly measure individual quarks in the detector. Instead, a cluster of energy, called a jet, in the direction of the quark shows up in the calorimeter.

$t\overline{t}$ event signatures

Since the t and $\overline{t}$ decay independently, $t\overline{t}$ events can be classified according to the different W decay modes as follows. The resulting final states for events are shown in Fig. 1.13.

Dilepton channels : If both $W's$ decay leptonically, this $t\overline{t}$ event is called a dilepton event. The particular dilepton channels which have been most studied are the ee, $\mu\mu$ and $e\mu$ channels. Their final state signature consists of two high-transverse momentum (p_T) leptons, two energetic jets from the hadronization of b quarks and large missing transverse energy (due to large momentum imbalance in the plane transverse

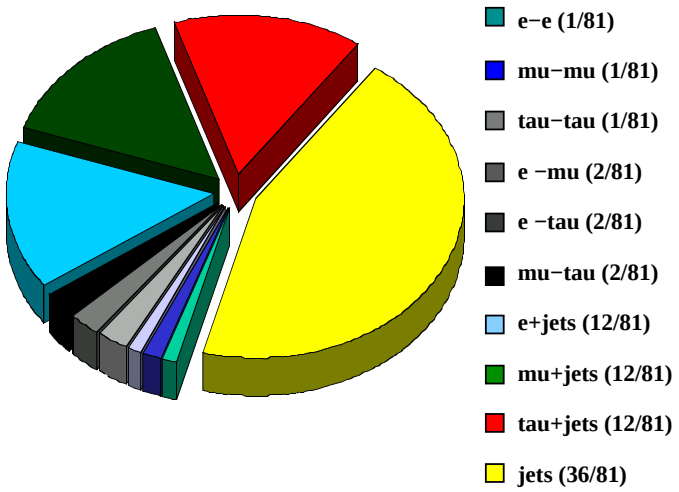

Figure 1.13: Pie chart of the event decay channels at Born level.

to the beam) from the two undetected neutrinos. Despite their low branching ratio, these channels are characterized by very low background. Moreover, since dilepton events contain two undetected neutrinos, it is impossible to do complete reconstruction of the event kinematics.

Lepton+jets channels: In this group of channels, one W boson decays leptonically, and the other decays hadronically. The final state has a signature of one high-p_T lepton (e or μ), large missing transverse energy, and four jets, two of which are b-jets. This channel has a a much larger branching ratio compared to the dilepton channel (as evident in Table 1.9), but it also suffers from a larger background from QCD multijet events where a jet is misidentified as a lepton and inclusive W boson production with associated jets.

All-jets channel: Events in which both W bosons decay hadronically are called all-jet events. The final state contains six jets, of which two are b-jets. Although this channel has the largest branching ratio, its identification is very challenging due to the presence of a huge background from QCD multijet processes.

τ channels are classified in a different category since τ leptons are difficult to identify experimentally. The work is in progress to analyze the τ decay channels. However, a fraction of the τ leptons decays leptonically to an electron or muon and

Decay mode	BR
$\tau^- \to e^- \overline{\nu}_e \nu_\tau$	$(17.84 \pm 0.06)\%$
$\tau^- \to \mu^- \overline{\nu}_\mu \nu_\tau$	$(17.36 \pm 0.06)\%$

Table 1.8: Branching fractions [70] of the real τ^- lepton decay.

Channel	Decay mode	BR at Born level	BR[39]
	$t\bar{t} \to e^+\nu_e e^-\overline{\nu}_e b\bar{b}$	1/81	$(1.14 \pm 0.02)\%$
	$t\bar{t} \to e^+\nu_e \mu^-\overline{\nu}_\mu b\bar{b}$	2/81	$(2.28 \pm 0.04)\%$
	$t\bar{t} \to \mu^+\nu_\mu \mu^-\overline{\nu}_\mu b\bar{b}$	1/81	$(1.14 \pm 0.02)\%$
ee	$t\bar{t} \to e^+_{(\tau)} e^-_{(\tau)} b\bar{b} + \nu's$	-	$(1.58 \pm 0.03)\%$
$e\mu$	$t\bar{t} \to e^+_{(\tau)} \mu^-_{(\tau)} b\bar{b} + \nu's$	-	$(3.16 \pm 0.06)\%$
$\mu\mu$	$t\bar{t} \to \mu^+_{(\tau)} \mu^-_{(\tau)} b\bar{b} + \nu's$	-	$(1.57 \pm 0.03)\%$
	$t\bar{t} \to e^+\nu_e q\overline{q'} b\bar{b}$	12/81	$(14.52 \pm 0.09)\%$
	$t\bar{t} \to \mu^+\nu_\mu q\overline{q'} b\bar{b}$	12/81	$(14.52 \pm 0.09)\%$
e+jets	$t\bar{t} \to e^+_{(\tau)} q\overline{q'} b\bar{b} + \nu's$	-	$(17.11 \pm 0.11)\%$
μ+jets	$t\bar{t} \to \mu^+_{(\tau)} q\overline{q'} b\bar{b} + \nu's$	-	$(17.04 \pm 0.11)\%$
all-jets	$t\bar{t} \to q\overline{q'} q\overline{q'} b\bar{b}$	36/81	$(46.19 \pm 0.46)\%$
	$t\bar{t} \to \tau$ final states	17/81	$(20.21 \pm 0.13)\%$

Table 1.9: $t\bar{t}$ decay channels, Born level and best known branching fractions [70]. Leptonic decay of W include both the decay modes : $W \to \ell\nu$ and $W \to \tau\nu \to \ell + \nu\nu\nu$. The branching fractions considered for the DØanalyses are denoted by ee, $\mu\mu$ and $e\mu$, e+jets and μ+jets, and all-jets.

two neutrinos. These events have the same signature as the events where the W boson decays directly to an electron or a muon and are treated as part of the signal in these channels.The leptonic τ decay modes are summarized in Table 1.8.

Table 1.9 summarizes the different $t\bar{t}$ decay modes and their branching ratios.

1.3.7 Measurement of Top Pair Production Cross-section

Since the discovery of the top quark, the experimental direction has turned to the examination of its production and decay properties. The precise measurement of the $t\bar{t}$ production cross-section is important for many reasons. Its measurement can be compared with the theoretical predictions to test the validity of the SM. A significant inconsistency from the QCD predictions would indicate either a novel production

mechanism, e.g., a heavy resonance decaying into $t\bar{t}$ pairs [85], or a novel decay mechanism, e.g. decay into supersymmetric particles [86]. For instance, the top quark may decay into charged Higgs bosons $t \to H^+b$, where H^+ preferably decays to either cs or $\tau\nu$, resulting in a final state different from the SM expectation. As a consequence, a significant contribution from $t \to H^+b$ would give rise to a visible SM cross-sections lower than the expected values.

$t\bar{t}$ is a dominating background to many interesting physics processes including production of a Higgs boson and many searches for new physics. So a detailed understanding of $\sigma_{t\bar{t}}$ is essential.

In addition, the cross-section measurement can help distinguish between various theories beyond the SM. One such theory, called topcolor, attempts to explain the large top quark mass by proposing additional coupling to the third generation quarks [87]. In topcolor, a new neutral gauge boson, called the Z', exists that couples to the top quark and decays to a $t\bar{t}$ pair. Production of Z'_t bosons would show up as an enhancement of the $t\bar{t}$ cross-section over the SM prediction. Other extensions to the SM that involve the top quark are reviewed in [88].

1.3.8 Dilepton final states of $t\bar{t}$

A unique signature of top arises when both W bosons decay leptonically producing a pair of high p_T leptons, large missing transverse energy ($\not{E}_T$) in the detector from two neutrinos, and two high p_T jets from the b quarks. Although dilepton channels have small branching ratios their identification becomes easier since there are few background processes with two high p_T leptons in the final state. The most copious of these backgrounds are not produced in association with large missing transverse energy. All of the backgrounds can be further discriminated because they do not usually occur in conjunction with high p_T jets, as is the case for top.

There are two categories of processes that can produce pairs of high p_T leptons

well-isolated from hadronic energy in addition to large $\not\!\!E_T$. Diboson production (WW, WZ) in association with jets not only satisfies this requirement, but can also mimic the leptonic kinematic distributions from $t\bar{t}$ very well. However, the cross section for these processes are very low. The only other process capable of generating the above signature is $\mathrm{Z}/\gamma^* \rightarrow ll$. However, there is no direct decay channel to dileptons and neutrinos, so the only physics background from these processes comes indirectly through the di-τ channel, where the τ's decay to electrons or muons. Despite a low branching ratio (BR), the $\sigma \times BR$ is still large. The leptonic spectra, however, are very soft in comparison to that expected for top events.

Aside from the above processes, there are several instrumental effects that can mimic the dilepton plus $\not\!\!E_T$ signature. Normal noise in the calorimeter produces a finite $\not\!\!E_T$ resolution. Hardware malfunctions of the calorimeter readout chain, incorrect jet energy scale correction, or poor muon momentum resolution can also cause an event to appear to have significant $\not\!\!E_T$ even in the absence of neutrino production. Jet fragmentation to leading π^0's which then decay to an overlapping pair of photons, or isolated photon production in conjunction with a conversion or an incorrectly associated track, can both produce objects which occasionally pass the electron identification criteria. Lastly, muons from the decay of initial heavy quarks, or subsequent mesons from any jet's fragmentation, can occasionally give rise to muons which sometimes appear isolated given our analysis criteria. In these ways $Z \rightarrow ee, \mu\mu+$ jets events can appear with substantial reconstructed $\not\!\!E_T$, $W + jets$ events can appear with two isolated leptons (one of them fake), and QCD multijet production can occasionally occur with fake $\not\!\!E_T$ and leptons.

In this thesis, the $t\bar{t}$ cross-section analysis for the dielectron channel is discussed.

Expt.	Decay channel	Observed $t\bar{t}$ events	Estimated background	$\sigma_{t\bar{t}}$ pb
DØ [89]				($m_t = 172.1$ GeV)
	lepton+jets	39	13.97 ± 2.22	5.31 ± 1.72
	dilepton	9	2.69 ± 0.66	6.02 ± 3.21
	all-jets	41	24.80 ± 2.37	7.33 ± 3.20
CDF [90]				($m_t = 175$ GeV)
	lepton+jets (SVX)	29	8.0 ± 1.0	5.1 ± 1.5
	lepton+jets (SLT)	25	13.2 ± 1.2	9.2 ± 4.3
	dilepton	9	1.3 ± 0.40	$8.4^{+4.5}_{-3.5}$
	all-jets			$7.6^{+3.5}_{-2.7}$

Table 1.10: The Tevatron Run I results on top pair production cross-section, the theoretical prediction being 4.5-6.2 pb.

1.3.9 Top Quark Measurements at the Tevatron

Run I: The DØ and CDF collaborations performed the measurements of the top pair production cross-section and top mass in several decays channels based on $\sim$110 pb^{-1} of data collected during the Tevatron Run I. The Run I results on ttbar cross-section are summarized in Table 1.10.

The all channels combined results from DØ [89]and CDF [90] are:

$\sigma_{t\bar{t}}(m_t = 172.1GeV) = 5.69 \pm 1.60$ pb (DØ)

$\sigma_{t\bar{t}}(m_t = 175GeV) = 6.5^{+1.7}_{-1.4}$ pb (CDF)

The largest source of uncertainty for both experiments were the statistical one associated with the relatively small data sets. Both results agree within one standard deviation to the theoretical predictions from the SM.

The all channels combined result on top mass from DØ [89]and CDF [90] are:

$m_t = 172.1 \pm 5.2(stat) \pm 4.9(sys)$ GeV $\;(D\emptyset\;)$

$m_t = 176.1 \pm 6.6$ GeV $\;(CDF)$

Combination of results from the DØ and CDF gave the world average on top mass to be $m_t = 174.3 \pm 5.1$ GeV. The current world average is $m_t = 178.0 \pm 4.3$ GeV, which

is mainly influenced by new, improved DØ measurement in the lepton+jets channel ($m_t = 180.0 \pm 3.6 \pm 4.0$ GeV) [65]. Fig. 1.14 shows an overview of the previous mass measurements and the current world average.

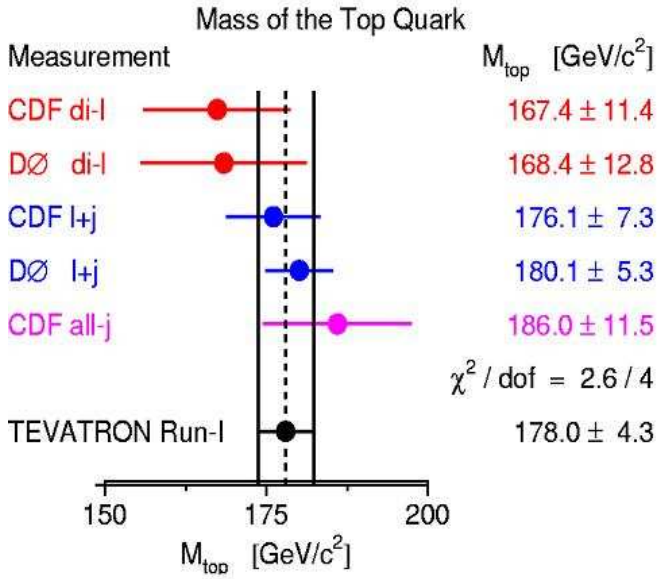

Figure 1.14: The highlights of Top quark mass measurements from Run 1.

Run II: The Run 1 Top quark measurements were consistent with the SM predictions but suffered large uncertainties due to small event samples. The Run II physics program with an increased integrated luminosity and improved detectors provide a basis for a precision measurement of the top quark cross-section and its properties. A very rich top physics program is currently in progress at DØ and CDF with larger dataset.

The DØ has recently reported $\sigma_{t\bar{t}} = 8.6^{+3.2}_{-2.7}(stat) \pm 1.1(syst) \pm 0.6(lumi)$ in dilepton channels [93] based on $\sim 230\,pb^{-1}$ of data, which is consistent with the SM prediction and measurements in other final states. We observed 13 events in the ee, $e\mu$ and $\mu\mu$ channels with an expected background of 3.2 ± 0.7 events. The dielectron channel, in particular, observed 5 candidate events with the expected signal and background contribution of 1.9 and 0.9 events, respectively. The cross-section analysis presented in this dissertation is an extension of the previous analysis in the dielectron channel

Expt.	Channel	Luminosity	$\sigma_{t\bar{t}}$ (pb) for $m_t = 175$ GeV
DØ			
	lepton+jets [91]	230 pb^{-1}	$6.7^{+1.4}_{-1.3}(stat)^{+1.6}_{-1.1}(syst) \pm 0.4(lumi)$
	lepton+jets (b-tag) [92]	230 pb^{-1}	$8.6^{+1.6}_{-1.5}(stat + syst) \pm 0.6(lumi)$
	dilepton [93]	230 pb^{-1}	$8.6^{+3.2}_{-2.7}(stat) \pm 1.1(syst) \pm 0.6(lumi)$
CDF			
	lepton+jets [94]	194 pb^{-1}	$6.6 \pm 1.1(stat)1.5(syst)$
	lepton+jets (b-tag) [95]	162 pb^{-1}	$6.0 \pm 1.6(stat) \pm 1.2(syst)$
	lepton+jets (SVT) [96]	162 pb^{-1}	$8.6^{+1.6}_{-1.5}(stat + syst) \pm 0.6(lumi)$
	dilepton [97]	197 pb^{-1}	$5.6^{+1.2}_{-1.1}(stat)^{+0.9}_{-0.6}(syst)$

Table 1.11: The Tevatron Run II results on top pair production cross-section.

with a larger dataset and improved understanding of our detector. These results [98] show significant improvement from the previous version of our analysis and are being presented as DØ results in the summer 2005 conferences. The latest Run2 results on $t\bar{t}$ cross-section by the CDF and DØ collaborations are summarized in Table 1.11.

The Tevatron Electroweak Working Group has recently come up with a new preliminary world average for the mass of the top quark obtained from the combination of DØ Run I and and CDF Run II measurements [99]. The resulting top mass is: $M_{top} = 174.3 \pm 3.4$ GeV, where the total error consists of a statistical part of 2.0 GeV and a systematic part of 2.8 GeV.

1.3.10 An outline of the dissertation

This dissertation describes a measurement of the $t\bar{t}$ production cross section in the dielectron channel using data from Run II of the Tevatron collected with the upgraded DØ detector at Fermilab. The data sample corresponds to an integrated luminosity of 384 pb^{-1}, which is ~3.5 times than the data used in Run I. The analysis employs kinematic and topological selections to select candidate events. The analysis results show considerable improvement from the previous pass of our analysis [93] based on 243 pb^{-1} of data and are being presented as the DØ collaboration results in the

ongoing summer 2005 conferences [98].

The theoretical description of the top quark and the motivation for an accurate measurement of its cross section have already been covered in detail earlier. It thus lays the foundations to understand the goal behind the original work presented in the later chapters. Chapter 2 describes the apparatus used to conduct the experiment. Briefly describing the operation of the Tevatron Collider which allows the production of top quark, this chapter mainly focusses on the DØ detector which is used to detect and record the particles produced in the collisions. Chapter 3 discusses the triggers used to select the events of interest to this analysis and presents the resulting data sample. It also details the Monte Carlo samples used for the study of signal and background in the analysis. Chapter 4 explains the techniques used in DØ to reconstruct and identify physics objects from the data collected by the detector. This chapter mainly focusses on the present study on improving the electron identification and better understanding of missing transverse energy. Chapter 5 presents measurement of the top quark cross section in the dielectron channel based on systematic and careful procedure of selecting candidate events from a large data set. It deals with the efficiencies for the $t\bar{t}$ signal selection and estimation of specific backgrounds. The estimation of systematic uncertainties on the measurement is also presented. Chapter 6 summarizes the results of the analysis presented in this dissertation. It also describes in brief the cross-section measurement obtained from the combination of all dilepton final states.

Chapter 2

The DØ Detector at Tevatron

"What we observe is not the nature itself, but nature exposed to our method of questioning." –Werner Heisenberg.

Fermi National Accelerator Laboratory, a high-energy physics laboratory, named after particle physics pioneer Enrico Fermi, is located 30 miles south west of Chicago in Illinois, USA and is spread over nearly 6800 acres of land [100]. It is the home of currently the world's most powerful particle accelerator, the Tevatron. The Tevatron collides counter rotating beams of protons and anti-protons at a center of mass energy, $\sqrt{s}$, of 1.96 TeV, after accelerating these particles in a 6.3 km ring to energies of up to 0.98 TeV [101]. These collisions occur at the center of two huge particle detectors : the Collider Detector at Fermilab (CDF) and the DØ detector, located at the BØ and the DØ beam crossing region of the Tevatron ring. These detectors measure the final states of the particles that are produced in the interactions initiated in the colliding beams.

The Tevatron Collider physics program is comprised of two stages : Run I and Run II. During the Run I physics program (1992-1996), $p\bar{p}$ collisions took place at $\sqrt{s}$ = 1.8 TeV and each experiment (CDF and DØ) collected an integrated luminosity of about 130 pb^{-1} data. Run I [102] produced a large number of exciting physics

results led by the discovery of top quark by both the experiments in 1995 [25][26]. After an upgrade phase of more than six years, the Tevatron started a new era in March 2001 with the increased center of mass energy ($\sqrt{s}$) of 1.96 TeV, referred to as Run II. Major efforts have been taken in order to increase the luminosity and thereby the physics potential of the collider. In addition, the detectors have been significantly upgraded to enhance their capability to observe interesting physics. The DØ experiment utilized the first year of collisions to commission the detector, trigger and electronics. The last major element to be completed - the central tracker - which is crucial for particle position and charge determination, was fully instrumented in April 2002, marking the beginning of DØ Run II program. Currently the Run II physics program is underway at Fermilab addressing some of the biggest questions in particle physics, and is expected to continue until about mid-2009 [103]. The Large Hadron Collider (LHC) at CERN [104] is expected to take the energy frontier away from Fermilab by the end of this decade, which will provide proton-proton collisions at $\sqrt{s}$=14 TeV with luminosities about one hundred times greater than at the Tevatron.

The data analyzed in this thesis were recorded by the DØ detector during Run II of the Tevatron in the years 2002-2004. This chapter briefly describes the technical details of the Fermilab Tevatron Complex and the DØ detector and its subsystems during the Run II. We focus on the subsystems used by this analysis, such as calorimeter, preshower and tracking systems. Also we discuss the trigger and data acquisition (DAQ) systems. This chapter also includes a discussion of proton anti-proton collisions and particle detection in collider interactions.

2.1 The Fermilab Accelerator Complex

Fermilab employs a series of accelerators to create the world's most energetic particle beams. Figure 2.1 gives a schematic description of the Fermilab accelerator complex. Each accelerator has both a minimum and maximum energy for which it can hold

the beam, and this is why there is a chain of accelerators. In this section, we will briefly describe the acceleration stages necessary to prepare the final beams. A very complete description of the Run II Tevatron accelerator complex operation can be found in [106], [107], and [108]. The first stage is known as the preaccelerator. The

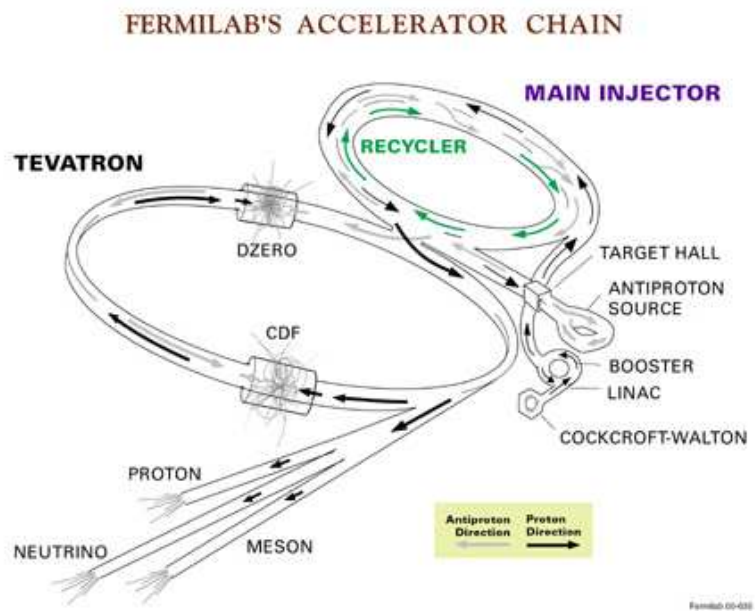

Figure 2.1: Schematic of the Fermilab accelerator chain. Adapted from [105].

proton beam originates as hydrogen gas which is ionized via a magnetron source to H^- ions. These ions are accelerated to 750 keV using Crockroft-Walton accelerator. A linear accelerator about 150 m long consisting of radio-frequency (RF) cavities is then used to accelerate the ions to 400 MeV. The H^- ions are then passed through a carbon foil that strips off the electrons, leaving bare protons. These protons then enter the Booster, a synchrotron ring with ≈478 m circumference, where they are constrained to a circular path using dipole magnets. Magnets of higher-order poles are used to maintain a focused beam.The Booster uses RF cavities to accelerate the protons over the course of about 20,000 revolutions to 8 GeV. During the acceleration process, the protons are grouped into a pulse train containing 5 to 7 bunches, each containing about 5-6$\times 10^{10}$ protons. The Booster injects its 8 GeV proton beam to the Main

Injector, which is a synchrotron 3 km in circumference. The Main Injector coalesces the proton bunches from the Booster into single high-density bunch of $\approx 5 \times 10^{12}$ protons and accelerates them to either 120 GeV or 150 GeV. The 150 GeV proton bunches are injected to the Tevatron, while the 120 GeV bunches are delivered to the anti-proton facility.

To make anti-protons, proton bunches from the Main Injector are focused on a nickel target, and anti-protons (with 8 GeV) are collected from the spray of particles created. The efficiency of this process is about 15 anti-protons produced for every million protons on the target. The 8 GeV anti-protons are transferred to the Debuncher, which is a 520 m long triangular storage ring. Here the bunch structure from the Main Injector is removed and the transverse momentum profile of the anti-protons is reduced. Next the anti-protons are transferred to the Accumulator, another 8 GeV storage ring, where they are further cooled (i.e. reduced in momentum space and transverse oscillations) and focused. The anti-protons are stored here until a sufficient number about $1.5 - 2 \times 10^{12}$ anti-protons have been accumulated.

The Tevatron is the final acceleration stage. It is a 6.3 km-circumference synchrotron ring. The Tevatron is currently the world's largest superconducting synchrotron accelerator. The superconducting magnets in this huge machine are cooled to 4.6 K using liquid Helium, producing fields of up to 4 Tesla. When the accelerator complex is ready, the Main Injector delivers 36 bunches of protons (about 2.7×10^{11} protons per bunch) to the Tevatron. After proton injection, 4 bunches at a time of anti-protons are transferred to the Main Injector where they, too, are accelerated to 150 GeV and injected into the Tevatron. When 36 bunches of anti-protons have been injected, the Tevatron accelerates the proton and anti-proton bunches in two oppositely rotating beams in the same beampipe up to a final energy of 980 GeV. The high-energy beams are then squeezed to a high density using focusing magnets (low beta quadrupole magnets) and brought into head on collisions with a center-of-mass

energy of 1.96 TeV. The time interval between the collisions is 396 ns. These collisions occur at two points on the Tevatron ring, referred to as interaction regions, occupied by the CDF and DØ detectors.

The interaction regions have a 3D-Gaussian shape and a width of about 30 cm along the beam-axis (the "z" direction), and about 30 μm in the transverse directions. The beam halos (protons and anti-protons in irregular orbits far from the beam center) are scrapped away with collimators.

The Tevatron is performing as desired and has already delivered an integrated luminosity of $\sim 1fb^{-1}$ by June 2005. The goal of the Tevatron is to deliver an integrated luminosity between 4.4 and 8.6 fb^{-1} by 2009.

2.1.1 Run II Upgrades

The major upgrades in Tevatron for the Run II include the construction of the Main Injector and the Anti-proton Recycler. The Main Injector is capable of delivering up to 3 times as many protons as the old Main Ring in Run I. The net result of these upgrades is an increase in $\sqrt{s}$ to 1.96 TeV and an ever increasing peak luminosity. The Tevatron operating parameters are listed in Table 2.1. The bunch structure for Run I and Run II is shown in Figure 2.2. In Run I, the accelerator delivered 6 bunches of protons and anti-protons ("6×6" bunches) with a crossing every 3500 ns. The complex now provides 36 bunches of protons and 36 bunches of anti-protons ("36×36" bunches) in the collider separated into 3 super bunches. Each super bunch has 12 bunches separated by 396 ns. Substantial changes in both the DØ and CDF detectors were made. Many were mandated by the change in accelerator timing and increased luminosity, but others were made to add new capabilities.

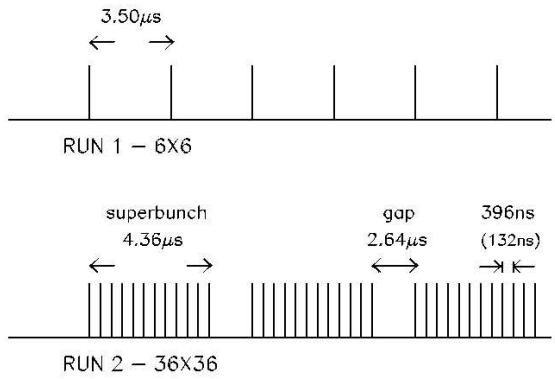

Figure 2.2: Tevatron bunch scheme for Run I (top) and Run II (bottom).

Parameters	Run Ib	Run IIa
Energy (GeV)	900	980
Bunches	6	36
Protons/bunch	2.3×10^{11}	2.7×10^{11}
Anti-protons/bunch	0.55×10^{11}	0.3×10^{11}
Total Anti-protons	3.3×10^{11}	11×10^{11}
Anti-proton production rate (/hr)	6.0×10^{10}	20×10^{10}
Typical Luminosity ($cm^{-2}s^{-1}$)	$\sim 1.6 \times 10^{31}$	$\simeq 1 \times 10^{32}$
Integrated Luminosity (pb^{-1}/week)	$\sim$3.2	$\sim$17.3
Bunch-spacing (ns)	$\sim$3500	396
Interactions/crossing (@ 50 mb)	2-3	2-3

Table 2.1: Tevatron operating parameters in Run Ib and Run Run IIa. Run Ib is the period of running from 1992 to 1996 and Run IIa is the period of running which started in 2002 and is still in progress.

2.2 $p\overline{p}$ Collisions

Most of the $p\overline{p}$ interactions initiated at the Tevatron result in a very small momentum exchange between the two hadrons which scatter the particles at small angles. These interactions do not produce physics useful for probing SM physics. In the more interesting collisions, however, a large momentum transfer occurs between constituents of the two particles, and the original proton and anti-proton are broken apart. A parton (a quark or gluon constituent) in the proton exchanges a force carrier boson with a parton in the anti-proton to create a hard-scattering reaction. The fragments

of the proton and anti-proton receive little transverse momentum in the collision and continue along nearly parallel to the beam-line, while the ejected partons enter the detector.

Such hard-scatter interactions of the protons can result in the production of any of the SM and possibly beyond SM particles. However, many of the SM particles are unstable and thus decay rapidly to lighter particles. Common examples of this are W and Z bosons as well as the Top quark. Generally, only electrons, muons, neutrinos, photons, and a few bound states (hadrons) of light quarks (u,d,s) are semi-stable and live long enough to reach the detectors. The different semi-stable particles are measured in various ways, as described later on.

2.3 Luminosity and Cross-Sections

In high-energy physics, the processes are often expressed with a cross-section, σ, which is a measure of the interaction probability per unit flux. In collider experiments, the flux corresponds to the size and amount of particles in the colliding beams and is referred to as luminosity, $\mathcal{L}$. The luminosity depends on a number of beam characteristics at the interaction point like the number of particles in each colliding beam, number of bunches and the transverse sizes of the bunches. The luminosity is given as:

$$\mathcal{L} = \frac{f_{rev} B N_p N_{\overline{p}}}{2\pi(\sigma_p^2 + \sigma_{\overline{p}}^2)} F(\sigma_l/\beta^*), \tag{2.1}$$

where f_{rev} is the revolution frequency, B is the number of bunches per beam, $N_{p(\overline{p})}$ is the number of protons (anti-protons) per bunch, $\sigma_{p(\overline{p})}$ is the transverse beam size of the proton (anti-proton) beam, and F is a form factor depending on the bunch length (σ_l) and the beta function at the interaction point (β^*). The Luminosity is thus proportional to the product of the number of particles in each beam passing through a unit area per unit time and is expressed in units of $\mathrm{cm}^{-2}\mathrm{s}^{-1}$. The cross-

section is expressed in units of barn where 1barn$\equiv 10^{-24}$ cm^2. The cross section when combined with the luminosity gives the interaction rate for a given process.

$$R = \sigma \mathcal{L}, \tag{2.2}$$

Perhaps a more interesting quantity than the interaction rate per unit time is the number of interactions (N) occurring in collisions over a given period of time. The number of times a given process occurs, N, is given by

$$N = \sigma \int \mathcal{L} dt \tag{2.3}$$

Where $\int \mathcal{L}$ dt is the luminosity integrated over time and it is referred to as the integrated luminosity, and is measured in units of inverse barns (b^{-1}). It has to be noted that for a particular interaction, the cross-section is fixed for a given center-of-mass energy and particle beam type, parameters which are set by the accelerator design. The goal of the accelerator is thus to maximize the integrated luminosity delivered to the experiments. Typical cross-sections for various interesting physical processes are usually of the order of pico-barns (pb), or $\equiv 10^{-36}$ cm^2. Thus integrated luminosity is often measured in inverse pico-barns (pb^{-1}). For example, a certain process of 1 pb cross-section is expected to occur 100 times during the delivery of 100 pb^{-1} integrated luminosity.

Thus the production cross section for a given process can also be expressed as

$$\sigma = \frac{dN/dt}{\mathcal{L}}, \tag{2.4}$$

2.4 Particle Detection at Collider Detectors

Particle detectors for high energy hadron colliders consist of three main components : the tracking system, the calorimeters and the muon system.

The tracking detectors are positioned closest to the interaction point and have the finest segmentation. They are designed to measure the three-dimensional trajectories (tracks) of the charged particles passing through them. The magnetic field bends the trajectory of charged particles and allows a measurement of their charge and momenta. The tracking detectors are built out of light (low Z) material to introduce as little interactions as possible while still detecting their presence (minimizing scattering and energy loss). Tracking system is thus very crucial in identifying electrons and muons. Modern tracking detectors consist of an inner high resolution silicon vertex detector, to provide precise primary and secondary vertex determination, and a large outer tracking system, to provide efficient track pattern recognition and improved momentum resolution.

Surrounding the tracking system, the calorimeter measures the energy of most of the particles (charged and neutrals except for muons and neutrinos) that reaches the calorimeter. This is done by using dense (high Z) materials sufficient to absorb the full energy of most incident particles, while making a measurement of the energy deposition. A particle hitting a dense material produces a shower of secondary particles. The measurement of the shower size allows determination of the particle energy, and the shower shape provides a way to identify between different types of particles, such as electrons, photons and hadrons. For example, the hadrons produce showers deeper in the calorimeter.

Since muons escape through the calorimeter, they are identified by means of additional tracking detectors (muon chambers with toroidal magnetic field) beyond them, which are designed to measure the trajectory and charge of the muon.

Neutrinos escape the detector completely and can only be partially reconstructed.

Their presence is inferred from an imbalance in the total transverse energy measured by the calorimeter, denoted by $\not{E}_T$. Excellent $\not{E}_T$ resolution is crucial for a wide range of searches, like precise measurement of W boson, top quark mass as well as searches for new physics involving supersymmetric particles.

Quarks and gluons which leave the hard-scattering region, do not live very long before they undergo hadronization, due to confinement, which is a non-perturbative aspect of the strong force that does not allow color-charged particles to be isolated. This process creates a jet of particles, each traveling in the general direction of the initial quark or gluon. These jets are detected as broad showers of charged particles and energy deposited in the calorimeter.

2.5 Overview of the DØ Detector in Run II

The DØ detector [110][111] [112] [113] is a general purpose nearly-hermetic particle detector, designed and constructed to study interactions originating from $p\overline{p}$ collisions at $\sqrt{s} = 1.96$ TeV at the Fermilab Tevatron Collider. The detector is optimized to measure final states containing photons, electrons, muons, jets, and neutrinos from a number of processes originating from $p\overline{p}$ interactions. It is particularly suited to study high-mass states and large transverse momenta (high-p_T) phenomena. After the completion of the Run II upgrade program, the new detector continues to detect these important physics signatures, while at the same time its physics reach has been extended to lower-p_T final states, as well as to vigorous B-physics. The prime physics focus of the DØ experiment in Run II are both detailed study of known physics and searches for new physics. An outstanding physics program is underway, including precision measurements of top quark properties; precision electroweak measurements based on the properties of the top quark and W boson; searches for the Higgs boson; searches for physics beyond the Standard Model (such as supersymmetry and extra dimensions); studies of CP violation and quark mixing in the B sector and rare B

decays.

2.6 The DØ Detector Components

Figure 2.3 shows the schematic side view of the Run II DØ detector. The DØ detector has undergone significant upgrades for Run II, which is designed to enhance its capabilities from Run I and to accommodate the decrease in bunch spacing from 3.5 μs in Run I to 396 ns in Run II. The upgraded DØ detector consists of three primary detector systems as we move from inside to outside : inner trackers, calorimeter, and muon systems, all symmetric about the Tevatron beam line. The inner tracking system has been completely replaced, and sits inside a 2 Tesla magnetic field provided by a super-conducting solenoid. The calorimeter itself remains unchanged, although the readout electronics has been completely replaced. Preshower detectors have been added between the solenoid and the calorimeter to provide electron identification and to compensate for the energy loss in the solenoid. A new 3-level trigger system and data acquisition system are used to handle the high event rate.

The tracking system consists of a Silicon Microstrip Tracker (SMT) and a Scintillating Central Fiber Tracker (CFT) enclosed within a 2T superconducting solenoid magnet. The tracking system is surrounded by two scintillator based Central (CPS) and Forward (FPS) Preshower detectors to provide electron identification and to compensate for energy losses in the solenoid.

The Calorimeter is made of four sampling Uranium-liquid Argon cryostats : a central cryostat covering the region $\mid \eta \mid < 1.2$, two forward cryostats extending the coverage to $\mid \eta \mid \sim 4$ and the Inter Cryostat Detector (ICD) to cover the overlapping pseudorapidity region.

The muon system consists of a central and forward scintillator based tracking detector, a toroidal magnet and special shielding material surrounding the accelerator beam pipe in forward direction. The purpose of the shielding material is to reduce

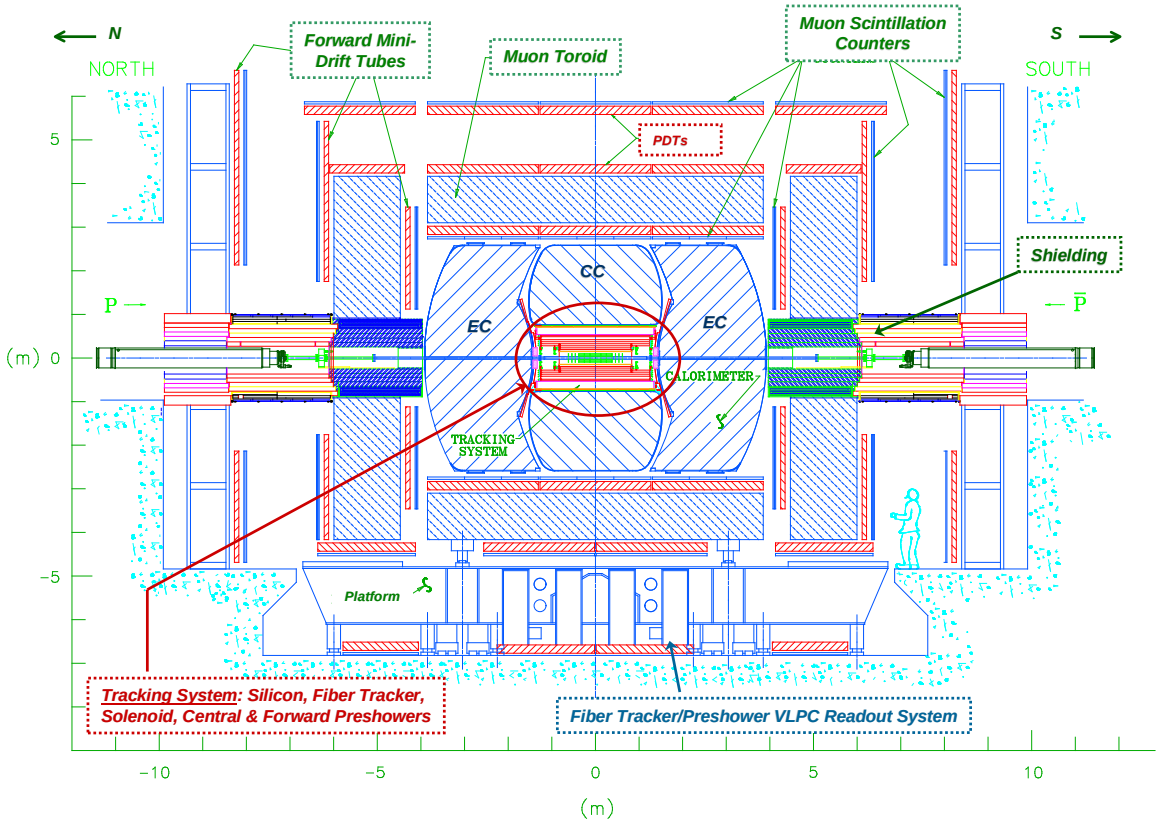

Figure 2.3: Side view of the DØ detector [111].

the presence of non-muon background particles originating from the beam halo and proton-antiproton fragments interacting with the beam pipe and the calorimeter.

The next sections provide an overview of the different subsystems of the DØ detector relevant to this analysis and their operation, following an introduction of the detector coordinate system and some important kinematic variables in the collider physics. Also, the trigger system, which selects the most interesting events to be written to tape, and the readout system will be discussed. A much more complete treatment can be found in [112][113].

2.6.1 Coordinate System and Kinematic Quantities

Before discussing the DØ detector, it is useful to define the DØ coordinate system and some basic concepts used. The DØ detector uses a standard right-handed coordinate

system with the center (0,0,0) at the center of the detector. Figure 2.4 shows the coordinate system used at DØ . In this system, the direction of the $+x-$axis is a vector pointing radially outwards from the center of the Tevatron ring, the $+y-$axis direction is vertically upwards and the $+z-$axis direction is along the proton direction. DØ has roughly cylindrical symmetry and particle collisions exhibit spherical symmetry (in their rest frame), motivating the choice of a combination of cylindrical and spherical coordinates (z,θ,ϕ). The polar angle, θ, is defined such that $\theta = 0$ lies along the beam pipe in the $+z$ direction while $\theta = \pi/2$ is perpendicular to the beam pipe. The azimuthal angle, ϕ, is defined such that $\phi = 0$ points away from the center of the Tevatron ring (also the positive $x-$axis). The upward direction, $\phi = \pi/2$, defines the positive $y-$axis.

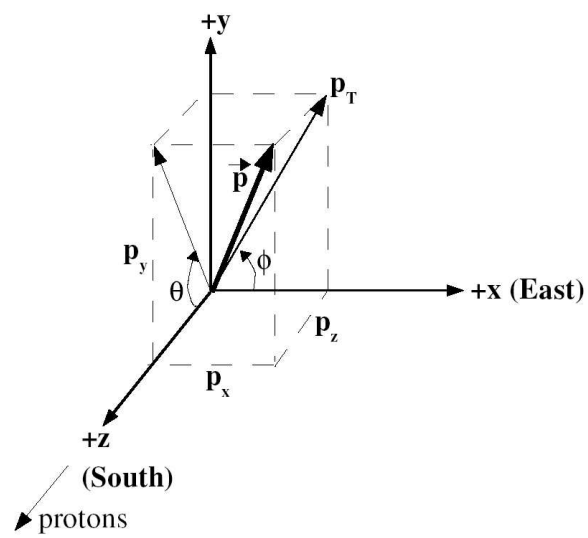

Figure 2.4: Diagram of p_T in the DØ coordinate system.

Another kinematic variable used in place of the polar angle θ is the rapidity, y, because the multiplicity of high energy particles (dN/dy) is invariant under Lorentz transformations along the $z-$axis. The rapidity is defined as

$$y = \frac{1}{2} \ln \left(\frac{E + p_z}{E - p_z} \right). \tag{2.5}$$

Where p_z is the particle momentum along the z-axis. Although y is useful, the quantity that most often is utilized is the pseudo-rapidity, η, defined as

$$\eta = -\ln \tan\left(\frac{\theta}{2}\right). \tag{2.6}$$

which approximates the true rapidity y for finite angles in the limit that $m/E \to 0$. It has to be noted here that in $p\overline{p}$ collider experiment like DØ, the dimensions of the beam along the x and y axis tend to be very small, but along the z-axis where the actual collisions take place the size of beam is not as limited. Because of this the primary interaction point in DØ has a Gaussian distribution in the z axis with mean $z = 0$ and $\sigma_z = 28$ cm. As a result of this beam structure there is another useful variable, the detector pseudo-rapidity, η_d. This pseudo-rapidity is computed with respect to an interaction point whose position is at $z = 0$. Because the real interaction point's position is distributed around $z = 0$, η (also called the "physics" pseudo-rapidity) and η_d may be different. The "physics" η of a particle is determined by θ of the particle as measured from the interaction point or primary vertex.

Since the parton-parton collisions do not occur at fixed $\sqrt{\hat{s}}$ and since a significant fraction of energy escapes the detector as the nucleon remnants carry it away down the uninstrumented beam pipe, the longitudinal boost of hard scatter particles is very difficult to measure. However, these particles can still be studied by applying conservation of energy and momentum in the transverse plane. Before the collision, the transverse energy of the system is zero. After the collision, the transverse energy of the proton and anti-proton remnants is negligible, making it possible to study the hard scatter particles in this plane. To do this effectively, variables for use in the transverse plane are defined:

- $E_T = E \sin\theta$: Transverse energy.
- $p_T = p \sin\theta = \sqrt{p_x^2 + p_y^2}$: Transverse momentum as shown in Figure 2.4.

- $\not{E}_T$: Missing transverse energy, or energy imbalance in the transverse plane.

2.6.2 Inner Tracking System

The entire tracking system (Figure 2.5) is new in Run II. The tracking detectors are constructed directly outside of the Tevatron beam pipe and consists of two subsystems : the Silicon Microstrip Tracker (SMT) and the Central Fiber Tracker (CFT). These tracking detectors are surrounded by a superconducting solenoidal magnet, providing a 2 Tesla magnetic field parallel to the beam line. The solenoidal field bends the paths of charged particles with a curvature inversely proportional to their transverse momenta. Observing the curvature of a particle's path allows for a precise measurement of its momentum, as well as the sign of the charged particle.

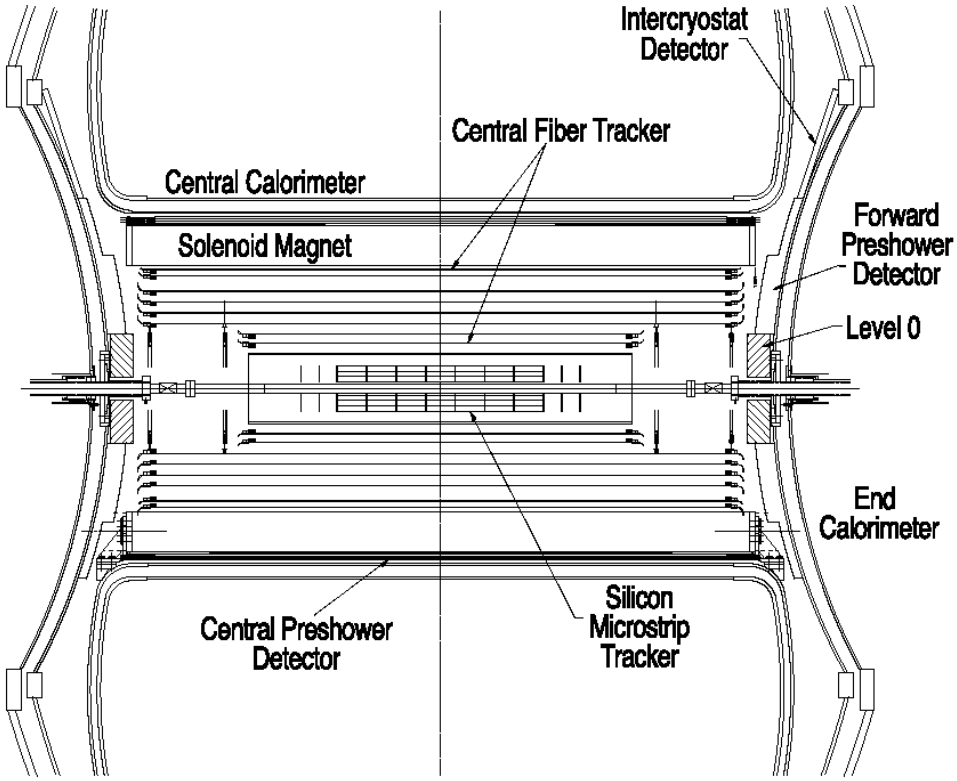

Figure 2.5: DØ tracking system [111].

Silicon Microstrip Tracker (SMT)

The detector nearest to the interaction region is the Silicon Microstrip Tracker (SMT), which provides the high resolution position measurements of the charged particle paths that are used to reconstruct tracks and determine the vertex information [114]. The large z distribution of the $p\overline{p}$ interaction region ($\sigma_z \sim 28$ cm) provides a challenge for designing a detector in which tracks are predominantly perpendicular to detector surfaces. This challenge motivates a detector geometry consisting of six 12 cm long barrels with interspersed disks (12 F-disks and 4 H-disks) of silicon wafers, creating a tracking coverage out to $|\eta|$=3. A schematic of the SMT geometry is shown in Figure 2.6. SMT has approximately 793,000 readout channels and provide a spatial resolution of approximately 10 μm in $r-\phi$ and 100 μm in $r-z$ plane. The tracks for high η particles are reconstructed in three dimensions primarily by the disks, while particles at small η are detected primarily by the barrels.

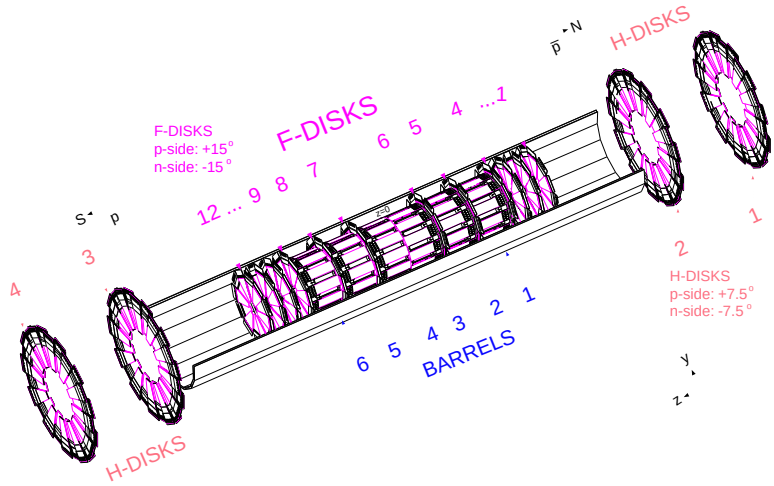

Figure 2.6: DØ Run II Silicon Microstrip Tracker detector.

Central Fiber Tracker

The scintillating central fiber tracker (CFT)[115] surrounds the SMT and provides tracking coverage up to $|\eta| < 2.0$. The combined hit information from the SMT

and CFT allows to improve the overall tracking quality not achievable by either detector alone. The CFT consists of eight concentric carbon fiber barrels holding layers of scintillating fibers. Each cylinder supports a doublet layer of fibers oriented parallel to the beam line (axial fibers). The odd numbered cylinders (counting from the inside to outside) hold an additional doublet offset at alternating angles of $\pm 3^0$ (stereo fibers). The axial fibers provide ϕ measurements at a fixed radius and, when combined with the stereo fibers, can provide a measurement of z. In total, the CFT contains 76,800 readout channels. Since the CFT covers more radial distance than the SMT, it is better for determining the p_T and charge of charged particles by measuring the curvature of the tracks in the 2T magnetic field. Each ionizing particle produces an average of about 10 photons in each fiber, which are then detected using a Visible Light Photon Counter (VLPC) that converts the photons into an electrical pulse. The position resolution provided by the CFT is on the order of 100 μm, corresponding to a ϕ resolution of 2×10^{-4} radians.

2.6.3 Preshower Detectors

There are two preshower detectors located just before the calorimeters : Central Preshower (CPS) covering $|\eta| < 1.2$ and a forward preshower covering $1.4 < |\eta| < 2.5$ (shown in Figure 2.5). These preshower detectors play an important role in improving calorimetry measurements and are also sensitive enough to aid tracking measurements, thus leading to enhance electron and photon identification.

The central preshower (CPS) [116] detector is located outside the solenoid, and is used primarily to complement the central calorimeter. In Run I, the DØ calorimeter had an excellent energy resolution. The Run II design placed the solenoid in front of the calorimeter, which added material and degraded its energy resolution. This is because the solenoid material can interact with particles, causing early showering before the calorimeter thus affecting the measurement of the particle's energy. To

mitigate this problem, the region between the solenoid and the central calorimeter cryostat has been instrumented with a Preshower detector. The preshower detector was designed to recover the energy resolution by obtaining an energy sampling of the particles which have just passed through the solenoid, upto about 2 radiation lengths of dense, uninstrumented material [117]. The Central Preshower Detector (CPS) is a cylindrical detector consisting of a lead radiator of two radiation lengths thickness followed by three layers of scintillating strips with triangular cross-section. The innermost layer of strips is arranged axially, while the two outer layers are arranged at stereo angles of $\pm 23\%$. Each strip of scintillator has a hole in the center, which is occupied by a wavelengh-shifting fiber. The wavelength shifting fibers carry the signal from the detector to the clear wave-guides, which transmit the light to the VLPC cassettes, just like those in the CFT. The initiation of a narrow electromagnetic shower in the lead improves the spatial resolution of the detector for electrons and photons. Thus, the CPS functions both as a calorimeter (by early energy sampling) and as a tracker (by providing precision position measurements).

The Forward Preshower Detector (FPS)[118] is very similar to CPS in its design and consists of a lead radiator of two radiation lengths thickness, sandwitched between two layers of scintillating material. Each layer is made from two thinner layers of scintillating fibers, arranged in a u-v geometry with a $\pm 23\%$ stereo angle. There are no axial layers in FPS. The inner layers usually detect minimum-ionizing particles (MIPs) while the outer layers also detect the beginnings of showers, which generate larger signals. These layers are aptly called the MIP and shower layers, respectively. The gains on the MIP layer channels are set to detect small signals (similar to the CFT), while the shower layer channels have lower gain (similar to the CPS) to measure showers.

The solenoid does not shadow the forward calorimeters from the interaction region at the center of the detector. The function of the FPS is therefore not to improve

energy resolution as in the case of the CPS; rather, its primary purpose is to discriminate between electrons and photons since the tracking efficiencies get worse in the forward regions. If a particle is not observed in the MIP layer but has a shower in the outer layer, it is likely to be a photon that did not interact in front of the lead. If there is signal in the MIP layer and a shower in the shower layer, then the incident particle is likely to be an electron[1].

2.6.4 Calorimeter System

The *DØ* calorimeters have been designed to provide excellent measurement of the energy of photons, electrons and hadronic jets, by inducing them to create showers of energy using a large amounts of dense material. The energy in the showers is then sampled at many points, to determine its shape and energy. This section explains in brief the energy measurement in the calorimeter.

Energy Measurement

EM objects interact primarily with materials via the following two processes: pair production ($\gamma \rightarrow e^+e^-$) and bremsstrahlung ($e \rightarrow e\gamma$). For each successive interaction the number of secondary particles increases while the average energy per particle decreases. It is the collection and measurement of these secondary particles that gives us information on the original EM object's energy. Because of these interactions, the energy of the original particle is expected to drop exponentially:

$$E(x) = E_0 e^{-x/X_0} \tag{2.7}$$

where E_0 is the particle's original energy, x is the distance traveled, and X_0 is the radiation length of the material being passed through. For uranium, X_0 is approximately

[1] A charged pion can have a signature similar to an electron in the FPS, but it generally has different showering properties in the calorimeter, where electrons and photons have very similar signatures.

3.2 mm.

For hadrons, the interaction with material occurs with the nuclei via the strong nuclear force. These interactions also produce secondary particles, most of them are neutral pions (π^0) and charged pions ($\pi^{\pm}$). While the π^0s produce electrons and photons which interact electromagnetically, the charged pions interact strongly. This type of particle shower tends to develop over longer distances and is also larger. The analog of the radiation length for hadronic interactions is the nuclear interaction length (λ_0), which is about 10.5 cm for uranium.

2.6.5 DØ Calorimeters

We preserve the excellent Run I calorimetry; however, the readout system has been upgraded. Figure 2.7 shows an overview of the *DØ* calorimeter system. The DØ calorimeter [113] is a compensating, sampling calorimeter with fine segmentation. It uses liquid Argon (LAr) as an active medium and depleted ^{238}U, stainless steel/copper plates as absorber materials. In a sampling calorimeter, the shower development of the incident particles is periodically sampled via the ionization of an active medium. By "compensating", it is meant that the ratio of the electromagnetic and hadronic response (e/h) is close to one. Calorimeter segmentation in the transverse and longitudinal shower directions, allows one to measure the shape of the shower development and determine the direction of the incident particles which helps in the identification of different types of particles such as electrons, photons and hadrons.

For the active material, LAr was chosen for several reasons : a) it provides uniform gain over the entire calorimeter, allowing for a channel-to-channel response stable over time and dependent on gap and absorber thickness, b) it is highly flexible in segmenting the calorimeter volume into readout cells, c) it is radiation hard, d) it is easy to calibrate. For the absorber material Uranium was chosen because its high density allows for a compact detector that contains almost all shower energy while

reducing the cost. It also improves the e/h compensation ratio. There are three liquid argon calorimeters housed in three separate cryostats - one central (CC) (with $|\eta| < 1.1$) and two endcaps (EC) (with $1.5 < |\eta| < 4.2$). In the inter-cryostat region ($1.1 < |\eta| < 1.4$), both "massless gaps" and an inter-cryostat detector (ICD) have been added to sample the shower energy that is lost by particles that transverse the module endplates and cryostat walls.

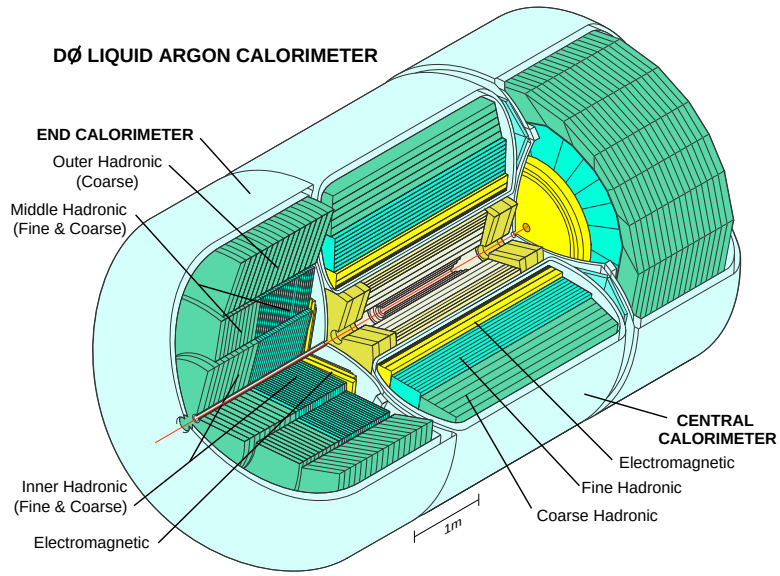

Figure 2.7: Overall view of the DØ calorimeter system [111].

The calorimeter modules themselves are further segmented into three distinct sections. In order of increasing radius, these are

- electromagnetic (EM) section with relatively thin uranium absorber plates.
- fine-hadronic (FH) with thick uranium plates.
- coarse-hadronic (CH) with thick copper or stainless steel plates.

2.6.6 Electromagnetic Calorimeter

Because the EM objects tend to decay over a shorter distance than hadrons, the innermost layers of both the CC and EC are the electromagnetic layers. The electro-

magnetic calorimeter is 21 radiation length deep and it is arranged in four readout layers (EM1 through EM4). These layers extend radially in the CC and along the z-axis in the EC. Each layer uses 3(4) mm thick uranium (^{238}U) absorber plates in the CC (EC). In the central cryostat, the transverse segmentation of the EM calorimeter is $\Delta\eta \times \Delta\phi = 0.1 \times 0.1$ in all layers except the third. The third layer (EM3) is expected to receive the maximum of electromagnetic showers and hence is segmented twice as finely into cells with $\Delta\eta \times \Delta\phi$=0.05 $\times$ 0.05, to allow for more precise location of the EM shower centroid. With this fine segmentation, the azimuthal position resolution for electrons with energy above 50 GeV is about 2.5 mm. In the Endcap cryostat, the segmentation is 0.1×0.1 except for $|\eta_d| > 3.2$, where the pad becomes too small and the segmentation is increased to 0.2×0.2.

2.6.7 Hadronic Calorimeters

The hadronic calorimeter surrounds the EM calorimeter in both the CC and EC cryostats and are 7-9 interaction length deep. The transverse segmentation of all hadronic modules is around 0.1×0.1. It consists of 3 (4) fine hadronic layers (FH) in CC (EC). These use slightly thicker uranium absorber plates, 6 mm thick. Finally, the coarse hadronic layer uses 46.5 mm thick copper (CC) or stainless steel (EC) absorbers. There is one CH layer in CC and three CH layers in EC.

The calorimeter layer depths in terms of their radiation (X_0) and nuclear interaction (λ_0) lengths are summarised in the Table 2.2 .

	EM (X_0)				**FH** (λ_0)				**CH** (λ_0)		
	EM1	EM2	EM3	EM4	FH1	FH2	FH3	FH4	CH1	CH2	CH3
CC	2	2	7	10	1.3	1.0	0.9		3		
EC	0.3	2.6	7.9	9.3	1.2	1.2	1.2	1.2	3	3	3

Table 2.2: Layer depths in the calorimeter.

From the readout point of view, each layer represents a discrete set of readout

cells. These readout cells (one from each layer) are grouped radially along the outward direction (approximate direction of a shower development) to form a $\Delta\eta \times \Delta\phi$ 0.2×0.2 readout geometry referred to as a tower. The readout tower geometry is shown in Figure 2.8. This is a "pseudo-projective" geometry. The term "pseudo-projective" refers to the fact that the centers of cells of increasing shower depth lie on the rays projecting from the center of the detector, but the cell boundaries are aligned perpendicular to the absorber plates.

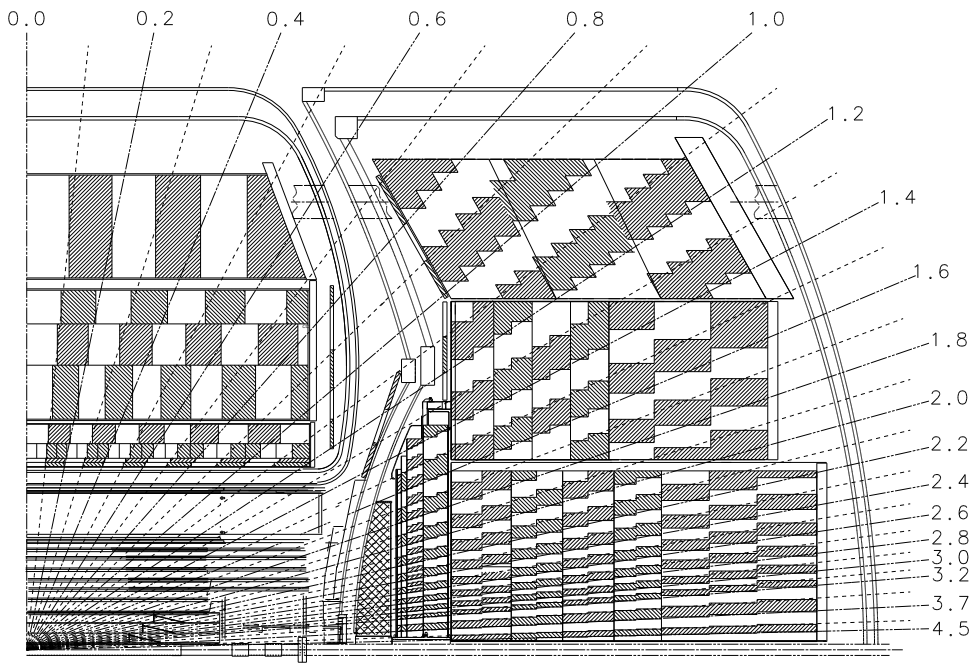

Figure 2.8: A quarter of the calorimeter in the $r - z$ plane of the detector showing the tower geometry.

Each layer consists of alternating layers of absorber plates and signal boards filled with LAr. A cell (readout cell) is a combination of several adjacent unit cells. A schematic view of the calorimeter unit cell is shown in Figure 2.9. The signal boards are made of copper readout pad sandwiched by two 0.5 mm thick G-10 insulator. The outer surfaces of the boards are coated with a highly resistive epoxy. An electric field is created by applying a positive high voltage of 2.0-2.5 keV between the resistive surfaces of the signal boards and the grounded absorber. When a particle enters the

calorimeter, it showers inside the absorber plate, and the secondary particles from the shower ionize the argon atoms. The ionization electrons drift toward the signal boards inducing a signal on the copper pad. The gap between the absorber plates is 2.3 mm, and the electron drift time across the gap is about 450 ns[4]. Readout electronics sample the charge on the pad, converting it to an analog signal proportional to the ionization energy recorded. To detect signals that can be very small, signals from several boards in the same η and ϕ regions are grouped together in depth to form a readout cell. The

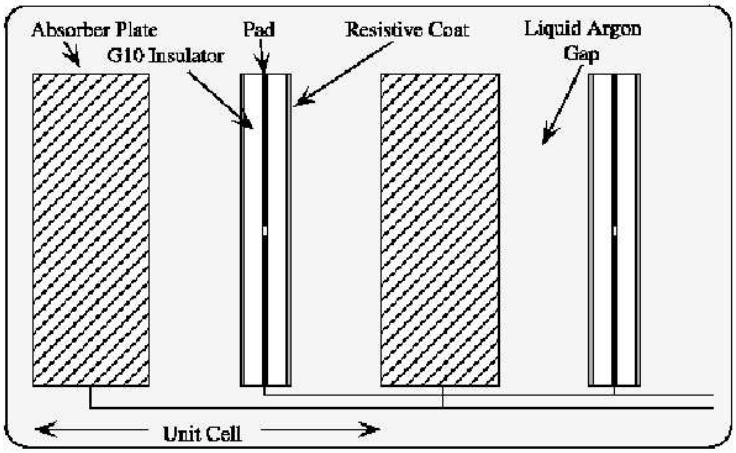

Figure 2.9: Unit Cell in the Calorimeter.

pattern and sizes of the readout cells were determined from several considerations. The transverse sizes of the cells were chosen to be comparable to the transverse sizes of showers : $\Delta R \sim 0.2$ for EM showers and $\Delta R \sim 0.5$ for hadronic showers. Segmentation finer than this is useful in measuring the shape of electrons and jets. Longitudinal subdivision within the EM, fine hadronic and coarse hadronic sections is also useful since the longitudinal shower profiles help distinguish EM objects and hadron jets.

[4]The gap thickness was chosen to be large enough to observe minimum ionizing particles (MIP) signals and to avoid fabrication difficulties.

2.6.8 Calorimeter Electronics

The calorimeter readout electronics has been upgraded to accommodate the reduced Run II bunch crossing time, and to maintain the Run I noise performance [120] [121]. A schematic of the calorimeter readout chain is shown in Figure 2.10 [122].

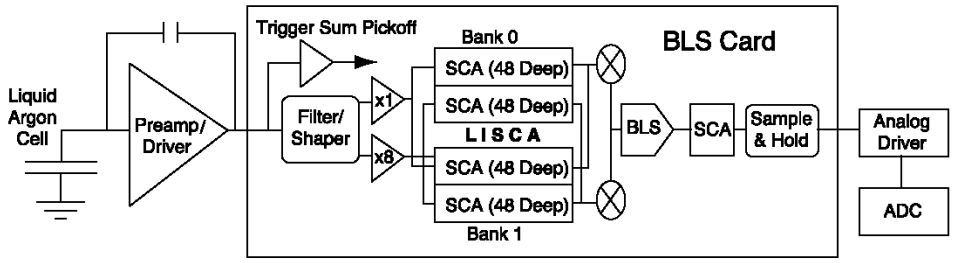

Figure 2.10: Calorimeter electronics readout chain [111].

The calorimeter has a total of about 55,000 channels. The signal from each calorimeter readout cell is triangulated with a very fast rise time and a decay time of 400 ns. Each signal is taken to a feed-through port (a sealed interface between the inside and outside of the cryostat) via 30 Ω resistive coaxial cables. The feed-through boards reorganize signal from the module-structure scheme to the physics scheme in which the readout channels are arranged in pseudo-projective η-ϕ towers. The calorimeter channel configuration is shown in Figure 2.11.

The signal is then conducted to the charge-sensitive preamplifiers. The preamplifiers integrate the charge produced in the calorimeter cells producing proportional voltages. The output signal from the preamplifier is approximately a step function with a rise time of 430 ns (the drift time in the liquid argon gap) and a longer decay time constant of 15 μs. The voltage pulses from preamplifiers (Figure 2.10) are carried by twist and flat cables to the shaper, which shapes the signal. Here, the preamplifier output signal is shaped into a shorter one with a 320 ns rise time and a 500 ns decay time. The shaped signals are sampled every 132 ns; the timing is tuned such that the shaped output can be sampled at its peak at about 320 ns. Because of this earlier

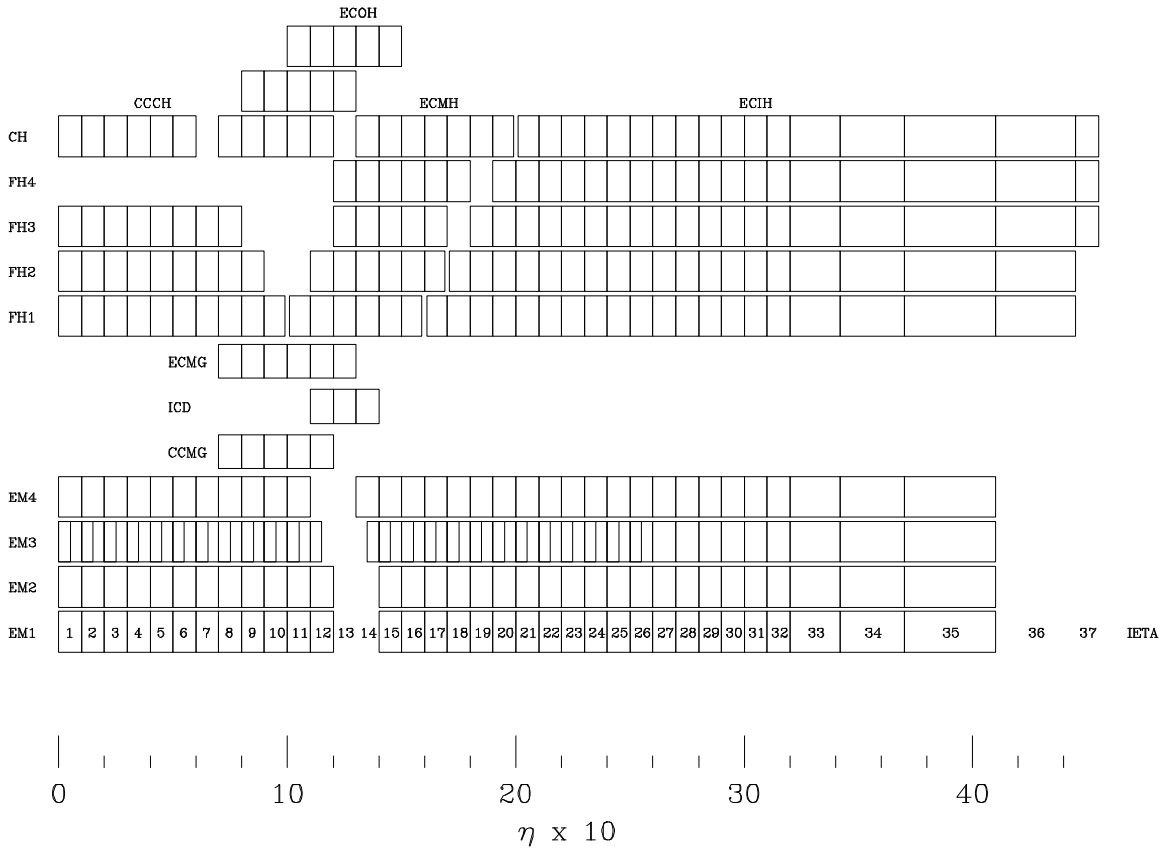

Figure 2.11: Calorimeter channel configuration in terms of depth and η.

sampling time compared to the liquid argon drift time of 430 ns, only two-thirds of the charge in the cell is used to form the preamplifier signal. Figure 2.12 shows the shape of signals from the calorimeter cell, the preamplifier and the shaper.

The shaped signals are stored in in an analog memory called the Switched Capacitor Array (L1 SCA) until a Level 1 trigger decision is made ($\sim$4 μs). If a positive decision is made, a baseline subtraction (i.e., removing of slowly varying offsets in the input voltage) is performed and the result is sent to a Level 2 SCA buffer to await a Level 2 trigger decision. Finally, the output signal is read out and sent to the Analog to Digital Converters (ADCs), which digitize the signals and then send them to the Data Acquisition System (DAQ).

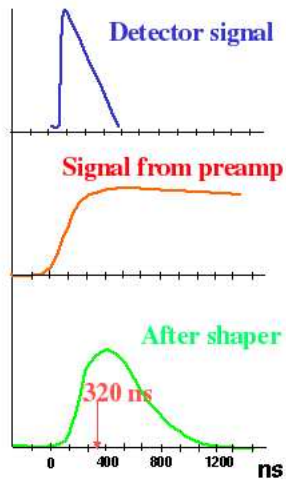

Figure 2.12: Electronics signal shape from the calorimeter cell, after the preamplifier and after the shaper.

2.6.9 Calorimeter Performance

The performance of the DØ calorimeter has been studied extensively in the past in test beams as well as during the Run I period. Its response to electrons and pions with energies between 10 GeV and 150 GeV was found to be linear to within 0.5% [119]. The energy resolution can be described as arising from three major sources. The first is the noise term that has a fixed value, independent of the observed signal. The second is the sampling term which reflects statistical fluctuations in the energy deposited in the argon and therefore scales like the square root of the signal size. The third is the constant term, which reflects how well the response of different parts of the detector are equalized, in other words, how well we understand and calibrate the entire calorimeter. It therefore scales linearly with signal size, assuming the energy is distributed over approximately the same number of readout cells, independent of energy. The energy resolution is thus described using the following functional form:

$$\frac{\sigma_E}{E} = \sqrt{\left(\frac{N}{E}\right)^2 + \left(\frac{S}{\sqrt{E}}\right)^2 + C^2} \tag{2.8}$$

where N, S and C are the noise, sampling, and constant terms, respectively. The energy resolution was measured to be [123]

$$\left(\frac{\sigma_E}{E}\right)^2 = (0.03\%)^2 + \left(\frac{15\%}{\sqrt{E}}\right)^2, \qquad \text{for electrons.} \quad (2.9)$$

$$\left(\frac{\sigma_E}{E}\right)^2 = (4.0\%)^2 + \left(\frac{45\%}{\sqrt{E}}\right)^2, \qquad \text{for pions.} \quad (2.10)$$

In Run II, the resolutions are expected to be worse since there is more material between the beam pipe and the calorimeter. The resolutions measured for Run II are discussed in more detail in the fourth chapter.

2.6.10 Muon System

Surrounding the calorimeter is the muon system [110] [111] designed to detect the passage of muons while making a measurement of their momenta. A large muon mass ($\sim$200 $m_{electron}$) causes muons to lose little energy via bremsstrahlung i.e, they do not readily initiate electromagnetic showers at the Tevatron energies. Energy loss for muons occurs primarily via ionization and excitation of the detector media, which are low energy-loss absorption processes. Therefore, muons above some energy threshold ($\sim$3.5-5.0 GeV) can exit the calorimeter. Because of this property, muon system is typically the outermost and physically the largest detector system. Being located outside the calorimeter, the muon system is well protected from the debris from the hadronic and electromagnetic showers by the thick calorimeter material. Thus, muons can be identified in the middle of hadron jets with much greater purity than electrons. The muon system consists of three primary components:

- Wide Angle MUon Spectrometer (WAMUS) covering $|\eta| < 1$
- Forward Angle MUon Spectrometer (FAMUS) covering $1 < |\eta| < 2$
- Solid-iron magnet generating a toroidal field of 1.8 T, and

The WAMUS consists of two types of detector components : proportional drift tubes (PDT's) and scintillator tiles. These components are arranged in three layers, referred to as A, B and C. Between the layers A and B,C there is a 1.8 T toroidal field. The FAMUS has a similar structure using mini drift tubes (MDT's) and scintillator pixels.

2.7 Trigger and Data Acquisition(DAQ) Systems

The proton-antiproton beams make about 1.7 million collisions per second at the center of the *DØ* detector. The information collected for each collision is called an event. Not every event needs to be saved to the tape. Actually, roughly only a few collisions in a million are of physics interest. Identification of possible interesting events which should be recorded for further analysis is performed using a technique known as "triggering", which proceeds by matching event properties to a predefined set of patterns which are characteristics of the physics processes of interest. The *DØ* trigger system is implemented as a hierarchy of three distinct stages: the level 1 (L1), Level 2 (L2), and Level 3 (L3) triggers as shown in Figure 2.13 [111]. Each trigger level is increasingly more refined than the previous, creating a filtering system which maximizes the efficiency for identifying interesting physics events while satisfying the event rate constraint.

The L1 trigger [124] provides the largest reduction in rate since it has to make a decision on every beam crossing to determine whether the event should proceed in the trigger chain. The L1 decision is based on the raw detector information and simple algorithms in Field Programmable gate Arrays (FPGA's) on specialized microprocessors. Condensed information from the calorimeter, preshower, CFT, and muon detectors is processed in parallel to make a preliminary triggering decision about each event. The L2 trigger [125] receives the information from L1 output and correlates the different pieces of information from the subdetectors to construct basic physics objects (electrons, muons, tracks and jets).

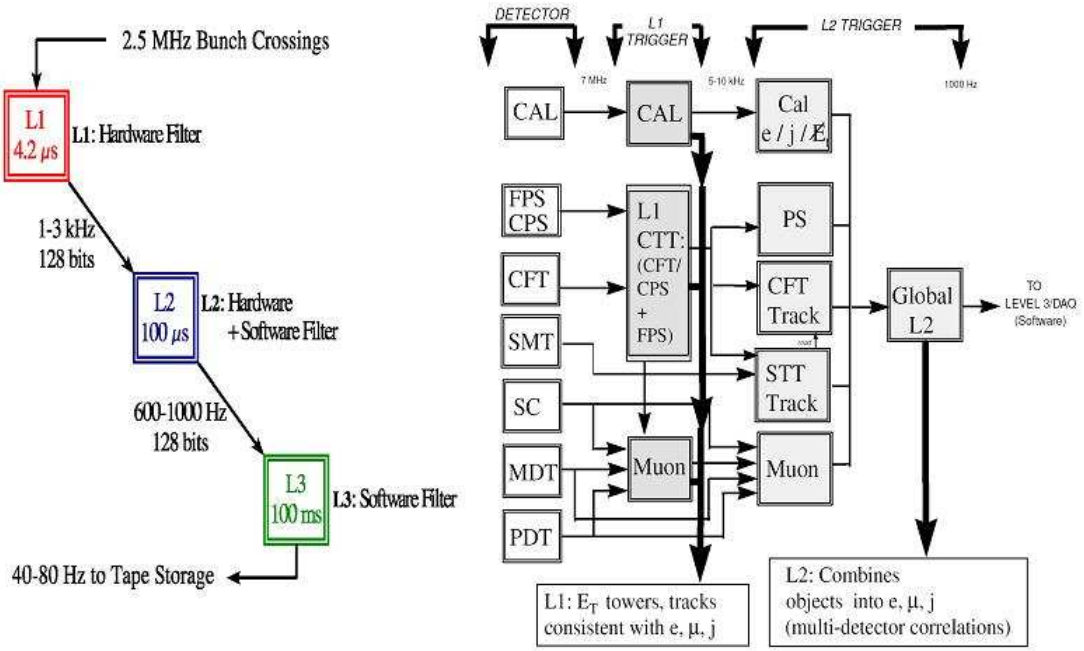

Figure 2.13: DØ trigger scheme with typical trigger rates (left). L1 and L2 trigger data pathway (right).

When the L2 trigger system issues an accept, the event is passed to the L3/Data Acquisition (DAQ) System. In contrast with L1 and L2, the L3 is a software based selection system running in a farm of parallel commercial processors [126]. At this point, the full detector information is obtained from the subdetector readout crates (ROCs). This event information is then routed to one of ∼125 Linux PC's in the L3 farm. Each PC processes the data with an identical copy of a filtering software package, reconstructing refined physics objects and applying sophisticated algorithms to arrive at a final trigger decision. The L3 system provides a trigger decision at an accept rate of around 50 Hz. The selected events are stored on a robotic tape accessible for offline event reconstruction. Thus, the reduction in the event rate due to the trigger selection is of the order of a million.

Calorimeter Triggers

Since this analysis requires only calorimeter triggers, the calorimeter triggers will be emphasized. At L1, four calorimeter towers are combined into a trigger tower of size 0.2×0.2 in $\Delta\eta \times \Delta\phi$. The energy is readout for two depth sections: the electromagnetic layers are combined, as are the fine hadronic layers. The calorimeter L1 trigger terms are of the form CEM(x, y) and CJT(x, y) where x is the number of towers above a transverse energy threshold of y GeV. CEM is the readout of the energy deposited in the electromagnetic section, CJT is the total transverse energy of the electromagnetic and fine hadronic layers combined in the tower. There are 1280 trigger towers of each type broken up into 32 divisions in ϕ_d and 40 divisions in η_d.

The L2 calorimeter trigger [127] consists of three processors which are designed for electron/photon, jet finding and $\not\!\!E_T$ calculation, respectively. Each processor uses information from the L1 trigger and combines appropriate sub-detector proto-objects into physics objects.

At L3, a fast version of the offline code for electron identification is used. The trigger decision is based on a combination of an energy threshold, a cut on the energy fraction in the electromagnetic calorimeter, and requirements on shape of the cluster.

Chapter 3

Data and Monte Carlo Samples

Collisions at the Tevatron occur every 396 ns, i.e. at a rate far beyond the capabilities of the data recording or analysis structures. As discussed in section 2.7, potentially interesting events are selected online using the DØ's three-tiered trigger system. The input rate from the various subdetector systems is about 2.5 MHz which is fed to the trigger system designed to filter events at a rate of 50 Hz. This chapter will describe in brief the triggers used to select the data sample with top-like events decaying through the dielectron mode. The requirements imposed for ensuring the good quality data selection for the analysis will be explained. In addition, the Monte Carlo samples utilized for estimating the signal efficiencies and background contributions will also be discussed.

3.1 Signal Triggers

The data sample analyzed are collected by using triggers specifically designed for high-p_T dielectron analyses. Before discussing the triggers used in the analysis it is necessary to define the terminology used regarding trigger selection. Level 1 electromagnetic requirements, based on information from the calorimeter, are identified using the notation CEM(n, x). The terms CEM(n, x) require an event to contain at

least n trigger towers with a minimum amount of electromagnetic (EM+Hadronic) energy of x GeV. No level 2 requirement was applied on the dielectron triggers except for the latest trigger list version (v13). Level 3 conditions are defined by the L3 filter used. The three filters used in this analysis are ELE_LOOSE(n, x), ELE_NLV(n, x), and ELE_SH(n, x). ELE_LOOSE and ELE_NLV are both electron triggers using a simple cone algorithm. ELE_NLV also applies some non-linearity corrections and uses vertex information. ELE_SH is the same as ELE_NLV with the addition of a shower shape requirement.

A complete description of each trigger requirement can be obtained by querying the trigger list database [128]. In particular, the triggers used in top physics analyses and the methods to calculate their efficiencies can be found in [129]. The triggers are broken down by trigger list version. The menu of trigger requirements that are used during data-taking has evolved with time resulting in several trigger list versions. The trigger list has changed a number of times in order to implement added functionality or to cope with higher luminosities, which translate into higher trigger rates. The data sample analyzed was collected using the triggers listed in Table 3.1.

The specific trigger conditions are

Level 1

- CEM(1,x): one calorimeter EM trigger tower with E_T >x GeV.
- CEM(2,x): two calorimeter EM trigger towers with E_T >x GeV.
- CEM(2,3)CEM(1,9): there must be at least one tower with at least 9 GeV of energy and only one different tower with at least 3 GeV of energy since the 9 GeV tower passes one of the two 3 GeV requirements.

Level 2

- L2CALDIEM(18) : the sum of the energy of of the two highest EM towers should be at least 18 GeV (only for v13 triggers).

Trigger List	Trigger Name	L1	L2	L3
v13	E20_2L20	CEM(1,11)	L2CALDIEM(18)	ELE_NLV(2,20)
	E21_2L20	CEM(2,6)	L2CALDIEM(18)	ELE_NLV(2,20)
	E22_2L20	CEM(2,3)CEM(1,9)	L2CALDIEM(18)	ELE_NLV(2,20)
	E20_2SH8	CEM(1,11)	L2CALDIEM(18)	ELE_SH(2,8)
	E21_2SH8	CEM(2,6)	L2CALDIEM(18)	ELE_SH(2,8)
	E22_2SH8	CEM(2,3)CEM(1,9)	L2CALDIEM(18)	ELE_SH(2,8)
	E20_2SH10	CEM(1,11)	L2CALDIEM(18)	ELE_SH(2,10)
	E21_2SH10	CEM(2,6)	L2CALDIEM(18)	ELE_SH(2,10)
	E22_2SH10	CEM(2,3)CEM(1,9)	L2CALDIEM(18)	ELE_SH(2,10)
	E20_2L15_SH15	CEM(1,11)	L2CALDIEM(18)	_NLV(2,15)_SH(1,15)
	E21_2L15_SH15	CEM(2,6)	L2CALDIEM(18)	_NLV(2,15)_SH(1,15)
	E22_2L15_SH15	CEM(2,3)CEM(1,9)	L2CALDIEM(18)	_NLV(2,15)_SH(1,15)
v12	E1_2L20	CEM(1,11)	—	ELE_NLV(2,20)
	E2_2L20	CEM(2,6)	—	ELE_NLV(2,20)
	E3_2L20	CEM(2,3)CEM(1,9)	—	ELE_NLV(2,20)
	E1_2L20_SH15	CEM(1,11)	—	_NLV(2,15)_SH(1,15)
	E2_2L20_SH15	CEM(2,6)	—	_NLV(2,15)_SH(1,15)
	E3_2L20_SH15	CEM(2,3)CEM(1,9)	—	_NLV(2,15)_SH(1,15)
v11	2EM_HI	CEM(2,10)	—	ELE_LOOSE(1,20)
v10	2EM_HI	CEM(2,10)	—	ELE_LOOSE(1,20)
v9	2EM_HI	CEM(2,10)	—	ELE_LOOSE(1,20)
v8	2EM_HI	CEM(2,10)	—	ELE_LOOSE(1,10)

Table 3.1: Summary of the dielectron triggers broken down by trigger list version.

Level 3

- ELE_LOOSE(1,x) : requires an $|\eta|$ <3 electron with E_T >x GeV meeting loose requirements.
- ELE_NLV(2,x): requires two $|\eta|$ <3.6 electrons with E_T >x GeV. Non-linearity and vertex corrections are also used.
- ELE_SH(2,x): requires two $|\eta|$ <3.6 electrons with E_T >x GeV with loose shower shape requirement.

In v12 and v13, an OR of the listed triggers is used:

- EX_2L20 or EX_2L15_SH15, where $X = 1, 2, 3$ (v12)

- E2X_2L20 or E2X_2SH8 or E2X_2L15_SH15, where $X = 0-2$ (v13.0 to v13.1)
- E2X_2L20 or E2X_2SH10 or E2X_2L15_SH15, where $X = 0-2$ (v13.2)

3.1.1 Trigger efficiencies

The probability of a single object to satisfy a particular trigger requirement is measured using the following general procedure. The first step consists of identifying a sample of events unbiased with respect to the trigger requirement under study. Offline reconstructed objects are then identified in the events. The efficiency is obtained by calculating the fraction of these offline reconstructed objects that satisfy the trigger condition under study. Single object efficiencies are in general parameterized as a function of the kinematic variables p_T, η, and ϕ of the offline reconstructed objects.

The efficiency for an offline electron to pass a specific trigger requirement is obtained using the "tag-and-probe" approach on a sample of $Z \to ee$ events in data. This method is discussed here using the L1 electron trigger efficiency as an example. First, two offline electrons with an invariant mass in a small window around the Z mass (80< M_{ee} < 100 GeV) are selected using the criteria discussed in section 4.1. One electron is randomly chosen, and, if the electron is matched to a trigger tower (or trigger towers) satisfying the L1 requirement within an $R = \sqrt{\Delta\eta^2 + \Delta\phi^2} = 0.4$ cone, it is designated as the "tag" electron. The second offline electron ("probe") is then used for the efficiency calculation by examining whether any trigger towers matched to it in a 0.4 cone pass the L1 requirement under examination. The efficiency is the number of matched probe electrons divided by the total number of probe electrons. It turns out that the L1 efficiency is flat in η_d and ϕ_d; however, there is a turn-on in p_T depending on the threshold of the trigger. An example of this is shown in Figure 3.1 for CEM(1,11). The function used to parameterize the L1 electron efficiency is

$$f(p_T) = \frac{A_2}{2}\left(1 + \mathrm{erf}\left(\frac{p_T - A_0}{A_1\sqrt{2}}\right)\right), \tag{3.1}$$

where A_0, A_1, and A_2 are parameters which can be interpreted as the p_T at which the efficiency reaches half its maximum value, the slope of the turn-on, and the maximum efficiency in the plateau region, respectively.

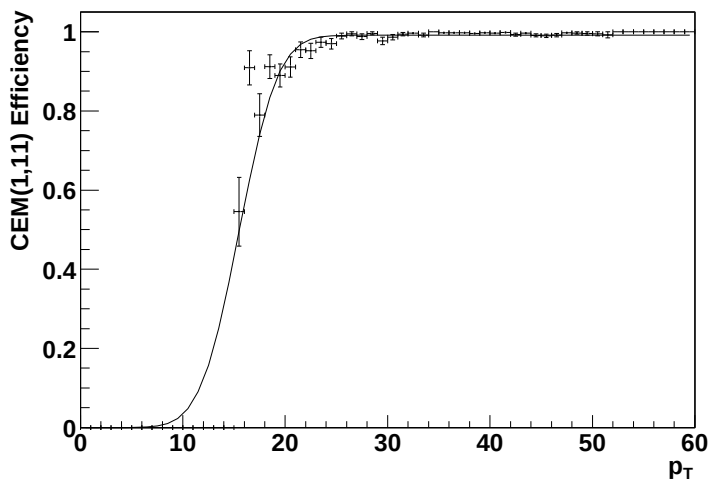

Figure 3.1: CEM(1,11) trigger turn-on curve.

A similar procedure is used to parameterize the L2 and L3 trigger turn on curves. A complete discussion of the trigger efficiency measurement for electrons can be found in [129].

One further complication arises for the dielectron analysis since there are two electrons. That is, the L1 triggers requiring two towers can be fired by one high-p_T electron with its energy split between two towers or by both electrons each firing a tower. In addition, jets deposit some energy in the EM layers of the calorimeter so these can occasionally fire an EM trigger as well. Fortunately, this versatility leads to a high L1 trigger efficiency. All of these scenarios are considered by the *top_trigger* package [129], which uses the parameterization derived for each L1, L2 and L3 condition to calculate the trigger efficiencies for the Monte Carlo.

The *top_trigger* package [129] version `v01-04-04` is used to calculate trigger efficiencies and simulate the effect of trigger on Monte Carlo samples. The *top_trigger* uses per object turn on curves for each trigger term. The final trigger efficiency is

the result of weighting the trigger efficiency for each trigger list with its corresponding luminosity. The systematic uncertainties on the trigger efficiencies are calculated from the errors in the individual object turn-on curve parameterizations (see more detailed description in section 5.8 and in [129]). The average trigger efficiencies for preselected $t\bar{t}$ events in dielectron final state is found to be 94.0 ± 0.4 (stat) $^{+1.4}_{-5.4}$(syst) (see chapter 5).

3.2 Data Set

The data sample used in the present analysis consists of data taken during the period June 2002 till August 2004. This corresponds to 384.1 pb^{-1} of integrated luminosity. Table 3.2 gives a breakdown of the integrated luminosities by trigger version.

All samples were reconstructed with reconstruction (RECO) versions p14.03.0x ($x = 1, 2, 3$), p14.05.0y ($y = 0, 2, 2dst$), p14.06.00 and p14.06.01. RECO writes out the data in two forms – the data summary tier (DST) and the thumbnail (TMB). The DSTs contain all of the information needed to perform any physics analysis or even to do a re-reconstruction of high-level physics objects. The TMBs, on the other hand, are about a tenth the size of the DSTs. They contain all of the physics information needed for most analyses, leaving out much of the lower-level information stored in the DSTs. The TMBs are then skimmed by the Common Samples Group (CSG) based on physics objects in order to reduce the volume of data to be analyzed. For this analysis, the DIEM skim, which requires two $|ID| = 10, 11$ EM objects with $p_T > 7$ GeV, is further skimmed by the top working group with tighter cuts applied. In this analysis, two skims are used. The DIEM skim, which requires 2 EM objects with $p_T > 15$ GeV, $|ID| = 10$ or 11, $f_{em} > 0.9$, $f_{iso} < 0.15$, and $\chi^2_{Cal7} < 50$, is the main sample used. However, the DIEM_EXTRALOOSE skim, which requires only 2 EM objects with $p_T > 15$ GeV and $|ID| = 10$ or 11, is used to obtain an estimate of the fake electron background and to measure the electron reconstruction

Trigger List	Delivered $\int \mathcal{L}$ (pb^{-1})	Recorded $\int \mathcal{L}$ (pb^{-1})	Good $\int \mathcal{L}$ (pb^{-1})	Reconstructed $\int \mathcal{L}$ (pb^{-1})
v8	35.6	24.8	20.3	20.08
v9	40.5	35.3	30.8	30.75
v10	18.4	16.6	15.5	15.48
v11	69.0	64.6	57.6	57.38
v12	250.2	230.4	217.4	217.41
v13	68.9	54.7	46.2	42.97
Total	482.6	426.6	387.7	384.1

Table 3.2: Breakdown of integrated luminosities by trigger list version at the different satges.

and cluster efficiencies. (These selection criteria will be discussed in section 4.1.) This skimming is done using the Ipanema version of the *top_analyze* package [130], which also converts the data from the TMB storage format to ROOT-tuples, which are more analysis-friendly.

3.2.1 Data Quality Selection

Of the data delivered by the Tevatron, only a fraction is recorded by the DØ detector. Out of this data only the fraction for which all detector systems are functioning well is used for the data analyses. Finally, only the fraction of data which is reconstructed by the reconstruction software package *RECO* is actually used for the data analyses presented. This breakdown of data, quantified in terms of luminosity for different trigger list versions (for the dielectron analysis) is presented in Table 3.2. It can be seen that the present dielectron analysis uses about 80 % of the delivered luminosity.

The data quality monitoring is performed on two levels, online and offline. It is crucial for a high data taking efficiency to catch the malfunction of detector components, of the readout or the triggering as early as possible. Online data quality monitoring guarantees to be able to react immediately and thus to maximize the data quality online.

However, there are data quality issues which are not recognized online. The

remaining deficient data is eliminated by offline data quality monitoring, as initially introduced in ref [131]. The idea is to compare basic distributions of physics objects or other variables that describe the detector performance of the data taken with canonical distributions. In a second step a list of possible data corruption methods is identified, quality measures are defined with a maximum discrimination power between usable and unusable data and criteria are defined to classify the data quality. Since the corruption of the data can occur on time scales much smaller than the length of a whole run, the classification is preferably done on the smallest possible units of data.

The data quality selection required for the data events analyzed is broken down in a run based, a luminosity block number (LBN) based, corresponding to approximately one minute of data taking and several thousand events recorded, and an event-by-event based selection.

Run quality selection: The good run selection is based on information stored in DØ's Run Quality Database [132]. For this analysis, runs marked "Not Bad" for the SMT, CFT, and calorimeter are used. This means that, during the runs, these detectors were fully functional and exhibited no major problems.

Luminosity block quality selection: Good luminosity block selection is based on the "Ring of Fire" list and the Bad Jet/Missing E_T Luminosity Block Number (MET LBN) lists.

- **Ring of Fire:** The Ring of Fire [133] list removes all luminosity blocks in which a $\phi-$ring of energy in the calorimeter appears. The ring was caused by a grounding problem, which is now resolved. This ring-activity used to leads to a large missing energy signature.
- **Bad JET/MET LBN List:** The Bad Jet/MET LBN lists are used to remove groups of about 20 sequential luminosity blocks with suspect

missing energy. This list is generated based on the following criteria [134]:

- The average $\not\!\!E_T$ shift ($\sqrt{<\not\!\!E_x>^2 + <\not\!\!E_y>^2}$) of the luminosity block groups must be less than 6 GeV.
- The average RMS-xy ($\sqrt{RMS(\not\!\!E_x)^2 + RMS\not\!\!E_y)^2}$) of the RMS values of the $\not\!\!E_x$ and $\not\!\!E_y$ distributions of the groups must be smaller than 20 GeV.
- The mean of the scalar transverse energy ($< SET >$) distribution of the groups must be greater than 60 GeV.

For luminosity calculations and removal of bad runs and bad luminosity blocks the *top_dq* package [135] (version v00-06-03) is used. Less than 5% of the data are affected by these run and luminosity block selections.

- **Event quality selection:** The selection of $t\bar{t}$ events involves requirements of jets and $\not\!\!E_T$, both of which are highly susceptible to backgrounds from calorimeter readout malfunctions. So care must be taken in devising an event-wide quality variable which is immune to variations in an event's real (as opposed to instrumentally originating) scalar E_T or number of jets. This is particularly true for $t\bar{t}$ events in which large scalar transverse energies can arise. A study to arrive at an event quality selection to remove such noisy events is described in [136]. This cut removes events which show a significant difference in the L1 and precision readout energies. This difference is quantified by the $L1_{conf}$ variable, which is defined to be the number of trigger towers with $E_T^{TT} < 2$ GeV and $E_T^{cal} - E_T^{TT} > 1$ GeV, where E_T^{cal} is the precision readout energy, divided by the total number of trigger towers with $E_T^{TT} < 2$ GeV. It also employs a coherent noise variable, cn, defined in detail in [133], which flags events with a coherent shift in the pedestal values of all cells in one or more ADC cards. In the end, this cut requires events to satisfy $L1_{conf} < 0.3$ OR $cn = 0$.

3.3 Monte Carlo

In addition to the data, event simulations are required in order to predict how events of interest look like in the detector. Such simulations are produced using Monte Carlo generators. The Monte Carlo generation proceeds in three steps. First, the event is simulated. Then, it is run through a model of the detector which predicts the detector response. Finally, it is reconstructed just like the data coming out of the detector.

In the first step, the $p\overline{p}$ interaction is simulated using programs like Herwig [137], Alpgen [138], or Pythia [139]. In this analysis, Alpgen v1.2, using CTEQ5L [140] parton distribution function (PDF), models the hard scatter for most processes. Then, the Alpgen output is run through Pythia v6.2, using CTEQ5L PDF, which handles fragmentation and decay. On top of Pythia, EvtGen [141] is used to model the decays of b hadrons, and TAUOLA [142] is used to model decay of τ's.

The DØ detector is modeled using the GEANT3 package [143]. This package is used to determine the effects of the detector material and magnetic field on the particles produced in the generators as they travel through the detector. It also models ionization and secondary particles produced through interactions with the dectector. The response of the detector is accounted for using the DØsim package. This package merges the hard scatter event with minimum bias events; adds SMT, CFT, calorimeter, and muon system noise and inefficiencies; and digitizes the simulated ionization and shower response. The output of DØsim has the same format as the raw data. Therefore, the MC can be run through RECO and reconstructed just as the data.

3.3.1 Monte Carlo Samples

This section provides information about the Monte Carlo samples used in the analysis to estimate efficiencies of object reconstruction, kinematical cuts and acceptance for signal and background processes. Unless otherwise stated, the samples are generated with Alpgen and run through Pythia for fragmentation and decay. The samples use the Tune A underlying event model [144]. The lepton parton cuts are $p_T > 0$ GeV and $|\eta| < 10$, and the jet parton cuts are $p_T > 8$ GeV and $|\eta| < 3.5$. The minimum distance between two jets is $\Delta R(j, j) > 0.4$, but no cut is applied on the minimum distance between a jet and a lepton. Various single and di-boson processes are simulated. In all cases, any τ leptons present are forced to decay to electrons or muons before further DØsim processing of events. The specific samples are described in Table 3.3 [145]. The number of events in each sample and the effective cross sections are also provided.

Signal Sample

The efficiencies of the object reconstruction, acceptance and kinematical cuts on the signal are obtained from a $t\bar{t} \rightarrow$ *dilepton* Monte Carlo sample. The top quark mass is taken to be 175 GeV. The Monte Carlo sample contains all dilepton final states, including τ leptons, with inclusive τ lepton decay.

Background samples

WW and WZ Monte Carlo samples have been generated in order to study the diboson background. Two WW samples are produced – $WW \rightarrow ll$ and $WWjj \rightarrow lljj$ – since millions of $WW \rightarrow ll$ events would need to be produced to study this background in the two jet bin. The WW cross sectin is normalized

to the next-to-leading order (NLO) cross section, which is 35% higher than the leading-order (LO) cross section. Since a NLO cross section for $WWjj$ is not available, the LO cross section for $WWjj$ is scaled up by 35%, and a 35% systematic uncertainty is applied to this cross section. The WZ sample is generated using Pythia only. In this sample, the W decays to quarks while the Z decays to ee or $\mu\mu$.

As with the WW sample, two $Z/\gamma^* \rightarrow \tau\tau$ samples are produced, a jet inclusive sample and a two jet sample. The $Z \rightarrow \tau\tau$ sample is produced using Pythia only. Both τ's decay leptonically, and there is an 8 GeV cut on the p_T of the e or μ produced in the decay. This sample is produced for $M_{\tau\tau} > 30$ GeV. The $Z/\gamma^* jj \rightarrow \tau\tau jj$ sample is produced using the standard Alpgen to Pythia chain. It is produced in two invariant mass regimes – $15 < M_{\tau\tau} < 60$ GeV and $60 < M_{\tau\tau} < 130$ GeV.

Finally, a jet inclusive sample and two jet sample are generated for the $Z/\gamma^* \rightarrow ee$ process. Both of these samples are generated in three mass bins – $15 < M_{ee} < 60$ GeV, $60 < M_{ee} < 130$ GeV and $130 < M_{ee} < 250$ GeV. The $Z/\gamma^* \rightarrow ee$ sample is generated using Pythia alone while the $Z/\gamma^* jj \rightarrow eejj$ sample is produced through the standard Alpgen to Pythia chain.

Process	Generator	PDF	$N_{evts}(k)$	σ(pb)
$t\bar{t} \to ll$	Alpgen	CTEQ5L	98	7.0
Z+jets Processes				
$Z/\gamma^* \to \tau\tau l\nu_l\nu_\tau l\nu_l\nu_\tau; l = e, \mu$ ($M_{\tau\tau} > 30$ GeV)	Pythia	CTEQ5L	150	12 ± 1
$Z/\gamma^* \to ee$ ($M_{ee} > 15$ GeV)	Pythia	CTEQ5L	240	295 ± 21
$Z/\gamma^* j \to eej$ (15< M_{ee} <60 GeV)	Alpgen	CTEQ5L	20	60.9±0.3
$Z/\gamma^* j \to eej$ (60< M_{ee} <130 GeV)	Alpgen	CTEQ5L	14	68.8±0.5
$Z/\gamma^* j \to eej$ (130< M_{ee} <250 GeV)	Alpgen	CTEQ5L	14	0.62±0.01
$Z/\gamma^* jj \to \tau\tau jj; \tau \to e, \mu$ (15< $M_{\tau\tau}$ <60 GeV)	Alpgen	CTEQ5L	10	3.06±0.04
$Z/\gamma^* jj \to \tau\tau jj; \tau \to e, \mu$ (60< $M_{\tau\tau}$ <130 GeV)	Alpgen	CTEQ5L	150	2.90±0.05
$Z/\gamma^* jj \to eejj$ (15< M_{ee} <60 GeV)	Alpgen	CTEQ5L	100	24.7±0.4
$Z/\gamma^* jj \to eejj$ (60< M_{ee} <130 GeV)	Alpgen	CTEQ5L	200	23.4±0.4
$Z/\gamma^* jj \to eejj$ (130< M_{ee} <250 GeV)	Alpgen	CTEQ5L	30	0.20±0.01
Diboson processes				
$WWl\nu l\nu$	Alpgen	CTEQ4L	121	1.38 ± 0.03
$WWjjl\nu l\nu jj$	Alpgen	CTEQ4L	20	0.29 ± 0.10
$WZjjll$	Alpgen	CTEQ4L	25	0.092 ± 0.032

Table 3.3: Monte Carlo samples used in the present analysis, together with generators, parton diustribution function, number of events and cross section for the various processes. The cross sections indicated for the inclusive Pythia $Z \to ee$ and $Z \to \mu\mu$ samples are for the central mass bins and derived from the DØ measured cross sections. The cross section for the Pythia $Z \to \tau\tau$ sample is also derived from the cross section measured in data.

Chapter 4

Event Reconstruction and Object Identification

If an event satisfies the prerequisites for one of the physics triggers, the information measured by all the detector components is stored on a disk. The raw event data is in the form of digitized signals such as charges, pulse heights, etc. During analysis, it is most convenient and intuitive for events to be recast in terms of the particles produced in the interaction. The reconstruction of physics objects from the raw detector data is performed by a software package known as DØRECO and can be divided into three primary stages.

- **Hit Finding:** The raw data is unpacked and converted into "hits" which consists of energy deposits in calorimeter cells, signals on tracking layers, etc. Each hit corresponds to an energy value, a spatial location, and their associated uncertainties.
- **Tracking and Clustering:** The adjacent hits are combined to form clusters in the calorimeter and preshowers or trajectories referred to as tracks in the tracking systems.

- **Particle Identification:** Clusters and tracks as well as other information are combined to form candidate signatures of physics objects such as electron, photon, jet, or muon. The identification criteria are quite loose at this stage to guarantee high efficiency.

In order to isolate $t\bar{t}$ events in the dielectron channel from background, we rely on four basic objects: electrons, jets, $\not\!\!E_T$, and primary vertices. Therefore, the reconstruction of these four objects are discussed in this chapter, followed by their identification and selection.

4.1 Electrons

High-p_T electrons are reconstructed from information in three subdetectors : the calorimeter, the tracking system and the central preshower detector. First, electron candidates are identified by detecting localized energy deposits in the electromagnetic (EM) calorimeter with an associated energy lost in the preshower. Consequently, confirmation is sought from the central tracking system since an isolated high p_T track should be pointing back to the interaction vertex.

4.1.1 Electromagnetic Cluster Reconstruction

The first step in the reconstruction of EM objects in DØ is the readout of the nearly 55,000 calorimeter channels (readout cells). The calorimeter readout is "zero-suppressed," meaning that only energies above pedestal and noise are read out. Zero-suppression is quantified as a ratio of the measured energy above the pedestal to the mean width of the noise (σ) in that channel. The suppression used is 2.5σ which means that the measured energy above the pedestal must be 2.5 times greater than the noise in the channel to be read out. Also, due to liquid

argon contamination, depleted uranium noise and deficiencies in the readout electronics, cells with unusually high energy can appear ("hot cells") affecting the reconstruction. To mark these cells and prevent their usage, a specifically designed algorithm is used called "NADA"[146]. The resulting calorimeter cells, with the same η and ϕ are grouped together to form towers[1].

The showers from electrons and photons are very similar: concentrated clusters of energy deposited mainly in the EM layers of the calorimeter. Hence, the reconstruction of these objects in the calorimeter uses the same algorithm. The standard EM clustering algorithm at DØ is the simple cone (Scone) algorithm based on towers. An EM tower consists of four EM layers and the first hadronic (FH1) layer. Starting with the highest transverse energy (E_T) EM tower, adjacent EM towers (above a threshold of E_T >50 MeV) in a cone of radius $R = \sqrt{\Delta\eta^2 + \Delta\phi^2} = 0.4$ around the hottest tower, are added together to form EM clusters in central calorimeter (CC). In endcap calorimeter (EC), EM clusters are a set of adjacent cells with a transverse distance of less than 10 cm from an initial cell with the highest energy content in EM3 layer.

Among all reconstructed clusters, genuine EM showers are expected to pass crude selection criteria imposed by the DØRECO:

- The cluster must have a minimum transverse energy (E_T) of 1.5 GeV.
- The cluster should be relatively narrow which is enforced by requiring that more than 40% of the cluster energy be contained in the central most energetic tower.
- The cluster must have at least 90% of its energy deposited in the electromagnetic layers of the calorimeter. The fraction of energy in the EM

[1] A calorimeter readout-tower is of size 0.1×0.1 in $\Delta\eta \times \Delta\phi$ and a trigger tower is of the size 0.2×0.2 in $\Delta\eta \times \Delta\phi$.

layers, or the EM fraction, is

$$f_{EM} = \frac{E_{EM}}{E_{tot}}, \tag{4.1}$$

where E_{EM} is the cluster energy in the EM layers and E_{tot} is the total energy of the cluster deposited in all layers within the cone.

- The cluster is required to be isolated in (η-ϕ) space, having an isolation fraction < 0.2. The isolation fraction is defined as

$$f_{iso} = \frac{E_{tot}(R < 0.4) - E_{EM}(R < 0.2)}{E_{EM}(R < 0.2)}, \tag{4.2}$$

where $E_{tot}(R < 0.4)$ is the total energy in the towers within a cone of radius $R = 0.4$ around the direction of the cluster, summed over the entire depths of the calorimeter except the Coarse Hadronic (CH) layers and $E_{EM}(R < 0.2)$ is the energy in the towers in a cone of radius $R = 0.2$ summed over the EM layers only.

The clusters passing the preceding criteria are selected as EM clusters or electron/photon candidates. For each electron/photon candidate, the centroid of the cluster is computed by weighting cell positions with the logarithm of the cell energies in the EM3 layer of the calorimeter (recall that the layer 3 is the most finely segmented in $\Delta\eta \times \Delta\phi$). The shower centroid together with the primary vertex is used to calculate the direction of the particle 4-momentum. At this level as no matching with the central tracks is required the ID of the object is set to 10. Electrons and high-p_T photons will produce EM showers in the preshower detectors. The 3D clusters reconstructed in the preshower detectors are matched to the EM clusters passing the above cuts by requiring them to be in a $\Delta\eta \times \Delta\phi$ (0.05×0.05) window around the EM cluster. If a preshower

3D cluster is matched, its position together with the primary vertex is used to recalculate the direction of the particle momentum.

At this juncture, a distinction between electrons and photons is made by finding matching tracks in the central tracking system. Since photons have no charge, they do not leave signals in the tracking system. A "road", 0.05×0.05 in $\Delta\eta \times \Delta\phi$, is defined between the calorimeter cluster and the primary vertex positions. A search for a track with $p_T > 1.5$ GeV is performed within this road. If one or more tracks are found, the candidate is considered as an electron and assigned an ID of ± 11 (11 for electrons and -11 for positrons) and the momentum direction is recalculated using the direction of the matched track. In the absence of the associated track, the candidate becomes a photon and assigned an ID of 10. An EM cluster with $|ID| = 10$ or 11 is termed a "loose" electron.

4.1.2 Electromagnetic Cluster Identification

The above criteria used in forming electron candidates are purposely quite loose. So after the reconstruction of electrons there remains a considerable amount of background which contaminates the reconstructed sample. Additional constraints must be applied to increase the discriminating power of the electron selection over the backgrounds. The following is a description of the standard quantities employed for the electron identification.

Electromagnetic Energy Fraction

The development of EM and hadronic showers is quite different so that shower shape information can be used to differentiate between electrons (and photons) and hadrons. Electrons deposit almost all their energy in the EM section of the calorimeter while hadrons are typically much more penetrating. As stated

above, genuine EM showers are expected to have a large EM fraction ($f_{EM} > 0.9$, as defined earlier). This EM fraction cut is a very strong cut against pions and most of them fail to pass it. We note also that this cut removes the electrons pointing to ϕ cracks positions, since they deposit more than 10% of their energy in the hadronic calorimeter.

Electromagnetic Shower Isolation

Electron candidates tend to be isolated in the calorimeter. The variable which allows us to quantify the degree of isolation of an EM cluster is isolation fraction f_{iso} , as defined previously. Electron candidates are required to satisfy $f_{iso} < 0.15$. Small values of isolation fraction correspond to the situation that most of the energy of the EM cluster is deposited in a narrow region of the EM layers in the calorimeter, contained in a small cone of radius $R = 0.2$ in η-ϕ space.

H-Matrix Technique

The shower shape of an electron or a photon has a distinctive profile from that of a jet. Fluctuations cause the energy deposition to vary from the average in a correlated fashion among the cells and layers. To obtain the best discrimination against hadrons, we use both longitudinal and transverse shower shapes, and also take into account the correlations between energy deposits in the calorimeter (preshower) cells. This is done using a covariance matrix (H-Matrix) technique [6]. A covariance matrix is built up with a set of variables describing the shower shapes. In the present analysis, the matrix is 7-dimensional.

- The longitudinal development is reflected through the fractions of shower energy in the four EM layers (EM1, EM2, EM3, EM4).

- To characterize the lateral development of the shower, we consider cluster width in r-ϕ plane in the third EM layer (EM3) which has the best granularity[2] .
- To parameterize the energy and impact parameter dependence of the matrix, the logarithm of the total shower energy and the longitudinal position of the event's primary vertex are included.

A separate matrix is built for each ring of calorimeter cells with the same $|\eta|$ coordinate. Each cluster is attributed a χ^2_{Cal7} which measures how closely the shower shape of an electron candidate matches expectations from Monte Carlo detector simulations. Thus by placing a cut on χ^2 we can distinguish an electromagnetic shower from a hadronic shower with some efficiency. Electrons tend to have small H-Matrix χ^2_{Cal7} values. This analysis requires H-Matrix $\chi^2_{Cal7} < 50$. Electron candidates are therefore selected by requiring $f_{EM} > 0.9$, $f_{iso} < 0.15$, and $\chi^2_{Cal7} < 50$. Electrons passing this calorimeter selections are called "medium" electrons.

Track Match

Although the EM cluster selection is very discriminant, QCD backgrounds contaminate the electron sample. In order to suppress the overwhelming QCD background, the cluster is required to be associated to a track in the central tracking system in a road satisfying satisfying the conditions:

$$|\Delta\eta_{EM,trk}| < 0.05 \text{ and } |\Delta\phi_{EM,trk}| < 0.05.$$

[2]Transverse segmentation of calorimeter modules is provided by readout of calorimeter cells as pseudo-projective towers of size 0.1×0.1 in η-ϕ sapce. The third EM layer typically contains 65% of the electron shower energy and its transverse segmentation is made finer (0.05×0.05).

To quantify the quality of the cluster-track matching, the track is extrapolated into the EM3 layer of the calorimeter and a $Prob(\chi^2_{spatial})$ defined according to

$$\chi^2_{spatial} = \left(\frac{\delta\phi}{\sigma_\phi}\right)^2 + \left(\frac{\delta z}{\sigma_z}\right)^2, \tag{4.3}$$

is computed for each available track. In these expressions, $\delta\phi$ is the angle difference in transverse direction (ϕ) and δz is the spatial difference in position between the track impact and the cluster at the EM3 floor of the calorimeter; and σ_ϕ and σ_z are the experimental resolutions of the associated quantities. The track with the highest $Prob(\chi^2_{spatial})$ is considered as track matched to the EM object.

4.1.3 Electron Likelihood

Although the track match confirmation does perform efficiently well in suppressing the QCD backgrounds, instrumental or "fake electron" backgrounds from QCD multijet events still pose a serious problem due to overwhelming nature of this background. The main backgrounds for high p_T electrons come from photons, or jets dominated by a leading π^0 which decays to two $\gamma\gamma$. In either case, there may be a track in the road to the EM cluster due to a photon conversion to e^+e^- or a low energy charged hadron close to the photon or π^0. So essentially we have two background components: photon conversions and hadronic overlaps. Monte Carlo studies of the QCD fake electron background have shown that the QCD background for electrons is still mainly made of neutral pions [147].

In order to distinguish real electrons from fakes, certain characteristics of these fakes must be considered in trying to choose the best discriminating variables. Photon conversions may be marked by the presence of a second track very close

to the EM track, and a large E_T/p_T (where E_T is the transverse energy of the cluster measured by the calorimeter and p_T is the transverse momentum of the associated track measured by the tracker). Their calorimeter quantities, however, would be nearly identical to that of an electron, though they may be slightly wider than an electron shower. Neutral pions may also have nearby tracks, as they are produced in association with other charged hadrons. Since the π^0 would have to overlap a track from the charged hadrons in order to fake an electron, the trackmatching could be poor; the track would not necessarily be isolated; and E_T/p_T would not tend toward 1, as expected for good electrons. Their χ^2_{cal} and f_{EM} may be worse due to the surrounding hadrons.

Likelihood-based confirmation of electron candidates has proven to be a more efficient technique of separating good electrons from background than using square cuts since a likelihood considers the entire shapes of the signal and background distributions [147]. The likelihood allows variables to be weighted by their effectiveness in discriminating signal and background unlike conventional cuts. That is, if an event fails a square cut, the event is rejected. However, by using a likelihood, signal events that would normally fail one square cut but look very signal-like in all other variables would, most likely, be retained in the selected event sample.

Formulation of Likelihood

The Likelihood method allows us to combine informations from various subdetectors into a single variable. The various steps involved in the formulation of likelihood function are :

- Selection of variables with good discriminating power between real (signal) and fake (background) electrons.

- The distributions of each variable are obtained for the signal and background samples.
- The above distributions are smoothed using linear smoothing techniques and normalized to unit area to produce probability distributions for each variable. Now, these distributions can be used to assign a probability for a given EM object to be signal or background:

$$P_{sig}(\mathbf{x}), P_{bkg}(\mathbf{x})$$

  where $\mathbf{x}$ is a vector of likelihood variables. That is, each likelihood variable for the object is assigned a probability to be signal or background from the probability distributions.
- Then, assuming these variables to be uncorrelated, these probabilities can be simply multiplied together to give an overall probability for the event:

$$P(\mathbf{x}) = \prod_i P(x_i).$$

- Finally, to differentiate between signal-like and background-like electron candidates, a likelihood discriminant is calculated:

$$\mathcal{L}_n(\mathbf{x}) = \frac{P_{sig}(\mathbf{x})}{P_{sig}(\mathbf{x}) + P_{bkg}(\mathbf{x})}. \tag{4.4}$$

  The closer $\mathcal{L}_n(\mathbf{x})$ tends toward 1, the more signal-like is the candidate, the closer $\mathcal{L}_n(\mathbf{x})$ tends toward 0, the more background-like is the candidate.

The present analysis uses electron likelihood based on seven parameters (for details see [147]). The performance of the likelihood in terms of signal and background discrimination in the central (CC) and endcap calorimeter (EC) regions are shown in Fig. 4.1. It can be seen that the signal containing real

electrons peaks around 1 and the background dominated by fake electrons peaks around 0. An electron is required to have a likelihood of larger than 0.85 in both CC and EC. This likelihood requirement has been found to have a signal efficiency of 87% in CC and 83% in EC. A medium electron passing the trackmatch and likelihood selections is referred to as a "tight" electron.

4.2 Electron Likelihood Studies

This section concentrates on the discussion of the studies done to improve the electron-likelihood and concludes with the presentation of new likelihood function. A complete description of this study can be found in our DØ note [148].

4.2.1 Sample Selection

The likelihood is trained entirely on data. The signal sample should be enriched in electrons while the background sample should be enriched in fake electrons.

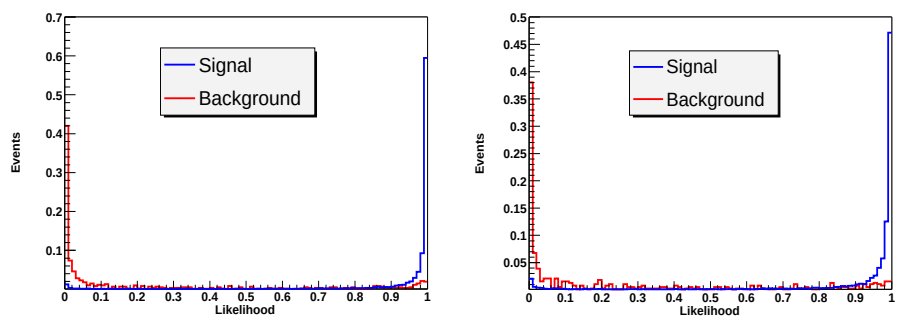

Figure 4.1: Signal and background discrimination of 7 parameter likelihood in the central (left) and endcap (right) calorimeter regions.

The signal sample is obtained from $Z \rightarrow ee$ events. This sample consists of two tight electrons with $p_T > 15$ GeV and the invariant dielectron mass is required to be in the Z mass window ($80 < M_{ee} < 100$ GeV). The background

sample is obtained from EM+jet events where the EM object and jet are back-to-back. These events are mainly QCD di-jet and γ+jet events where the jet or photon fakes a reconstructed electron. The background sample is selected with one tight electron and one good jet with $p_T > 15$ GeV. We require missing transverse energy < 15 GeV to remove W's from the sample. Back-to-back condition is imposed by requiring $\Delta\phi(electron, jet) > 2.5$.

4.2.2 Discriminating variables

The present version of electron likelihood uses seven quantities which combines information from the calorimeter and the tracking systems:

- f_{EM}.
- H-Matrix χ^2_{Cal7}.
- E_T/p_T
- $Prob(\chi^2_{spatial})$.
- Distance of closest approach (DCA) which measures the shortest distance of the selected track to the line parallel to the $z-$axis which passes through the primary vertex position.
- Number of tracks in a $\Delta R = 0.05$ cone, around and including the candidate track : This variable is meant to suppress fake electrons from photon conversions. In these events one would expect more than one track; wherereas, a real electron should just show one track.
- Total track p_T in a $\Delta R = 0.4$ cone around, but excluding, the candidate track. This variable is meant to remove π^0 produced in association with charged hadrons. The tracks that are present with good electrons will tend to have extremely low p_T; whereas, tracks from jets will tend to have large p_T.

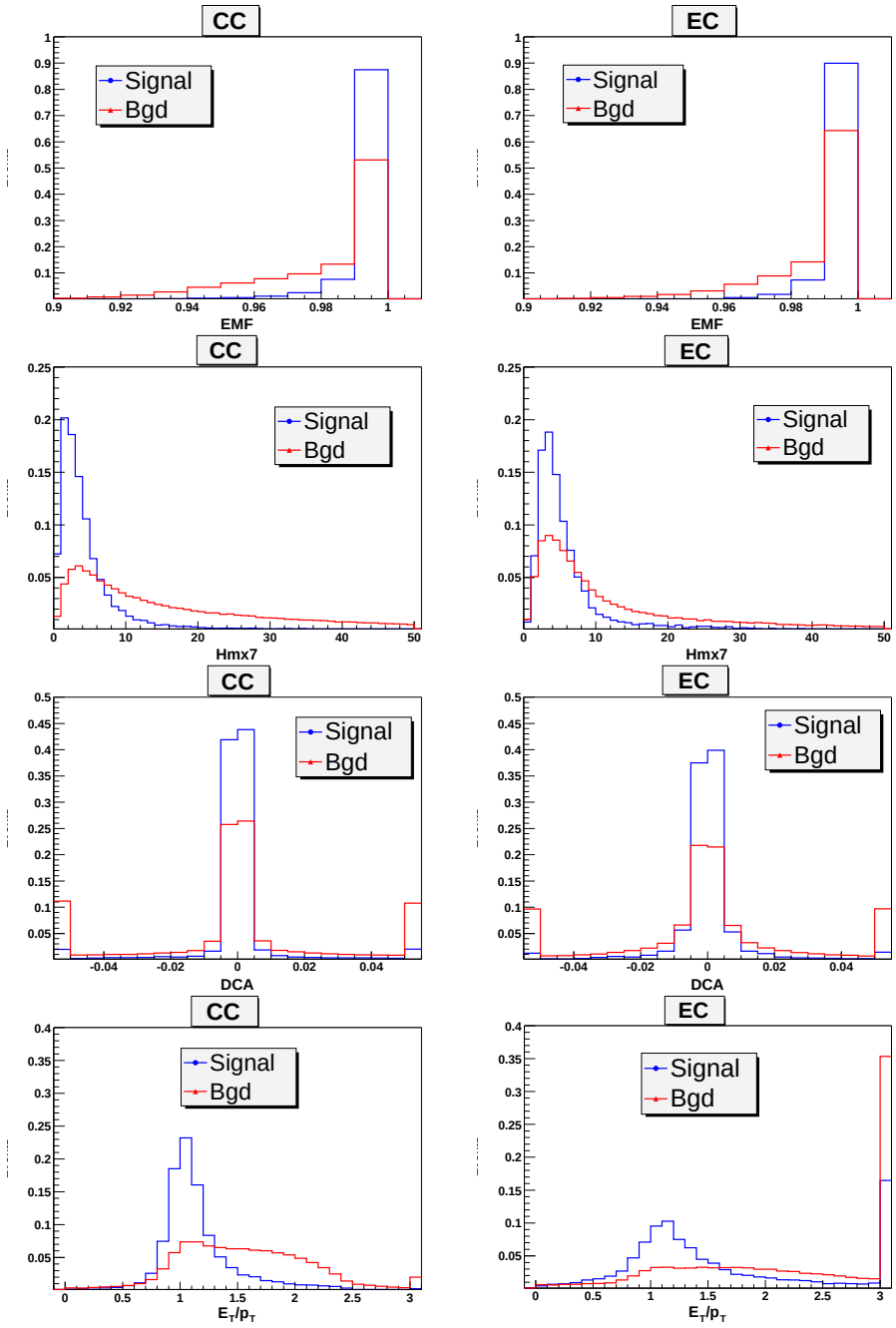

Figure 4.2: Signal-to-background discriminations of f_{EM}, H-Matrix χ^2_{Cal7}, DCA, and E_T/p_T in the CC (left) and EC (right)

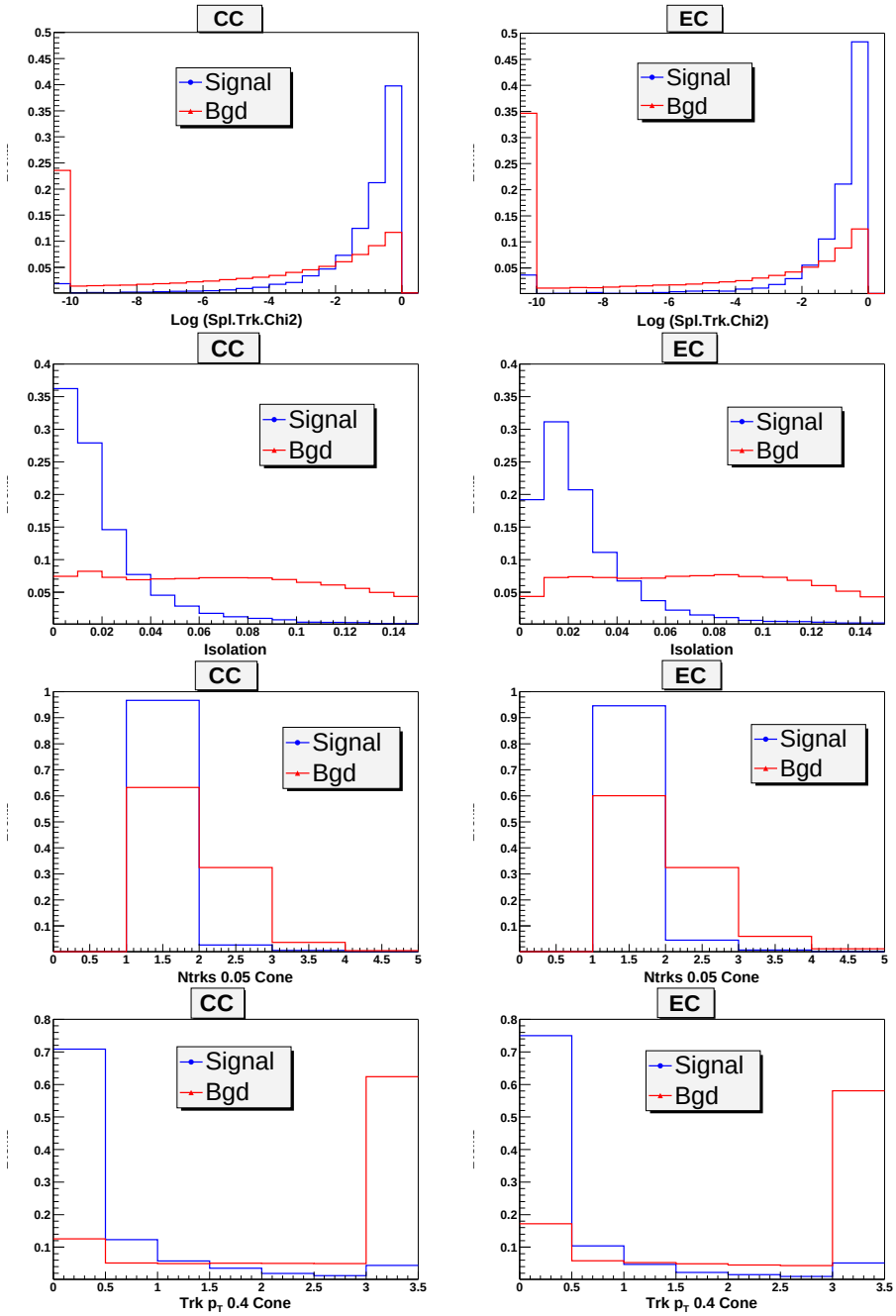

Figure 4.3: Signal-to-background discriminations of $Prob(\chi^2_{spatial})$, f_{iso}, number of tracks (N_{trks}) in 0.05 cone and total track p_T ($\sum p_T^{trk}$) in 0.4 cone in the CC (left) and EC (right)

We also consider some additional variables :

- Isolation Fraction (f_{iso}).
- Total track p_T in the halo between $\Delta R = 0.05$ and $\Delta R = 0.4$ cones: We introduce this variable since the above two track related variables might be correlated by virtue of design.

The performance of these variables in discriminating signal from background has been shown for the CC and EC electrons separately in Fig. 4.2 and Fig. 4.3. Here CC refers to the region $|\eta_d| < 1.1$ and EC refers to $1.5 < |\eta_d| < 2.5$. In these distributions, the final bin is an "overflow" bin. It can be seen that H-Matrix χ^2_{Cal7}, E_T/p_T, $Prob(\chi^2_{spatial})$, $N_{trks}(\Delta R = 0.05)$, $\sum p_T^{trks}(\Delta R = 0.4)$ and f_{iso} provide good discrimination between the signal and background. f_{EM} and DCA provides moderate discrimination.

4.2.3 Correlations

The formulation of electron likelihood invokes the approximation that the input variables are independent. However, one might expect some correlations due to the fact that these variables are all good indicators of electron-ness. We have investigated the correlations between the discriminating variables. We want the correlations between the likelihood input variables to be small, because, otherwise, we do not have an additional information and hence we do not gain very much in the likelihood. Also this reduces the sensitivity of the algorithm to the sample on which it was tuned. To quantify the degree of correlation between the input variables, we calculate the correlation coefficients, ρ, for each pairwise combination of the inputs, x and y, where

$$\rho = \frac{\mathrm{cov}(x,y)}{\sigma_x \sigma_y} = \frac{\sum(x_i - \overline{x})(y_j - \overline{y})}{\sqrt{\sum(x_i - \overline{x})^2}\sqrt{\sum(y_j - \overline{y})^2}}. \tag{4.5}$$

	f_{EM}	χ^2_{Cal7}	$\chi^2_{spatial}$	E_T/p_T	DCA	N_{trks}	$\sum p_T^{trk}$	$\sum p_T^{trkhalo}$	f_{iso}
f_{EM}	1	-0.448	0.064	-0.027	-0.004	-0.057	-0.033	-0.030	-0.533
χ^2_{Cal7}		1	-0.189	0.036	-0.002	0.124	0.041	0.033	0.261
$\chi^2_{spatial}$			1	-0.074	-0.005	-0.067	-0.032	-0.019	-0.099
E_T/p_T				1	0.030	0.107	0.051	0.024	0.061
DCA					1	-0.012	-0.001	0.001	0.001
N_{trks}						1	0.183	0.024	0.086
$\sum p_T^{trk}$							1	0.079	0.070
$\sum p_T^{trkhalo}$								1	0.072
f_{iso}									1

	f_{EM}	χ^2_{Cal7}	$\chi^2_{spatial}$	E_T/p_T	DCA	N_{trks}	$\sum p_T^{trk}$	$\sum p_T^{trkhalo}$	f_{iso}
f_{EM}	1	-0.425	0.073	-0.129	-0.023	-0.016	-0.016	-0.067	-0.507
χ^2_{Cal7}		1	-0.097	0.083	0.003	0.063	0.023	0.048	0.227
$\chi^2_{spatial}$			1	-0.222	-0.001	-0.060	-0.042	-0.064	-0.103
E_T/p_T				1	-0.028	0.133	0.099	0.094	0.125
DCA					1	-0.013	-0.008	-0.002	-0.036
N_{trks}						1	0.279	0.072	0.084
$\sum p_T^{trk}$							1	0.115	0.060
$\sum p_T^{trkhalo}$								1	0.150
f_{iso}									1

Table 4.1: Correlation coefficiencts between the discriminating variables for the signal sample in the central (top) and endcap (bottom) calorimeter.

The value of ρ ranges from 0, when there is no correlation, to ± 1, when there is complete correlation or anti-correlation [149]. Table 4.1 shows the 9×9 correlation matrices between signal inputs in the CC and EC.

We find that most of the combinations have correlation coefficients close to zero and hence mutually uncorrelated. However, f_{EM} and χ^2_{Cal7}, f_{EM} and f_{iso} , exhibit some significant correlation. H-Matrix χ^2_{Cal7} and isolation has small magnitude of correlation. Fig. 4.4 demonstrates the correlations between these correlated variables. N_{trks} and $\sum p_T^{trk}$ show small correlation, which we expect by virtue of their design. We are able to get rid of this small correlation between them if we switch to $\sum p_T^{trk}$ in the halo. Similar conclusions are drawn from the 9×9 correlation matrices between background inputs in the CC and EC [148].

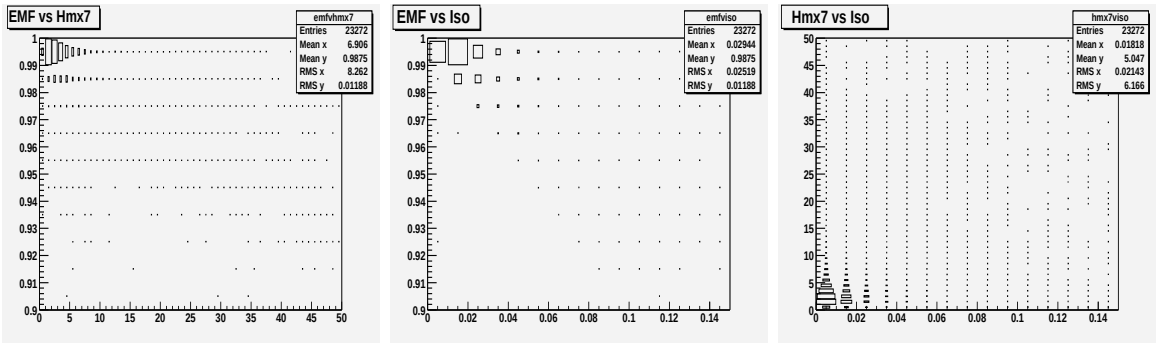

Figure 4.4: Correlations between (a) f_{EM} and H-Matrixχ^2_{Cal7}, (b)f_{EM} and f_{iso}, and (c) χ^2_{Cal7} and f_{iso} for the signal sample in the central calorimeter region.

4.2.4 Kinematic dependences of variables

We have examined in detail the kinematic dependences (p_T, η and ϕ) of the discriminating variables (see [148]) . This is very important in the sense that we want to use these variables in the construction of likelihood, which will have potential application to other analyses in which the topology of the event may be very different.

4.2.5 3-parameter Likelihood

It is always preferred to construct a likelihood with fewer variables, which, in general, is always easier to understand. Also, the chances of its kinematic dependence is less. To start with, we construct a likelihood function based on only three variables : N_{trks}, $\sum p_T^{trk}$ (halo), and $\chi^2_{spatial}$. These variables have been chosen based on good discrimination power and insignificant correlations. The performance of the likelihood is tested by running over the signal and background samples. Figure 4.5 shows that the likelihood separates signal from background very well after the preselection cuts. This separation power can also be seen in Figure 4.5 by looking at signal and background efficiencies when cutting at different thresholds of the likelihoods. Here we also compare the

performance of this likelihood with the currently used 7-parameter likelihood. We see that the new likelihood performs reasonably well. Its performance is worse in CC than the current version. But it performs remarkably well in the EC and its performance matches with that of the current likelihood.

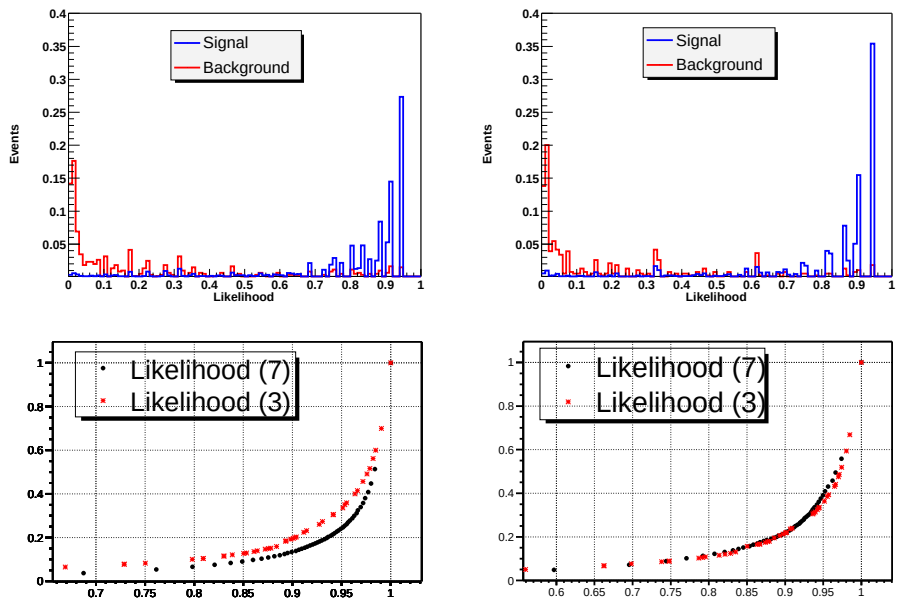

Figure 4.5: Signal-to-background discrimination of the 3-parameter likelihood in the CC (top-left) and EC (top-right). Background efficiency vs. signal efficiency after preselection for various 3-parameter likelihood cuts in the CC (bottom-left) and EC (bottom-right).

4-parameter Likelihood

Now we look at the effect of adding the fourth variable in the likelihood to extract better performance. It was found that the addition of f_{EM}, DCA or χ^2_{Cal7} has very marginal effect on the performance. Addition of E_T/p_T makes noticeable effect on the performance in CC only (see figure 4.6). In comparison to the present likelihood, the 4-parameter likelihood with E_T/p_T underperforms in CC and matches with the performance in EC. As can be seen in figure 4.6 that the addition of f_{iso} as the fourth variable results in a marked improvement in the likelihood performance in the CC and EC. This likelihood performs almost

equally well as the current likelihood in the CC and even better in the EC in terms of better background rejection for a given signal efficiency.

The kinematic (p_T, η, ϕ) dependences of the likelihood efficiency for the 3- and 4-parameter likelihoods have been discussed in detail in our DØ note [148].

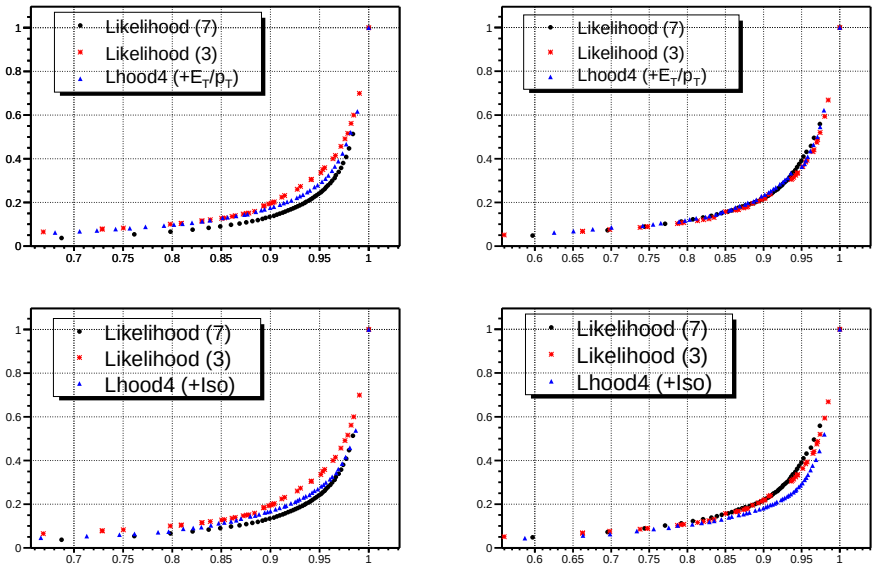

Figure 4.6: Background efficiency vs. signal efficiency for various likelihood cuts for the 4-parameter likelihood with E_T/p_T in the CC (top-left) and EC (top-right). Identical distributions for the 4-parameter likelihood with f_{iso} are shown in bottom-left and bottom-right plots.

4.2.6 Electron Efficiencies and Scale Factors

The efficiency for an electron candidate to pass all criteria for a tight electron is divided into three parts. The efficiency to be reconstructed as an EM cluster and pass all identification criteria for a "medium" electron is refered to as the "electron reconstruction and identification (Reco*ID)" efficiency. The probability for a medium electron to be matched to a track is refered to as the track match efficiency. Finally, the probability for a track matched electron to pass the electron likelihood is called the likelihood efficiency.

The detailed procedure to compute electron efficiencies is described in Ref. [150]. The Reco*ID efficiency is determined using a $Z \rightarrow ee$ data sample selected on the basis of a tight electron matched to a central track and a second central track (the probe track), both objects required to have an invariant mass consistent with the mass of the Z boson. The rate at which the probe track is matched to a reconstructed medium electron allows to derive this efficiency. The electron track match probability is derived from $Z \rightarrow ee$ events selected on the basis of a tight electron matched to a central track and a second medium electron (the probe electron), both objects required to have an invariant mass consistent with the mass of the Z boson. The rate at which the probe electron is matched to a central track allows to derive the track matching probability. Finally, the efficiency for the likelihood selection is derived from $Z \rightarrow ee$ events selected on the basis of one tight electron matched to a central track and a medium electron matched to a central track. The rate at which the medium electron passes the likelihood selection gives the likelihood efficiency.

Efficiency	Data	Monte Carlo	Scale factor
Reco*ID (CC)	0.944±0.002	0.950±0.001	0.996±0.001(stat)±0.029(syst)
Reco*ID (EC)	0.900±0.009	0.945±0.001	0.876±0.001(stat)±0.067(syst)
Track match (CC)	0.964±0.001	0.980±0.000	0.985±0.001(stat)±0.007(syst)
Track match (EC)	0.700±0.004	0.895±0.001	0.782±0.004(stat)±0.054(syst)
Likelihood (CC)	0.858±0.002	0.941±0.001	0.912±0.002(stat)±0.015(syst)
Likelihood (EC)	0.844±0.003	0.924±0.001	0.963±0.004(stat)±0.027(syst)

Table 4.2: Single medium electron efficiencies in $Z \rightarrow ee$ data and Pythia Monte Carlo integrated on the whole data and Monte Carlo samples. The errors on the efficiencies are statistical only. These efficiencies are valid for the 15 GeV p_T cut used in the dielectron analysis.

The measured efficiencies are summarised in Table 4.2. It is clear that the efficiencies measured in data and Monte Carlo are not the same. The Monte Carlo tends to have higher efficiencies since it does not describe all of the features of the real detector. Therefore, correction or scale factors, $\kappa = \epsilon(Z_{data})/\epsilon(Z_{MC})$,

are used to scale to Monte Carlo efficiencies to the data efficiencies. The summary of scale factors is given in Table 4.2.

4.2.7 Electron Energy Resolution and Smearing

The electron energy resolution in MC is better than in the data, and the position of Z peak in MC is also shifted from that in data. This is not surprising as the MC can't be expected to reproduce all the features of data from a real detector. For this reason, the electron cluster energy in the MC is smeared to reproduce the resolution in data, and a scale factor is applied to shift the peak location. The energy resolution of electrons can be parameterized as:

$$\frac{\sigma(E)}{E} = C \oplus \frac{S}{\sqrt{E}} \oplus \frac{N}{E}, \tag{4.6}$$

where C, S, and N are constant, sampling, and noise terms, respectively. Hence, the energy of the Monte Carlo electrons are adjusted by

$$\begin{aligned} E' = E \times [\alpha \quad &+ \quad \xi_1 = Gaus(0, \sigma = \alpha c) \\ &+ \quad \xi_2 = Gaus(0, \sigma = s\sqrt{\alpha/E}) \\ &+ \quad \xi_3 = Gaus(0, \sigma = n/E)], \end{aligned} \tag{4.7}$$

where α is the scale factor and ξ_1, ξ_2, and ξ_3 are random oversmearings obtained from Gaussian distributions with a mean of zero and a width of σ. c, s, and n are constant, sampling, and noise oversmearing coefficients. The ref. [151] provides a detailed analysis of how these parameters are obtained. It has been seen that the scale factor and oversmearing provided by $\sigma = \alpha c$ alone is sufficient to tune the electron energy in the MC to match the data.

Table 4.3 gives the values of the scale and over-smearing terms in three regions: CC (in fiducial), CC (not in fiducial), and EC. An in fiducial electron is at

Electron Type	Scale Factor	Oversmearing Parameter
CC (in fiducial)	1.003±0.001	0.045±0.004
CC (not in fiducial)	0.950±0.011	0.115±0.009
EC	0.996±0.005	0.034±0.009

Table 4.3: Scale factors and oversmearing parameters for MC electrons [151].

Electron Type	C	$S(\sqrt{GeV})$
CC (in fiducial)	0.0439±0.0002	0.224±0.002
CC (not in fiducial)	0.1116±0.0011	0.385±0.013
EC	0.0316±0.0005	0.258±0.006

Table 4.4: Energy resolution parameters for high-p_T electrons [151].

least 0.01 radians in ϕ away from one of the 32 evenly spaced ϕ-cracks in the calorimeter. This distinction is made since a different energy scale is applied to in fiducial and not in fiducial electrons.

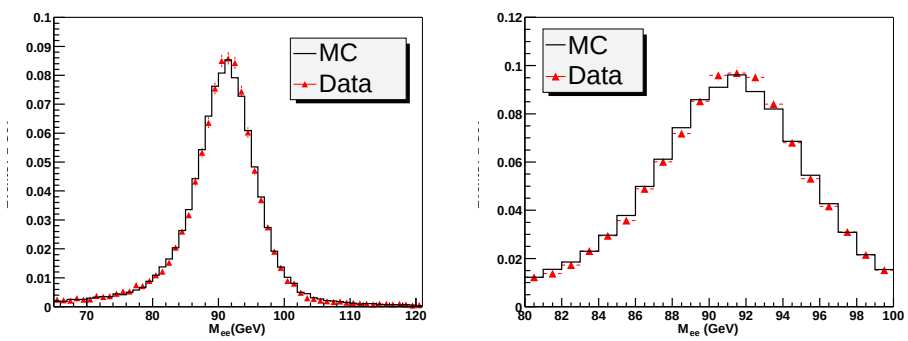

Figure 4.7: Invariant dielectron mass spectrum in ee events with zero or more jets. The right plot is zoomed in the region of Z mass.

Once the MC electron energy has been scaled and over-smeared, the electron energy resolution is determined by comparing the energy of generated electrons to that of matched reconstructed electrons. Table 4.4 lists the values of constant and sampling terms for in fiducial CC, not in fiducial CC, and EC electrons. Since high-p_T electrons are being used, the noise term is negligible. Fig. 4.7 illustrates the agreement between the smeared MC and dielectron data selected by requiring two tight electrons.

	CCCC	CCEC	ECEC
Data Efficiency	0.997±0.001	0.958±0.002	0.898±0.009
MC Efficiency	0.999±0.000	0.993±0.000	0.977±0.003
κ_{sign}	0.998±0.001	0.965±0.003	0.919±0.012

Table 4.5: Efficiencies and scale factors for oppositely charged electron pairs when both are in CC, one of them in CC, and both in EC.

4.2.8 Electron Charge

As discussed in section 2.6.2, the magnetic field makes it possible to determine the charge of a physics object. The two electrons in $Z \rightarrow ee$ or $t\bar{t} \rightarrow ee$ events are required to be oppositely charged. There is a small inefficiency with this cut since straight, high-p_T tracks can sometimes be reconstructed with the wrong sign. The efficiencies of this cut in $Z \rightarrow ee$ data and MC, and the resultant scale factors, are listed in Table 4.5.

4.2.9 Kinematic distributions of electrons

Fig. 4.8 shows the kinematic distributions of electrons in $Z \rightarrow ee$ events. We see a reasonably good agreement between data and MC in them.

4.3 Jets

A parton (quark or gluon) will appear as a jet in the detector due to color confinement through a process known as hadronization. The hadronization process produces a large number of colorless hadrons that appear in the detector as a collimated "jet" of hadronic particles and deposit a cluster of energy in the calorimeter, typically the shape of a cone. Pions make up the majority of particles in a jet, since they are the lightest hadrons. The methods used for reconstructing, identifying, and calibrating the jets are described in this section.

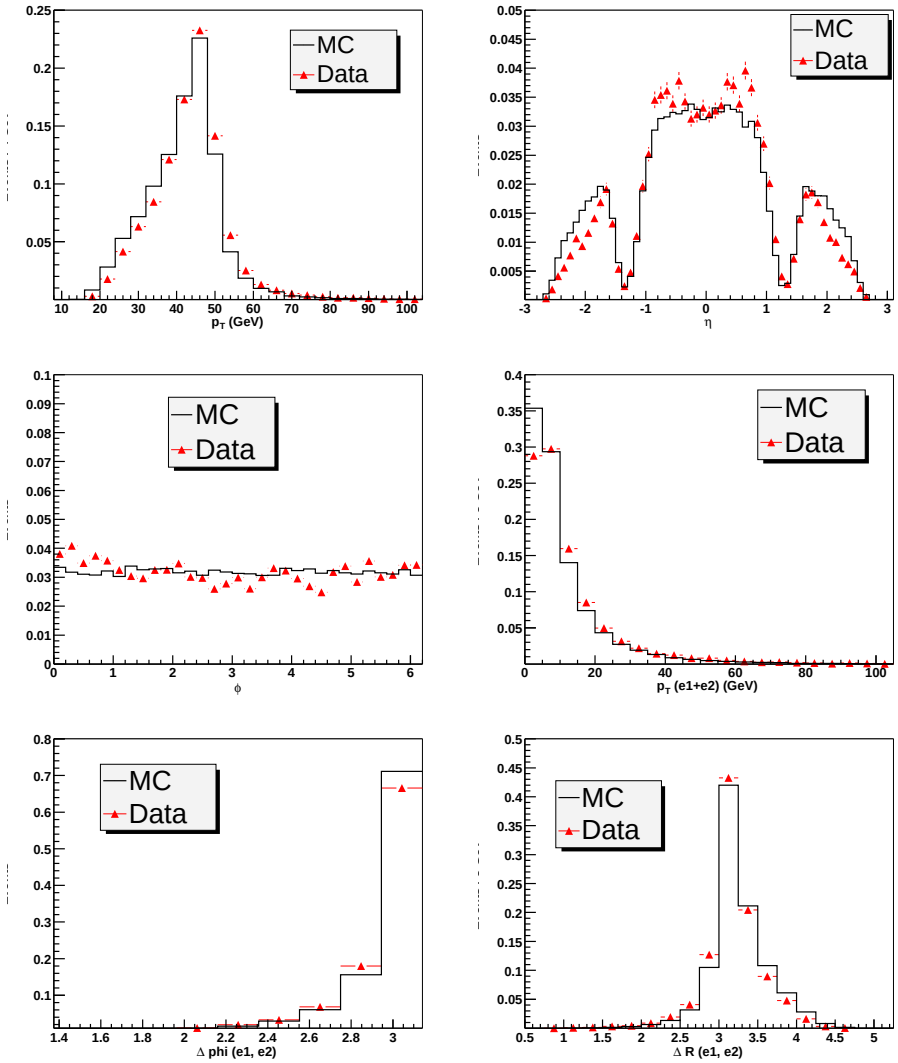

Figure 4.8: p_T, η and ϕ distributions of leading electron in $Z \rightarrow ee$ events. Distributions of dielecton system : $|\overrightarrow{p_T^{e1}} + \overrightarrow{p_T^{e2}}|$, $\Delta\phi(e^1, e^2)$ and $\Delta R(e^1, e^2)$.

4.3.1 Jet Reconstruction

The ideal jet algorithm should reconstruct the kinematic properties of the initial hadronic particle. Jets are reconstructed using the Run II *improved legacy cone* algorithm [152], which proceeds as follows:

- **Preclustering:** "Seeds" are formed from calorimeter towers with $E_T > 0.5$ GeV. Cells in the coarse hadronic calorimeter, the end cap massless gap or the end cap hadronic layer 16 or 17 are not considered as seeds due to an

enhanced noise level. Beginning with the highest E_T tower, preclusters are formed of adjacent towers within a cone of radius $\Delta R < 0.3$. Only towers with $E_T > 1$ GeV are included in preclusters.

- **Cone clustering:** The E_T weighted centroid of a precluster is used as the initial cone center of a jet. From it, all towers within a cone of radius $\Delta R < 0.5$ are included in the jet, and the E_T weighted centroid is recalculated. This new center is then used as the cone axis, the energy in the cone of $\Delta R < 0.5$ is calculated again, and another new center is found. This procedure is iterated until a stable cone axis is found. Each stable cone found is defined as the proto-jet. Duplicate proto-jets (those with the same axes) are removed, as well as those with total $E_T < 8$ GeV.

- **Merging and Splitting:** The proto-jets are compared for the overlapping regions as they may share some towers. If the E_T contained in the overlapping region between two jets is greater than half of the E_T of either jet, the two jets are merged, and the jet energy and axis are recomputed. Otherwise, the jets are split, the towers are added to the nearest cone center only, and the energies and axes of each jet are recomputed.

As for electrons, zero suppression and the hot cell killer are used to reduce calorimeter noise. In addition, the T42 algorithm [153][154] is applied to obtain a finer treatment of calorimeter noise, which, in turn, improves the reconstruction of calorimeter objects. For the T42 algorithm, an isolated cell is considered a noise cell and thus discarded if it is not "signal-like". A cell is considered "signal-like" if its energy is positive and above a high threshold of $+4\sigma$, or if its energy is above $+2\sigma$ and in addition the energy of a neighbouring cell is above $+4\sigma$. The T42 algorithm has been found to reduce the number of fake jets clustered on noise, or "noise jets," by about a factor of two.

4.3.2 Jet Identification

A set of quality cuts are applied to each reconstucted jet in order to distinguish real jets from fake ones.

- $0.05 < f_{EM} < 0.95$ **:** The EM fraction is the fraction of total jet energy deposited in the EM layers of the calorimeter. Jet ID requires $0.05 < f_{EM} < 0.95$ which removes isolated electromagnetic particles at the high end and jets with a disproportionate amount of hadronic energy at the low end.
- **Coarse Hadronic Fraction (CHF)** < 0.4**:** The coarse hadronic fraction defines the fraction of total jet energy in the coarse hadronic (CH) layers of the calorimeter. Jet ID requires CHF < 0.4. The noise level is higher in CH section and this cut is essentially aimed at removing those jets clustered around noise in the CH section.
- **Hot Fraction (HotF)**< 10**:** To remove jets clustered from hot cells, a cut on the ratio of the highest to the next-to-highest transverse energy cell in the calorimeter (HotF) is applied at HotF< 10.
- $n90 > 1$**:** To remove those jets clustered from a single hot tower, the number of towers containing 90% of the jet energy ($n90$) is required to be greater than 1.

The jets passing all the quality criteria are referred to as "good" jets and the jets failing any of these criteria are referred to as "bad" jets. Fig. 4.9 shows the distributions of good jet multiplicity and the above jet quality variables in $Z \rightarrow ee$ data and Monte Carlo.

Even when these quality cuts are applied, a significant number of noise jets still survive in data. A comparison of the energy in the L1 calorimeter towers to the

energy obtained in the precision readout turns out to be very discriminating against noise jets. Therefore, an additional variable "L1Conf" has been derived using this information. Defining $L1SET$ to be the scalar sum of the trigger towers' E_Ts in the same cone as the jet, the cut used to reject noise jets is

$$L1Conf = \frac{L1SET}{p_T^{jet}(1 - CHF)} > 0.4 \text{ (in CC, EC) or } > 0.2 \text{ (in ICD)},$$

where CC is $|\eta_d| < 0.8$, EC is $|\eta_d| > 1.5$, and ICD is $0.8 < |\eta_d| < 1.5$ [155]. The efficiency for this cut is very high ($> 99.5\%$) in all three regions. Fig. 4.9 shows the distribution of L1Conf variable of good jets in $Z \rightarrow ee$ data. The jets failing Level 1 confirmation requirement are called "Noise" jets.

4.3.3 Jet Energy Scale

The raw energies of reconstructed jets are affected by noise, calorimeter response, showering effects, and the underlying event. Therefore, the standard jet energy scale (JES) corrections are applied in an attempt to correct the jet energies back to the particle level energy, the energy the particle had before interacting with the calorimeter. The corrected jet energy (E_{corr}) is obtained from the measured energy (E_{meas}) by

$$E_{corr} = \frac{E_{meas} - O}{R \times S},$$

where R is the calorimeter response to a jet, S is the fraction of shower leakage outside the jet cone ($\Delta R = 0.5$), and O is the energy offset due to the underlying event, energy pile-up, multiple interactions, electronic noise, and uranium noise. R is determined by requiring E_T balancing in $\gamma + jet$ events; S is obtained by measuring the energy profiles of jets; and O is derived from energy

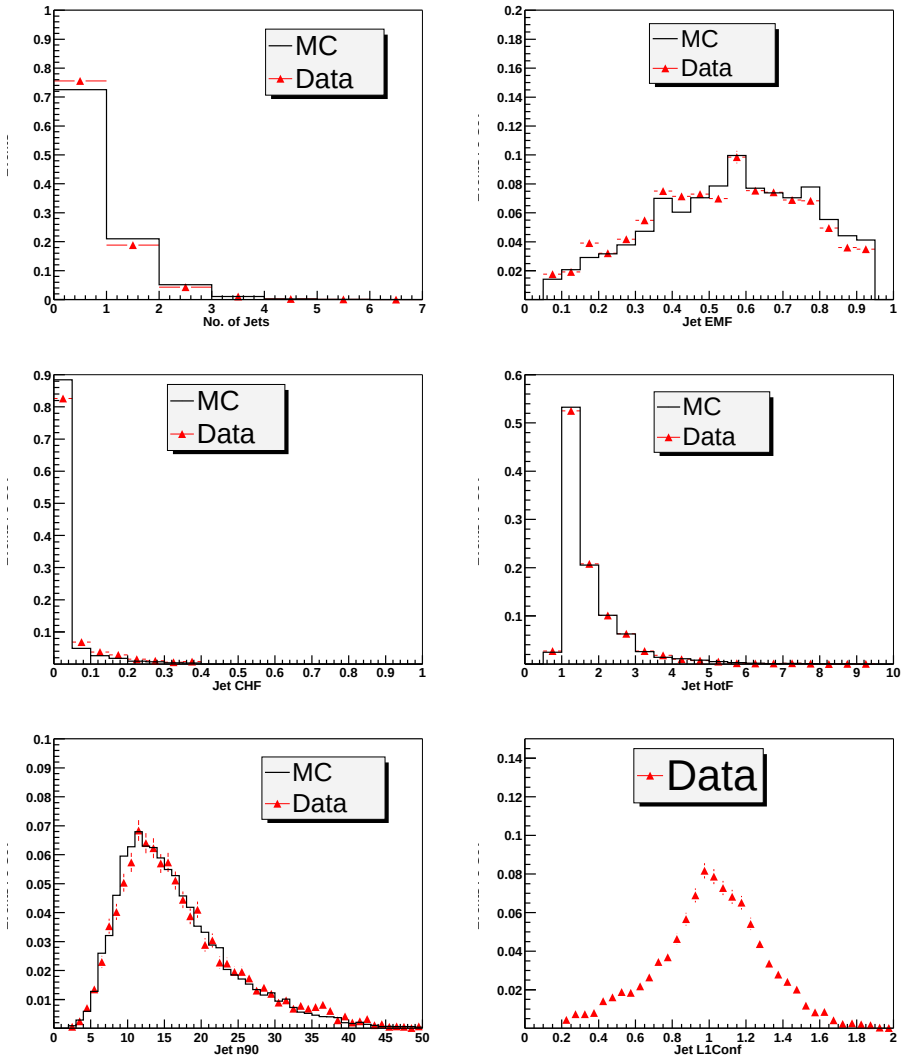

Figure 4.9: Distributions of good jet multiplicity and the five jet quality variables (EMF, CHF, HotF, n90 and L1Conf) in $Z \rightarrow ee$ events.

densities in minimum bias trigger events. In this analysis, jet correction package ($JetCorr\ v5.3$) [156] is used to correct jet energies in both the data and Monte Carlo. The corrections are done jet-by-jet, and different corrections are used for jets in data and Monte Carlo.

4.3.4 Jet Energy Resolution

The jet energy resolutions [157] are derived using two samples, one for jets above $p_T \approx 50$ GeV and one for jets with $p_T < 50$ GeV. For high energy jets ($p_T > 50$ GeV), a dijet sample is used. This sample is binned into several bins based on average p_T of the dijet system ($< p_T >= (p_T^1 + p_T^2)/2$). In each bin, the distribution of the transverse momentum asymmetry,

$$\mathcal{A}_{jj} = \frac{|p_T^1 - p_T^2|}{p_T^1 + p_T^2}, \tag{4.8}$$

is obtained. The width of this distribution, $\sigma_{\mathcal{A}}$, gives the jet p_T resolution by

$$\frac{\sigma_{p_T}}{p_T} = \sqrt{2}\sigma_{\mathcal{A}_{jj}}. \tag{4.9}$$

For jets with $p_T < 50$ GeV, a back-to-back photon+jet sample is used in which the asymmetry variable is defined

$$\mathcal{A}_{\gamma j} = \frac{p_T^j + p_T^\gamma}{p_T^\gamma}. \tag{4.10}$$

Since the resolution of the photon is considerably better than the resoltuion of the jet, $\sigma_{p_T^\gamma}$ can be ignored. The jet resolution can then be written

$$\frac{\sigma_{p_T^j}}{p_T^j} = \sigma_{\mathcal{A}_{\gamma j}} \times R_{\gamma j}, \tag{4.11}$$

where $R_{\gamma j} = p_T^\gamma / p_T^j$ corrects for the imbalance between average jet and photon p_T in each p_T bin.

The results from the two p_T ranges are combined, and the jet energy resolution

$\|\eta\|$ Range	Data			Monte Carlo		
	N	S	C	N	S	C
0.0< $\|\eta\|$ <0.5	5.05	0.753	0.0893	4.26	0.658	0.0436
0.5< $\|\eta\|$ <1.0	0.0	1.20	0.0870	4.61	0.621	0.0578
1.0< $\|\eta\|$ <1.5	2.24	0.924	0.135	3.08	0.816	0.0729
1.5< $\|\eta\|$ <2.0	6.42	0.0	0.974	4.83	0.0	0.0735

Table 4.6: Jet energy resolution constants for jets in data and Monte Carlo.

is parameterized using

$$\frac{\sigma_{p_T^j}}{p_T^j} = \sqrt{\frac{N^2}{p_T^2} + \frac{S^2}{p_T} + C^2}. \tag{4.12}$$

The fit parameters are summarized in Table 4.6.

4.3.5 Jet/EM Separation

Electrons and photons are reconstructed as both jets and as EM objects. Therefore, it is imperative to separate isolated electrons from jets in order to avoid double-counting these objects. Moreover, different energy scales are required for electrons and jets.

The EM energy scale is applied to electrons, photons, and jets dominated by photons (namely π^0's) since all of these objects tend to have similar shower shapes in the calorimeter. All other objects are considered to be jets, to which the jet energy scale is applied. A good EM cluster in the calorimeter is defined by the standard electron preselection cuts in the calorimeter: $|ID| = 10\text{or}11$, $f_{EM} > 0.9$, $f_{iso} < 0.15$, and $\chi^2_{Cal7} < 50$. Reconstructed and identified jet candidates are not considered as jets but as EM candidates if they overalp with an EM object ($\Delta R(EM, Jet) < 0.5$)) with the following selection criteria:

- $p_T > 15$ GeV (after jet energy scale correction)
- $|\eta| < 2.5$
- $f_{EM} > 0.9$, $f_{iso} < 0.15$, and $\chi^2_{Cal7} < 50$

If the EM object does not pass tighter selection cuts, it is simply ignored instead of being reconsidered as a jet and having the jet energy scale applied. It is true that a real jet could look like an EM object, in which case, this treatment is incorrect. However, from the study in $Z \rightarrow ee$ events, it has been found that this effect is not a problem. Only about 1% of Z events have more than two EM objects, and a large fraction of these extra EM objects are most likely π^0's or photons. Since this effect is so small, this Jet/EM separation treatment is applicable.

4.3.6 Jet Scale Factor

As with the electrons, jet reconstruction and identification efficiencies in the Monte Carlo are not the same as in the data. Therefore, a scale factor must also be applied to the Monte Carlo jets. This scale factor is derived on a γ+jet sample and is found to be E_T dependent. Instead of applying the jet scale factor in the analysis, the scale factor curves are folded in when *top_analyze* is run over the Monte Carlo samples. Hence, the jet reconstruction and identification efficiencies in the *top_analyze* output agree with the data.

4.3.7 Kinematic Distributions of Jets

Figure 4.10 shows the distributions of p_T and η of leading and next-leading jets above p_T >20 GeV in $Z \rightarrow ee+ \geq 2$ jet events in data and Monte Carlo. A nice agreement between the data and Monte Carlo can be seen.

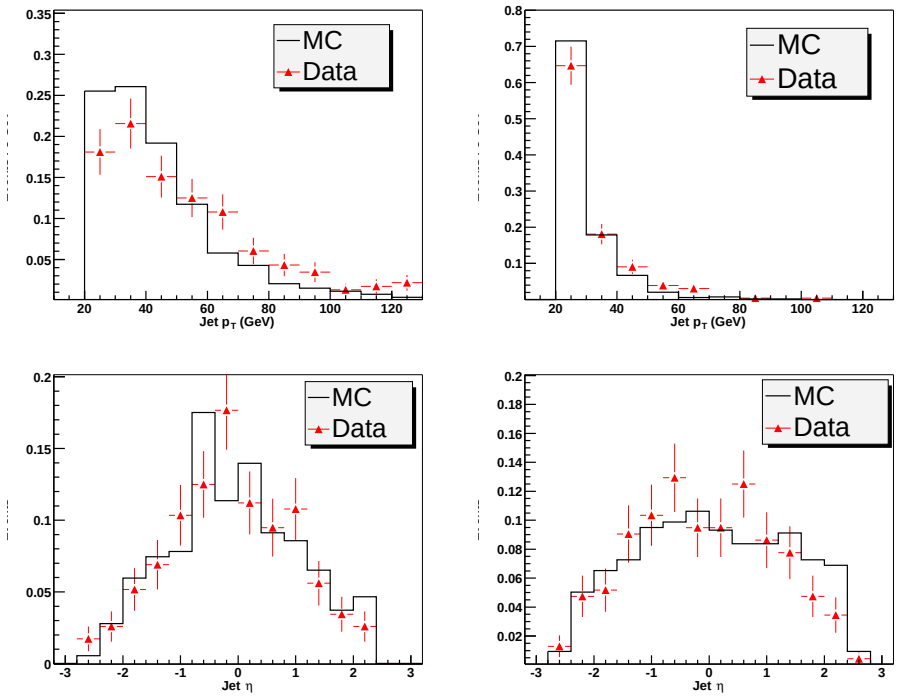

Figure 4.10: Distributions of p_T and η of leading (left) and next-leading (right) jets above p_T >20 GeV in $Z \rightarrow ee+ \geq 2$ jet events in data and Monte Carlo.

4.4 Missing Transverse Energy

The protons and antiprotons colliding at the Tevatron have equal and opposite momenta, indicating that the total vector momentum sum in any event should be zero. However, as discussed previously, the hard-scatter interactions occur between the partons of the parent proton and antiproton. These partons share the total momentum of the parent and are not constrained to any particular momentum value. The partons tend to carry very little momentum in the plane transverse to the beam path. Thus, to a good approximation, the transverse momentum (energy) can be considered a conserved quantity.

As neutrinos interact very weekly with matter, their direct observation is impossible; rather, their presence is inferred from any imbalance of the moment (energy) in the event. That is, the neutrinos appear as "missing" transverse energy, $\not{E}_T$. However, the large $\not{E}_T$ observed in data can also be the the result

of the following:

- Non-interacting particles (not yet observed) predicted by models beyond the standard model (e.g. sparticles - LSP, graviton).
- Mis-measurement of the "visible" final state (vertex position, jet and EM object's energy) owing to energy resolution of physics objects.
- Calorimeter effects such as the accidental preseence of "hot cells" and coherent noise, which can be generically characterized as the energy deposition not related to the real events .

The $\not{E}_T$ is defined by the net imbalance in the transverse energy deposited in the calorimeter. The $\not{E}_T$ has the magnitude of the vector sum of the measured transverse energies of the calorimeter cells used in the calculation, pointing in the opposite direction in ϕ in order to balance the energy in the transverse plane. This analysis uses the standard $\not{E}_T$ calculated from the transverse energies of calorimeter cells with positive energy above 100 MeV (passing T42 selection) except for the cells in the coarse hadronic (CH) layers. The CH cells are included only if they are clustered within a reconstructed jet. The cells from the CH are noisy and when the $\not{E}_T$ is computed with all of them, its resolution decreases. The raw $\not{E}_T$ is calculated by RECO before any corrections are applied. The $\not{E}_T$ is found by using the folowing formulas:

$$\not{E}_x = -\sum_{cells} E_T cos(\phi),\ \ \not{E}_y = -\sum_{cells} E_T sin(\phi),\ \ \not{E}_T = \sqrt{\not{E}_x{}^2 + \not{E}_y{}^2} \qquad (4.13)$$

where $\not{E}_x$ and $\not{E}_x$ are the components of missing transverse energy along the x- and y-axes, respectively. It is obvious from the above expressions that, in order to calculate the E_T of the calorimeter cells, the position of the vetex that affects the E_T must be known and also an accurate measurement of the scalar energy

of the cells must be done. These are the two sources of the mis-measurement of the $\not\!\!E_T$ of the "visible" final state.

4.4.1 Corrections to $\not\!\!E_T$

To be used in analysis, the $\not\!\!E_T$ must be a "real" energy and for that, the raw $\not\!\!E_T$ is corrected at different steps. First the $\not\!\!E_T$ is reconstructed with all cells except those from the CH. But it is considered that the CH fraction of jets used in the analysis is signal and not noise and it must be taken into account in $\not\!\!E_T$ calculation: it is subtracted from the $\not\!\!E_T$. This is called the CH correction.

Because the measured EM and jet energies are re-calibrated to reflect their true energies in the detector, this change in energy impacts the $\not\!\!E_T$. So the $\not\!\!E_T$ must also be corrected in order to account for the change in energy imbalance. We vectorially subtract the portion of each jet energy scale as well as EM scale correction. The jet energy scale (JES) correction has a considerably larger impact on the $\not\!\!E_T$ than the EM energy corrections. Only jets that pass the quality criteria described in previous section are used for this correction. The $\not\!\!E_T$ after these corrections is termed the calorimeter $\not\!\!E_T$.

In addition, muons, which usually behave as minimum-ionizing particles, deposit very little of their energy (typically about 2 GeV) in the calorimeter. The calorimeter $\not\!\!E_T$ does not account for the presense of these objects; therefore, some of the energy imbalance in the transverse plane is due to these muons, not neutrinos. Hence, one more correction to the $\not\!\!E_T$ must be made: the momentum of all the identified muons must be subtracted vectorially from the $\not\!\!E_T$ after the expected energy deposition in the calorimeter is subtracted. This $\not\!\!E_T$ is what is used in the analysis.

4.4.2 Motivation for $\not\!\!E_T$ study

Top quark cross-section analysis in dilepton channels ($t\bar{t} \rightarrow l^+l^-b\bar{b}\nu\bar{\nu}$) faces a formidable instrumental background from the $Z/\gamma^*(\rightarrow ll) + jets$ events. These events, in principle, have no intrinsic $\not\!\!E_T$ in the absence of neutrinos, but, they can pick "fake" $\not\!\!E_T$ caused by energy resolution fluctuations or calorimeter noise, and hence mimic top-antitop event signature. The $\not\!\!E_T$ is thus crucial element of the dilepton analyses because it is the primary discriminant used to reject resonant Z production as well as low mass Drell-Yan production. Thus the understanding of $\not\!\!E_T$ is of paramount importance in order to reduce and estimate this instrumental background for the $t\bar{t}$ cross-analysis. A considerable effort has been devoted to better understand the $\not\!\!E_T$ behavior in data and Monte Carlo using $Z \rightarrow ee$ events. The results of the comprehensive study in this direction can be found in our DØ notes [158] [159] [136] and a few snapshots of the results will be discussed here.

4.4.3 Study of $\not\!\!E_T$ behavior in data and Monte Carlo

In order to understand and quantify $\not\!\!E_T$ behavior, we have studied $\not\!\!E_T$ distribution, resolutions and fake rate by comparing the $\not\!\!E_T$ seen in the data with that expected from the Monte Carlo (MC) in $Z \rightarrow ee$ events.

$\not\!\!E_T$ distribution, resolution and fake rate: Figure 4.11 shows comparison of the normalized $\not\!\!E_T$ distributions in $Z \rightarrow ee$ events in data and Monte Carlo for the case of inclusive events, events with 0 jet, events with 1 jet and events with at least 2 jets. It can be seen that the $\not\!\!E_T$ in data has a broader spectrum than the MC. There is disagreement between data and MC not only in the "tail" but also in the "core" of the $\not\!\!E_T$ distribution. The data has a non-gaussian high $\not\!\!E_T$ tail. The discrepancy is more pronouced in inclusive and 0 jet distributions.

However, the situation becomes better for 1 jet sample and even better for the 2 jet sample. By looking at the RMS values of the $\not\!\!E_T$ distributions, we find that the $\not\!\!E_T$ resolution deteriorates as the number of jets increases in the events, which is indicative of the fact that $\not\!\!E_T$ resolution is largely dominated by jet resolutions.

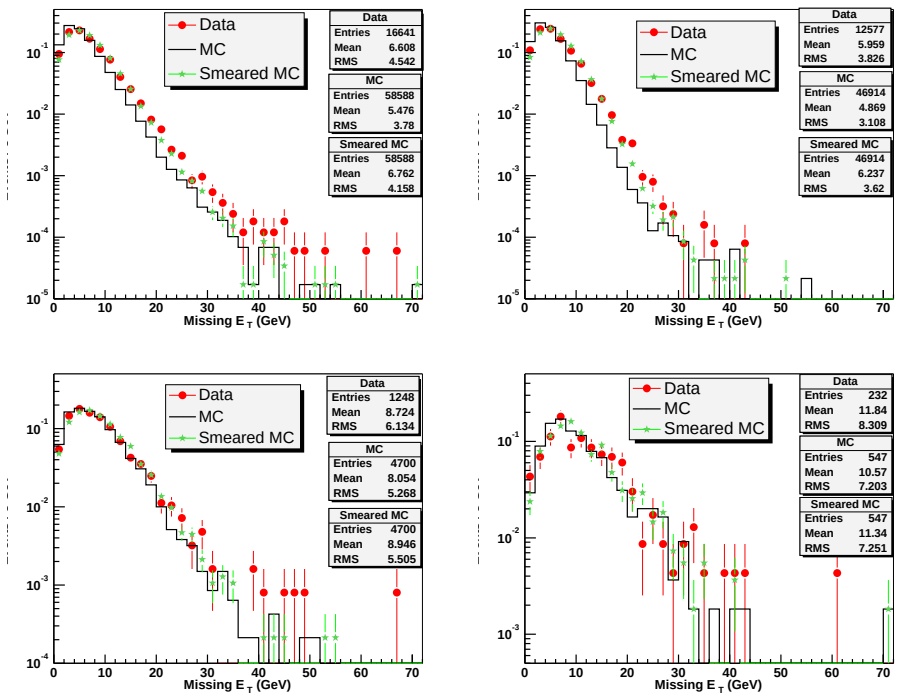

Figure 4.11: $\not\!\!E_T$ distributions in data and Monte Carlo for the inclusive Z sample (top-left), Z+ 0 jet events (top-right), Z+ 1 jet events (bottom-left) and Z+ $\geq$2 jets events (bottom-left). Effect of $\not\!\!E_T$ oversmearing is also demonstrated (discussed later).

$\not\!\!E_T$ fake rate gives the probability of events to survive different $\not\!\!E_T$ thresholds. In Figure 4.12 we show the $\not\!\!E_T$ fake rates as a function of $\not\!\!E_T$ in $Z \rightarrow ee$ events in data and Monte Carlo for the case of inclusive events, events with 0 jet, events with 1 jet and events with at least 2 jets. Disagreement between the data and MC is clearly evident in these distributions. Events in data exhibit higher $\not\!\!E_T$ fake rates and the discrepancy increases significantly as $\not\!\!E_T$ increases. Also, as the jet multiplicity increases, the agreement between the data and MC tend to

become better.

4.4.4 $\not\!\!E_T$ Oversmearing

Even without non-gaussian tails from calorimeter readout malfunctions, the fundamental cell-level resolution of the calorimeter produces finite $\not\!\!E_T$ resolution. Given our reliance on this variable, it is important that we reproduce its

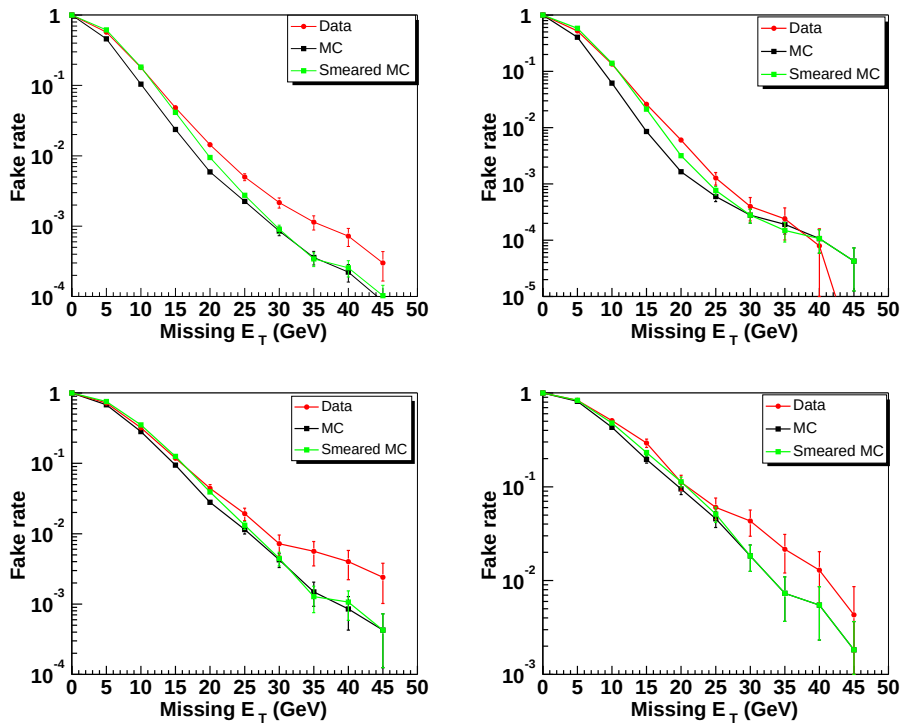

Figure 4.12: $\not\!\!E_T$ fake rates in data and Monte Carlo for the inclusive Z sample (top-left), Z+ 0 jet events (top-right), Z+ 1 jet events (bottom-left) and Z+ $\geq$2 jet events (bottom-right). Effect of $\not\!\!E_T$ oversmearing is also demonstrated (discussed later).

resolution as accurately as possible in the Monte Carlo because we rely directly, or as a cross-check, on simulation for some of our backgrounds, particularly $Z \rightarrow ee$, or $Z \rightarrow \tau\tau \rightarrow ee$. The latter has little inherent $\not\!\!E_T$ and a worse detector resolution might affect this background.

Even after implementing all the resolutions and smearings in Monte Carlo and incorporating all the corrections in the $\not\!\!E_T$, the fully corrected $\not\!\!E_T$ distribution

in $Z \rightarrow ee$ events in data does not match with that expected from Monte Carlo as seen earlier. So we attempt to further smear the $\not\!\!E_T$ in Monte Carlo to bring it in agreement with data for the core of the distribution where top and diboson backgrounds are negligible. Our DØ note [159] describes in detail how the oversmearing is obtained. In brief, the $\not\!\!E_T$ resolution is found to be a function of unclustered scalar E_T ($\sum E_{Tunclus}$), which is the scalar E_T of the event minus the p_T's of all the reconstructed objects (electrons and jets). The $\not\!\!E_x$ and $\not\!\!E_y$ resolutions in data and Monte Carlo are investigated as a function of $\sum E_{Tunclus}$, and it is found that that the $\not\!\!E_T$ resolutions are worse in data than in Monte Carlo. A smearing parameter for the x and y components for the $\not\!\!E_T$ is defined by separately subtracting, in quadrature, the $\not\!\!E_x$ and $\not\!\!E_y$ resolutions in data and Monte Carlo as a function of $\sum E_{Tunclus}$, respectively. The $\not\!\!E_T$ oversmearing parameters are then obtained by fitting these parameters vs $\sum E_{Tunclus}$ for different jet multiplicies.

Figure 4.13 show the data-Monte Carlo comparison of $\not\!\!E_{xy}$ resolutions (which combines $\not\!\!E_x$ and $\not\!\!E_y$ resolutions as they look quite similar in the different Z samples) as a function of $\sum E_{Tunclus}$ for the inclusive Z events and events with different jet multiplicity. The resulting smearing factors vs $\sum E_{Tunclus}$ for these cases are also shown there. The fits to the smearing factors in case of Z events with different jet multiplicities show a bit of slope thus reflecting a small dependence on the unclustered scalar energy. Table 4.7 shows the p0 and p1 coeficients of the fits obtained for the different jet multiplicity bins.

We observe that the exhibited behavior is uncorrelated with jet multiplicity. The weighted average smearing factor displays a slope with the following smearing coefficients:

$$\sigma_{E_T}(\Sigma E_{Tunclus}) = 2.633 + 0.008717 \times \Sigma E_{Tunclus}$$

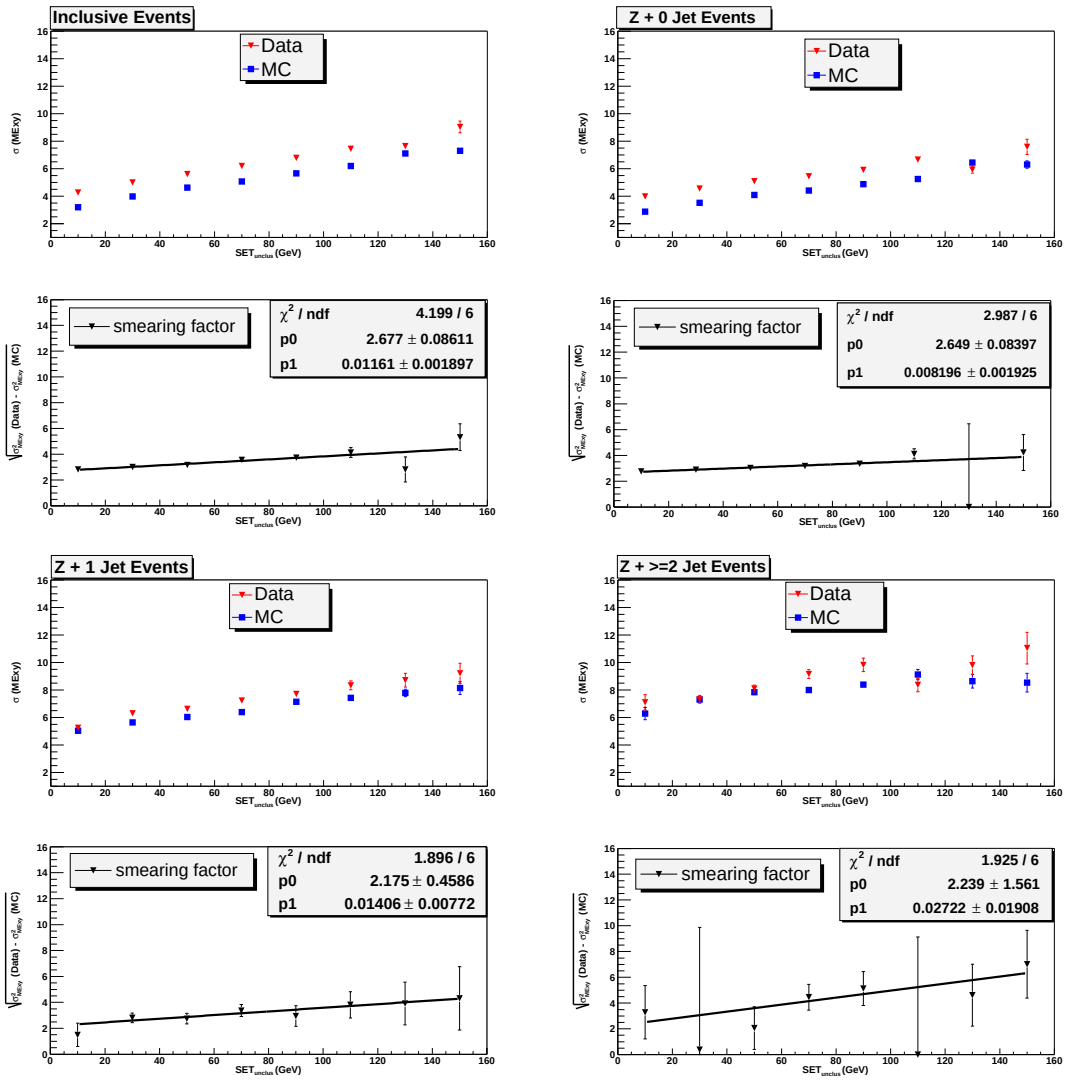

Figure 4.13: $\not{E}_{xy}$ resolutions and the corresponding smearing factors vs unclustered Scalar E_T for inclusive inclusive Z sample (top-left), Z+ 0 jet events (top-right), Z+ 1 jet events (bottom-left) and Z+ $\geq$2 jet events (bottom-right).

The $\not{E}_x$ and $\not{E}_y$ components of the $\not{E}_T$ have been smeared by the above mentioned oversmearing parameters to get the resultant $\not{E}_T$. The effect of $\not{E}_T$ oversmearing can be seen in Figure 4.11 for the inclusive Z events and events with different jet multiplicities. The smeared Monte Carlo describes better the core of the $\not{E}_T$ distribution in data. Figure 4.12 shows the effect of oversmearing on the $\not{E}_T$ fake rates where again we find that the smeared Monte Carlo provides a better

Jet Multiplicity	p0	p1
Njet=0	2.649±0.08397	0.008196±0.001925
Njet=1	2.175±0.4586	0.01406±0.00772
Njet≥2	2.239±1.561	0.02722±0.01908

Table 4.7: Oversmearing parameters for each jet multiplicity bin obtained from the fit parameters in Figure 4.13

description of the $\not\!\!E_T$ fake rate in data especially in the core region.

4.5 Vertex and Track

The interaction point of an event is called the vertex. There are two types of vertices: primary and secondary. A primary vertex is the original interaction point with the largest number of associated tracks, while a secondary vertex is a displaced vertex due to long-lived meson decay (e.g. B, K_s or D). The x and y coordinates of the primary vertex are close to zero since the cross sectional extent of the beam is ≈ 40 μm [160]. However, the z coordinate has a range with a rms width of 28 cm and with a central value close to zero [161]. The reconstruction and selection of primary and secondary vertices is described in detail in [162]. Hits from the silicon microstrip tracker (SMT) and central fiber tracker (CFT) are used to reconstruct the trajectories of charged particles and the event vertex. Because of the magnetic field in the z-direction, the hits of a charged particle lie along a curve, whose curvature in the x-y plane is used to measure its transverse momentum. The track finding algorithm is based on Kalman filter technique of local road finders [163]. Tracking is first done for each individual layer to produce track segments; the track segments are matched between layers to form global track candidates; a fit of a track and nearby hits is then performed and the track is accepted (rejected) if the fit is good (poor) as determined by the $\chi 2$ value [164].

4.6 Primary Vertex Selection

The primary vertex candidates are found as follows: 1. Select global tracks with at least one hit in the SMT; 2. Fit a vertex position from them; 3. Remove bad tracks with a large contribution to the $\chi 2$; 4. Repeat this procedure. Finally, the vertex candidate containing at least three tracks and with one of those having the greatest p_T is selected as the primary vertex of the event. Since many quantities such as the $\not\!\!E_T$ and the electron track match are calculated with respect to the primary vertex, several cuts are applied in order to ensure that a candidate event has high-quality reconstructed vertex. The primary vertex must be within the SMT fiducial region ($|z_{PV}| < 60$ cm). In addition, the vertex must have at least three tracks attached to it ($N_{trk} \geq 3$).

Two primary vertex reconstruction algorithms exist in the DØ software. The *d0reco* package implements one during the reconstruction while the one that is used for the analysis is applied later in the *d0root* package. Both algorithms use the same vertex selection method but differ in track selection and fitting techniques. *d0reco* uses a less tighter cut on the impact parameter significance of tracks entering the fitter as compared to *d0root*. Since the $\not\!\!E_T$ and other quantities that depend on the primary vertex are calculated with respect to the *d0reco* vertex, not the *d0root* vertex, the two vertices must be consistent. Therefore, the cut, $|z_{PV}(d0reco) - z_{PV}(d0root)| < 5$ cm, is applied. Finally, both electrons are required to originate from the same primary vertex since the track match depends on the primary vertex position. Hence, a cut on the impact parameter of each electron track with respect to the primary vertex in z is applied: $|\Delta z(e, PV)| < 1$ cm.

	$\epsilon_{data}(Zee)$	$\epsilon_{MC}(Zee)$	scale factor
$z_{PV}\&N_{trk} \geq 3$			
$\mathrm{N_{jet}} \geq 0$	0.971±0.001	0.988±0.000	0.983±0.001
$\mathrm{N_{jet}} \geq 1$	0.990±0.002	0.994±0.001	0.997±0.003
$\mathrm{N_{jet}} \geq 2$	0.997±0.003	0.993±0.003	1.003±0.006
$\Delta z(d0reco, d0root)$			
$\mathrm{N_{jet}} \geq 0$	0.994 ± 0.000	0.996 ± 0.000	0.998 ±0.001
$\mathrm{N_{jet}} \geq 1$	0.998 ± 0.001	0.997 ± 0.001	1.000 ±0.001
$\mathrm{N_{jet}} \geq 2$	0.997 ± 0.003	0.998 ± 0.002	0.999 ±0.005
$\Delta z(PV, e)$			
$\mathrm{N_{jet}} \geq 0$	0.985 ± 0.001	0.998 ± 0.000	0.987±0.001
$\mathrm{N_{jet}} \geq 1$	0.987 ± 0.002	0.999 ± 0.000	0.989±0.003
$\mathrm{N_{jet}} \geq 2$	0.979 ± 0.008	1.000 ± 0.000	0.979±0.008

Table 4.8: Primary vertex cut efficiencies (in %) in Zee data and MC and a scale factor as a function of jet multiplicity. All errors are statistical.

4.6.1 Primary Vertex Cut Efficiencies, and Scale Factors

Table 4.8 lists the vertex cut efficiencies measured in $Z \rightarrow ee$ Monte Carlo and data in terms of jet multiplicity. The Monte Carlo models the data very well for the vertex cuts, and the $Z \rightarrow \mu\mu$ channel shows similar behavior. Therefore, for the sake of simplicity, it was decided that scale factors averaged between the dielectron and dimuon channels would be used for all three dilepton cross section measurements. These scale factors are listed in Table 4.9. Differences are given by systematic errors when they are statistically significant.

	scale factor
$\epsilon^{PV}(\mathrm{N_{jet}} \geq 0)$	$0.981 \pm 0.001(stat)$
$\epsilon^{PV}(\mathrm{N_{jet}} \geq 1, \mathrm{N_{jet}} \geq 2)$	$0.993 \pm 0.002(stat) \pm 0.004(syst)$
$\epsilon^{d0reco,d0root}$	$0.998 \pm 0.001(stat) \pm 0.002(syst)$
$\epsilon^{PV,\ell}$	$0.987 \pm 0.001(stat)$

Table 4.9: Primary vertex scale factors used in the dilepton channels. Statistical errors are taken as the uncorrelated sum of the statistical errors from the dielectron and dimuon samples. Where statistically significant, the differences in efficiencies between $Z \rightarrow ee$ and $Z \rightarrow \mu\mu$ are taken as systematics. This is the case for the primary vertex efficiency in events with one or more jet bin efficiency and for the distance between the $d0reco$ and the $d0root$ primary vertices.

Chapter 5

Measurement of $t\bar{t}$ Production Cross Section

This chapter describes the analysis strategy pursued in the measurement of the top-antitop ($t\bar{t}$) production cross section in proton-antiproton ($p\overline{p}$) collisions at the Tevatron center of mass energy ($\sqrt{s}$) of 1.96 TeV in dielectron decay mode ($p\overline{p} \rightarrow t\bar{t} \rightarrow be^{+}\nu_{e}\bar{b}e^{-}\overline{\nu_{e}}$). The analysis utilizes 384 pb^{-1} of data collected by the Run II upgraded DØ detector and is based on the application of event's kinematic and topological selections to extract the $t\bar{t}$ signal.

5.1 Event Signature and Backgrounds

The experimental signature of the $t\bar{t}$ event decaying through the dielectron channel consists of two high transverse momentum (p_T) electrons, two high p_T jets from the hadronization of b-quarks, and substantial missing transverse energy ($\not{E}_T$) from two undetected neutrinos (ν). Additional jets are often produced from initial-state and final-state radiation. Although the branching fraction for $t\bar{t}$ decaying to dielectron mode is small ($\sim$1.2%), this channel tends

to be relatively cleaner than the *lepton + jets* channels, which have a huge background from $W + jets$ events. It benefits from the fact that there are very few background processes with two isolated, high-p_T electrons. We distinguish two categories of backgrounds: "physics" and "instrumental".

5.1.1 Physics Backgrounds

Physics backgrounds are processes in which the two oppositely charged electrons arise from electroweak boson decays and the $\not\!\!E_T$ originates from high p_T neutrinos. The potential physics backgrounds to the $t\bar{t}$ event signature are:

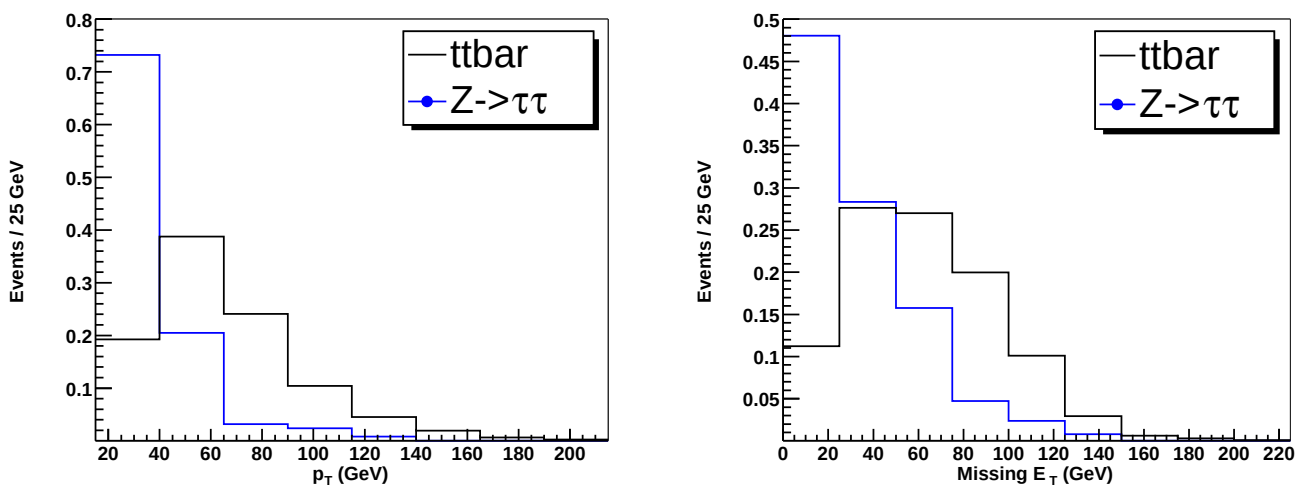

Figure 5.1: Leading electron p_T (left) and $\not\!\!E_T$ (right) distributions in $Z/\gamma^*(\rightarrow \tau^+\tau^- \rightarrow e^+e^-\nu\overline{\nu})+ \geq$2 jets events.

- $Z/\gamma^*(\rightarrow \tau^+\tau^- \rightarrow e^+e^-\nu\overline{\nu})$+jets: The Drell-Yan or Z production processes, resulting in dielectrons and neutrinos through τ decays, resemble the top event signature. Although the Z cross section (σ) is large, requiring two jets in the final state decreases the cross section significantly. Despite a small branching ratio (BR) of τ's to electrons ($\sim$18%), the $\sigma \times BR$ for this process is still large ($\sim$0.1 pb). However, the resulting electron p_T

spectrum is softer than that of electrons in $Z \rightarrow e^+e$ or $t\bar{t} \rightarrow e^+e$ decays (see Figure 5.1). There also tends to be less $\not\!\!E_T$ than in background processes involving W's (see Figure 5.1).

- Diboson production ($WW(\rightarrow e^+e^-\nu\overline{\nu})$+jets) [165]: The WW production cross section is small, but these events are very top-like in electron p_T and $\not\!\!E_T$ (see Figure 5.2). The requirement of two jets in the final state minimizes this process's contribution significantly ($\sigma \times BR$ ~0.03 pb).

- Heavy flavor QCD production: It provides a negligibly small background. Although the $c\bar{c}$ and $b\bar{b}$ cross section are very large, but electrons from these decays are typically soft and non-isolated. There also tends to be little $\not\!\!E_T$.

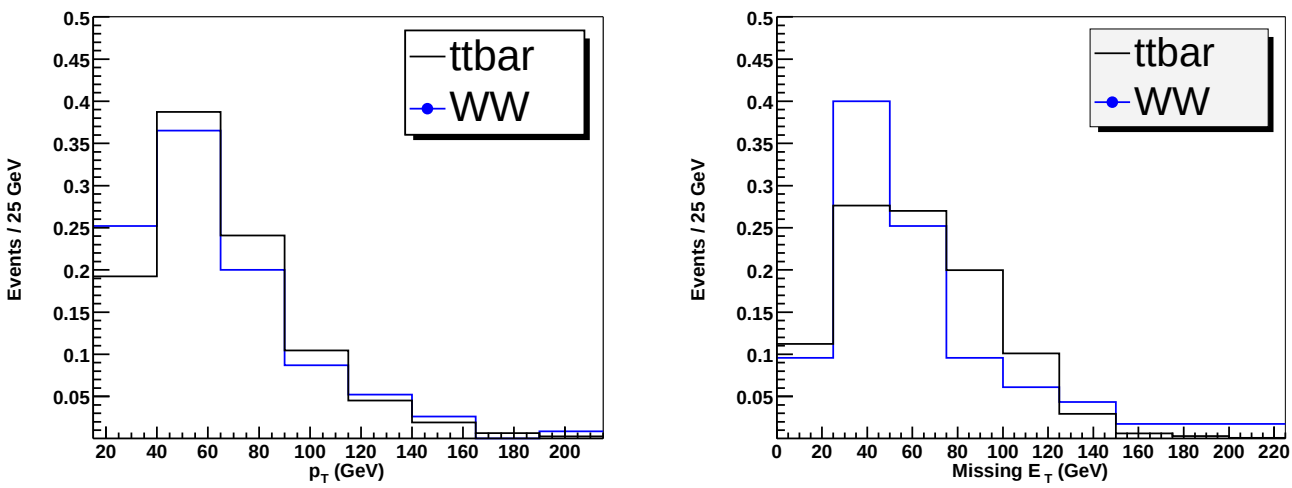

Figure 5.2: Leading electron p_T (left) and $\not\!\!E_T$ (right) distributions in $W^+W^-(\rightarrow e^+e^-\nu\overline{\nu})+ \geq$2 jets events.

5.1.2 Instrumental Backgrounds

There are several backgrounds which arise due to instrumental effects, mainly from the mismeasurement of $\not\!\!E_T$ and misidentication of electrons.

- $Z/\gamma^*(\rightarrow e^+e^-)+$ jets : This process has a large cross section compared to $t\bar{t}$ even when two jets are required. It also has two high p_T electrons in the final state. However, this process produces no significant $\not\!\!E_T$ since no neutrinos are involved. Thus, the occurrence of fake $\not\!\!E_T$ from the resolution effects or noise in the calorimeter can cause $Z/\gamma^* \rightarrow e^+e^-$ events to mimic the top event signature. It is the largest single background in the current dielectron anlysis.

- $W + jets$: This process has a large cross section and significant $\not\!\!E_T$, but a high-p_T jet must fake an isolated electron. The contribution from this background is very small.

- QCD multijet: The cross section for this process is huge. However, two high-p_T jets must fake isolated electrons, and spurious $\not\!\!E_T$ must be produced since jets in these multijet processes should balance. This background actually turns out to be insignificant.

5.2 Event Selection and Optimization

The event selection in this analysis proceeds mainly by directly selecting on the objects which make up the $t\bar{t}$ final state. We require two high p_T electrons, two high p_T jets, and substantial missing E_T in the event. We also consider topological variables to distinguish the topological characteristics of the $t\bar{t}$ events. The variables we utilize are:

- $H_T = \Sigma p_T^{jets}$, which is the scalar sum of the p_T of the jets in the event with $e^+e^-+ \geq 2$ jets.

- $H_T^e = \Sigma p_T^{jets} + p_T^{leadingelectron}$. This variable is particularly effective against $Z \rightarrow \tau\tau$ and fake electron background.

- Sphericity ($\mathcal{S}$): The event's normalized momentum tensor is given by [166]

$$\mathcal{M}_{ij} = \frac{\sum_o p_i^o p_j^o}{\sum_o |\vec{p^o}|^2}, \tag{5.1}$$

where $\vec{p^o}$ is the momentum vector of a reconstructed object o, i and j are cartesian coordinates. It has three eigenvalues $\lambda_1 \geq \lambda_2 \geq \lambda_3$. λ_1 is a measure of the flatness of the momentum tensor ellipsoid; λ_2 is a measure of its width; and λ_3 is a measure of its length. The sphericity $\mathcal{S}$ of an event is defined as $\mathcal{S} = \frac{3}{2}(\lambda_1 + \lambda_2)$, so that $0 \geq \mathcal{S} \geq 1$. Sphericity is essentially a measure of the summed $p\perp^2$ with respect to the event axis. The objects included in the sum are the jets and the electron from the W decay. Large values of $\mathcal{S}$ are indicative of isotropic events. The $t\bar{t}$ events are quite isotropic as is typical for the decay of a heavy object. This variable is effective when we have to disentangle several backgrounds and hence is used in the event selection (see Figure 5.3).

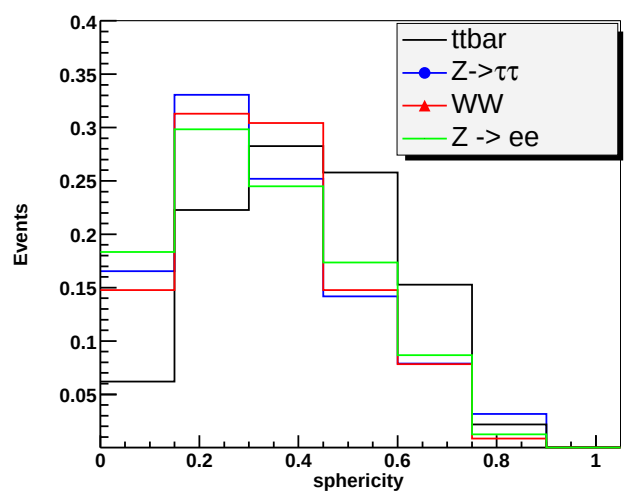

Figure 5.3: Distribution of sphericity in $e^+e^-+ \geq$2 jets events for $t\bar{t}$, WW, $Z \to \tau\tau$ and $Z \to ee$ Monte Carlo samples.

The key strategy in the analysis involves optimization of kinematic and topological selection cuts in order to reject as much background (B) as possible while retaining as much of the signal (S) as possible. We use the optimized event selection criteria from the previous pass of our analysis based on 240 pb^{-1} which is under publication [93]. The cut optimization was done by performing a grid search of possible choices of electron p_T, jet p_T, width of Z mass window, $\not\!\!E_T$ and various topological variables (H_T, H_T^e, sphericity). Optimal cuts are obtained by minimizing $\sqrt{S+B}/S$ as the figure of merit (fom), which is proportional to the relative statistical error on the measured cross section. For similar fom's, S/B and signal efficiency are also used to select the most ideal set of cuts. The details of the cut optimization are discussed in our analysis note [145].

5.2.1 Signal Selection Criteria

We choose the cuts itemized in Table 5.1. We select triggered events demanding two electrons passing tight electron-identification criteria (see section 4.1.2) with $p_T > 15$ GeV. The electrons must be in the central calorimeter (CC:$|\eta_{det}^{e1,2}| < 1.1$) or endcap (EC: $1.5 < |\eta_{det}^{e1,2}| < 2.5$) calorimeter region. The electrons are also required to be oppositely charged and must originate from a good primary vertex (see section 4.5). The sample selected using these requirements is referred to as the "preselected sample".

Since $Z/\gamma^* \rightarrow e^+e^-$ dwarfs the other backgrounds and the signal, this must be the primary background to reject. Cutting concurrently on the $\not\!\!E_T$ as well as dielectron invariant mass (M_{ee}) is a very powerful way to suppress most of the $Z/\gamma^* \rightarrow e^+e^-$ background (though it still remains the largest source of background). Figure 5.4 shows the $\not\!\!E_T$ vs M_{ee} distributions for the signal and backgrounds.

EM Preselection: 2 tight electrons ($e1$,$e2$) with p_T >15GeV ($\lvert\eta^{e1}_{det}\rvert < 1.1$ OR $1.5 < \lvert\eta^{e1}_{det}\rvert < 2.5$) ($\lvert\eta^{e2}_{det}\rvert < 1.1$ OR $1.5 < \lvert\eta^{e2}_{det}\rvert < 2.5$) Opposite charge Primary vertex cuts Dielectron Trigger
+ $p_T^{j1} > 20$ GeV (Leading jet)
+ $p_T^{j2} > 20$ GeV (Next-leading jet)
+ $M_{ee} < 80$ GeV OR $M_{ee} > 100$ GeV
+ $\not\!\!E_T > 40(35)$ GeV when $M_{ee} < 80(> 100) GeV$
+ Sphericity > 0.15

Table 5.1: Event selections in the $t\bar{t} \rightarrow ee$ analysis. "Tight" refers to tight electron identification criteria in section 4.1.2.

Unlike in Run I, this analysis excludes entirely the events in the Z mass window ($80\ GeV < M_{ee} < 100\ GeV$). This is because the observed $\not\!\!E_T$ fake rate is considerably higher than in Run I due to worse jet (and electron) energy resolutions which widen the $\not\!\!E_T$ distribution. Although the electrons and the Z mass are fairly well resolved and understood, the increased width and tails in the $\not\!\!E_T$ distribution make it quite common for a Z event to have high $\not\!\!E_T$. Hence, to obtain reasonable background levels, $\not\!\!E_T$ cut is not applied in the Z mass window, but , rather the resonance has been removed entirely for now.

In addition, this analysis considers using different $\not\!\!E_T$ cuts below and above the Z mass window. The $\not\!\!E_T$ is required to be at least 40 GeV below the Z window and 35 GeV above the Z window. The motivation for the asymmetrical cut on $\not\!\!E_T$ is to suppress severely the $Z/\gamma^* \rightarrow \tau^+\tau^- \rightarrow e^+e^-$ background which lies mainly in the low mass region (see Figure 5.4).

Also, to further reject background, at least two jets with $p_T > 20$ GeV are required. Finally, a cut on the sphericity of the event ($\mathcal{S} > 0.15$) is applied in order to take advantage of the topological peculiarities of $t\bar{t}$ events and gain even more discrimination between signal and background. This requirement rejects

events in which jets are produced in a planar geometry due to gluon radiation. Signal acceptances, efficiencies and the expected $t\bar{t}$ contribution are derived from the $t\bar{t} \rightarrow l^+l^-$ Monte Carlo (MC) sample with m_t=175 GeV. The contributions from physics backgrounds are extracted from the respective MC samples. However, the contribution from instrumental backgrounds are obtained from data because the MC does not reproduce all the features in the data accurately.

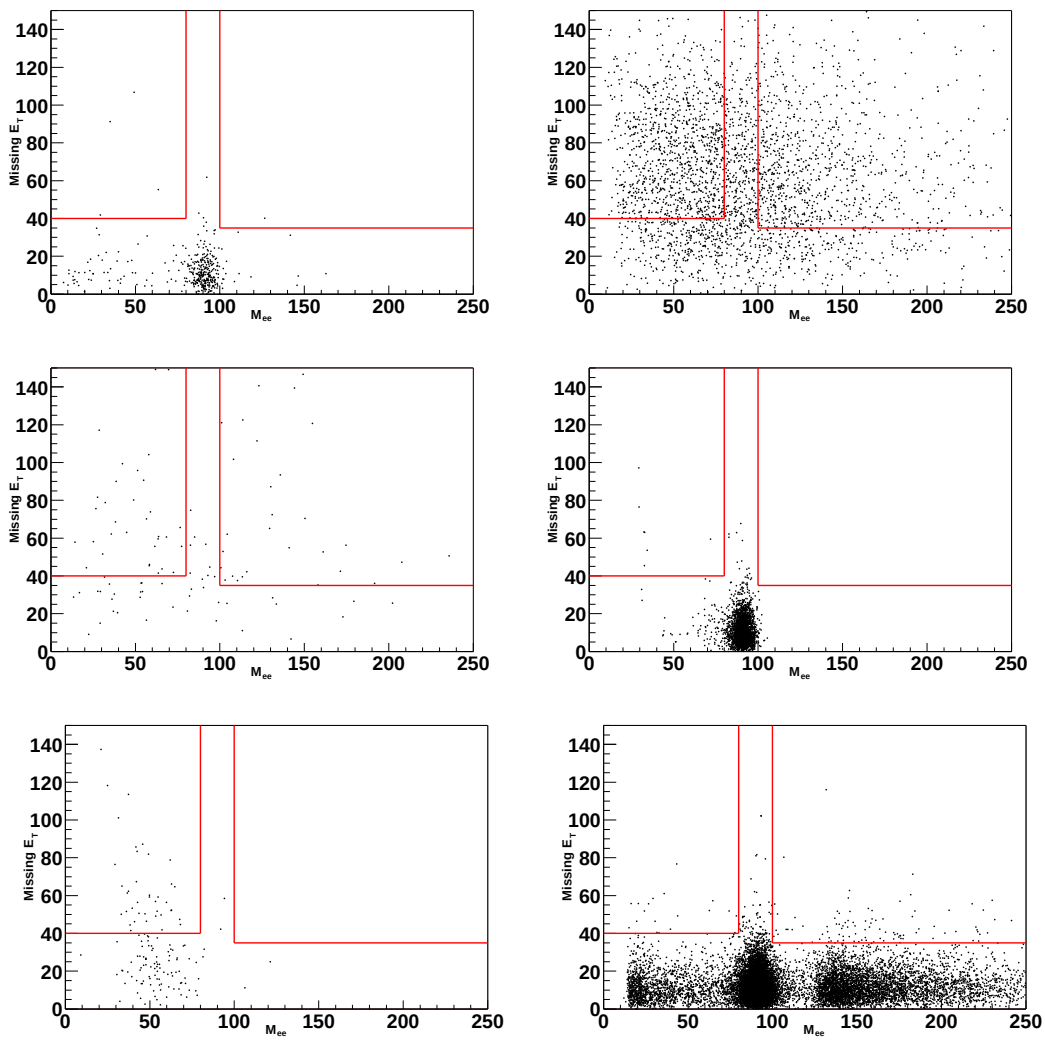

Figure 5.4: $\not\!\!E_T$ vs. invariant mass of the two electrons in the event. The distributions are shown after requiring two tight electrons and 2 jet cuts for: data (top left), top (top right), WW (middle left), WZ (middle right), $Z \rightarrow \tau\tau$ (bottom left), and $Z \rightarrow ee + 2$ jets Alpgen Monte Carlo. Also shown is the applied cut on $\not\!\!E_T$ vs electron invariant mass.

Category	Cut	Efficiency	Total Efficiency
Electrons	Reco,EM Acc, ID, p_T >15GeV	0.414±0.004	0.414±0.004
	Assoc. Track Match	0.853±0.004	0.353±0.004
	Likelihood> 0.85	0.822±0.005	0.291±0.004
	Opposite Sign	0.995±0.001	0.289±0.004
	$\kappa_{reco+id}$	0.965	0.279±0.003
	$\kappa_{trk+lhood}$	0.792	0.221±0.002
	κ_{sign}	0.991±0.001	0.219±0.002
Trigger		0.940±0.004	0.206±0.002
Jets	≥ 1 jet ($p_T > 20$ GeV)	0.965±0.003	0.198±0.002
	≥ 2 jets, ($p_T > 20$ GeV)	0.695±0.007	0.138±0.002
Vertex	$\lvert z_{PV}\rvert < 60$ cm, $N_{trk} > 2$	0.992	0.137±0.002
	$\Delta z(d0reco, d0root) < 5$cm	0.999	0.137±0.002
	$\Delta z(e, PV) < 1$ cm	1.000	0.137±0.002
	κ_{vtx}	0.984	0.134±0.002
M_z cut	$M_{ee} < 80$ GeV or $M_{ee} > 100$ GeV	0.855±0.006	0.115±0.002
$\not{E}_T$	$\not{E}_T > 40(35)$, $M_{ee} < 80(> 100)$	0.762±0.008	0.086±0.002
Topological	$Sphericity > 0.15$	0.936±0.005	**0.082±0.002**

Table 5.2: Efficiencies of object identification and kinematic selection on $t\bar{t} \rightarrow ee$ Monte Carlo.. The efficiency is computed with respect to $t\bar{t} \rightarrow ee$ events where both electrons are allowed to come from either $W \rightarrow e$ or $W \rightarrow \tau \rightarrow e$. The scale factors for which systematic and statistical errors are correlated among channels are given without errors, and their uncertainties are instead included in the section 5.8.

5.3 $t\bar{t}$ Event Selection Efficiencies

The final selection criteria is applied to the $t\bar{t}$ Monte Carlo in order to obtain the efficiencies at the different levels of selection as well as the overall efficiency for signal. The efficiency breakdown is summarized in Table 5.2. These efficiencies are calculated for electrons originating either from direct decays of the W or from W decays to τ where the τ then decays to e.

Since Monte Carlo detector simulation does not reproduce all features of the data, we apply correction factors to account for differences in efficiency between data and Monte Carlo as discussed in section 4.2.6. Since electrons are found to have different efficiencies and corresponding correction factors in the CC and

Cut	κ_{CCCC}	κ_{CCEC}	κ_{ECEC}
Cluster selection, EM ID	0.992 ± 0.000	0.872 ± 0.000	0.767 ± 0.000
Track Match, Likelihood	0.821 ± 0.000	0.682 ± 0.000	0.567 ± 0.000
Opposite sign	0.998 ± 0.001	0.965 ± 0.003	0.919 ± 0.012
Vertex	0.984 ± 0.003	0.984 ± 0.003	0.984 ± 0.003

Table 5.3: Summary of the correction factors relating Monte Carlo and data efficiencies. Errors are statistical only.

EC, the appropriate factors for dielectron final state are applied depending on whether the event has two electrons in the CC (CCCC), one in the CC and one in the EC (CCEC), or both in the EC (ECEC). These scale factors are given in Table 5.3. The scale factors shown in Table 5.2 are derived from the ones in Table 5.3 by weighting according to the number of events in each region; that is,

$$\kappa_w = \frac{\kappa_{CCCC} N_{CCCC} + \kappa_{CCEC} N_{CCEC} + \kappa_{ECEC} N_{ECEC}}{N_{CCCC} + N_{CCEC} + N_{ECEC}}$$

where N_{CCCC}, N_{CCEC}, and N_{ECEC} are the numbers of events in $t\bar{t}$ Monte Carlo with two electrons in the CC, one in the CC and one in the EC and both in the EC respectively.

The total signal efficiency obtained by multiplying all the efficiencies and scale factors listed in Table 5.2, is

$$\epsilon_{top} = 0.082 \pm 0.002(\text{stat})^{+0.012}_{-0.044}(\text{syst}).$$

The biggest drop in efficiency occurs at the first level of selection. This inefficiency results mainly from inefficient electron reconstruction and from limiting the acceptance to only CC and EC electrons. The 15 GeV cut also removes many of the events involving τ decays, since electrons produced in τ decays tend to be softer than those from W's decays. Requring a second jet with p_T above 20 GeV and the cutting hard on $\not\!\!E_T$ are two other large inefficiencies;

however, these cuts are required to keep the background in check. The $\not\!\!E_T$ cut is considerably harsher than the comparable cut in Run I; however, the $\not\!\!E_T$ resolution is considerably worse in Run II requiring a stiffer cut.

Using a $t\bar{t}$ cross section of 7 pb and a branching fraction of 0.01584 (accounting for the decays involving $W \to \tau \to e$ and using the latest particle data group (PDG) numbers [70]), the expected event yield is $3.49^{+0.35}_{-0.40}(\text{stat} + \text{syst})$ events. The breakdown of the systematic uncertainties on the signal efficiency is presented in section 5.8.

5.4 Estimation of Physics Backgrounds

The two main physics backgrounds in the dielectron channel arise from $WW \to e^+e^-$ and $Z \to \tau^+\tau^-$, where both τ's decay to electrons. Both of these have two high p_T electrons and significant $\not\!\!E_T$; however, the fraction of time they are produced with two jets is small. The contributions from both of these backgrounds are obtained from Monte Carlo (MC) just as the expected yield for signal was obtained.

5.4.1 $Z/\gamma^* \to \tau^+\tau^-$

The $Z/\gamma^* \to \tau^+\tau^-$ background contribution is estimated using Alpgen $Z/\gamma^*(\to \tau^+\tau^-)$jj MC sample. In terms of Monte Carlo to data scale factors and object smearing it is evaluated in the same way as the expected signal contribution. However, in a sample of $(Z \to ee)jj$ Monte Carlo generated with the same settings, the predicted yield does not match the observation because the jet p_T spectrum of the Monte Carlo sample is softer than the p_T spectrum of jets in the data. Therefore, a correction factor is obtained which normalizes the

expected number of $(Z \to ee)jj$ events to the number of observed $(Z \to ee)jj$ events in a Z mass window ($80 < M_{ee} < 100$ GeV). This correction factor, called K_Z factor, comes out to be 1.117 ± 0.083 (for details, see our analysis note [169]). The correction factor remains stable when the window is widened to $75 < M_{ee} < 105$ GeV. This K_Z factor is then applied to the background prediction from $Z/\gamma^*(\to \tau^+\tau^-)$jj MC sample. The predicted yield after all selections and this correction is $0.30^{+0.10}_{-0.14}$ (stat+syst) events. The statistical uncertainty on the K_Z factor is taken as a systematic uncertainty on the Z background prediction and is labeled "Normalisation" in the table of systematics given in section 5.8.

5.4.2 Diboson production (WW, WZ)

The WW background is estimated using a $WWjj$ Alpgen sample. The expected contribution is obtained in the same way as the signal expectation. Monte Carlo to data scale factors are applied in the same way as for the signal prediction. The expected number of WW events is scaled up by 35% to account for the difference in the MC and theoretical NLO cross sections [170], and a 35% systematic is applied to account for this discrepancy. The total expected event yield from this background is then $0.19 \pm 0.07(stat)$ events.

The contribution from WZ is taken into account using a $WZ \to jjll$ MC sample. This sample, in which the W decays to jets, does contribute before the Z mass window cut. In fact, this is a larger source of background than WW at the one and two jet cut levels because the branching fraction of $W \to jj$ is about six times higher than the branching fraction of $W \to e\nu$. In addition, WZ does not need to be produced with extra jets in this decay channel unlike in WW since the W decays to two high p_T jets. The Z mass cut removes nearly most of this background, making it insignificant after all cuts. The total expected event

Cut	WW	$WZ \to jjll$	Total
$N_{ele}^{p_T>15} \geq 2$	12.14±0.14	8.00±0.09	20.14±0.16
$N_{jets}^{p_T>20} \geq 1$	0.80±0.04	7.27±0.09	8.07±0.10
$N_{jets}^{p_T>20} \geq 2$	0.38±0.14	3.54±0.07	3.92±0.15
M_Z Cut	0.33±0.12	0.15±0.01	0.48±0.12
$\not\!\!E_T$ Cut	0.24±0.09	0.009±0.004	0.25±0.09
Sphericity	0.195±0.07	0.007±0.004	0.20±0.07

Table 5.4: Predicted diboson backgrounds at each cut level. Errors are statistical only.

yield from the diboson backgrounds is $0.20 \pm 0.07(stat)$ events. The breakdown of the diboson backgrounds at each cut level can be seen in Table 5.4.

5.5 Instrumental Backgrounds : Fake $\not\!\!E_T$

The key background to reject in the dielectron analysis is $Z/\gamma^* \to ee$ + fake $\not\!\!E_T$. Direct Z/γ^* decays to dielectrons produce no neutrinos, and therefore no real $\not\!\!E_T$. However, these events can occur with sufficient $\not\!\!E_T$ and pass the selection criteria for several reasons: (a) single object energy resolutions are finite and worse than originally expected, (b) presence of hot cells in the calorimeter or malfunctioning of readout towers can produce a spurious excess or deficit of energy, (c) large scale failures of the calorimeter readout chain can cause the precision readout to generate large positive (or negative) energies unrelated to physics, and (d) the unreconstructed portion of an event from soft gluons and other low energy deposition is not modelled well in the default Monte Carlo.

None of these effects are reliably simulated in the Monte Carlo; hence this background is estimated from the data. This background has proved to be the most difficult to understand and reject. Considerable effort has been devoted to : 1) substantial clean-up of the high, non-Gaussian $\not\!\!E_T$ tail in the data , 2) more accurate modelling of the $\not\!\!E_T$ and $\not\!\!E_T$ fake rate in Monte Carlo, and 3)

selection of improved non-signal data samples to more accurately describe the $\not\!\!E_T$ behavior of the dielectron signal sample. Please refer to our DØ notes [158] [136] [159]. focussed on detailed description of these studies.

The fake $\not\!\!E_T$ background can also originate from QCD multijet events, where two jets are misidentified as electrons coupled with fake $\not\!\!E_T$. We estimate the above two backgrounds together in data since these instrumental effects are not well described by the simulation.

5.5.1 Method

Estimating the $\not\!\!E_T$ fake background involves two steps. First, we apply the tight electron selection in the data and count the number of $e^+e^- + \geq 2$ jets events below the $\not\!\!E_T$ cut in each of the mass regions ($M_{ee} < 80$ GeV and $M_{ee} > 100$ GeV) since what lies below is dominated by Z/γ^* and QCD multijet background. The number of dielectron events which fail our $\not\!\!E_T$ selection in the low and high M_{ee} bins are referred to as $N_{tight}^{M_{ee}<80}$ and $N_{tight}^{M_{ee}>100}$, respectively. Second, we determine the $\not\!\!E_T$ fake rate, $f_{\not\!\!E_T}$, from a sample which does not contain signal or physics backgrounds. This fake rate expresses a correspondence between the number of observed events that would fail and that would pass the $\not\!\!E_T$ selection. We select single photon sample and $f_{\not\!\!E_T}$ is calculated as the number of events that fall above the $\not\!\!E_T$ cut, $N_\gamma^{\not\!\!E_T>35,40}$, divided by those below the $\not\!\!E_T$ cut, $N_\gamma^{\not\!\!E_T<35,40}$,

$$f_{\not\!\!E_T} = \frac{N_\gamma^{\not\!\!E_T>35,40}}{N_\gamma^{\not\!\!E_T<35,40}} \tag{5.2}$$

Then the number of expected $\not\!\!E_T$ background events summed over the low and high M_{ee} regions is,

$$N_{Z/\gamma^*,QCD} = N_{Tight}^{M_{ee}<80} \times f_{\not\!\!E_T}(40\ GeV) + N_{Tight}^{M_{ee}>100} \times f_{\not\!\!E_T}(35\ GeV) \qquad (5.3)$$

Because this analysis is sensitive to our understanding of the $\not\!\!E_T$ in Z events, we have pursued a multi-prong approach for quantifying the $f_{\not\!\!E_T}$. It is important to obtain samples which have no $t\bar{t}$ or physics background (i.e. with real $\not\!\!E_T$) component. Such samples need to be similar in terms of kinematics and resolutions to the Z/γ^* events to be rejected. The kinematic similarities must particularly be present for the jets since jets have a major impact on the $\not\!\!E_T$ resolution. We need a complete model which details the entire $\not\!\!E_T$ spectrum that would be observed in a pure sample of Z + 2 jets events. This entails a description of the core Gaussian resolution, as well as any extended tails that would occur in the data. Extensive study has been done to determine such a sample, namely, single photon + jets sample, and the details can be found in our DØ note [145].

5.5.2 $\not\!\!E_T$ and $\not\!\!E_T$ Fake Rates

We examine the $\not\!\!E_T$ behavior in three samples:

- $Z \rightarrow ee + 2$ jet data sample: This is the signal sample also called "tight" sample, used to estimate number of Z/γ^*+ QCD low $\not\!\!E_T$ events, N_{Tight}. We apply our signal trigger selection, full electron identification cuts, calorimeter and vertex event quality cuts, and kinematic selections on additional jets. This selection produces a sample highly pure in $Z \rightarrow ee$ events. This is the sample we wish to describe in the $\not\!\!E_T$ regime where signal,

or physics backgrounds, are negligible. For most purposes, this is for $\not\!\!E_T$ below approximately 25 GeV.

- Single photon + jets sample : It has no signal or physics backgrounds, and is used to obtain $\not\!\!E_T$ fake rate, $f_{\not\!\!E_T}$. It is selected using single photon or electron triggers and all other kinematic cuts are the same. The photons are basically electromagnetic clusters with no track matched in a 0.05×0.05 road and no likelihood cut applied. These photons could then be real photons or QCD multijet processes where jets fake photons.

- $Z \rightarrow ee$ + 2 jets Alpgen MC sample : We apply exactly the same $Z \rightarrow ee$ event selection criteria. This sample is used to validate understanding of tight and single photon $\not\!\!E_T$ distributions. The addition of the Monte Carlo for comparisons allows us, at the very least, to make statements about the core $\not\!\!E_T$ resolution that is valid in the tight sample since then both data and Monte Carlo will essentially be Z samples. Comparison with the data samples described earlier may also permit some statement about whether we understand any high $\not\!\!E_T$ tail observed in the data. As described in our DØ note and section 4.4.4, we have attempted to provide a more accurate description of the core $\not\!\!E_T$ resolution in the Monte Carlo, by applying "$\not\!\!E_T$ oversmearing" beyond the electron and jet energy resolution oversmearings. We have found that by applying the $\not\!\!E_T$ smearing to the $Z(\rightarrow ee)jj$ MC sample, a reasonable agreement between data and MC can be obtained for the $\not\!\!E_T$ distribution. Thus, the MC can be used as a cross check to the $f_{\not\!\!E_T}$ estimate in data.

Figure 5.5 shows the $\not\!\!E_T$ distributions for the three samples. We can see that single photon sample and $\not\!\!E_T$ oversmeared MC provide reasonable description of the $\not\!\!E_T$ distribution in data. The apparent excess of high $\not\!\!E_T$ events in data over that suggested by the MC is not statistically significant. We conclude that

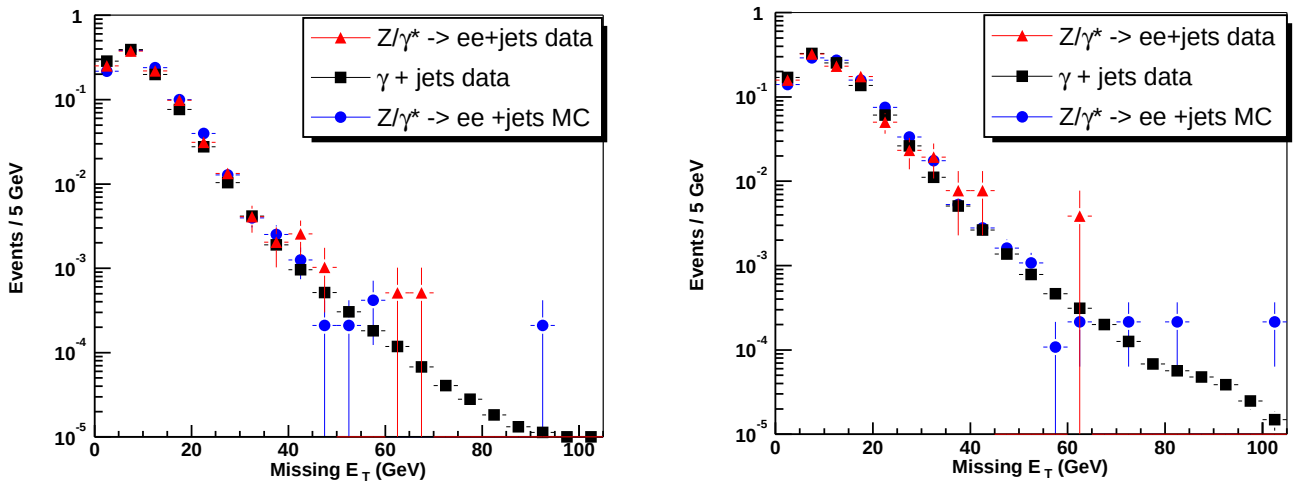

Figure 5.5: $\not\!\!E_T$ distributions for single photon, tight dielectron, and $Z \rightarrow ee$ Alpgen Monte Carlo samples with all cuts applied. The 1 jet case is on the left and ≥ 2 jet case on the right.

the MC provides a reasonable description of the data, although we will require a higher statistics data sample with no signal present for the calculation of $f_{\not\!\!E_T}$. Fig. 5.5 also shows the $\not\!\!E_T$ distributions in Z+1 jet data sample, single photon sample and Z+1 jet Alpgen MC sample; and we arrive at the similar conclusion.

The $f_{\not\!\!E_T}$ fake rate as a function of $\not\!\!E_T$ cut is presented in Figure 5.6 for the three samples for two jet multiplicities – 1 jet and $\geq$2 jets. It can be seen that the $\not\!\!E_T$ fake rate distributions of the tight dielectron data sample, $Z \rightarrow ee$ Monte Carlo sample, and single photon sample all agree. Clearly, the single photon and $Z \rightarrow ee$ MC samples describe the $\not\!\!E_T$ of the Z sample very well in the two jet case, which is what is needed for this analysis. Table 5.5 indicates the fake probabilities for the three samples for 35 and 40 GeV cuts.

The fake rate in the Monte Carlo for the 2 jet cut is found to be within the statistical uncertainty of the fake rate for the 2 jet plus sphericity cut. Because we cannot calculate a sphericity in the single photon sample which is not on the same footing as that in a 2 electron sample, we use the 2 jet fake rate

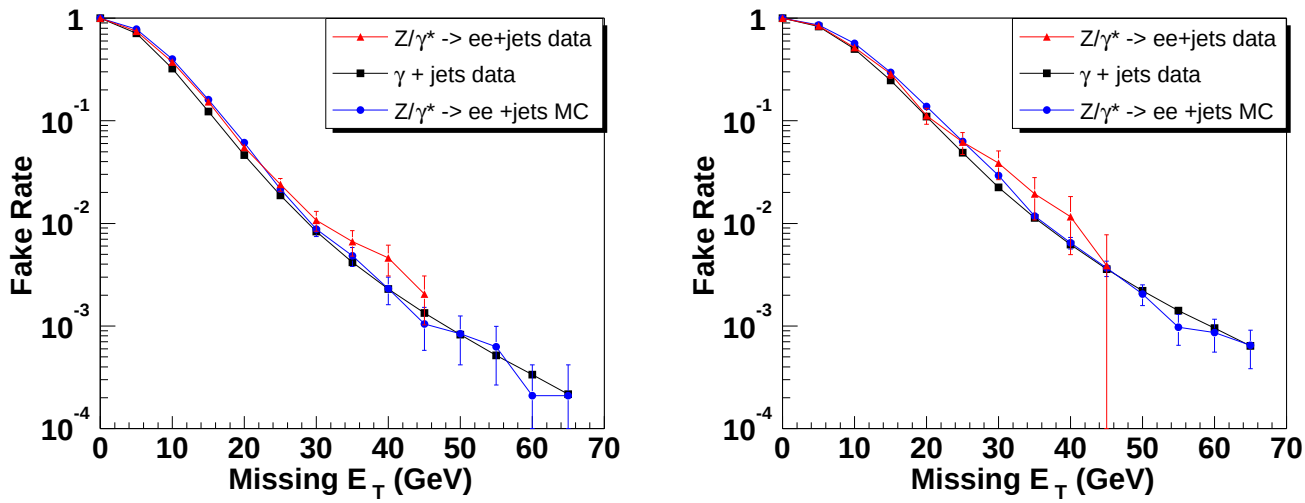

Figure 5.6: $\not\!\!E_T$ fake rates for single photon, tight dielectron, $Z \rightarrow ee$ Alpgen Monte Carlo samples with all cuts applied. The 1 jet case is on the left and ≥ 2 jet case on the right.

for this analysis. Several trends are apparent in these plots. First, agreement between all samples is improved as the jet multiplicity rises, presumably due to the $\not\!\!E_T$ resolution becoming dominated by the jet resolution. Second, the photon sample is in good agreement with the tight sample in the 2 jet bin. We use the $f_{\not\!\!E_T}$ rate from the high statistics single photon sample to estimate the $\not\!\!E_T$ fake background. Also, the background contribution derived using the $\not\!\!E_T$ fake rate from the MC sample provides a nice cross check.

Background Yield

Table 5.5 lists the measured fate rates for the different samples for $\not\!\!E_T$ thresholds of 35 GeV and 40 GeV. Now that the $\not\!\!E_T$ fake rate has been determined, the number of $\not\!\!E_T$ fakes can be estimated. In order to obtain this estimate, the number of events passing all cuts except the $\not\!\!E_T$ cut in the low and high mass bins in the tight dielectron sample, designated $N_{tight}^{M_{ee}<80}$ and $N_{tight}^{M_{ee}>100}$, respectively, must be obtained. Then, the expected fake $\not\!\!E_T$ background is calculated

	$\not{E}_T > 35$ GeV	$\not{E}_T > 40$ GeV
Tight:		
= 1 jet	0.0065±0.0017	0.0046±0.0015
≥ 2 jet	0.0179±0.0079	0.0107±0.0062
Single Photon:		
= 1 jet	0.0042±0.00002	0.0023±0.00002
≥ 2 jet	0.0113±0.0001	0.0062±0.0001
Z + 2 jet Monte Carlo		
= 1 jet	0.0048±0.0010	0.0023±0.0007
≥ 2 jet	0.0117±0.0011	0.0065±0.0008

Table 5.5: $\not{E}_T$ fake rates measured in the tight sample, in the single photon sample and in Alpgen Z+1 jet and Z+2jet Monte Carlo.

	$M_{ee} < 80$ GeV		$M_{ee} > 100$ GeV	
Cut	$f_{\not{E}_T}^{>40}$	$N_{tight}^{b_{M<75}}$	$f_{\not{E}_T}^{>35}$	$N_{tight}^{b_{M>100}}$
$N_{jets}^{p_T>20} \geq 2 + M_{ee}$+$\not{E}_T$ cuts	0.0062 ± 0.0001	66	0.0113 ± 0.0001	17
Sphericity>0.15	0.0062 ± 0.0001	53	0.0113 ± 0.0001	12

Table 5.6: $\not{E}_T$ fake ratios, numbers of tight events below the $\not{E}_T$ cut, and total expected $\not{E}_T$ fakes for the last two cut levels.

using eqn. 5.3. Table 5.6 gives the fake ratios and numbers of tight events below the $\not{E}_T$ cut ($N_{tight}^{M_{ee}<80}$ and $N_{tight}^{M_{ee}>100}$) for several kinematic and topological requirements in the cut progression. The $\not{E}_T$ fake yield for the last two levels of selection (see Table 5.5) are 0.60 ± 0.16(stat) and 0.46 ± 0.15(stat) events.

The N_{Tight} taken from the data sample might have the contribution from the signal and physics backgrounds. Table 5.7 shows the contribution from signal and backgrounds to N_{Tight} in the two mass bins. This contribution is subtracted

	$M_{ee} < 80$ GeV	$M_{ee} > 100$ GeV
Cut	$t\bar{t}$+WW+$Z \rightarrow \tau\tau$	$t\bar{t}$+WW+$Z \rightarrow \tau\tau$
$N_{jets}^{p_T>20} \geq 2 + M_{ee}$+$\not{E}_T$ cuts	0.57+0.75+0.73=1.47	0.45+0.06+0=0.51
Sphericity>0.15	0.54+0.14+0.60=1.28	0.44+0.05+0=0.49

Table 5.7: Signal and physics backgrounds contribution to N_{Tight} for the last two cut levels.

from the N_{Tight} used in two mass bins and $\not\!\!E_T$ fakes are corrected. After this correction, the $\not\!\!E_T$ fakes contribution at the final level of selection is

$$N_{Z/\gamma*,QCD} = 0.45 \pm 0.15 \text{ events.}$$

Since the Monte Carlo and data $\not\!\!E_T$ agree very well, the Z + 2 jet Alpgen sample is used to cross-check this result. Using the procedure for calculating the signal expectation, the Z + 2 jet Monte Carlo gives an expectation of 0.61 ± 0.19(stat) and 0.47 ± 0.17(stat) for the last two lines of Table 5.6 respectively. These expectations are fully consistent with the estimates from data. Since these agree so well, we do not apply a systematic uncertainty to this background estimate.

5.6 Instrumental Backgrounds : Fake Electron

The second instrumental background arises from multijet processes where one or more jets fragment or shower such that they appear electron-like, or a direct photon acquires a track and appears electron-like. For instance, W+jets, can contribute to this effect when a high p_T jet fakes an isolated high p_T electron. We calculate this background by first obtaining an electron fake rate, f_e, which gives the probability that an energy cluster in the calorimeter exhibiting most of its energy in electromagnetic layers (EM object) passes our tight electron selection. This fake rate is derived from a sample devoid of real electrons. We then apply this probability to a signal sample in which only one of the two electrons is required to be tight (a "loose-tight" sample). In this way, we are able to predict how many of these events would appear to have two tight electrons.

5.6.1 Electron Fake Rates

The electron fake rate, f_e, is defined as the fraction of loose electrons which survive when tight electron identification criteria are applied. That is,

$$f_e = \frac{N_{tight}}{N_{loose}}.$$

This probability is measured in a data sample with two loose EM objects and selected using the signal triggers. Certain conditions must be applied in order to remove electrons from real physics objects in the sample, which would bias f_e. Events with $\not\!\!E_T$ <15 GeV are selected in order to remove Ws from the sample. Since there are two loose electrons in these events, we omit cases where invariant mass of the objects falls between 75 GeV and 105 GeV in order to remove the Z resonance. Moreover, a loose electron is considered only if the other one in the event has no track in a 0.05×0.05 road in $\eta \times \phi$ ($P(\chi^2_{trk}) < 0.0$). This requirement removes $Z/\gamma^* \rightarrow ee$ events, which would contaminate the sample with real electrons from Drell-Yan production.

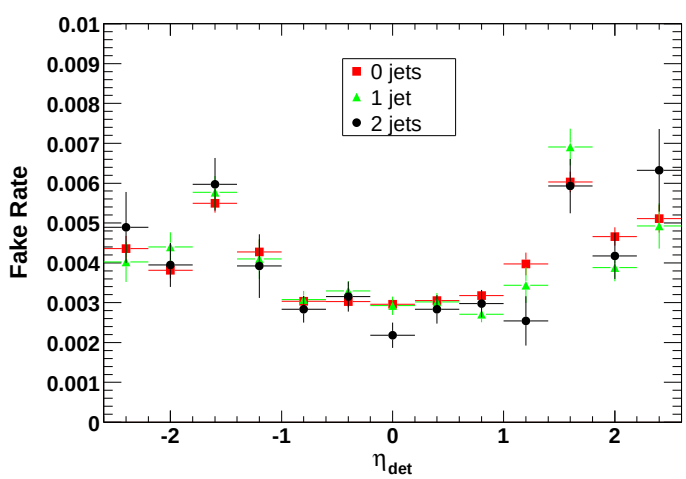

Figure 5.7: Electron fake rate, f_e, as a function of η_{det} for different jet multiplicities.

Number of Jets	f_e^{CC}	f_e^{EC}
0	0.0032 ± 0.0001	0.0050 ± 0.0001
1	0.0032 ± 0.0001	0.0051 ± 0.0002
≥ 2	0.0031 ± 0.0002	0.0050 ± 0.0003

Table 5.8: Electron fake rate f_e for different jet multiplicities.

Figure 5.7 shows the electron fake rate, f_e, as a function of η_{det} for different jet multiplicities and indicates that the η_{det} distributions and f_e of fake electrons are independent of jet multiplicity. This claim is further illustrated by Table 5.8, in which the average fake rates in the CC and EC for different jet multiplicities are shown.

The fake rates for different jet multiplicities as a function of p_T appear in Figure 5.8. Since f_e appears to be flat with η_{det} within a cryostat, and independent of

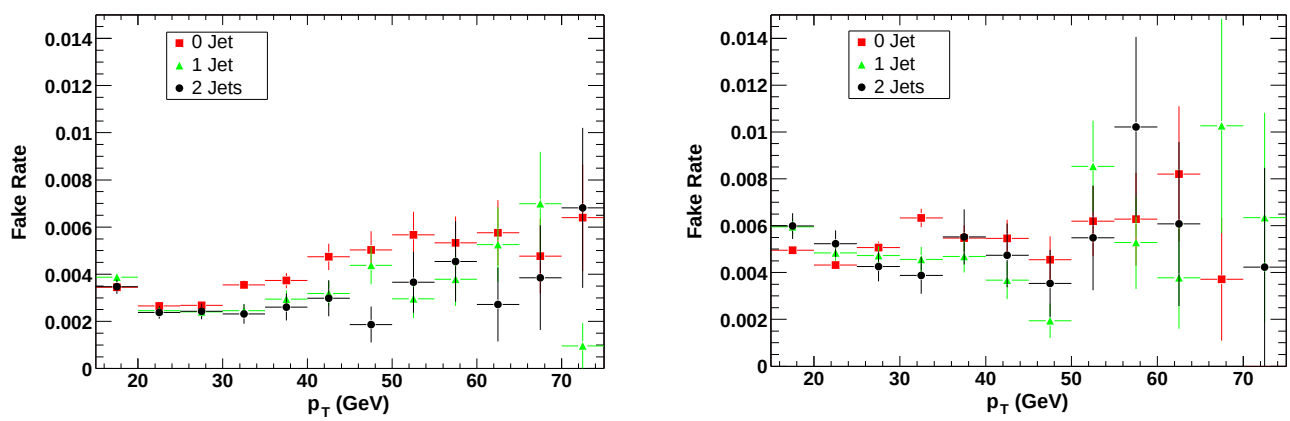

Figure 5.8: Electron fake rate f_e as a function of p_T for different jet multiplicities. The plot on the left shows CC electrons while the one on the right shows EC electrons.

the number of jets or electron p_T, we utilize the the CC and EC average fake rates for the two jet bin in Table 5.8 for this analysis. Since the electrons in the signal events are required to be oppositely-charged, fake rates for positrons and electrons can be obtained using the charge distributions of tight electrons. We find that there are equal numbers of positively and negatively charged ob-

Cut	CC	EC
$N_{EM} > 1$	18810	8393
$N_{jets} > 0$	3474	1343
$N_{jets} > 1$	566	194
M_Z	501	176
$\not\!\!E_T$	55	15
Sphericity	45	11

Table 5.9: Numbers of events in data with one tight and one loose electron, N_{lt}, passing the progression of cuts listed.

jects. The deviation from equal numbers of events is 0.6 %, which is taken as a systematic error on the fake rate. Thus, the fake rate is halved for a loose electron to fake a tight electron of a given sign. That is,

$$f_{em}^{+} = f_{em}^{-} = \frac{f_{em}}{2} \tag{5.4}$$

Then,

$$f_{em}^{CC\pm} = 0.00155 \pm 0.0001 \text{ and } f_{em}^{EC\pm} = 0.00250 \pm 0.00015 \tag{5.5}$$

5.6.2 Background Yield

To estimate the fake electron background yield, we select events in which there are loose electrons, one of which is further required to be a tight electron. The number of 'loose-tight' events which pass all of the other selection criteria, N_{lt}, in the CC and EC separately are then multiplied by the corresponding $f_{em}^{\pm}$ to obtain the expected number of fakes:,

$$N_{WQCD} = N_{lt}^{CC} f_{em}^{CC\pm} + N_{lt}^{EC} f_{em}^{EC\pm}.$$

Table 5.9 gives the numbers of 'loose-tight' events at different levels of the cut progression. After all cuts are applied, 0.096 ± 0.033 events are expected.

Cut	CCCC	CCEC	ECEC
$\not\!\!E_T$	468	342	79
Sphericity	333	219	52

Table 5.10: Numbers of events in data with two loose electrons, N_{ll}, passing the progression of cuts listed.

It should be noted that N_{WQCD} contains the QCD multijet background as well since this background has two jets faking as electrons. That is, the tight electron in the 'loose-tight' sample may actually be a fake electron from a jet. Since this QCD multijet background was counted along with the fake $\not\!\!E_T$ background obtained from the data, this contribution must be removed from the fake electron background yield estimate to avoid double counting. To do this, the number of events with two loose electrons which pass other selection criteria, N_{ll}, is counted, separating the events into CCCC, CCEC, and ECEC events. These numbers are multiplied by the respective EM fake rates $f_{em} f_{em}^{\pm}$ to evaluate QCD contribution:

$$N_{QCD} = N_{ll}^{CCCC} f_{em}^{CC} f_{em}^{CC\pm} + N_{ll}^{CCEC} f_{em}^{CC} f_{em}^{EC\pm} + N_{ll}^{ECEC} f_{em}^{EC} f_{em}^{EC\pm}.$$

Table 5.10 gives the numbers of 'loose-loose' events in data. This yields 0.0038±0.0007 QCD events. It can be seen that the QCD multijet contribution turns out to be negligible. The total number of background events from fake electron is thus

$$N_{efake} = N_{WQCD} - N_{QCD} = 0.092 \pm 0.033.$$

Selection Cut	EM fakes	$Z \to ee, \not{E}_T$ fakes	$Z \to \tau\overline{\tau}$	WW/WZ	$t\bar{t}$
$N_{ele}^{p_T>15} \geq 2$	51.1 $\pm$1.6	25531^{+2522}_{-2669}	$76^{+9.6}_{-15.5}$	$20.14^{+1.55}_{-2.17}$	$8.56^{+0.66}_{-0.80}$
$N_{jets}^{p_T>20} \geq 1$	9.03$\pm$0.57	2644^{+464}_{-434}	$8.59^{+1.61}_{-2.16}$	$8.07^{+0.65}_{-2.26}$	$8.26^{+0.65}_{-0.77}$
$N_{jets}^{p_T>20} \geq 2$	1.33$\pm$0.16	$357.4^{-67.55}_{-67.5}$	$1.19^{+0.24}_{-0.40}$	$3.92^{+0.45}_{-1.14}$	$5.72^{+0.55}_{-0.56}$
M_Z Cut	1.19$\pm$0.14	$84^{+16.5}_{-19.9}$	$1.17^{+0.23}_{-0.38}$	$0.48^{+0.21}_{-0.31}$	$4.89^{+0.46}_{-0.52}$
$\not{E}_T$ Cut	0.12$\pm$0.04	0.59$\pm$0.16	$0.35^{+0.11}_{-0.14}$	$0.25^{+0.13}_{-0.18}$	$3.73^{+0.37}_{-0.43}$
Sphericity	0.09$\pm$0.03	0.45$\pm$0.15	$0.30^{+0.10}_{-0.14}$	$0.20^{+0.11}_{-0.15}$	$3.49^{+0.35}_{-0.40}$

Table 5.11: Expected signal and different backgrounds at each level of selection. Errors are statistical and systematic added in quadrature.

5.7 Expectations and Observations

The expected $t\bar{t}$ signal (based on $\sigma_{t\bar{t}}$ =7 pb and m_t = 175 GeV) and background yields have been listed at the successive stages of selection in Table 5.11 : (i) e^+e^-+ $\geq$0 jet, (ii) e^+e^-+ $\geq$1 jet,(iii) e^+e^-+ $\geq$2 jets, (iv) Z mass window removal, (v) $\not{E}_T$ cut and (vi) sphericity cut . The total standard model expectation from signal and background is compared to the observations in data at each cut level in Table 5.12. We see that the observations in data show quite good agreement within uncertainties with the predicted signal plus background contributions throughout the analysis. The good agreement between predictions and observations in the first four lines of the table (when the sample is background dominated) establishes confidence that the backgounds have been modelled properly in the Monte Carlo. As is clearly evident from the table that the $Z/\gamma^* \to ee$ contribution dominates over the other background sources at each level. Removing the Z mass window and application of $\not{E}_T$ cut efficiently suppresses this background.

A summary of the signal and background expectations along with statistical and systematic uncertainties at the final level of selection is presented in Table 5.13. This table also shows that five events in the data pass all of the selection cuts. The prediction and observation exhibits very good agreement as we expect

Selection Cut	Data	Total Expectation
$N_{ele}^{p_T>15} \geq 2$	23713	25686^{+2522}_{-2669}
$N_{jets}^{p_T>20} \geq 1$	2784	2678^{+464}_{-434}
$N_{jets}^{p_T>20} \geq 2$	369	$369.5^{+69.43}_{-67.5}$
M_Z Cut	88	$91.7^{+16.5}_{-19.9}$
$\not\!\!E_T$ Cut	5	$5.04^{+0.44}_{-0.51}$
Sphericity	5	$4.53^{+0.41}_{-0.47}$

Table 5.12: Observation in data and total expectation from signal and backgrounds at the different levels of selection. Errors are statistical and systematic added in quadrature

Category	Yield	Stat Err	Sys Err
WW	0.20	0.07	$^{+0.08}_{-0.13}$
$Z \rightarrow \tau\tau$	0.30	0.06	$^{+0.08}_{-0.13}$
$\not\!\!E_T$ Fakes	0.45	0.15	0.00
EM Fakes	0.09	0.03	0.00
Total Bkg	1.04	0.18	$^{+0.11}_{-0.18}$
Expected signal	3.49	0.08	$^{+0.34}_{-0.39}$
Selected Events	5.00	2.24	–

Table 5.13: Summary of expectations and observations alon with statistical and systematic errors for $t\bar{t}$ in the $\rightarrow ee$ channel.

$4.53^{+0.41}_{-0.47}$ events and observe 5 events. The run numbers, event numbers, and kinematics of these candidate events are listed in the Appendix-C.

Table 5.14 lists the signal efficiency, signal to background ratio and figure of merit at different levels of selection after the 2 jet requirement. As expected, the signal to background ratio improves at the subsequent levels of selection. Although the last two levels of selection provide quite similar figure of merits (and hence statistical error on the measured cross section), the sphericity cut enjoys better signal to background ratio. We have also compared these parameters with that obtained in our previous version of analysis based on 243 pb^{-1} data, which is under publication [93]. The present analysis enjoys significantly better signal to background ratio and figure of merit leading to less error on the

Cut	Eff_{signal}	S/B	f.o.m.($\sqrt{(S+B)}/S$)
$N_{jets}^{p_T>20} \geq 2$	13.44±0.23	0.016±0.001	3.361±0.123
M_Z Cut	11.49±0.22	0.056±0.002	1.958±0.051
$\not{E}_T$ Cut	8.75±0.19	2.847 ±0.439	0.602±0.019
Sphericity	8.19±0.18	3.356±0.586	0.610±0.018
Analysis with $243pb^{-1}$	7.06 ±0.23	2.054±0.249	0.882±0.030

Table 5.14: Signal Efficiency, Signal to background Ratio and Figure of Merit at different levels after the 2 jet requirement and also comparison with the previous Analysis using 243 pb^{-1} data.

measured cross section. This has been made possible due to significant reduction in the instrumental backgrounds particularly the $\not{E}_T$ fakes with respect to the previous analysis.

5.7.1 Kinematic distributions

We look at the comparison of kinematic and topological distributions at various cut levels in order to check how well the signal and background estimation agrees with observation in the data. Figures 5.9 through 5.14 show the distributions of leading electron p_T and η; leading jet p_T and η; jet multiplicity, H_T, sphericity, $\not{E}_T$, dielectron invariant mass (M_{ee}) and $\Delta\phi(leading\ jet, \not{E}_T\ )$ for the backgrounds and expected signal compared to data in $e^+e^- + \geq 2$ jets events (corresponding to third line of Table 5.11). Figures 5.15 through 5.19 show these distributions after removing Z mass window which corresponds to the fourth line of Table 5.11. The distributions at these two levels of selection show that the signal is totally swamped by the backgrounds and $Z \rightarrow ee$ completely dominates over other backgrounds. However, the nice agreement between the expectation and observation in data establishes confidence in our background estimation. Figures 5.20 through 5.26 show these kinamtical and topological distributions for the final level of selection in Table 5.11. In three

distributions, the data show an agreement within statistical errors with the predicted background and signal contributions. The distributions show that the sample is enriched with the $t\bar{t}$ signal at this stage. Figure 5.27 demonstrates the signal plus background expectations and observations in data in different jet multiplicities (0 jet, 1 jet and $\geq$2 jets) for events passing the electron, Z window, $\not{E}_T$ and topological selection. We see a reasonably good agreement between predictions and observations. In all cases, the contribution is normalized to a $t\bar{t}$ cross section of 7 pb.

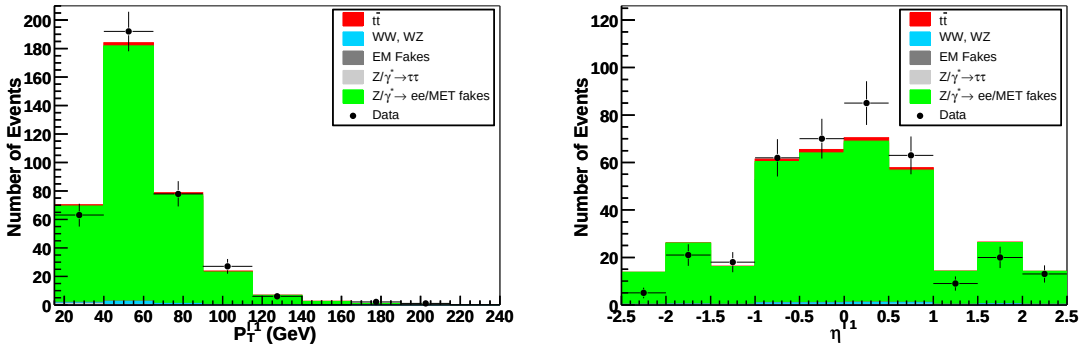

Figure 5.9: Distributions of the p_T and η of the leading electron for the background, $t\bar{t}$ and data in $e^+e^- + \geq 2$ jets events (see line 3 of Table 5.11).

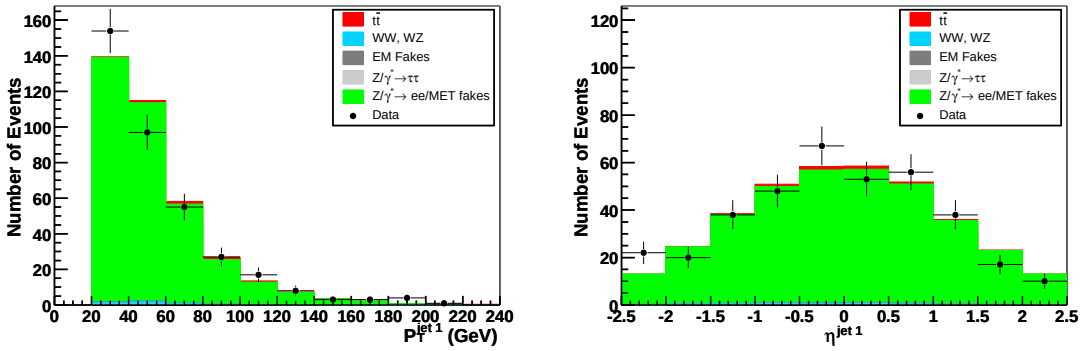

Figure 5.10: Distributions of the p_T and η of the leading jet for the background, $t\bar{t}$ and data in $e^+e^- + \geq 2$ jets events (see line 3 of Table 5.11).

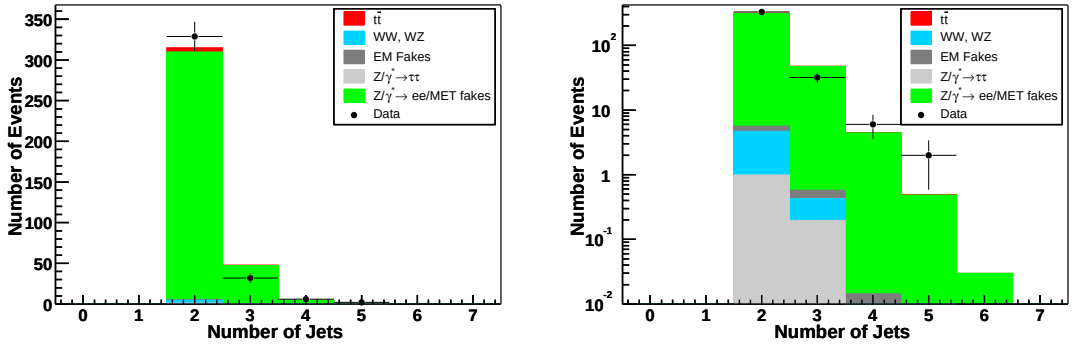

Figure 5.11: Distributions of the jet multiplicity on linear (left) and log (right) scales for the background, $t\bar{t}$ and in $e^+e^- + \geq 2$ jets events (see line 3 of Table 5.11).

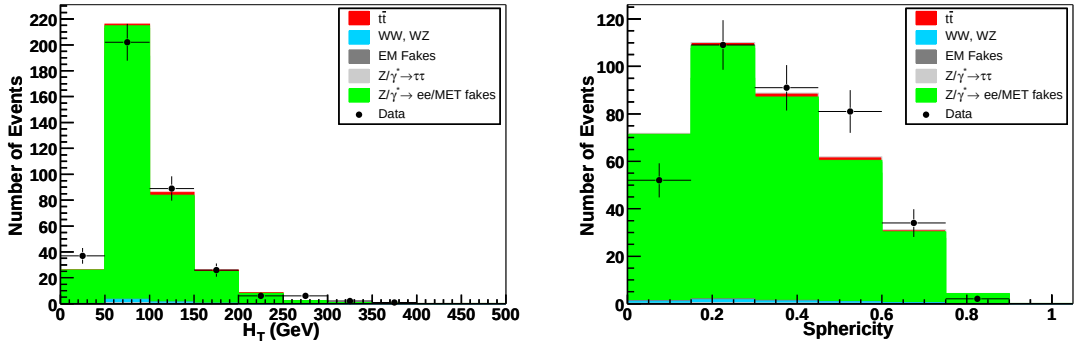

Figure 5.12: Distributions of the H_T^{jet} (left) and sphericity (right) for the background, $t\bar{t}$ and in $e^+e^- + \geq 2$ jets events (see line 3 of Table 5.11).

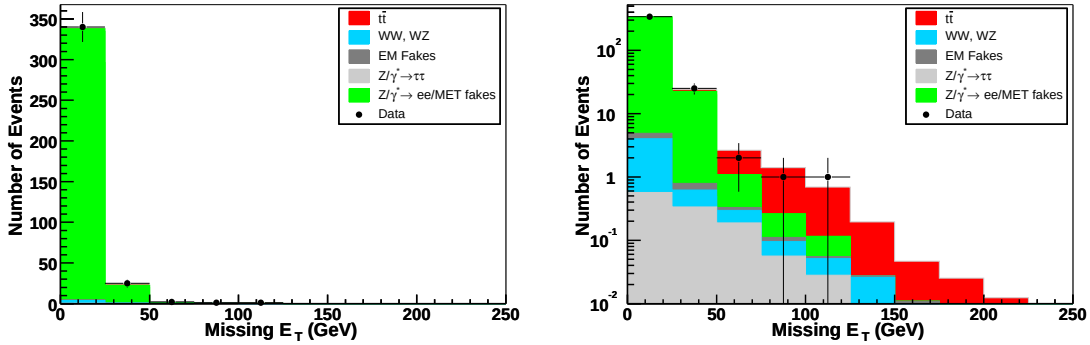

Figure 5.13: Distributions of the $\not{E}_T$ on linear (left) and log (right) scales for the background, $t\bar{t}$ and data in $e^+e^- + \geq 2$ jets events. (see line 3 of Table 5.11).

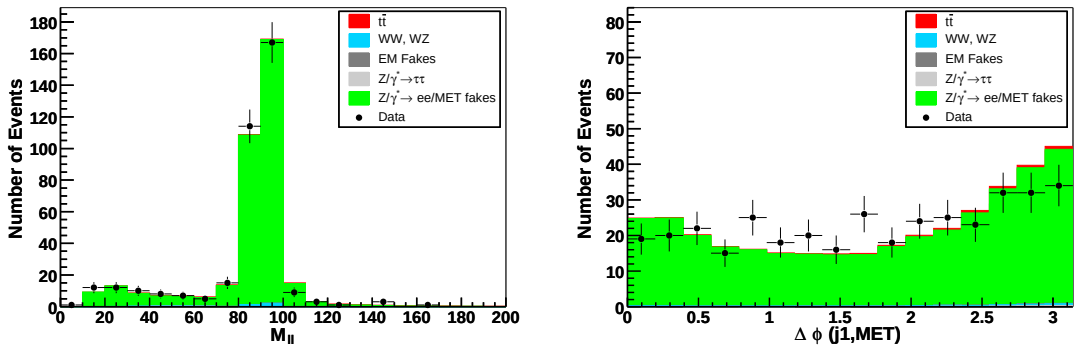

Figure 5.14: Distributions of the dielectron invariant mass (left) and $\Delta\phi(j^1, \not{E}_T)$ (right) for the background, $t\bar{t}$ and data in $e^+e^- + \geq 2$ jets events. (see line 3 of Table 5.11).

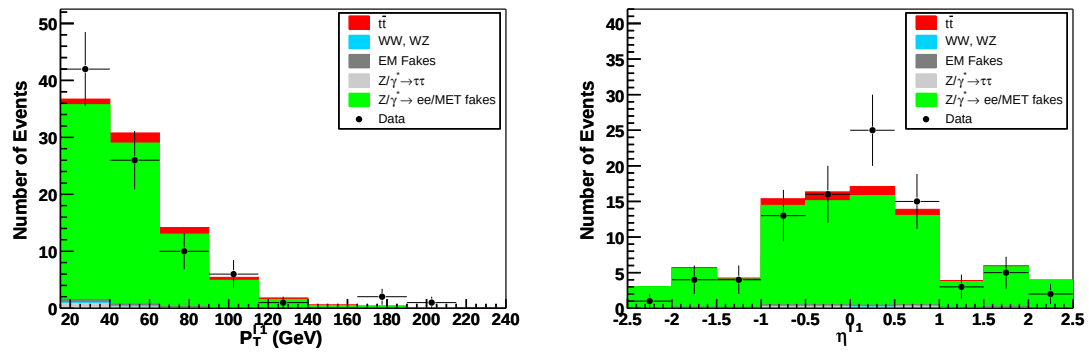

Figure 5.15: Distributions of the p_T and η of leading electron for the background, $t\bar{t}$ and data after requiring two jets and removing the Z window (Table 5.11).

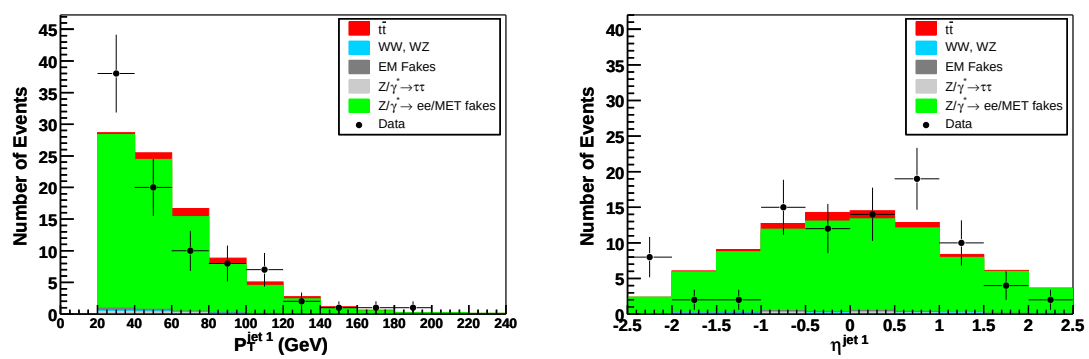

Figure 5.16: Distributions of the p_T and η of leading jet for the background, $t\bar{t}$ and data after requiring two jets and removing the Z window (Table 5.11).

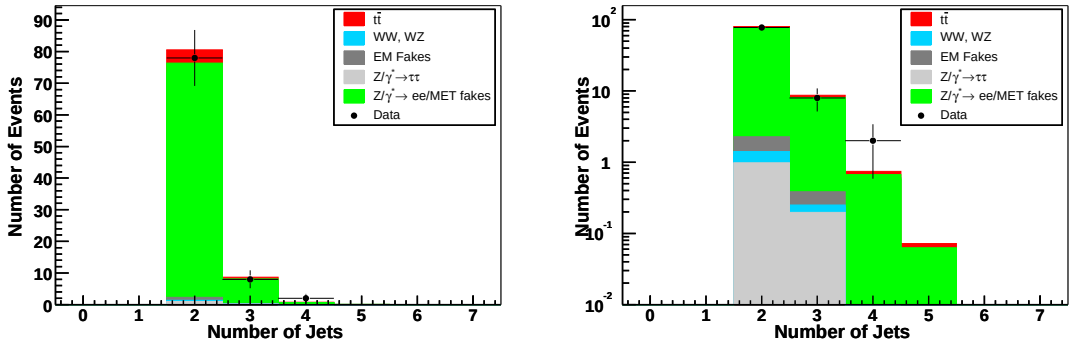

Figure 5.17: Distributions of the number of jet on linear (left) and log (right) scales in the event for the background, $t\bar{t}$ and data after requiring two jets and removing the Z window (Table 5.11)

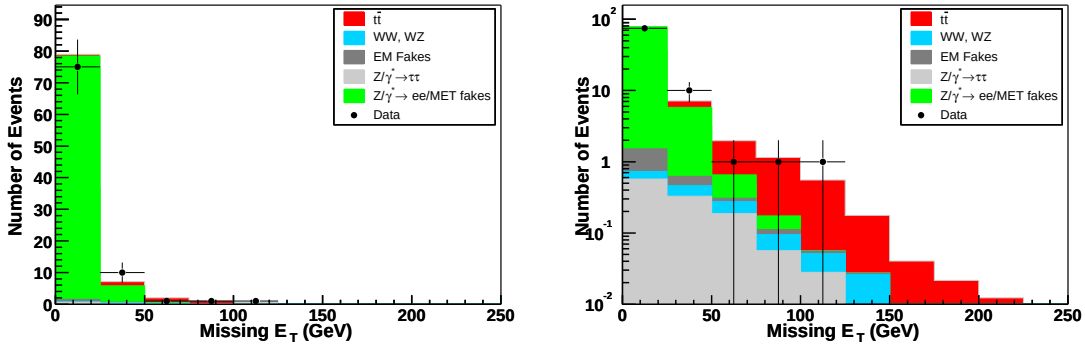

Figure 5.18: Distributions of the $\not{E}_T$ on linear (left) and log (right) scales for the background, $t\bar{t}$ and data after Z mass cut (Table 5.11).

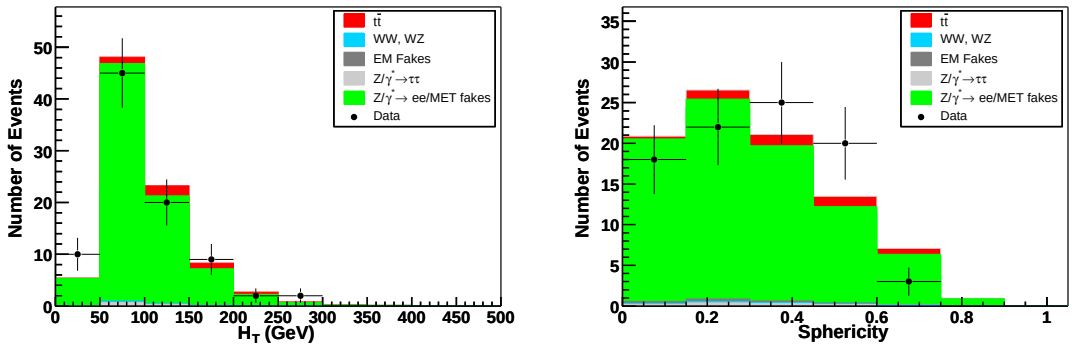

Figure 5.19: Distributions of the H_T^{jet} (left) and sphericity (right) for the background, $t\bar{t}$ and data after Z mass cut (Table 5.11).

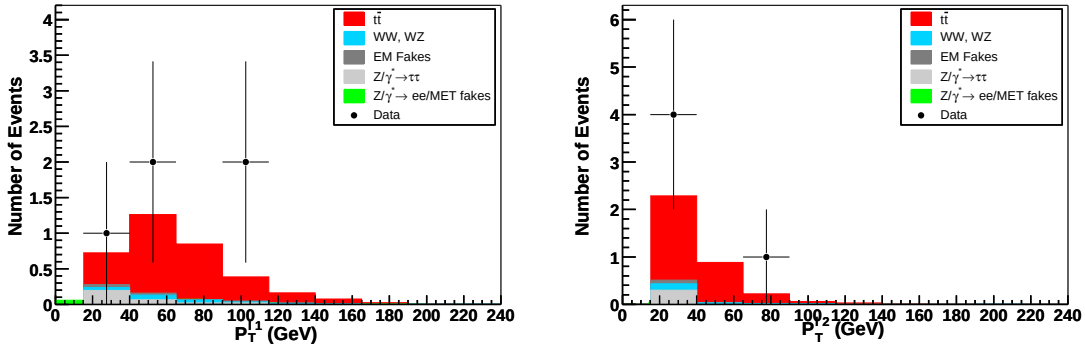

Figure 5.20: Distributions of the p_T of leading (left) and next-leading (right) electron for the background, $t\bar{t}$ and data after all cuts.

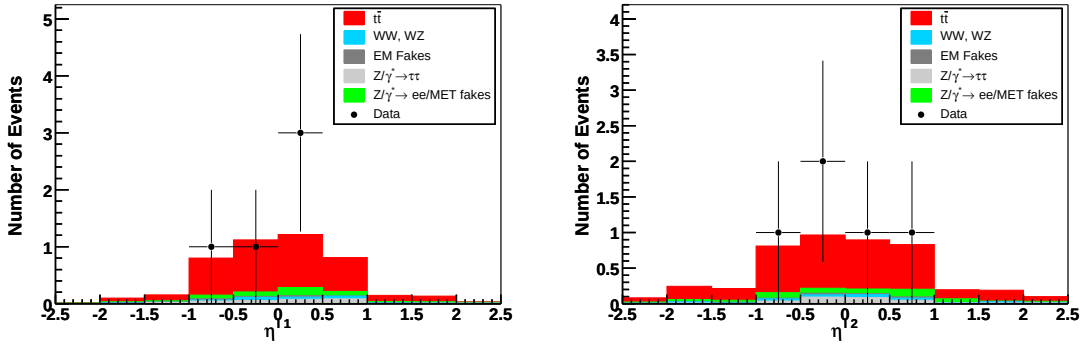

Figure 5.21: Distributions of the η of leading (left) and next-leading (right) electron for the background, $t\bar{t}$ and data after all cuts.

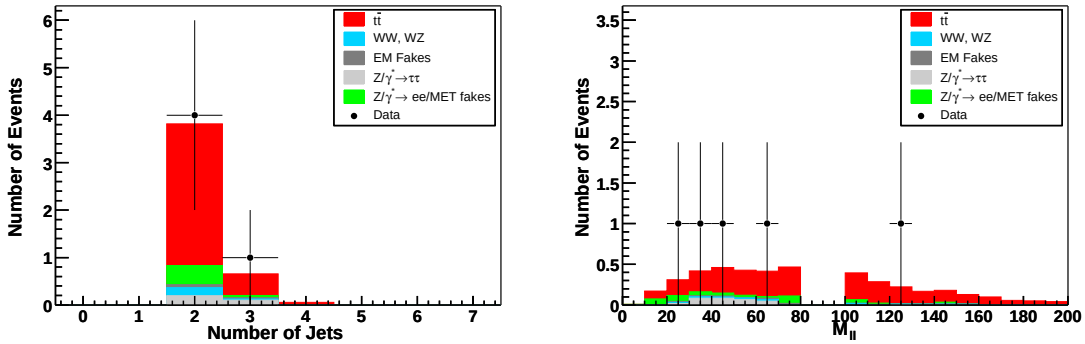

Figure 5.22: Distributions of the number of jet (left) and dielectron invariant mass (right) in the event for the background, $t\bar{t}$ and data after all cuts..

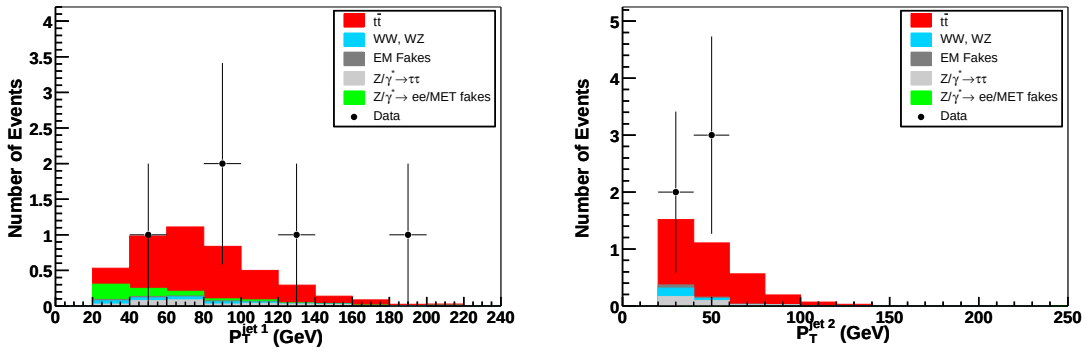

Figure 5.23: Distributions of the p_T of leading (left) and next-leading (right) jet for the background, $t\bar{t}$ and data after all cuts.

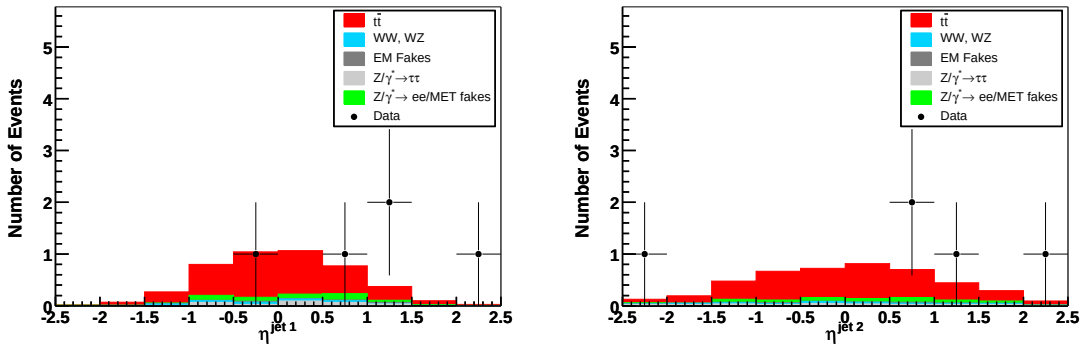

Figure 5.24: Distributions of the η of leading (left) and next-leading (right) jet for the background, $t\bar{t}$ and data after all cuts.

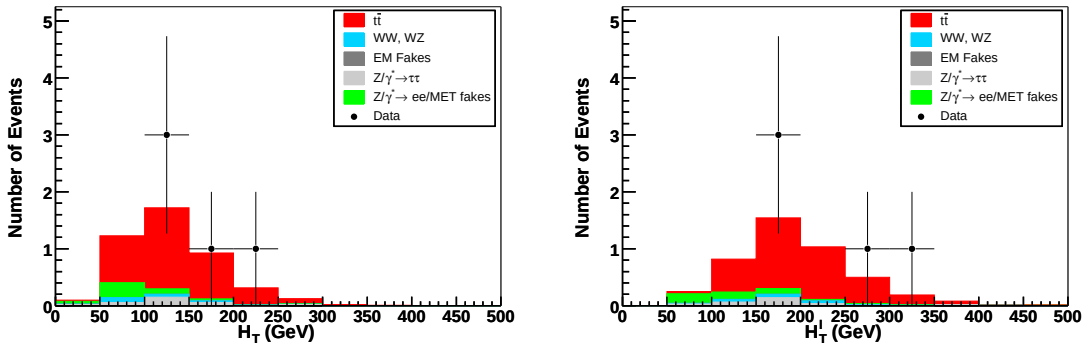

Figure 5.25: Distributions of the H_T^{jet} (left) and H_T^e (right) for the background, $t\bar{t}$ and data aafter all cuts.

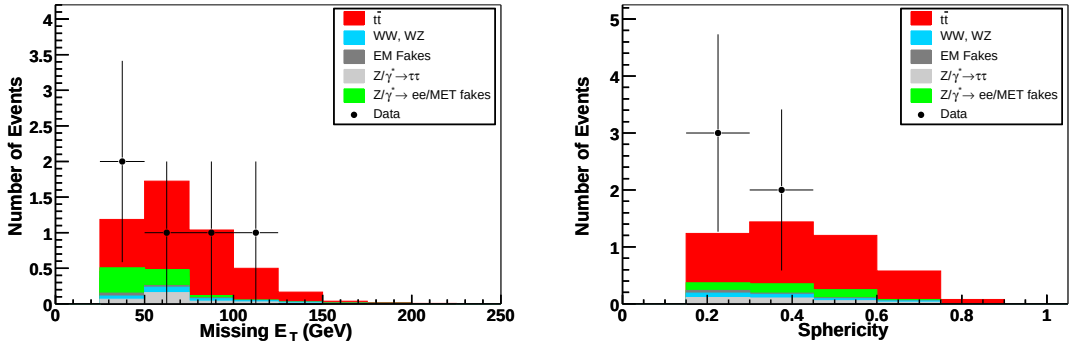

Figure 5.26: Distributions of the $\not\!\!E_T$ (left) and sphericity (right) for the background, $t\bar{t}$ and data after all cuts.

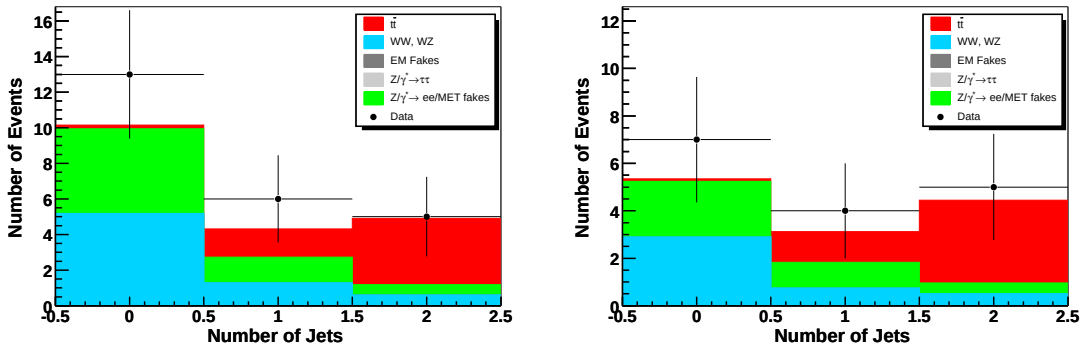

Figure 5.27: Expectation and Observation in different jet multiplicities before the sphericity cut (left) and and after all cuts (right).

5.8 Systematic Uncertainties

We combine the results from the dielectron analysis with the results from dimuon and $e\mu$ analyses, to arrive at the measurement in dilepton final states. The systematic uncertainties in the dilepton channels can be subdivided into uncertainties on the signal efficiencies and on the background. Efficiencies can have uncertainties of statistical nature or arising from systematic effects such as sample or cut dependence. If a given efficiency has uncertainties of both statistical and systematic nature and

if the statistical component is correlated between channels then the statistical and systematic components are summed quadratically. If the statistical component is independent among channels then it is included into the "uncorrelated systematics". A brief description of the sources of uncertainties is presented below.

- **Uncertainty associated with the primary vertex selection efficiency:** The scale factor for the primary vertex efficiency is stable within statistical errors as a function of the number of jets (for $N_{jet} \geq 1, 2$) and over the $Z \to ee$ and $Z \to \mu\mu$ samples as detailed in the dilepton analysis note [169]. The only systematic uncertainty taken into account arises from the limited statistics of the data and Monte Carlo samples used to determine the scale factor. Half of the difference between the measured primary vertex scale factor in $Z \to ee$ and $Z \to \mu\mu$ is taken as systematic on this scale factor, yielding a systematic uncertainty of 0.4%.

- **Uncertainty associated with the $|\Delta z(d\emptyset reco, d\emptyset root)|$ <5cm requirement** The systematic error on this scale factor is taken as half of the difference between the scale factor derived in $Z \to ee + 1$jet data and $Z \to \mu\mu$+1 jet data. The resulting systematic uncertainty is 0.2%

- **Uncertainty associated with the $\Delta z(PV, \ell)$ cut efficiency:** The scale factor obtained for this selection is quite stable for different jet multiplicities and between $Z \to ee$ and $Z \to \mu\mu$. The only uncertainty considered is therefore of statistical origin, equal to 0.1%. Half of the difference between the scale factor obtained on $Z \to ee$ and $Z \to \mu\mu$ is taken as systematic uncertainty.

- **Uncertainty associated with electron reconstruction and identification efficiency:** The scale factor for electron reconstruction and identification (for medium electron) efficiency is plotted versus the distance between the electron and the closest jet as explained in [169] [145]. The scatter of the scale factors versus this distance (RMS) is taken as the systematic uncertainty. The uncer-

tainties for CC and EC are determined separately. This gives a systematic error of 2.9% per electron in CC and 6.7% per electron in EC.

- **Uncertainty associated with the electron tracking and likelihood efficiency:** This uncertainty for CC electrons is taken to be the larger RMS of the scatter of scale factors in the plots of scale factor versus η and ϕ (detailed view in our DØ notes [169] [145]). In the EC, the η distribution of scale factors is convoluted with the η spectrum of electrons in $t\bar{t}$ Monte Carlo. The systematic uncertainty is taken to be the convolution of statistical errors from the scale factor measurement and the $t\bar{t}$ sample.

- **Uncertainty associated with the Trigger Efficiency:**

  In section 3.1, it is shown that electron trigger efficiencies versus p_T are obtained from the Z sample. Since this sample has limited statistics, the statistical errors on the fit to the turn-on curves are varied by $\pm 1\sigma$ to obtain the systematics for L1 and L3 separately.

  Jets might fire the electron triggers. A turn on curve for jets firing an electron trigger at level-1 has been derived and is included in the calculation of the trigger efficiency. This turn on curve has a statistical error band which is used to determine a systematic on this effect. The effect of this additional systematic on the ee channel is negligible due to the tighter electron criteria at level-3 of the electron trigger. The uncertainties due to trigger have been rederived to incorporate new triggers from version 13 trigger list.

- **Uncertainty associated with the Jet Energy Scale (JES):** The uncertainty on the preselection efficiency associated with the jet energy scale is derived by varying the JES by $\pm 1\sigma$ where

$$\sigma = \sqrt{\sigma^2_{stat,data} + \sigma^2_{stat,MC} + \sigma^2_{syst,data} + \sigma^2_{syst,MC}} \tag{5.6}$$

- **Uncertainty associated with Jet energy resolution:** The uncertainty on the jet energy resolution in data is already included in the systematic uncertainty due to the jet energy scale. The energy of jets in Monte Carlo is smeared to the jet energy resolution of data. The jet energy resolution in Monte Carlo has an uncertainty which is not taken into account in the jet energy scale. To account for this, the parameters of the jet energy smearing are varied by the size of the uncertainty on the jet energy resolution parameters in Monte Carlo.
- **Uncertainty associated with the Jet Reconstruction and Jet Identification:** The systematic errors are obtained by running the analysis with the scale factor varied by $\pm 1\sigma$.
- **Uncorrelated uncertainty:** Uncorrelated uncertainty arises from statistical components to systematic errors which are in addition independent between the 3 channels. If a systematic arises from the limited size of a sample but that same sample is used in ee and $e\mu$ analyses for example then this uncertainty will not be counted as an uncorrelated systematic, because the two channels can be affected by the same statistical fluctuation.
- **Uncertainty due to theoretical cross sections:** WW background Monte Carlo, the leading order WW production cross section differs by 35% from the theoretical NLO production cross section. A theoretical prediction for the NLO cross section does not exist for the $WW + 2$jet process; therefore, the leading order cross section obtained from the generator is scaled up by 35%, and a 35% systematic uncertainty is introduced.
- **Uncertainty due to normalisation:** This uncertainty refers to the normalisation of the Z/Drell-Yan background. In the jet bin used for cross section calculation this background is normalised to the observed number of events with 2 leptons and 2 jets but before the topological cuts. The normalisation factor has an uncertainty due to the limited statistics of both the Monte Carlo and

Systematic Source	Signal	Backgrounds	
	$t\bar{t}$	WW	$Z \to \tau\tau$
Primary Vertex	± 0.4	± 0.4	± 0.4
$\Delta z(d\emptyset_{reco}, d\emptyset_{root})$	± 0.2	± 0.2	± 0.2
Lepton Promptness	± 0.1	± 0.1	± 0.1
EM Reconstruction,ID	± 6.2	± 6.4	± 6.7
EM Tracking and Likelihood	± 4.2	± 3.6	± 3.7
L1 EM Trigger	$+1.2 - 5.3$	$+1.4 - 6.4$	$+2.7 - 15.5$
L3 EM Trigger	± 0.8	± 1.1	± 4.1
JES	$+3.1 - 5.0$	$+6.8 - 10.1$	$+15.6 - 21.8$
Jet ID	$+4.2 - 3.3$	-37.3	-25.0
Jet Resolution	$+1.8$	-30.5	$+8.4 - 5.7$
Theoretical cross section	–	± 35	–
Normalisation	–	–	± 7.4
Uncorrelated	± 2.3	± 13.0	

Table 5.15: Summary of the relative systematic uncertainties for signal and backgound in % .

data sample with 2 jets and two well identified leptons.

- **Uncertainty due to Luminosity:** A very conservative error of 6.5% is applied to the luminosity measurement, as discussed in [172].

Table 5.15 gives a summary of the systematic uncertainties for the $t\bar{t}$, WW, and $Z \to \tau\tau$ processes.

5.9 Cross Section

The production cross section (σ) can be expressed by :

$$\sigma = \frac{N^{obs} - N^{bkg}}{\mathcal{L}\epsilon^{sig} BR}, \tag{5.7}$$

where N^{obs} is the number of events observed, N^{bkg} is the expected number of background events, $\mathcal{L}$ is the integrated luminosity, ϵ^{sig} is the signal efficiency, and BR is the branching ratio to the channel being studied. These inputs for $t\bar{t}$ events decaying through dielectron mode are listed in Table 5.16. The systematic uncertainty on the

Channel	Observed	Background	$\epsilon_{t\bar{t}}$	Br	$\mathcal{L}$ (pb^{-1})
ee	5	1.0	0.082	0.01584	384.1

Table 5.16: Number of observed events, estimated background , $t\bar{t}$ selection efficiency, decay branching ratio for $t\bar{t} \rightarrow e^+e^- + X$, and integrated luminosity for the dielectron channel.

cross section measurement is obtained by varying the background and efficiencies, within their errors. The $t\bar{t}$ cross section at $\sqrt{s} = 1.96$ TeV in the dielectron channel is

$$\sigma_{t\bar{t}} = 7.9^{+5.2}_{-3.8} \text{ (stat) } ^{+1.3}_{-1.0} \text{ (syst) } \pm 0.5 \text{ (lumi) pb}$$

, which is in good agreement with the Standard Model prediction of 6.77 ± 0.42 pb [78]. This result exhibits significant improvement from our previous analysis result, $\sigma_{t\bar{t}} = 14.9^{+9.4}_{-7.0}$ (stat) $^{+2.5}_{-1.8}$ (syst) ± 1.0 (lumi) pb, based on 243 pb^{-1} of data [145]. It can be seen that both statistical and systematic errors on the cross-section have gone down considerably. The uncertainty on the measured cross-section is still statistically dominated. The main sources of systematic uncertainties are electron identification and jet energy scale.

5.9.1 Combined Dilepton Results

The $t\bar{t}$ cross section measurements have also been conducted in other dilepton channels, namely, eμ and $\mu\mu$. In Table 5.17 we summarize the predicted (signal+background) and observed number of events in different channels. Predicted and observed distributions for various event kinematic and topological variables are shown in Fig. 5.28 and Fig. 5.29.

The cross section inputs for the three dilepton channels are summarized in Table 5.18.

The systematic uncertainty on the cross section measurement is obtained by varying the background and efficiencies, within their errors, with all the correlations be-

Category	ee	$\mu\mu$	eμ	ll
Z/γ^*	$0.30^{+0.10}_{-0.15}$	$1.01^{+0.22}_{-0.34}$	$1.22^{+0.33}_{-0.39}$	$2.53^{+0.41}_{-0.54}$
WW/WZ	$0.20^{+0.10}_{-0.14}$	$0.20^{+0.08}_{-0.07}$	$1.13^{+0.45}_{-0.48}$	$1.53^{+0.47}_{-0.50}$
Instrumental leptons	0.54 ± 0.15	0.13 ± 0.04	$2.13^{+2.50}_{-1.66}$	$2.97^{+2.50}_{-1.67}$
Total background	$1.0^{+0.2}_{-0.3}$	$1.3^{+0.3}_{-0.4}$	$4.5^{+2.6}_{-1.8}$	$6.8^{+2.6}_{-1.8}$
Expected signal	3.5 ± 0.4	2.5 ± 0.3	$11.3^{+1.2}_{-1.4}$	$17.3^{+1.3}_{-1.5}$
SM expectation	$4.5^{+0.4}_{-0.5}$	$3.8^{+0.4}_{-0.5}$	$15.8^{+2.8}_{-2.3}$	$24.1^{+2.9}_{-2.4}$
Selected events	5	2	21	28

Table 5.17: Expected background and observed and expected signal yields. The expected signal yield assumes a 7 pb production cross section. The errors shown are the quadratic sum of the statistical and the systematic errors.

Channel	Obs. events	background	$\epsilon_{t\bar{t}}$	B	$\mathcal{L}$ (pb^{-1})
ee	5	1.0	0.082	0.01584	384.1
$e\mu$ [98] [174]	21	4.5	0.139	0.03155	367.7
$\mu\mu$ [98] [169]	2	1.3	0.064	0.01571	362.6

Table 5.18: Number of observed events, estimated background, $t\bar{t}$ selection efficiency, decay branching ratio for $t\bar{t} \to ll' + X$ including the $W \to \tau\nu \to (e,\mu)\nu\nu$ contribution, and integrated luminosity for each channel.

tween the channels and between the different classes of background taken into account [173]. The dominant systematic uncertainties are summarized in Table 5.19.

The preliminary $t\bar{t}$ production cross sections at $\sqrt{s}$ =1.96 TeV in dilepton channels are measured to be:

$$\begin{aligned}
\text{ee} \quad &: \quad \sigma = 7.9^{+5.2}_{-3.8}\,(\text{stat})\,^{+1.3}_{-1.0}\,(\text{syst})\ \pm 0.5\,(\text{lumi})\ \text{pb} \\
\text{e}\mu \quad &: \quad \sigma = 10.2^{+3.1}_{-2.6}\,(\text{stat})\,^{+1.6}_{-1.3}\,(\text{syst})\ \pm 0.7\,(\text{lumi})\ \text{pb} \\
\mu\mu \quad &: \quad \sigma = 1.8^{+4.8}_{-3.0}\,(\text{stat})\,^{+1.0}_{-1.2}\,(\text{syst})\ \pm 0.1\,(\text{lumi})\ \text{pb} \\
\text{dilepton} \quad &: \quad \sigma = 8.6^{+2.3}_{-2.0}\,(\text{stat})\,^{+1.2}_{-1.0}\,(\text{syst})\ \pm 0.6\,(\text{lumi})\ \text{pb.}
\end{aligned}$$

in good agreement with the standard model prediction of 6.77 ± 0.42 pb [78]. This cross-section is based on an assumed top mass of 175 GeV. Instead of folding the uncertainty due to top mass into the systematic errors, the dependence of $\epsilon_{t\bar{t}}$ on

Table 5.19: Summary of systematic uncertainties on $\sigma_{t\bar{t}}$.

Source	$\Delta\sigma_{t\bar{t}}$ (pb)
Jet energy calibration	$+0.5-0.5$
Jet identification	$+0.5-0.4$
Muon identification	$+0.5-0.4$
Electron identification	$+0.4-0.3$
Trigger	$+0.7-0.4$
Other	$+0.4-0.4$
Total	$+1.2-1.0$

top mass is used to derive a slope for the $t\bar{t}$ cross section vs m_t. In the region $160 < m_t < 180$ GeV, the measured cross section is found to decrease by 0.08 pb per GeV increase in m_t.

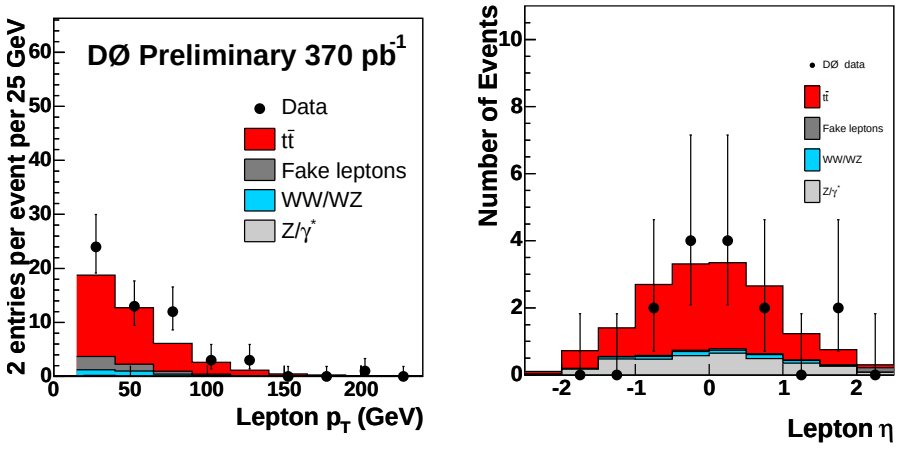

Figure 5.28: Observed and predicted distributions for lepton p_T and η for the various backgrounds and the signal.

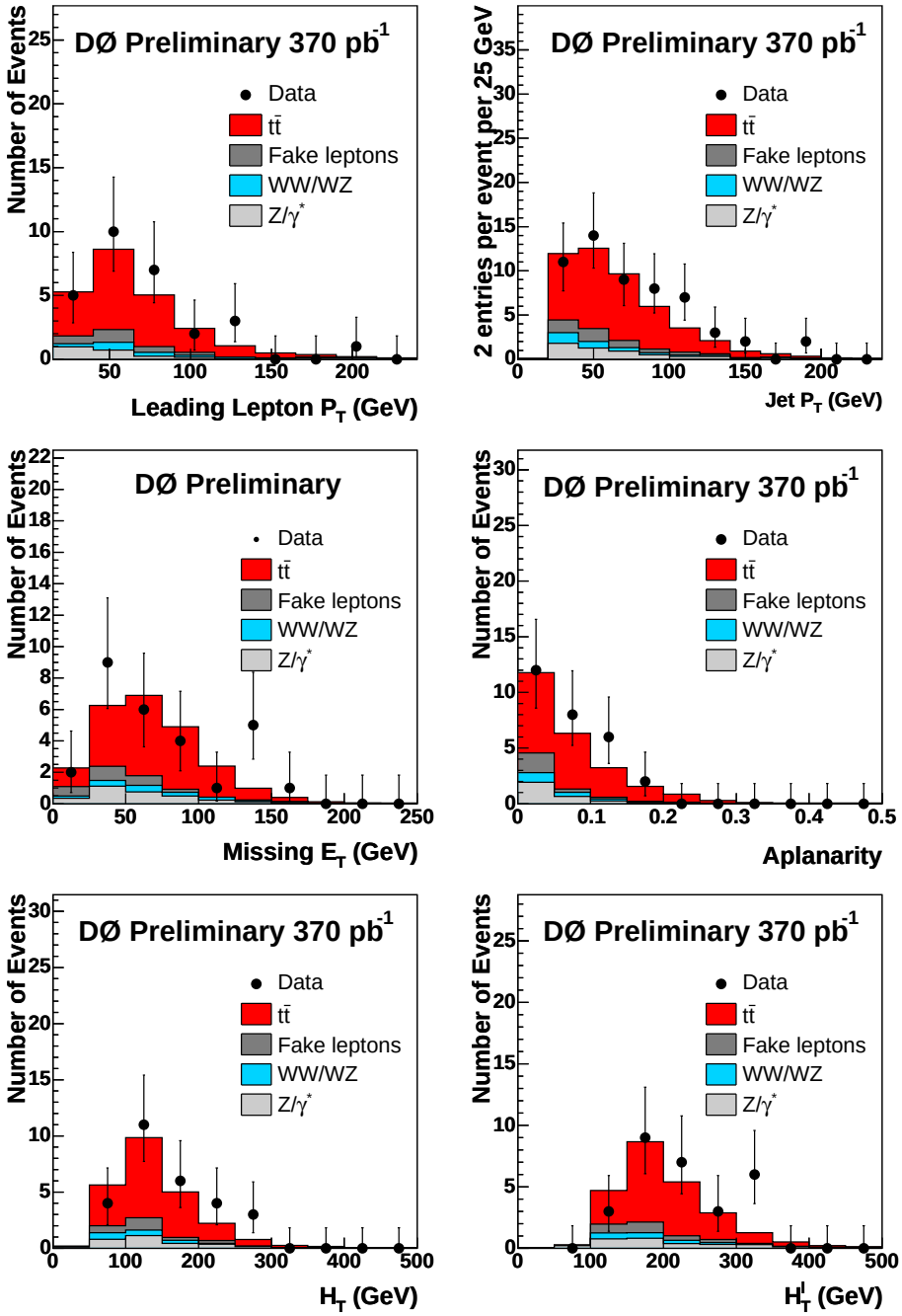

Figure 5.29: Observed and predicted distributions for the various backgrounds and the signal. From top to bottom, leading-lepton p_T, jet p_T, $\not\!\!E_T$, aplanarity, scalar sum of jet p_T (H_T) and scalar sum of jet p_T and leading lepton p_T (H_T).

Chapter 6

Summary

The measurement of the top-antitop pair production cross section in $p\overline{p}$ collisons at $\sqrt{s} = 1.96$ TeV in the dielectron decay channel using 384 pb^{-1} of DØ data yields a $t\overline{t}$ production cross-section of

$$\sigma_{t\overline{t}} = 7.9^{+5.2}_{-3.8}\ \text{(stat)}\ ^{+1.3}_{-1.0}\ \text{(syst)}\ \pm 0.5\ \text{(lumi) pb}$$

. This measurement [98] is based on 5 observed events with a prediction of 1.04 background events. The cross-section corresponds to the top mass of 175 GeV, and is in good agreement with the Standard Model expectation of 6.77 ± 0.42 pb based on next-to-next-leading-order (NNLO) perturbative QCD calculations [78]. This analysis shows significant improvement from our previous cross-section measurement in this channel [93] with 230 pb^{-1} dataset in terms of significantly better signal to background ratio and uncertainties on the measured cross-section.

Combination of all the dilepton final states [98] yields a yields a $t\overline{t}$ cross-section of

$$\sigma_{t\overline{t}} = 8.6^{+2.3}_{-2.0}\ \text{(stat)}\ ^{+1.2}_{-1.0}\ \text{(syst)}\ \pm 0.6\ \text{(lumi) pb}$$

, which again is in good agrrement with theoretical predictions and with measurements in other final states. Hence, these results show no discernible deviation from

the Standard Model. Fig. 6.1 shows the summary of cross-section measurements in different final states by the DØ in Run II. This measurement of cross-section in the dilepton channels is the best dilepton result from DØ till date. Previous DØ result based on analysis of 230 pb^{-1} of data (currently under publication in Physics Letters B) is $\sigma_{t\bar{t}} = 8.6^{+3.2}_{-2.7}$ (stat) $^{+1.1}_{-1.1}$ (syst) ± 0.6 (lumi) pb. It can be seen that the present cross-section suffers from less statistical uncertainty. This result is also quite consistent with CDF collaboration's result of $\sigma_{t\bar{t}} = 8.6^{+2.5}_{-2.4}$ (stat) $^{+1.1}_{-1.1}$ (syst) pb. These results have been presented as DØ 's preliminary results in the high energy physics conferences in the Summer of 2005 (Hadron Collider Physics Symposium, European Physical Society Conference, etc..).

The uncertainty on the cross-section is still dominated by statistics due to the small number of observed events. It can be seen that we are at a level where statistical uncertainties are becoming closer to the systematic ones. Future measurements of the cross section will benefit from considerably more integrated luminosity, leading to a smaller statistical error. Thus the next generation of measurements will be limited by systematic uncertainties. Monte Carlo samples with higher statistics are also being generated in order to decrease the uncertainty on the background estimation. In addition, as the jet energy scale, the electron energy scale, the detector resolutions, and the luminosity measurement are fine-tuned, the systematic uncertainties will continue to decrease.

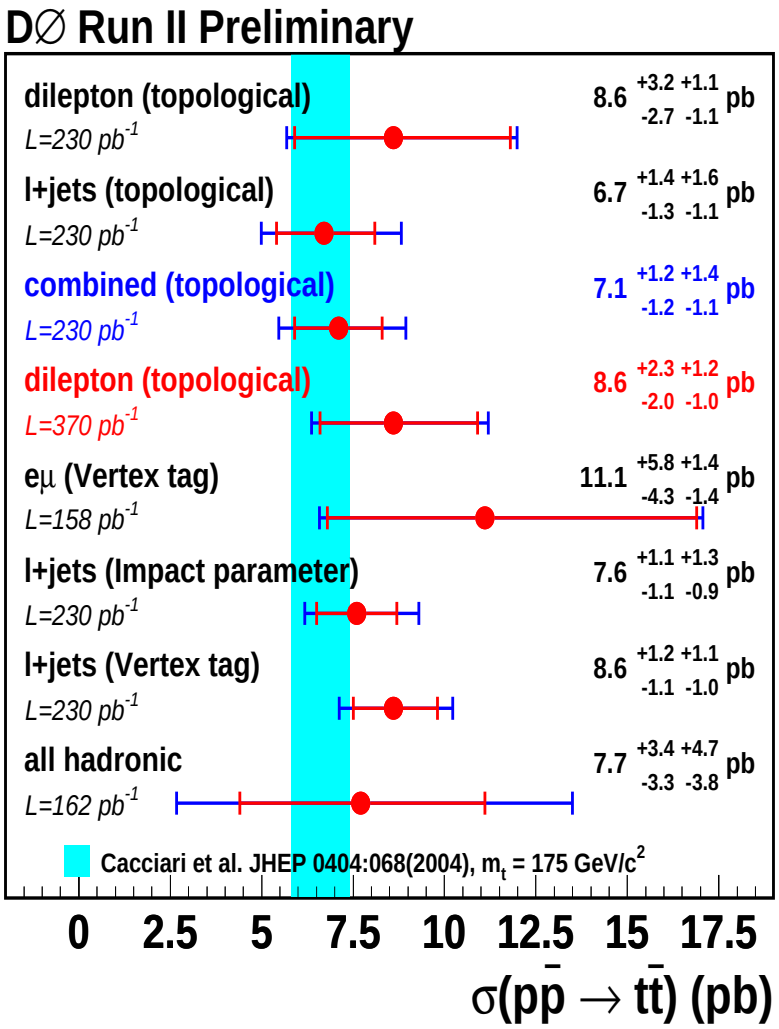

Figure 6.1: The preliminary DØ results for the different cross-section analyses [175]. The bands represent the theoretical predictions for the $t\bar{t}$ cross-section, for m_t =175 GeV. Listed are the measured cross-sections from the different analyses, with their statistical and systematic uncertainties quoted separately. Also shown is the integrated luminosity on which each measurement is based. The result from the dilepton analysis discussed in the dissertation is also quoted as "dilepton topological (370 pb^{-1})".

Appendix A

The parton model description of the top pair production

Although protons and antiprotons collide at the Tevatron, the energies are high enough that during a hard-scattering event the particles get close enough together to 'see' the parton substructure : as a collection of quarks and gluons. The parton model is shown schematically in Figure A.1, which illustrates how a proton-antiproton collision results in a $t\bar{t}$ pair produced via the quark-antiquark annihilation process.

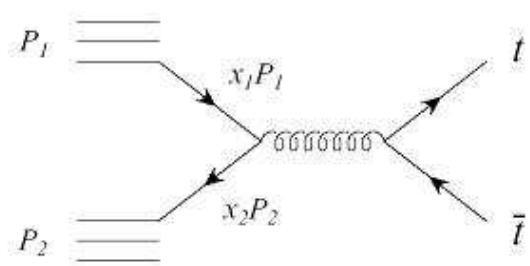

Figure A.1: The parton-model description of $t\bar{t}$ production.

If the proton four-momentum is given by P_1 and the antiproton four-momentum is P_2 in the center-of-momentum frame, we can write the momenta as (following [67]):

$$P_1 = (E, 0, 0, p);\ P_2 = (E, 0, 0, -p) \tag{A.1}$$

The square of the total energy in the center-of-momentum frame is given by:

$$S \equiv (P_1 + P_2)^2 = (2E)^2 \tag{A.2}$$

On the other hand:

$$(P_1 + P_2)^2 = P_1^2 + P_2^2 + 2P_1.P_2 \approx 2P_1.P_2 \tag{A.3}$$

where the mass of the proton has been neglected ($P_1^2 = P_2^2 = m_p^2$) in the approximation above. Comparing above two equations:

$$S \approx 2P_1.P_2 \tag{A.4}$$

If the parton from the proton and antiprotons has the momentum fraction x_1 and x_2 respectively, we can define the square of the total energy in the partonic process as:

$$\hat{s} = (x_1.P_1 + x_2.P_2)^2 \approx 2x_1x_2P_1.P2 = x_1x_2S \tag{A.5}$$

Since there has to be at least enough energy to produce a $t\bar{t}$ pair at rest we must have $\hat{s} \geq 4m_t^2$. Therefore, in order to produce a $t\bar{t}$ pair we must have:

$$x_1x_2 \geq \frac{4m_t^2}{S}. \tag{A.6}$$

Now, the probability of finding a parton with momentum-fraction x falls with increasing x. If we make the simplifying approximation that $x_1 \sim x_2 = x$ we find:

$$x = \frac{2m_t}{\sqrt{S}} \tag{A.7}$$

Appendix B

The $\sqrt{s}$ dependence of the $\sigma_{t\bar{t}}$

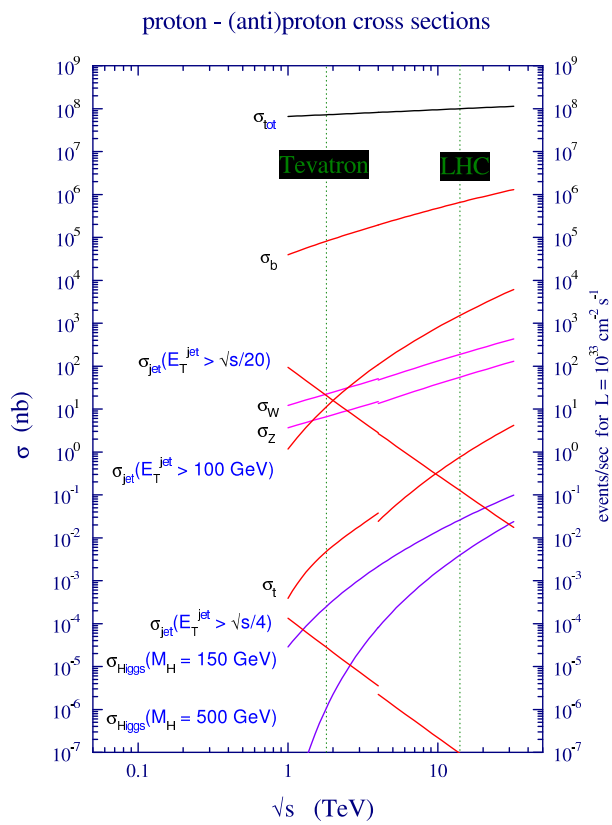

Figure B.1: QCD predictions for hard scattering cross sections at the Tevatron and the LHC.

The $\sigma_{t\bar{t}}$ rises with increasing $\sqrt{s}$ due to the increased phase space available and the higher probability to find a parton with $x \simeq 2m_t/\sqrt{s}$ from the incoming hadron.

Appendix C

Candidate Events

Object	p_T (GeV)	η	ϕ
ele1	55.4	-0.04	1.93
ele2	19.9	0.45	3.50
jet1	97.7	-0.37	3.03
jet2	37.0	1.11	5.98
$\not{E}_T$ (GeV)	106.4		
M_{ee} (GeV)	49.8		
Sphericity	0.30		

Table C.1: Kinematics for event 121971122 in run 166779.

Object	p_T (GeV)	η	ϕ
ele1	34.6	0.40	5.87
ele2	30.0	-0.52	1.67
jet1	55.2.1	2.12	5.95
jet2	54.9	0.64	3.63
jet3	35.4	1.45	3.75
$\not{E}_T$ (GeV)	56.0		
M_{ee} (GeV)	63.6		
Sphericity	0.16		

Table C.2: Kinematics for event 16809090 in run 170016.

Object	p_T (GeV)	η	ϕ
ele1	97.6	0.29	1.42
ele2	18.9	-0.17	0.75
jet1	120.6	1.11	5.60
jet2	51.8	0.64	3.81
$\not{E}_T$ (GeV)	91.8		
M_{ee} (GeV)	34.3		
Sphericity	0.38		

Table C.3: Kinematics for event 13511001 in run 178177.

Object	p_T (GeV)	η	ϕ
ele1	95.6	-0.69	5.57
ele2	88.5	0.55	5.94
jet1	194.2	1.14	2.54
jet2	30.4	2.28	3.06
$\not{E}_T$ (GeV)	40.7		
M_{ee} (GeV)	126.3		
Sphericity	0.15		

Table C.4: Kinematics for event 50812363 in run 178737.

Object	p_T (GeV)	η	ϕ
ele1	41.6	0.27	5.91
ele2	28.5	-0.05	0.45
jet1	85.0	0.74	3.34
jet2	48.9	-2.00	2.08
$\not{E}_T$ (GeV)	41.7		
M_{ee} (GeV)	29.8		
Sphericity	0.30		

Table C.5: Kinematics for event 4006566 in run 192663.

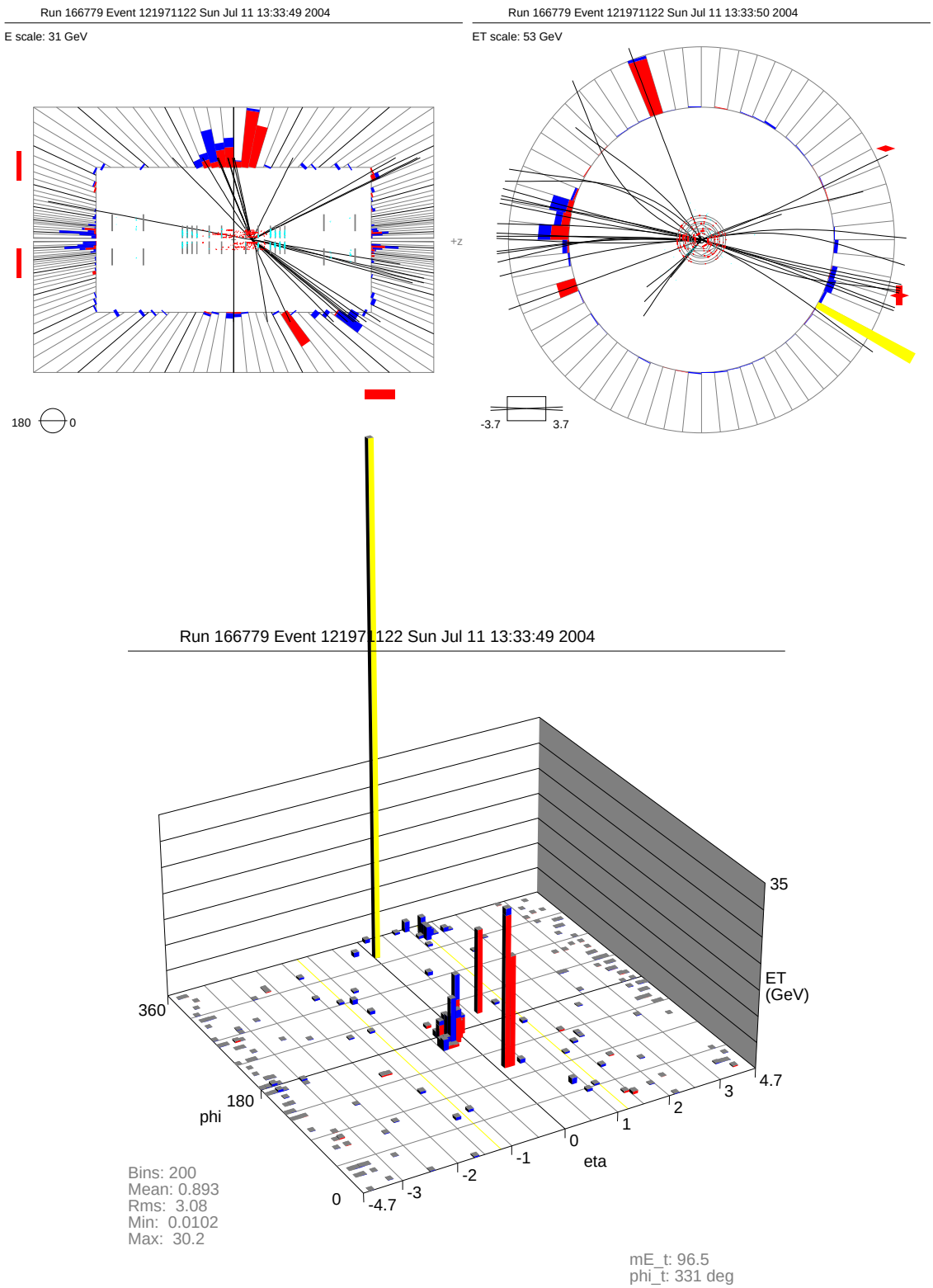

Figure C.1: Run 166779 Event 121971122: RZ view (upper right), XY view (upper left), Lego view (lower). Electrons, jets and $\not\!\!E_T$ are shown by red, blue and yellow respectively.

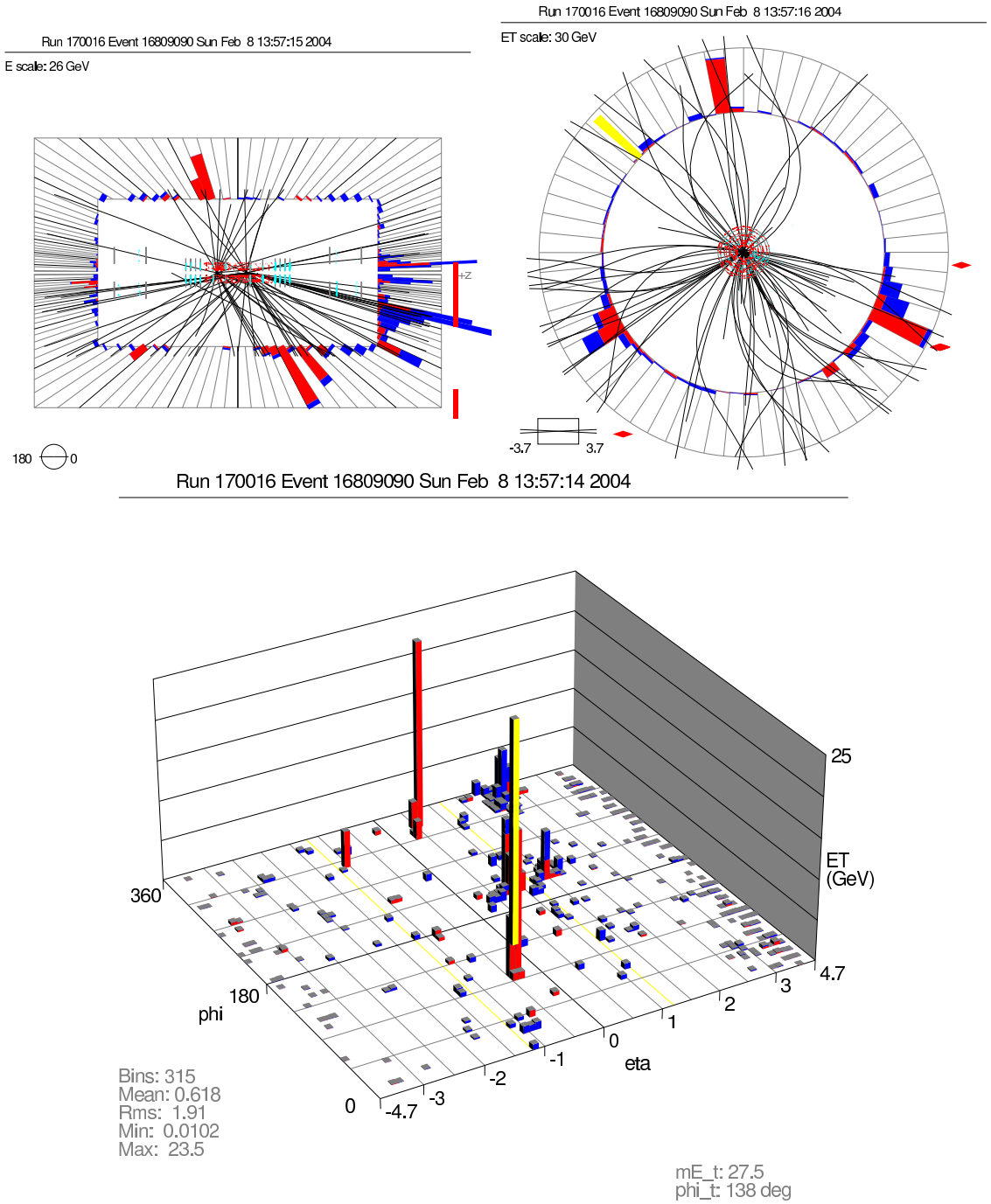

Figure C.2: Run 170016 Event 16809090: RZ view (upper right), XY view (upper left), Lego view (lower).

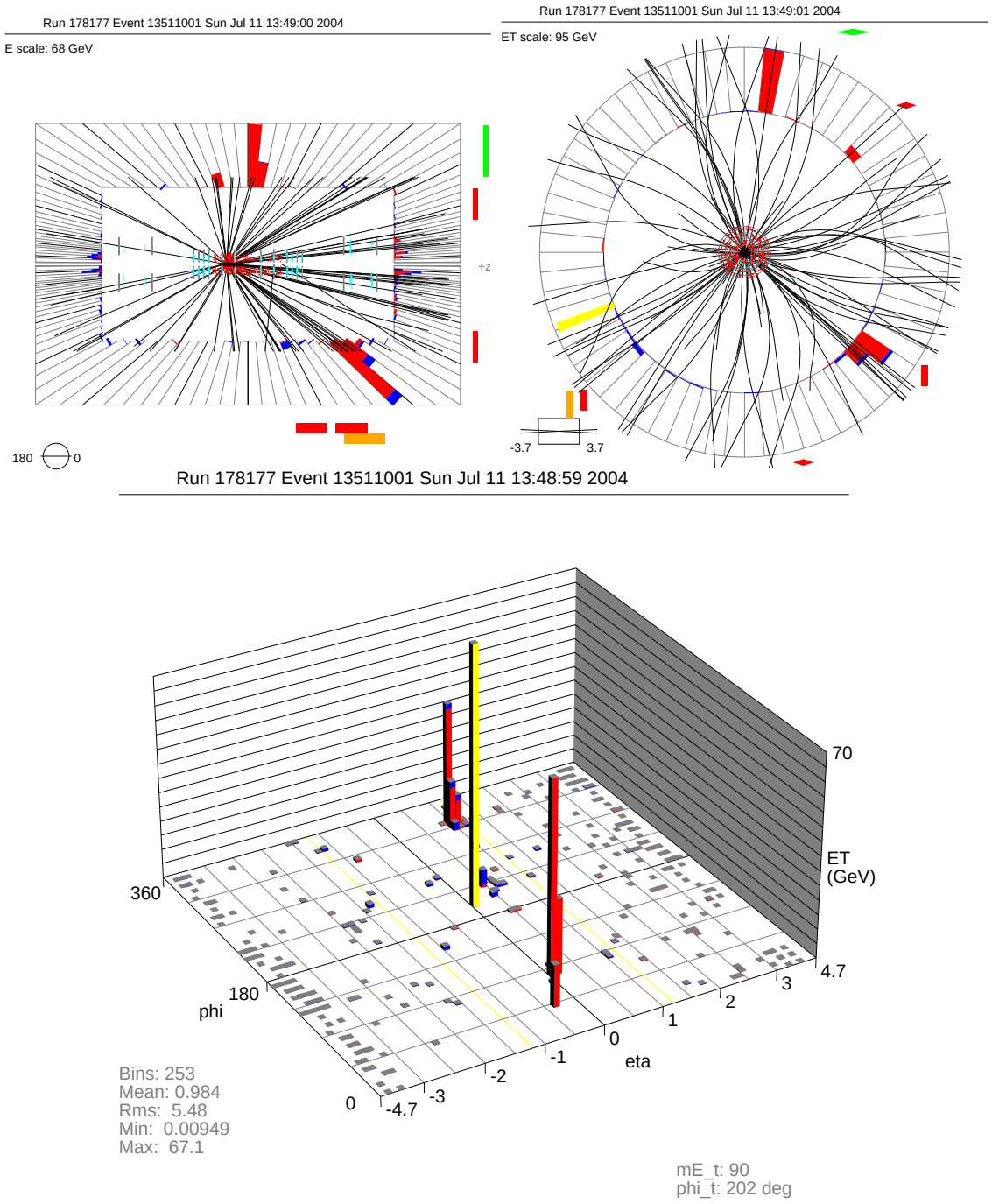

Figure C.3: Run 178177 Event 13511001: RZ view (upper right), XY view (upper left), Lego view (lower).

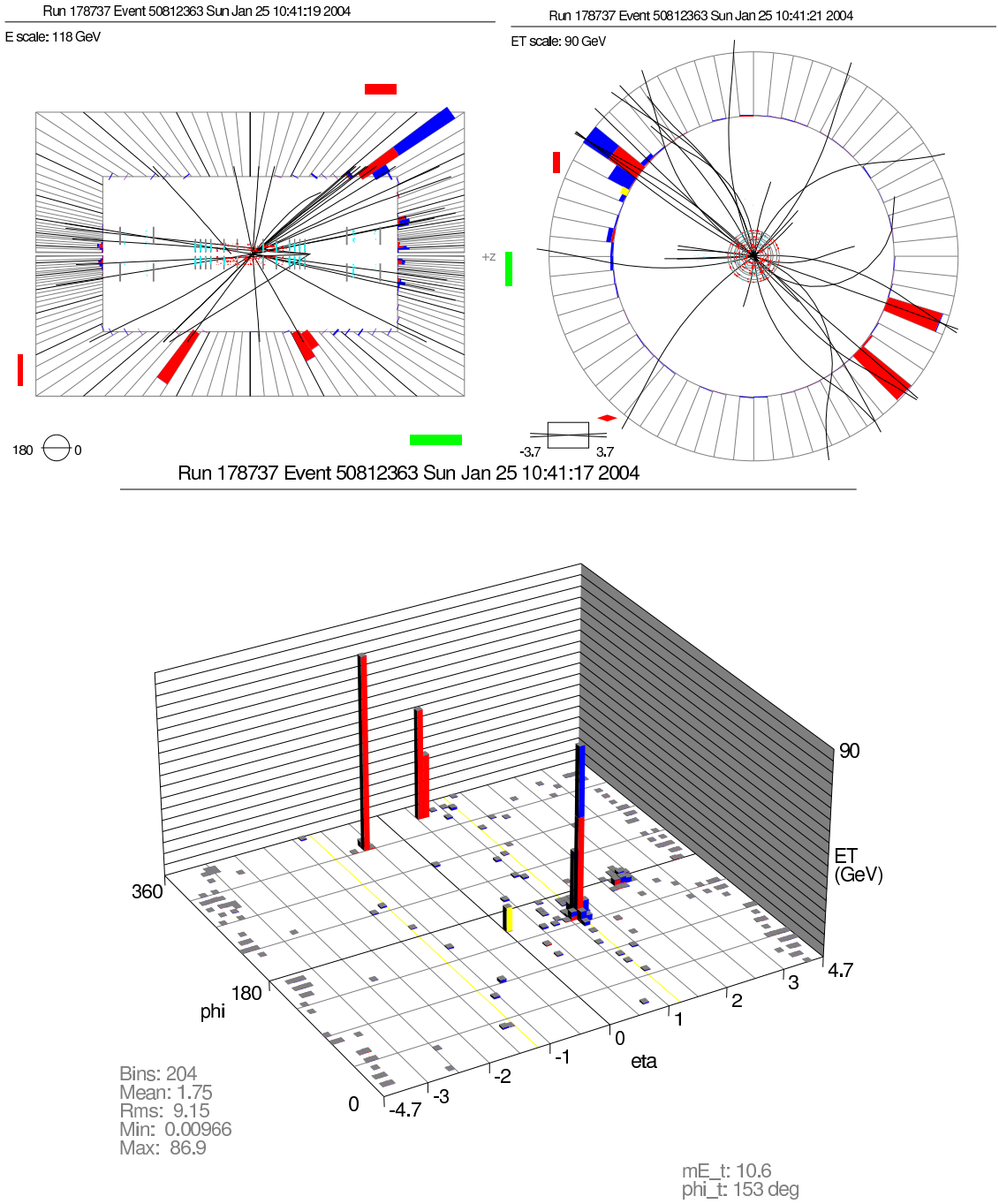

Figure C.4: Run 178737 Event 50812363: RZ view (upper right), XY view (upper left), Lego view (lower).

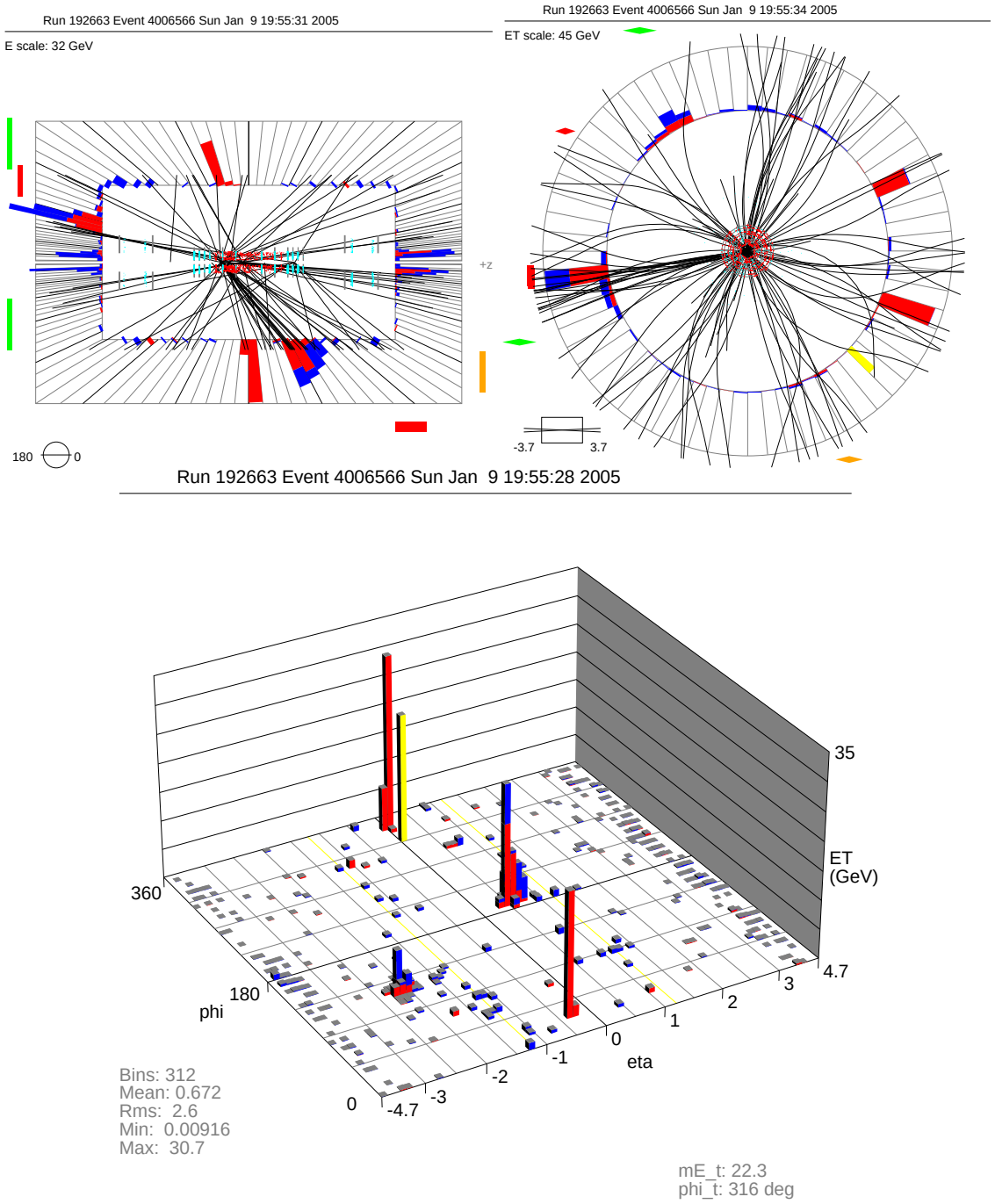

Figure C.5: Run 192663 Event 4006566: RZ view (upper right), XY view (upper left), Lego view (lower).

Bibliography

[1] J. Thomson, Philosophical Magazine, Vol. 44, Series 5, 293 (1897).

[2] N. Bohr, Philosophical Magazine, 26, 1 (1913); W. Heisenberg, Z. Phys. 77, 1 (1932); Philosophical Magazine,27, 488 (1913).

[3] E. Rutherford, Philosophical Magazine, 21, 669 (1911); Nature 92, 423 (1913).

[4] J. Chadwick, Nature, 129, 312 (1932).

[5] P. A. M. Dirac, Proc. R. Soc., London A114, 243, 710 (1927).

[6] E. Fermi, Z. Phys. 88, 161 (1934).

[7] R. P. Feynman, Phys. Rev. 76, p.749, 769 (1949); *QED : The Strange Theory of Light and matter*, Princeton University Press, Princeton, New Jersey, 1985.

[8] Y. Yukawa, Proc. Phys. Math. Soc., Japan, 17, 48 (1935).

[9] Murray Gell-Mann, Phys Lett 8, 214 (1964); G. Zweig, CERN Report No. 8182/TH401 (1964).

[10] S. L. Glashow, Nucl. Phys., 22, 579 (1961); A. Salam and J. C. Ward, Phys Lett 13, 168 (1964); S. Weinberg, Phys Lett 19, 1264 (1967).

[11] S. L. Glashow, J. Iliopoulos, and L. Maiani, Phys. Rev. D 2, 1285 (1970).

[12] A. Salam, *Elementary particle Theory*, ed. N. Svartholm (Almquist and Wiksells, Stockholm, 1969) p.367.

[13] D. Griffiths, *Introduction to Elementary Particles*, John Wiley & Sons, Inc., 1987.

[14] V. Barger and R. Phillips, *Collider Physics*, Addison-Wesley, 1987.

[15] F. Halzen, A. Martin, *Quarks and Leptons: An Introductory Course in Modern Particle Physics*, John Wiley & Sons, Inc., 1984.

[16] Chris Quigg, *Gauge Theories of the Strong, Weak, and Electromagnetic Interactions*, Addison-Wesley (1983).

[17] Gordon, L. Kane, *Modern Elementary Particle Physics*, Addison-Wesley (1993).

[18] M. Peskin, D. Schroeder, *An Introduction to Quantum Fied Theory*, Westview Press, 1995.

[19] M. K. Gaillard, P. D. Grannis, and F. J. Sciulli, Rev. Mod. Phys. 71, S96 (1999).

[20] The Super Kamiokande Collaboration, Phys. Rev. Lett. 81, 1562 (1998).

[21] L. Alvarez-Guamè, et al., *Particle Data Group*, Phys. Lett. B 592, 246 (2004).

[22] P. W. Higgs, Phys. Lett. 12, 132 (1964); Phy. Rev. 145, 1156 (1966); F. Englert and R. Brout, Phys. Rev. Lett. 13, 321 (1964).

[23] UA1 Collaboration, Phys. Lett. B 122, 103 (1983); Phys. Lett. B 126, 398 (1983).

[24] UA2 Collaboration, Phys. Lett. B 122, 476 (1983); Phys. Lett. B 129, 130 (1983).

[25] S. Abachi, et al., Phys Rev Lett 74:2632-2637, 1995.

[26] F. Abe, et al., Phys Rev Lett 74:2626-2631, 1995.

[27] C. Campagnari and M. Franklin, Rev. of Mod. Phys. 69,137 (1997).

[28] S. J. Wimpeny and B. L. Winer, Ann. Rev. Nucl. Part. Sci. 46, 149 (1996).

[29] D. Chakraborty, J. Konigsberg, D. Rainwater, Ann. Rev. Nucl. Part. Sci. 53:301-351,2003.

[30] P. C. Bhat, H. B. Prosper and S. S. Snyder, Int. J. Mod. Phys. A13, 5113 (1998).

[31] M. Kobayashi and T. Maskawa, Prog. Theor. Phys. 49,652 (1973).

[32] M. L. Perl et al, Phys Rev Lett 35,1489 (1975).

[33] S. W. Herb et al, Phys Rev Lett 39,252 (1977).

[34] Ch. Berger et al, Phys. Lett. B 76, 243 (1978); J. K. Bienlein et al, Phys. Lett. B 78, 360 (1978); C. W. Darden Phys. Lett. B 76, 246 (1978).

[35] J. H. Kuhn, arXiv: hep-ex/9707321.

[36] E. Leader and E. Predazzi *An Introduction to gauge Theories and The New Physics*, Cambridge University, Cambridge, UK,p.76.

[37] D. Schaile and P. M. Zerwas, Phys Rev D 45,3262 (1992).

[38] G. L. Kane and M. E. Peskin, Nucl. Phys. B 195,29 (1982).

[39] C. Albajar et al (UA1 Collaboration), Phys. Lett. B 256, 121 (1991) [Erratum-idid B 262, 497 (1991)].

[40] ARGUS Collaboration, Phys. Lett. B 192, 245 (1987); CLEO Collaboration, Phys. Rev. Lett. 71, 1680 (1993);

[41] L. Montanet et al, *Review of Particle Properties, Particle Data Group*, Phys Rev D 50:1173-1823 (1994).

[42] W. Bartel et al, Phys. Lett. B 146, 437 (1984).

[43] *Review of Particle Properties, Particle Data Group*, Phys. Lett. B 239, PVII, 167 (1990).

[44] Yoshida et al, Phys. Lett. B 198, 570 (1987); Adachi et. al., Phys. Rev. Lett. 60, 97 (1988); Igarashi et al, Phys. Rev. Lett. 60, 2359 (1988); Sagawa et. al., Phys. Rev. Lett. 60, 93 (1988); K. Abe et. al., Phys. Lett. B 234, 382 (1990).

[45] Abrams et al, Phys. Rev. Lett.63, 2447 (1989); Abreu et. al., Phys. Lett. B 242, 536 (1990);Abreu et al, Nucl. Phys. B 2367, 511 (1991); Akrawy et. al., Phys. Lett. B 236, 364 (1990); Decamp et. al., Phys. Lett. B 236, 511 (1990); Adriani et. al., Phys. Rep. 236, 1 (1993).

[46] M. mangano and T. Trippe, Phys. Rev. D 54, 309 (1994).

[47] C. Rubia, *Physics Results of the UA1 Collaboration at the CERN $p\overline{p}$ Collider*, CERN-EP/84-135,*Invited Talk given at Int. Conf. on Neutrino Physics and Astrophysics, Dortmund, West Germany, June 11-16, 1984.*

[48] G. Arnison et al (UA1 Coll.), Phys. Lett. B 147, 493 (1984).

[49] J. P. Revol, *Proceedings of the 6th Workshop on Grand Unification* (World Scientific, Singapore) p.275.

[50] C. Albajar et al (UA1 Coll.), Z. Phys. C 37, 505 (1988).

[51] C. Albajar et al (UA1 Coll.), Z. Phys. C 48, 1 (1990).

[52] T. Akessan et al (UA2 Coll.), Z. Phys. C 46, 179 (1990).

[53] F. Abe et al (CDF Coll.), Phys. Rev. Lett. 64, 147 (1990).

[54] F. Abe et al (CDF Coll.), Phys. Rev. Lett. 64, 142 (1990); Phys. Rev. D. 43, 664 (1991).

[55] F. Abe et al (CDF Coll.), Phys. Rev. Lett. 68, 447 (1992); Phys. Rev. Lett. 68, 3398 (1992); Phys. Rev. Lett. 69, 28 (1992); Phys. Rev. D. 45, 1448 (1992); Phys. Rev. D. 45, 3921 (1992).

[56] F. Abe et al (CDF Coll.), Phys. Rev. Lett. 68, 447 (1992); Phys. Rev. D. 45, 3921 (1992).

[57] S. Abachi et al (DØ Coll.), Phys. Rev. Lett. 724, 2138 (1994).

[58] F. Abe et al (CDF Coll.), Phys. Rev. Lett. 73, 225 (1994).

[59] S. Abachi et al (DØ Coll.), Phys. Rev. Lett. 74, 2422 (1995); Phys. Rev. Lett. 74, 2632 (1995); Phys. Rev. Lett. 75, 3226 (1995); Phys. Rev. D. 52, 4877 (1995).

[60] S. Abachi et al (DØ Coll.), Phys. Rev. Lett. 74, 2632 (1995).

[61] F. Abe et al (CDF Coll.), Phys. Rev. Lett. 74, 2626 (1995).

[62] S. Abachi et al (DØ Coll.), Phys. Rev. Lett. 85, 256 (2000).

[63] S. Abachi et al (DØ Coll.), Phys. Rev. Lett. 87, 102001 (2001).

[64] F. Abe et al (CDF Coll.), Phys. Rev. D 59, 092001 (1999).

[65] V. M. Abazov et al (DØ Coll.), Nature 429, 638 (2004).

[66] P. W. Higgs, Phys. Lett. 12, 132 (1964); Phys. Rev. Lett. 12, 508 (1964); Phys. Rev. 145, 1156 (1966); F. Englert and R. Brout, Phys. Rev. Lett. 13, 321 (1964); G. S. Guralnik, C. R. Hagen and T. W. B. Kibble, Phys. Rev. Lett. 13, 585 (1964).

[67] S. Willenbrock, hep-ph/0211076 (2002).

[68] *LEP Electroweak Working Group* http://lepewwg.web.cern.ch/LEPEWWG/ (2004).

[69] *LEP Collaboration*, arXiv:hep-ex/0312023.

[70] *Particle Data Group, Review of Particle Properties*, Phys Lett. B 592, 246 (2004).

[71] B. W. Harris et. al., Phys. Rev. D 40, 66 (2002).

[72] V. M. Abazov et al (DØ Coll.), Phys. Lett. B 622, 265 (2005).

[73] H. L. Lai et. al., Eur. Phys. J. C 12, 375 (2000).

[74] E. Berger and H. Contopanagos, Phys. Rev. D 57, 253 (1998).

[75] P. Nason, S. dawson and R. K. Ellis, Nucl. Phys. B 303, 607 (1988); W. Beenakker, H. Kuijf, W. L. van Neerven and J. Smith, Phys. Rev. D 40, 54 (1989).

[76] S. Catani et al, Nucl. Phys. B 478, 273 (1996); Phys. Lett. B 378, 329 (1996).

[77] R. Bociani, S. Catani,, M. L. Mangano and P. Nason, Nucl. Phys. B 529, 424 (1988).

[78] M. Cacciari et. al., JHEP. 404, 68 (2004).

[79] N. Kidonakis and R. Vogt, Phys. Rev. D 68, 114014 (2003).

[80] N. Kidonakis and R. Vogt, Eur. Phys. J. C33, s466 (2004).

[81] S. Catani et. al., arXiv:hep-ph/0005233.

[82] T. Affolder et. al. (CDF Coll.), Phys. Rev. Lett. 86, 3233 (2001).

[83] D. Acosta et. al. (CDF Coll.), arXiv: hep-ex/0505091.

[84] (DØ Coll.),DØ note 4833 (2005).

[85] C. T. Hill and S. J. Parke, Phys. Rev. D. 49, 4454 (1994).

[86] H. P. Niles, Phys. Rep. 110, 1 (1984); H. E. haber and G. L. Kane, Phys. Rep. 117, 75 (1985).

[87] R. M. Harris, C. Hill and S. J. Parke, hep-ph/9911288 (1999).

[88] E. Simmons, hep-ph/0011224 (2000).

[89] V. M. Abazov et al (DØ Coll.), Phys. Rev. D 67, 012004 (2003).

[90] T. Affolder et.al (CDF Coll.), Phys. Rev. D 64, 032002 (2001).

[91] V. M. Abazov et al (DØ Coll.), Phys. Lett. B 626, 45 (2005).

[92] V. M. Abazov et al (DØ Coll.), Phys. Lett. B 626, 35 (2005).

[93] V. M. Abazov et al (DØ Coll.), Phys. Lett. B 626, 55 (2005).

[94] D. Acosta et al (CDF Coll.), arXiv: hep-ex/0504053.

[95] D. Acosta et al (CDF Coll.), Phys. Rev. D 71, 072005 (2005).

[96] D. Acosta et al (CDF Coll.), Phys. Rev. D 71, 052003 (2005).

[97] D. Acosta et al (CDF Coll.), Phys. Rev. Lett. 93, 142001 (2004).

[98] *Measurement of the $t\bar{t}$ Production Cross-Section at $\sqrt{s}$ = 1.96 TeV in Dilepton Final States using 370 pb^{-1} of DØ data*, http://www-d0.fnal.gov/Run2Physics/top/index.html **DØ Collaboration Results for Summer 2005 Conferences**.

[99] *Combination of CDF and DØ Results on top-quark mass*, arxiv:hep-ex/0507006 (2005).

[100] `http://www.fnal.govpub/about/whatis/history.html`.

[101] `http://www.totse.com/en/fringe/fringe_science/tevatron.html`.

[102] `http://d0server1.fnal.gov/projects/results/runi/highlights/runi_summary.html`

[103] `http://www-d0.fnal.gov/runcoor/RUN/run2_lumi.html`.

[104] The Large hadron Collider, `http://lhc.web.cern.ch/lhc/`.

[105] `http://www.fnal.gov/pub/about/whatis/picturebook/descriptions/00_635.html`.

[106] `http://www-ad.fnal.gov/runII/index.html`

[107] `http://www.fnal.gov/pub/inquiring/physics/accelerators/chainaccel.html`.

[108] `http://www-bd.fnal.gov/public/chain.html`.

[109] S.Eidelman et.al., Phy. Lett.B592,1(2004).

[110] T. LeCompte, H. T. Diehl, *The CDF and DØ Upgrades for Run II*, Annu. Rev. Nucl. Part. Sci., 50:71-117, 2000.

[111] DØ Collaboration, *The Upgraded DØ Detector*, to be submitted in Nucl. Instr. And Methods A.

[112] DØ Collaboration, *The DØ Upgrade : The Detector and its Physics*, Fermilab-Pub-96/357-E.

[113] S. Abachi et al., *The DØ Collaboration :The DØ detector* , Nucl. Instr. And Methods A 338, 185 (1994).

[114] *The DØ Upgrade Silicon Tracker Technical Design Report*, DØ Note 2169.

[115] *The DØ Upgrade Central Fiber Tracker Technical Design Report*, DØ Note 4164.

[116] M.Adams et al.,*Design Report of the Central Preshower Detector for the DØ Upgrade*, DØ Note 3014.

[117] J. Brzezniak, et al., *Conceptual Design of a 2 Tesla Superconducting Solenoid for the Fermilab DO Detector Upgrade*, DØ Note 2167.

[118] *The DØ Upgrade : Forward Preshower, Muon System and Level2 Trigger*, DØ Note 2894.

[119] *Design Report: The DØ Experiment at the Fermilab Proton-Antiproton Collider*, DØ Note 137 (1984).

[120] L. Groer, *DØ Calorimeter Upgrades for Tevatron Run II*, DØ Note 4240.

[121] R. Zitoun, *Study of the Non Linearity of the DØ Calorimeter Readout Chain*, DØ Note 3997.

[122] Junjie Zhu, Ph.D. Thesis, University of Maryland (2004).

[123] B. Abbott et al. (*DØ* Collaboration), Phys. Rev. Lett. **80** (1998); Phys. Rev. **D58** (1998).

[124] *DØ Run II Level 1 Trigger Framework Technical Design Report"*, http://www.pa.msu.edu/hep/d0/ftp/l1/framework/l1fw_tdr_05june98.txt.

[125] D. Edmunds et al., DØ Note **3402** (1998).

[126] A. Boehnlein et. al., DØ Note **3630** (1999).

[127] M. Adams et. al.,DØ Note **3651** (1999).

[128] `http://d0db.fnal.gov/trigdb/cgi/trigdb_main.py`.

[129] B. Vachon, et al., DØ Note 4512 (2004).

[130] `http://www-d0.fnal.gov/Run2Physics/top/d0_private/wg/top_analyze`

[131] M. Klute et. al., *Top Group Root-tuples selection and Data Quality Monitoring*, DØ Note 3942, 2002

[132] *The DØ Run Quality Data Base*, http://d0db-prd.fnal.gov/run/runQuery.html

[133] L. Duflot, et al., *cal_event_quality Package*,DØ Note 4614.

[134] `http://www-d0.fnal.gov/~d0upgrad/d0_private/software/jetid/certification/Macros/Runsel/v5.1/runselection.summary`

[135] `http://www-d0.fnal.gov/d0dist/dist/releases/development/top_dq`

[136] K. Ranjan, Ashish Kumar, B. Choudhary and R. Kehoe,*Calorimeter Event Quality Using Level 1 Confirmation*, DØ Note 4554 (2004).

[137] C. Corcella, et al., *Herwig 6.5*, hep-ph/0011363, 2001.

[138] M. Mangano, et al., hep-ph/0206293,2003.

[139] T. Sjöstrand, L. Lönnbald, *Pythia 6.2*, hep-ph/0108264,2001.

[140] J. Pumplin, et al., *New Generation of Parton Distributions with Uncertainties from Global QCD Analysis*, JHEP 0207:012, 2002.

[141] D. Lange, et al., *The EvtGen Event Generator Package*, Proceedings of CHEP, 1998.

[142] S. Jadach, et al., *TAUOLA Library Version 2.5.*, Comp. Phys. Comm.,76:361, 1993.

[143] R. Brun and F. Carminati, CERN Program Library Long Writeup W5013, 1993.

[144] R. Field, `http://www.phys.ufl.edu/~rfield/cdf/tunes/rdf_tunes.html`

[145] S. Anderson, ..Ashish Kumarr, et al., *Measurement of the ttbar Production Cross-section at center of mass energy 1.96 TeV in Dilepton Final States*, DØ Note 4683, (2004).

[146] B. Olivier et al., DØ Note 3687 (2000).

[147] J. Kozminski et. al., *Electron Likelihood for p14*, DØ Note 4449 (2004).

[148] Ashish Kumar et. al., *Electron Likelihood Study*, DØ Note 4769 (2005).

[149] L. Lyons, *Statistics for Nuclear and Particle Physicists*, Cambridge University Press, 1986.

[150] C. E. Gerber et al.,DØ Note 4655 (2004).

[151] S. Jain, DØNote 4402 (2004).

[152] G. Blazey, et al., DØ Note 3750 (2000).

[153] J-R. Vlimant, et al., DØ Note 4146 (2003).

[154] G. Bernardi, et at, DØ Note 4335 (2004).

[155] `http://www-d0.fnal.gov/computing/algorithms/calgo /jet/jetID_p14.html`.

[156] J. L. Agram et al., DØ Note 4720 (2005).

[157] M. Agelou, et al., DØ Note 4419 (2004).

[158] A. Kumar, et al.,*Missing Transverse Energy Studies in $Z \to ee + X$ and $Z \to \mu\mu + X$ Events*, DØ Note 4480, 2004.

[159] A. Kumar, et al.,*Oversmearing of Missing Transverse Energy in $Z \to ee + X$ Monte Carlo Events*, DØ Note 4551, 2004.

[160] http://www-d0.fnal.gov/trigger/stt/doc/svtstat_970307/svtbeam.html.

[161] D. Chapin et. al., DØ Note **4403** (2004).

[162] A. Schwartzman and M. Narain, DØ Note 3907 (2001).

[163] D. Adams et. al., DØ Note **2958** (1996); H. Greenlee, DØ Note **4303** (2003).

[164] A. Khanov, DØ Note **3778** (2000); G. Hesketh, DØ Note **4079** (2003); H. Greenlee, DØ Note **4180** (2003); H. Greenlee, *DØ* Note **4293** (2003).

[165] J. M. Campbell and R. K. Ellis, Phys. Rev. D. 60, 113006 (1999).

[166] P. Söding, G. Wolf, Ann. Rev. Nucl. Part. Sci. 31:231-93, 1981.

[167] N. Amos, et al., DØ Note 2791 (1996).

[168] V. M. Abazov et al (DØ Coll.), Phys. Rev. D. 71, 072004 (2005).

[169] S. Anderson ... Ashish Kumar et al.,*Measurement of the ttbar Production Cross section at $\sqrt{s} = 1.96$ TeV in ee and $\mu\mu$ final states using 370 pb^{-1} of data*, DØ Note 4827, 2005.

[170] L. Dixon, Z. Kunszt, and A. Signer, arXiv: hep-ph/9907035.

[171] S. Anderson ... Ashish Kumar et al.,*Measurement of the ttbar Xsec in the dilepton channels at sqrt(s) = 1.96 TeV (topological)*, DØ Note 4420, 2004.

[172] T. Edwards, et al., DØ Note 4328 (2004).

[173] E.Barberis, J.-F. Grivaz, M. Kado, DØ Note 4246 (2003).

[174] M. Besancon, F. Deliot and V. Shary, DØ Note 4877 (2005).

[175] E. Busato's Talk in Hadron Collider Physics Symposium, July 4-9, 2005, Les Diablerets, Switzerland.